

**Structure and dynamics of molecules and molecular aggregates in
gas phase studied by femtosecond spectroscopy**

Dissertation

zur Erlangung des Doktorgrades der Naturwissenschaften

vorgelegt beim Fachbereich Biochemie, Chemie und Pharmazie (FB 14)
der Goethe-Universität
in Frankfurt am Main

von

Maksim Kunitski
aus Gresk, Weißrussland

Frankfurt 2009

(D30)

vom Fachbereich Biochemie, Chemie und Pharmazie (FB 14)
der Goethe-Universität als Dissertation angenommen.

Dekan: Herr Prof. Dr. Dieter Steinhilber

1. Gutachter: Herr Prof. Dr. B. Brutschy

2. Gutachter: Herr Prof. Dr. J. Wachtveitl

Datum der Disputation:..... 22 Juni 2010

to my mother and wife...

Abstract

Large amplitude intramolecular motions in non-rigid molecules are a fundamental issue in chemistry and biology. The conventional approaches for study these motions by far-infrared and microwave spectroscopy are not applicable when the molecule is non-polar. Therefore, in the current thesis an alternative approach for the investigation of large amplitude intramolecular motions was developed and tested. This new method is based on femtosecond rotational degenerate four-wave mixing spectroscopy (fs DFWM), which is a particular implementation of rotational coherence spectroscopy. The method was successfully applied for the investigation of pseudorotation in pyrrolidine and the ring-puckering vibration in cyclopentene.

Another important subject is the photophysics of molecules and molecular clusters which have an ultrashort lifetime of their electronically excited state (photoreactivity). These ultrashort lifetimes often represent a protective mechanism causing photostability. The photoreactivity is usually the manifestation either of an “elementary” reaction, such as proton or electron transfer, which occurs in the excited state or of a fast non-radiative deactivation processes, such as internal conversion *via* conical intersection of the electronically excited and ground state. Due to a short-lived excited state, the conventional vibrational spectroscopic methods, such as IR depletion detected by resonance two-photon ionization spectroscopy (IR/R2PI), are not applicable for the structural investigation of these systems. Therefore, new approach, termed IR depletion detected by multiphoton ionization with femtosecond laser pulses (IR/fsMPI), was developed for studying the structure of photoreactive microsolvated molecules. The IR/fsMPI technique was applied for investigating the clusters of 1*H*-pyrrolo[3,2-*h*]quinoline with water/methanol as well as adenine- and 9-methyl-adenine-hydrates.

In addition, the excited state dynamics of bifunctional azaaromatic molecule 7-(2'-pyridyl)indole (7PyIn) was studied by femtosecond pump-probe resonance excitation multiphoton ionization technique (fs REMPI). Under electronic excitation of this molecule a fast proton transfer (phototautomerization) takes place, which is followed by radiationless excited state deactivation process. The fs REMPI spectra lead to the conclusion that the phototautomerization in 7PyIn is coupled with a twisting of the molecule, and that the twisting provides an efficient channel for ultrafast radiationless excited state deactivation. This pattern of excited-state tautomerization/deactivation might be quite general.

Contents

1	Introduction	1
2	Methods and Instruments	5
2.1	Generation of femtoseconds pulses.....	6
2.1.1	Femtosecond laser setup	6
2.1.2	Generation of the second and the third harmonics.....	7
2.1.3	TOPAS	8
2.1.4	Inverted autocorrelator	9
2.2	Femtosecond Degenerate Four-Wave Mixing	12
2.2.1	Introduction	12
2.2.2	Technique	13
2.2.3	Theory of the pump-probe non-resonant degenerate four wave mixing signal	15
2.2.4	Simulation of fs DFWM spectra	17
2.2.5	Preparation of the gas phase sample	21
2.2.5.1	Gas cell with the heat-pipe principle	21
2.2.5.2	Molecular beams.....	24
2.3	Vibrational analysis of molecular clusters by IR/fsMPI	25
2.3.1	Introduction	25
2.3.2	Conventional ns IR/R2PI	26
2.3.3	IR/fsMPI principle	27
2.3.4	Experimental IR/fsMPI setup.....	28
2.3.5	The source of infrared radiation	30
2.3.6	Nozzle source	32
2.3.7	Dual beam technique.....	35
2.4	Pump-probe Resonant Excitation Multiphoton Ionization.....	37

3	Results.....	38
3.1	Femtosecond Degenerate Four-Wave Mixing experiments	38
3.1.1	Missing levels lead to additional lines: the influence of nuclear spin statistics on femtosecond degenerate four wave mixing spectroscopy of polyatomic systems.....	39
3.1.2	Large amplitude intramolecular motions studied by fs DFWM: pyrrolidine and cyclopentene molecules.....	45
3.2	Structure and Dynamics of short-lived excited state molecules and clusters	54
3.2.1	Structural characterization of 1 <i>H</i> -pyrrolo[3,2- <i>h</i>]quinoline microhydrates with ultrashort-lived electronically excited states	54
3.2.2	Proton transfer with a twist? Femtosecond dynamics of 7-(2'-pyridyl)indole in supersonic jets	61
3.2.3	Structure of adenine monohydrates by femtosecond multiphoton ionization detected IR spectroscopy	65
4	Overview and Future Perspectives	70
5	Bibliography.....	72
6	Summary	81
7	Zusammenfassung	85
8	Personal contribution to the papers	90
9	Publications	93
9.1	Missing levels lead to additional lines: the influence of nuclear spin statistics on femtosecond degenerate four wave mixing spectroscopy of polyatomic systems.....	93
9.2	Pseudorotation in pyrrolidine: rotational coherence spectroscopy and ab initio calculations of a large amplitude intramolecular motion.....	103
9.3	Ring-puckering motion in cyclopentene studied by time-resolved rotational coherence spectroscopy and ab initio calculations	115
9.4	Detection and structural characterization of clusters with ultrashort-lived electronically excited states: IR absorption detected by femtosecond multiphoton ionization.....	129
9.5	Separation of different hydrogen-bonded clusters by fs UV-ionization-detected infrared spectroscopy: 1 <i>H</i> -pyrrolo[3,2- <i>h</i>]quinoline•(H ₂ O)(<i>n</i> =1,2) complexes	133

9.6 Proton transfer with a twist? Femtosecond dynamics of 7-(2'-pyridyl)-indole in condensed phase and in supersonic jets	143
9.7 The structure of adenine monohydrates studied by femtosecond multiphoton ionization detected IR spectroscopy and quantum chemical calculations.....	149
Acknowledgments.....	159
Curriculum Vitae	161

List of Figures

Fig. 2.1-1	The femtosecond laser setup. 1 - autocorrelator, 2 - spectrometer, 3 - fast photodiode.....	7
Fig. 2.1-2	The optical scheme of third harmonic generation.....	8
Fig. 2.1-3	TOPAS output energies vs. wavelength. The wavelengths produced by down-conversion of the signal radiation are shown in blue, whereas the wavelengths originated from idler radiation are shown in green. S – signal, I – idler, SHS – second harmonic of signal, SHI – second harmonic of idler, SFS – sum frequency of signal (with 800 nm), SFI – sum frequency of idler (with 800 nm), FHS – fourth harmonic of signal, FHI – fourth harmonic of idler, SH(SFS) – second harmonic of sum frequency of signal, SH(SFI) – second harmonic of sum frequency of idler.	9
Fig. 2.1-4	The inverted single-shot autocorrelator (left) and standard single-shot autocorrelator (right).	11
Fig. 2.2-1	Left: Formation of a polarization grating by two femtosecond laser pulses (pump). Right: Probing the grating with the third femtosecond pulse (probe). The fourth pulse (signal) is a Bragg scattering of the third probe pulse at the polarization grating.	13
Fig. 2.2-2	The energy diagram of the femtosecond pump-probe non-resonant degenerate four-wave mixing. $ g\rangle$ is the rotational manifold of the vibronic ground state. The pump pulses 1 and 2 are coinciding in time, as well as probe pulse 3 and signal 4	14
Fig. 2.2-3	The optical scheme of the fs DFWM experiment.	14
Fig. 2.2-4	Vapour cell based on the heat-pipe principle.....	23
Fig. 2.3-1	Energetic diagram of the conventional nanosecond IR/R2PI method.	26
Fig. 2.3-2	One-color (267 nm) two-photon ionization scheme of PQ:methanol (left) and corresponding mass spectra obtained with the femtosecond and nanosecond laser pulses under the same experimental conditions (right).	28
Fig. 2.3-5	The IR-OPO laser: 1 – polarizer, 2 – OPO resonator, 3 – pyroelectric detectors, 4 – prism, 5 – delay stage.	30
Fig. 2.3-7	The normalized ion signals of two monomers and two clusters: 1Me-Adenine (red), Thymine (black), (1Me-Adenine)-(H ₂ O) complex (blue) and (1Me-Adenine)-(Thymine) hetero-dimer (green).	35
Fig. 2.3-8	Left: Principle of the dual beam technique; Right: the corresponding TOF spectrum of adenine with water.	36
Fig. 2.3-9	The IR/fsMPI spectra of adenine: (a) ion signal of S and R peaks, (b) the ratio of the signal to reference.....	36

Fig. 2.3-10	The energetic diagram of the fs pump-probe REMPI.....	37
Fig. 3.1-1	a), b) and c) Schematic view of sulphur dioxide (SO ₂), nitrogen dioxide (NO ₂) and nitromethane (CH ₃ NO ₂) molecules, respectively, with principal axes of inertia.....	39
Fig. 3.1-2	The frequency and corresponding time-domain spectra of two diatomic molecules having the same rotational constant <i>B</i> : top – with two <i>non-identical</i> nuclei, bottom – with the <i>identical zero spin</i> nuclei.	40
Fig. 3.1-3	Left: Simulations of the fs DFWM spectra of SO ₂ and NO ₂ . a) and b) - SO ₂ , c) and d) - NO ₂ without/with consideration of nuclear spin statistics. Right: Experimental and simulated fs DFWM spectra of nitromethane: e) Fitted simulation of the spectrum using nuclear spin statistics, f) Experimental fs DFWM spectrum (this work), g) Simulation of the spectrum without consideration of nuclear spin statistics. For assignment of rotational recurrences see text.	42
Fig. 3.1-4	Simulations of the rotational quantum beat frequency spectrum of nitromethane. Only $\Delta J=2$, $\Delta \tau=+2$ transitions are taken into account. All <i>J</i> manifolds contribute, without/with consideration of nuclear spin statistics, respectively.	43
Fig. 3.1-5	Two out-of-plane modes of a five-membered ring.....	45
Fig. 3.1-6	The two dimensional potential of the skeletal motion of pyrrolidine and two minima energy structures of pyrrolidine: equatorial and axial. Two ways of going from the equatorial to the axial conformers are shown by arrowed lines: dashed – ring inversion, solid – pseudorotation.....	46
Fig. 3.1-7	The envelope structures of pyrrolidine and corresponding pseudorotational angles ϕ . In all these structures four atoms of the ring are in one plane, while the fifth one (indicated by a red arrow) is not. This pucker rotates around the ring during pseudorotation.	46
Fig. 3.1-8	The two dimensional potential for the skeletal motion of cyclopentene. The arrowed line shows the ring inversion path.	47
Fig. 3.1-9	Left: Pseudorotational potential and corresponding levels with their relative Boltzmann populations at temperatures of 68K (a) and 298K (b). Right: The probability density functions of the first six pseudorotational levels. The parity of levels is shown by red (even) and blue (odd) colors.	48
Fig. 3.1-10	The experimental fs DFWM spectrum (red) of pyrrolidine at room temperature (298K) and the fitted simulation (blue), using the one-dimensional model for pseudorotation.....	49
Fig. 3.1-11	The energy potential and the rotational constants <i>A</i> and <i>B</i> of pyrrolidine along the pseudorotational path: red – from the fitted simulation of fs DFWM spectrum at room temperature; blue and green – calculated with the aug-cc-pVDZ basis set at both the B3LYP and MP2 levels of theory. The MP2/aug-cc-pVTZ calculations are shown by green circles. These	

List of Figures

	geometries were further used for single point CCSD(T)/aug-cc-pVTZ calculations (black crosses).....	49
Fig. 3.1-12	Two geometric parameters, an angle ϕ and a distance x , which are usually used for the description of the ring-puckering vibration.	51
Fig. 3.1-13	Fs DFWM spectra of cyclopentene in the gas cell at room temperature: red - experimental, blue - fitted simulation based on the one-dimensional model for the ring-puckering vibration.	52
Fig. 3.1-14	Dependence of the rotational constants A and B on the reduced puckering coordinate Z : red - calculated at B3LYP/cc-pVTZ; dark blue squares - calculated at SOSMP2/cc-pVDZ; green - derived from the fitted simulation of the experimental fs DFWM spectrum of cyclopentene at room temperature (standard deviation is shown by error bars); blue dashes - taken from the MW work of Lopez et al. [94]; black dashes - taken from the MW work of Scharpen [93] The dashed vertical line indicates the equilibrium reduced puckering coordinate Z_{min} deduced from the fit. $\phi/Z \approx 13.75$	53
Fig. 3.2-1	IR/fsMPI spectra measured for PQ:methanol _{1,2} mass channels. The calculated IR spectra (B3LYP/6-31G**) are plotted with bars. Relevant cluster structures are inserted.	55
Fig. 3.2-2	A comparison of the FDIR spectrum (a) measured upon excitation of the transition at 28061 cm^{-1} with the IR/fsMPI spectra recorded in (b) $1^+:2$, (c, e) $1^+:1$, and (d) $1^+:0$ cluster channels. The spectrum e) was recorded at lower water concentration than the c) one. The inserted mass spectrum shows the corresponding cluster ion distribution. The dotted lines indicate: blue – bands of 1:2 clusters; red – bands of the 1:1 cluster; dark - free OH stretch.....	57
Fig. 3.2-3	The ground state vibrational spectra of the 1:1 (a, red) and 1:2 (c) complexes. The “IR fingerprints” of the relevant cluster structures, calculated at the B3LYP/cc-pVDZ level of theory, are depicted by the stick spectra (b, d-f).	58
Fig. 3.2-4	Normal modes showing H-bonded NH and OH stretching motions, calculated for the 1:1 and 1:2 PQ/water complexes: a) 3314 cm^{-1} , b) 3155 cm^{-1} , c) 3349 cm^{-1} , d) 3300 cm^{-1} , e) 3103 cm^{-1}	59
Fig. 3.2-5	The two rotameric structures of 7-(2'-pyridyl)indole.	61
Fig. 3.2-6	Left: pump-probe REMPI spectra (\circ) obtained in a supersonic jet for normal and its N-deuterated analogue (∇); solid lines are the results of the fitting procedure. Right: oscillatory components of the data and their Fourier transforms (inset).....	62
Fig. 3.2-7	The ionization-detected absorption of three pyridylindoles.	63
Fig. 3.2-8	Schematic primary hydration sites of 9H-adenine and 9-methyladenine.	65

-
- Fig. 3.2-9** IR/fsMPI spectra of the 9-methyladenine:water (left) and adenine:water (right) complexes compared to calculated stick spectra. The corresponding cluster geometries are shown as well.66
- Fig. 3.2-10** The fragmentation pattern of the adenine hydrates in the monomer mass channel $1:0^+$ (left) and the energy diagram that shows possible dissociation paths in the ground, electronic excited and cationic states (right). Δk denotes change of a process rate after IR absorption.67

List of Tables

- Table 2.2-1** Symmetry classification of rotational levels in the D_2 group.19

List of Acronyms

PQ	1 <i>H</i> -pyrrolo[3,2- <i>h</i>]quinoline
7PyIn	7-(2'-pyridyl)indole
Ade	Adenine
9mAde	9-methyladenine
fs DFWM	Femtosecond Degenerate Four-Wave Mixing
IR/fsMPI	Infrared femtosecond multi photon ionisation
REMPI	Resonance excitation multiphoton ionization
RCS	Rotational Coherence Spectroscopy
SHG	Second Harmonic Generation
THG	Third Harmonic Generation
IR/R2PI	IR depletion detected by resonant two-photon ionization
TOF	Time-of-flight spectrometer
TOPAS	Traveling-wave optical parametric amplifier of superfluorescence
CPA	Chirped pulse amplification
ESPT	Excited state proton transfer
BBO	β -BaB ₂ O ₄
RIPS	Raman-induced polarization spectroscopy
CARS	Coherent anti-Stokes Raman spectroscopy
IVR	Intramolecular vibrational energy redistribution
FFT	Fast Fourier Transform
DFM	Difference Frequency Mixing
OPO	Optical Parametric Oscillator
MW	Microwave spectroscopy

1 Introduction

Rotation and vibrations of molecule as well as elementary reactions like proton and electron transfer, or intramolecular processes like internal conversion occur at time scales from picoseconds (10^{-12} s) to femtoseconds (10^{-15} s). It was always a desire for chemists to observe these ultrafast processes. Recent advances in the ultrashort laser technology have made this possible and thus a series of new directions of research, called femtochemistry, was opened up. The pioneering experiments in this new area were performed by Zeweil and co-workers [1-8]. The utmost acknowledge was the award of the Noble prize in chemistry to A.H. Zeweil in 1999 for his contributions in real-time monitoring of transition states in chemical reactions [3, 4, 7]. Nowadays femtochemistry is one of the most rapidly developing fields in modern science. It addresses a wide range of problems from fundamental physical investigations on small molecules to materials science and biology.

Most of the ultrafast experiments on molecular dynamics have been carried out using the pump-probe technique [8]. A variety of different pump-probe schemes has been developed [1, 8]. The basic principle remains however the same. Namely, a first femtosecond pulse (pulses), called pump, prepares the system under investigation in a nonequilibrium state, and thus defines the time zero. The subsequent time evolution of the state is monitored by another femtosecond pulse (pulses), referred to as a probe, at successive time delays.

One of the applications of the ultrafast pump-probe technique is to study the dynamics of molecular rotation. The femtosecond pump pulse, due to the broad spectral bandwidth, can coherently excite many rotational levels within a given vibronic manifold, producing a coherent superposition state (rotational wavepacket). The time evolution of this state gives rise to rotational coherence effects, which can be monitored by the probe pulse using different detection schemes [9]. The rotational coherence effects appear in the experimental observations as equidistant sequences (pattern) of signals, called recurrences or transients. The positions of these transients depend in a simple way on the rotational constants of the species being studied [9]. Therefore such experiments can be useful in gaining structural information about a molecule of interest. This new spectroscopic technique was termed Rotational Coherence Spectroscopy (RCS) [9].

The time-domain approach to rotational spectroscopy has a significant advantage over the conventional frequency-domain methods. This is due to the fact that with increasing size of a species, the spacing between rotational levels decreases, which results in congestion of

frequency spectrum. Contrary to that the time-resolved rotational spectrum becomes sparser with increase of the species size, since the separation of the recurrences is proportional to the moments-of-inertia.

Femtosecond Degenerate Four-Wave Mixing (fs DFWM) [10-14], a particular implementation of RCS, has proven to be a powerful tool for studying the structure of non-polar molecules. Recently we have extended the scope of this method towards investigation of the dynamics of large amplitude intramolecular motions. Fs DFWM spectroscopy was successfully applied for gaining insight into pseudorotation of pyrrolidine and the ring-puckering vibration of cyclopentene. Both molecules belong to the biologically relevant group of five-membered ring compounds.

Another application of pump-probe technique is the observation of the excited state dynamics of molecules or molecular aggregates. This can be done as follows. The pump pulse excites a molecule or a molecular complex from its initial into some electronically excited state, the dynamics of which is going to be studied. A delayed probe pulse transfers the system from the excited state to another state that can be easily detected by some means. By variation of the time delay between pump and probe pulses, the population dynamics of the excited state may be monitored. Commonly, the probe wavelength is tuned to ensure the ionization of the excited molecules by either one or multi photon absorption. The produced ion current can be measured by means of Time-Of-Flight (TOF) mass spectrometry, which additionally allows for mass selection – a mandatory requirement for clusters studies. This technique is called pump-probe Resonance Excitation Multi Photon Ionization (REMPI).

Recently we have shown an application of femtosecond lasers for the vibrational spectroscopy of molecular clusters [15]. Conventionally, for this purpose, one uses the size and isomer selective double-resonance two-photon ionization detected IR depletion (IR/R2PI) spectroscopy [16-19]. It utilizes nanosecond laser pulses with wavelengths in UV and mid-infrared and allows for vibrational analysis in the region of CH, NH and OH stretches. The basic idea behind the method can be explained as follows. The molecules of the sample are initially affected by the tunable IR laser radiation. After approximately 50-100 ns the UV laser pulse is introduced to the sample; its wavelength matches the $S_1 \leftarrow S_0$ electronic transition of molecule under study, thus, allowing the efficient ionization of the molecule by the resonant two-photon ionization (R2PI). If the wavelength of the first IR laser pulse matches any vibrational transition, the ground electronic state of the molecule becomes depopulated, which results in decreasing the efficiency of R2PI. This is showed up as a depletion of the ion current, which can be detected by the TOF

spectrometer. In this way a mass-selective vibrational spectrum of the sample is recorded. In combination with quantum chemical calculations this technique provides structural information not only about monomers but also about cluster systems (microsolventations). However when the excited state life-time of the molecules is too short, in comparison to the laser pulse duration, the described method cannot be applied, since in this case the efficiency of R2PI is extremely low. Therefore, in order to study the molecules with short-lived excited state, femtosecond laser pulses should be applied at the R2PI detection step. We termed this new spectroscopic approach IR/fsMPI (IR depletion detected by multiphoton ionization with femtosecond pulses).

All three methods described above require the sample to be in the gas-phase. There are several reasons for that. Thus, rotational coherence effects, detected by RCS, arise only under collision-free conditions, since collisions change the orientation of molecules randomly, demolishing the rotational phase [9]. Collision-free in this context means that a collision rate is much slower than the rotation of a molecule (dozens of picoseconds). This condition is fulfilled neither in liquids nor in dense gases (benzene, 1 bar, 25 °C: ~100 ps between collisions). Therefore the sample pressure must usually be kept below 50 mbar (benzene, 25 °C, >2 ns between collisions) in the RCS experiments at room temperature. The other two methods: pump-probe REMPI and femtosecond two-photon ionization detected IR (IR/fsMPI) spectroscopy also imply the molecules to be isolated from any perturbative factors and to have their internal degrees of freedom cooled down. These two conditions can be only met in molecular beams under supersonic expansion. Furthermore, molecular jets are widely utilized as sources of formation of the molecular clusters.

The outline of the thesis is as follows:

In chapter 2 the laser setup designed for production of tuneable femtosecond radiation is described. The chapter proceeds with an introduction of three methods that are utilized in this work: fs DFWM (2.2), IR/fsMPI (2.3) and pump-probe REMPI (2.4). In addition the auxiliary experimental tools, which were developed in the course of this PhD work, are presented.

Chapter 3 presents the results obtained by means of the three aforementioned methods. The chapter is divided into two parts. The first part (3.1) is devoted to fs DFWM experiments. Initially, the influence of nuclear spin statistics on fs DFWM spectroscopy of polyatomic systems is considered (3.1.1). Thus, it will be shown that for the molecules, which have identical nuclei about one of the principal axis of inertia, additional features appear in fs DFWM

spectrum; these features can be only explained by considering nuclear spin statistics. The second part of the chapter (3.1.2) is devoted to large amplitude intramolecular motions such as pseudorotation and ring-inversion, which is an inherent property of non-aromatic five-membered rings. Two molecules of this group, pyrrolidine and cyclopentene, were studied by fs DFWM technique.

The second part (3.2) of the Results chapter deals with the bifunctional molecules and their microsolvated clusters. These molecules possess both a hydrogen bond donor and an acceptor groups. When these two groups are close enough or they are bridged by a solvent molecule, forming a microsolvated complex, an excited state proton transfer (ESPT) may take place, resulting in a very short lifetime of the excited state. Thus, the IR/fsMPI method was utilized to study the photoreactive complex of 1*H*-pyrrolo[3,2-*h*]quinoline with a solvent like water or methanol (3.2.1). The chapter proceeds by the results on 7-(2'-pyridyl)-indole, where the ultrashort excited state dynamics, measured by pump-probe REMPI, strongly suggests that a photoinduced intramolecular proton transfer take place in this molecule and, moreover, is accompanied by the mutual twisting of the pyridyl and indole moieties (3.2.2). The section is ended by considering the adenine- and 9-methyladenine monohydrates (3.2.3), which have also ultrashort excited state lifetimes. The vibrational spectrum of adenine-water cluster was assigned to amino and N3 (N9-H) bound forms. Furthermore, it was concluded that for the N9-H bound hydrate excited state dissociation is more efficient than internal conversion (IC), whereas for the amino bound species, IC is dominant.

2 Methods and Instruments

In this chapter the methods and instruments used in the current work are described. All three methods employ femtosecond laser pulses. Therefore the first part is devoted to the femtosecond laser system. The second part introduces the femtosecond Degenerate Four-Wave Mixing (fsDFWM) technique, one particular implementation of Rotational Coherence Spectroscopy. The second experimental method described in this chapter is infrared-induced ion depletion spectroscopy utilizing multiphoton ionization by femtosecond pulses (IR/fsMPI). This technique was developed for measuring IR spectra of photoreactive molecular clusters. In combination with quantum chemistry calculations the structure of the molecular complex under investigation can be obtained. The excited state life-time of these molecular systems can be measured by a method termed pump-probe Resonance Excitation Multiphoton Ionization (REMPI), which is described in the last part of the chapter.

2.1 Generation of femtosecond pulses

2.1.1 Femtosecond laser setup

Experiments on a gas-phase sample usually require relatively high laser intensities. In all the experiments described below, fs laser pulses of several hundreds microjoules per pulse were utilized. Since the pulses are very short (~ 200 fs), their peak power is in the gigawatt range. Such high power in the amplification stages can cause detrimental nonlinear pulse distortion or even destruction of the gain medium or of optical elements. Therefore, a different approach is usually used for the generation of intense femtosecond laser pulses, called chirped pulse amplification (CPA) [20]. Like many common nanosecond laser systems, the CPA based fs laser implies the use of two stages: one for generation and one for amplification. However, prior to amplification, weak femtosecond pulses from the oscillator are stretched temporally to hundreds of picoseconds by means of a strongly dispersive optical system, called the stretcher. Stretched pulses can be readily amplified without damaging the gain medium. Then, the amplified pulses pass through an optical system with opposite dispersion, called compressor, which temporally compresses the pulses back to femtosecond durations.

The femtosecond CPA laser setup, used in the present work, is shown in **Fig. 2.1-1**. It consists of three main parts: the femtosecond oscillator, the stretcher-compressor unit and the regenerative amplifier. The commercial Ti:sapphire oscillator (Mira Basic, Coherent) pumped by a diode-pumped laser (Verdi 5, Coherent) produces 120 fs (FWHM autocorrelation) pulses with a central wavelength of 800nm. The repetition rate and the pulse energy are 75 MHz and 5.0 nJ, respectively. Next, these seed pulses are directed into the stretcher/compressor unit (4800 Series, Quantronix), where they are temporally stretched up to several hundreds picoseconds. The stretched pulses are further amplified in the regenerative amplifier (4800 Series, Quantronix) by passing several times through the gain medium (Ti:sapphire). The gain medium is pumped by nanosecond laser pulses of the Nd:YLF laser (527DP-H, Quantronix) with the wavelength of 527 nm and a repetition rate of 1 kHz. Subsequently, the amplified pulses are directed into the stretcher/compressor unit using the same optical path, where they are compressed back to durations in the femtosecond range. Not every pulse from the oscillator is amplified, but only every 75.000th one, thus the oscillator high repetition rate of 75 MHz is decreased to 1 kHz. In order to synchronize the Pockels cell of the amplifier with the sequence of the incoming oscillator pulses, a fast photodiode is utilized. Thus, the laser system produces 240 fs (FWHM autocorrelation) laser pulses with a repetition rate of 1 kHz, a central wavelength of 800 nm and an energy of about 800 μ J/pulse. The amplification gain is therefore about 160.000 times (52dB).

Usually the amplification brings about the elongation of the laser pulses (in our case the amplified pulses are twice longer than those from the oscillator). There are several reasons for that. The first one is the reduction of the spectral bandwidth of the pulse. This is the result of the limited gain bandwidth of the amplifier and called gain narrowing phenomenon. The narrower the spectrum of a femtosecond pulse, the longer its duration. The further reasons for the pulse elongation are various optical nonlinearities and chirp sources that cannot be compensated in the compressor.

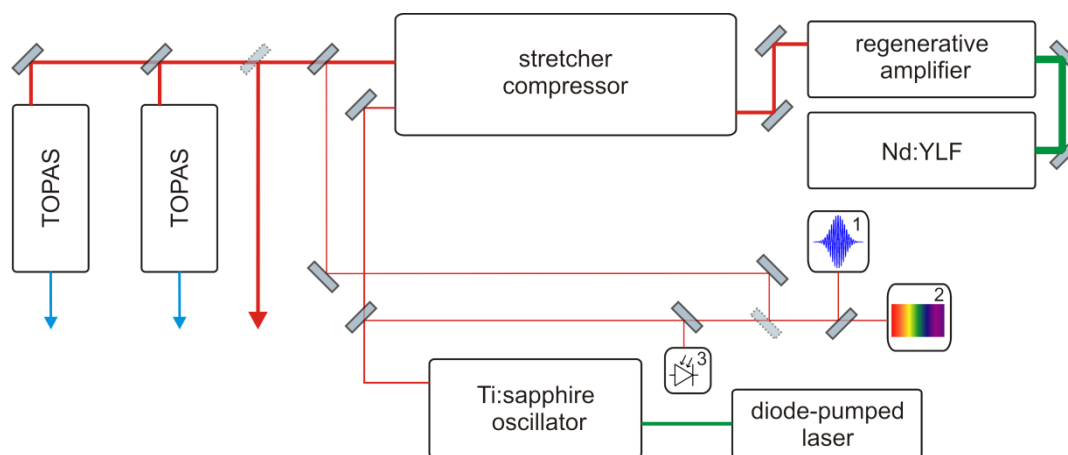


Fig. 2.1-1 The femtosecond laser setup. 1 - autocorrelator, 2 - spectrometer, 3 - fast photodiode.

Though the oscillator wavelength can be slightly tuned (775-825nm), it is frequently desirable to have fs pulses in the visible and ultraviolet wavelength regions. For instance, the $S_1 \leftarrow S_0$ origin transition of most molecules corresponds to the wavelengths in the near and middle UV regions (200-400 nm). Therefore, two additional conversion tools were utilized in the IR/fsMPI and pump-probe REMPI experiments. The first tool is based on the generation of the second and the third harmonics of the fundamental wavelength at 800 nm. Tunability in a wider spectral range was achieved by a commercially available collinear optical parametric amplifier of superfluorescence, called TOPAS.

2.1.2 Generation of the second and the third harmonics

Generation of the second and third harmonic of fundamental radiation of 800 nm provides two additional wavelengths: 400 nm and 267 nm.

Second harmonic generation (SHG) is conventionally done by using the media exhibiting so-called $\chi^{(2)}$ nonlinearity, the property that gives rise to the phenomenon of frequency doubling [21]. One of these media is a BBO (β -BaB₂O₄) crystal; because of its high conversion efficiency it is widely used in different conversion schemes. SHG is the simplest scheme, which consists of a single BBO crystal. Of two types of SHG, type I and type II, the former is the most frequently

used. Type I SHG means that the two input photons of 800nm having an ordinary polarization - with respect to the crystal axis - polarization combine to form one photon of a double frequency (400 nm) and extraordinary polarization.

The third harmonic generation (THG), in principle, can be done by analogy with SHG using the medium with $\chi^{(3)}$ nonlinearity. Commonly, however, the easier and more efficient way is to employ two conversion steps: frequency doubling and subsequent sum frequency generation. Both processes are based on nonlinear crystal materials having $\chi^{(2)}$ nonlinearity.

The optical scheme of THG is depicted in **Fig. 2.1-2**. First, the second harmonic (400 nm, in dark blue) is generated by passing the fundamental wavelength (800 nm in red) through the BBO1 crystal. After the BBO crystal the two wavelengths 400 nm and 800 nm are separated into two beams by means of a dichroic mirror (DM). The polarization of 800 nm radiation is then rotated by an angle of $\pi/2$ using a half-wave plate in order to match the polarization of the 400 nm prior to entering BBO2 crystal. In BBO2 crystal two beams are mixed to produce the sum frequency radiation at 267 nm (light blue), which is the third harmonic of fundamental wavelength.

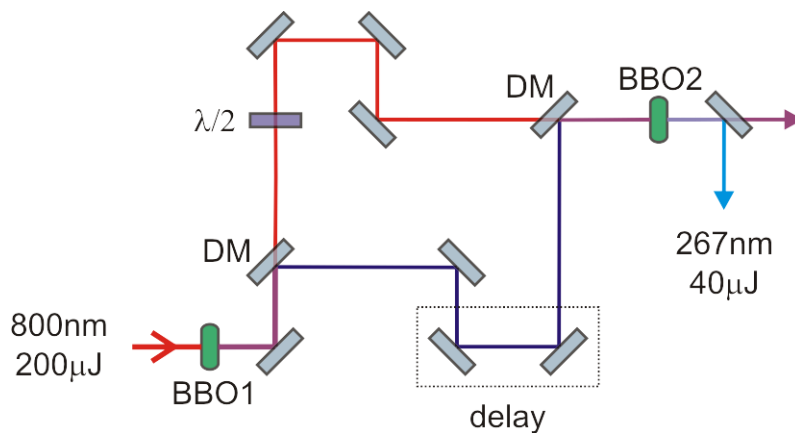


Fig. 2.1-2 The optical scheme of third harmonic generation.

2.1.3 TOPAS

TOPAS is the commercially available **T**raveling-wave **O**ptical **P**arametric **A**mplifier of **S**uperfluorescence (Light Conversion Ltd). Parametric generation in TOPAS is accomplished within five stages using a single BBO crystal. On the first stage superfluorescence is generated and subsequently amplified by passing through the crystal on the next four stages.

TOPAS is pumped by the fundamental wavelength of the Ti:sapphire laser and originally allows for generation of radiation in the near infrared region: 1160-1620 nm (signal) and 1608-2650 nm

(idler). This range may be considerably extended by frequency up- and down-conversion. The possible wavelengths are presented in Fig. 2.1-3.

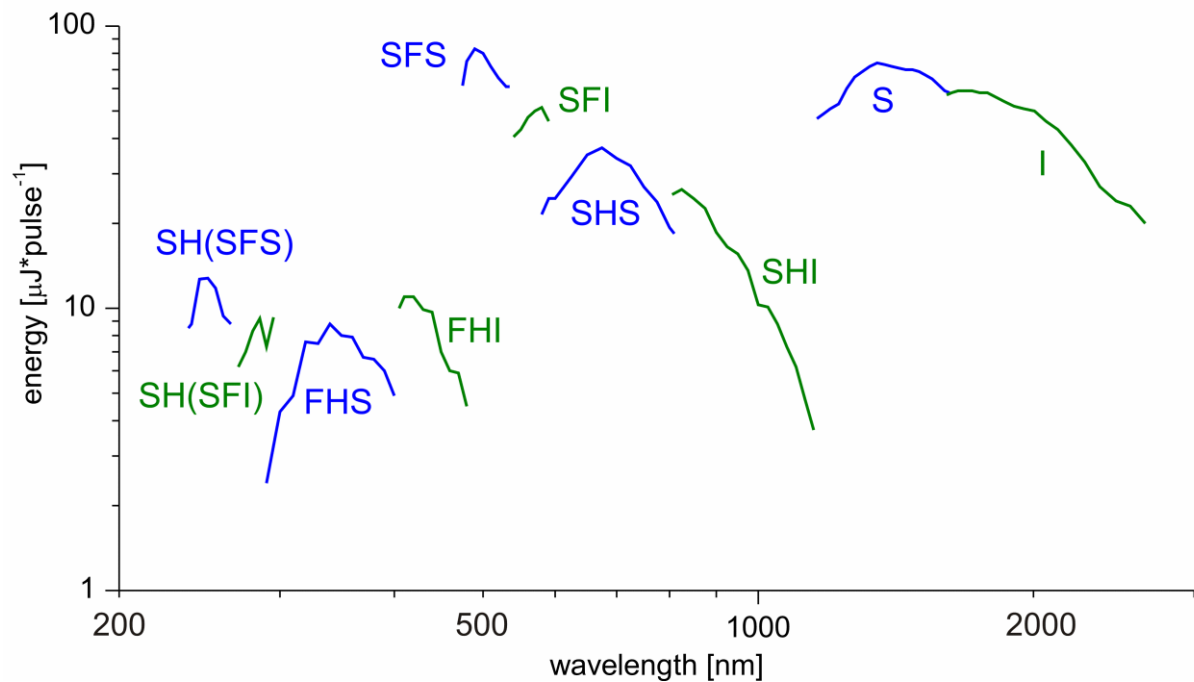


Fig. 2.1-3 TOPAS output energies vs. wavelength. The wavelengths produced by down-conversion of the signal radiation are shown in blue, whereas the wavelengths originated from idler radiation are shown in green. S – signal, I – idler, SHS – second harmonic of signal, SHI – second harmonic of idler, SFS – sum frequency of signal (with 800 nm), SFI – sum frequency of idler (with 800 nm), FHS – fourth harmonic of signal, FHI – fourth harmonic of idler, SH(SFS) – second harmonic of sum frequency of signal, SH(SFI) – second harmonic of sum frequency of idler.

2.1.4 Inverted autocorrelator

The CPA technique allows for the generation of intense fs pulses, however improper alignment of the stretcher-compressor unit can cause a significant spatial and temporal beam distortion. One of these distortions is an angular chirp, which means that the different spectral components of the pulse have slightly different directions of propagation. This is also shown up as the front of a fs pulse being tilted in the near field (the pulse front is not orthogonal to its direction of propagation) [22]. In the focal region (far field) such pulses are both spatially and temporally larger than non-distorted ones [22, 23]. This leads to the reduction of the intensity in the focus by a factor of 2 or more, which is of great importance in frequency conversion (e.g. in TOPAS) or in experiment, where the efficiency (signal) is usually improved by proper focusing of the beams. A tilted front occurs when the angular dispersion, which is introduced both in the stretcher and in the compressor, is not completely canceled.

The presence of an angular chirp is rather difficult to detect using standard diagnostic techniques such as beam profilers, spectrometers and conventional autocorrelators. For this purpose two

new autocorrelators were designed: an interferometric inverted field autocorrelator and an inverted single-shot autocorrelator. The main operating principle of both autocorrelators is the same; it consists in splitting the laser beam into two parts, one of which is subsequently inverted with respect to another one in either the vertical or horizontal plane, which is collinear to the direction of propagation. These two pulses are spatially and temporally overlapped in the interferometric inverted field autocorrelator in order to produce the interferometric pattern, which can be monitored by a CCD camera [22]. If there is no tilt in a pulse front the interferometric pattern will remain uniform over the whole beam area even by changing the delay between the two pulses. This interferometric method is, however, not the best choice when both the pulse duration and the front tilt should be detected simultaneously. In this respect the inverted single-shot autocorrelator is preferred [23, 24]. Here two inverted pulses, coincided in time, are overlapped at some small angle in a BBO crystal, generating a stripe (trace, prolonged stretched ellipse) with the wavelength shorter by a factor of two than that of incident radiation. The thickness of the stripe relates to the pulse duration, while the angle formed by this stripe with the plane of the two incident beams depends on the pulse front tilt. Thus only the angle of 90° indicates that there is no angular chirp in the pulse under test. Other angles indicate that the stretcher-compressor unit must be aligned. The optical scheme of the inverted single shot autocorrelator is shown in **Fig. 2.1-4**. The input pulse is split in the horizontal plane into two parts by means of beam splitter BS. One part remains in this horizontal plane and is directed by two mirrors (one of which is M2) into the BBO crystal. The other part is transferred to the higher horizontal plane using a vertical retro-reflector (VRR) and subsequently directed into the BBO crystal by mirror M1 (beam paths on this higher plane are shown by dashed lines). The two beams are overlapped in the BBO crystal in the vertical plane at an angle of 2ϕ (see **Fig. 2.1-4**, side view). If the front of the input pulse is horizontally tilted, two replicas of this pulse have opposite angles of the tilt prior to entering the BBO crystal (see **Fig. 2.1-4**). This causes the autocorrelation trace (second harmonic after the BBO crystal) to have an additional vertical component (see **Fig. 2.1-4**), whereas a horizontal trace means that there is no tilt in the pulse front.

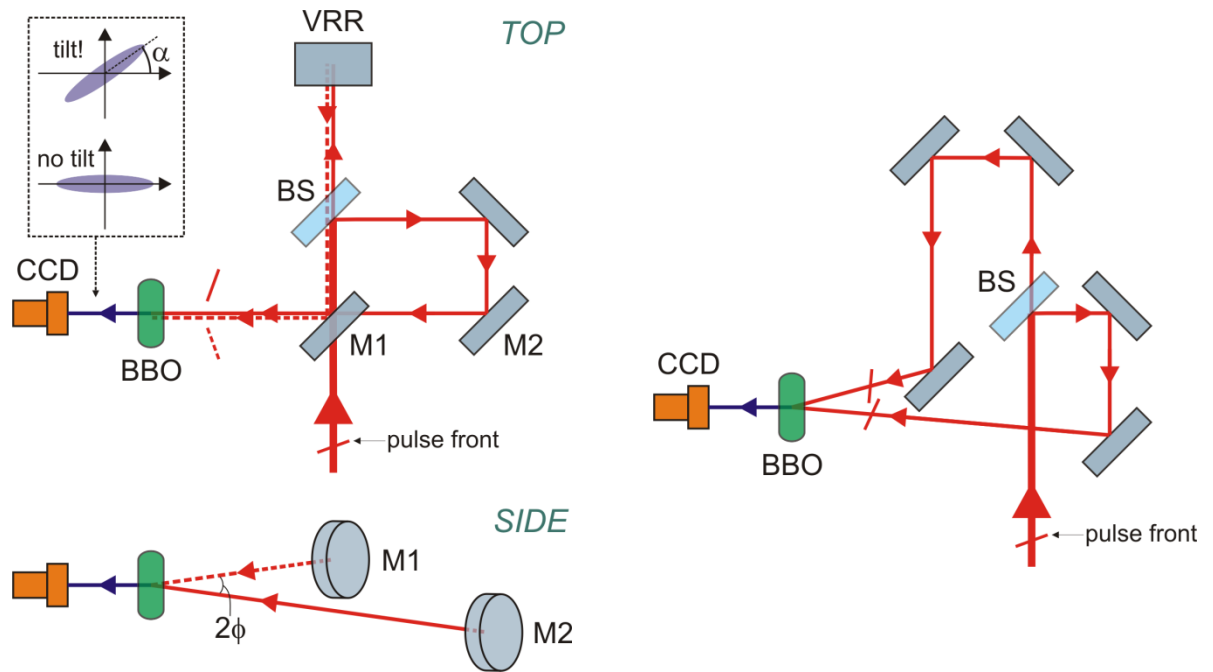


Fig. 2.1-4 The inverted single-shot autocorrelator (left) and standard single-shot autocorrelator (right).

The angle γ by which the front of the pulse is tilted can be calculated as follows [24]:

$$\gamma = \arctan \left[\left(1 - \frac{\lambda}{n} \frac{dn}{d\lambda} \right) \tan \alpha \sin \phi \right], \quad (2.1-1)$$

where n and $dn/d\lambda$ are the index of refraction and the dispersion of the BBO crystal at the wavelength λ , respectively; α is the angle by which the trace is rotated with respect to the horizontal axis; ϕ is the half angle at which the two replicas of the incident beam are overlapped in the BBO crystal. It follows from eq. (2.1-1) that the smaller the overlapping angle 2ϕ , the higher the slope of the autocorrelation trace (α) resulting from the front tilt γ . Thus, by reducing the angle at which two beams are overlapped in the BBO crystal, a very small tilt of the pulse front can be detected.

For comparison the optical scheme of conventional single-shot autocorrelator is also shown in **Fig. 2.1-4**. All beam paths in the scheme lay in the same horizontal plane, therefore, the autocorrelation trace is vertical. There is, however, no rotation of the trace associated with the tilt of the pulse front.

2.2 Femtosecond Degenerate Four-Wave Mixing

2.2.1 Introduction

The pump-probe rotational fs DFWM technique is a particular implementation of rotational coherence spectroscopy (RCS). In general, RCS is based on coherent excitation of the molecular rotational energy levels employing ultrashort laser pulses in order to generate a rotational wavepacket from an ensemble of molecules [9, 25]. The periodic movement of this wavepacket on the picosecond timescale is probed via a vector property ('antenna'), like the transition dipole moment or the axis of maximum polarizability (in fs DFWM). The obtained time-resolved spectrum consists of equidistant signal double-peaks, so-called rotational recurrences, and is a manifestation of rotational coherence effect [26]. This can be understood qualitatively by the picture of a classically spinning top, which exhibits periodic realignments that are directly related to its moments-of-inertia at fixed rotational energy. However, the rotational coherence effect can only be explained by a quantum mechanical description of rotation. Namely, if molecules were "allowed" to rotate with arbitrary speeds, there would be no such effect, since the superposition of all rotating 'antennas' in a molecular ensemble would be destructive on all time scale. Because of the quantization of the rotational speeds there is a constructive interference of these 'antennas' at certain times, which shows up as signal recurrences.

The main advantage of the RCS approach over the frequency-resolved spectroscopy is that, in contrast to a frequency spectrum, a time-resolved spectrum becomes sparser with increase of the species size. This property makes RCS applicable for the structural study of large molecules, which is usually not suitable for conventional frequency-resolved spectroscopic methods.

Different experimental implementations have been successfully used for RCS. One can classify them by the way of signal detection into two groups: The first group consists of "noncoherent" methods, which are based on the detection of incoherent signals, such as fluorescence (fluorescence depletion methods) [14, 27, 28] or ion currents (multiphoton ionization methods) [29-33]. The methods of the second group detect the coherent signals (e.g. laser radiation). They commonly exploit non-linear optical effects such as four wave mixing and the Raman induced Kerr effect. The most widely used coherent methods are RIPS [34], CARS [35] and DFWM [10-14].

Coherent non-linear RCS methods have several advantages over the other RCS implementations. Since coherent approaches are based on Raman type scattering processes, they can be applied for

the structural investigation of non-polar molecules. Another advantage is the background-free detection, which causes a high signal-to-noise ratio.

In the following a brief explanation of the fs DFWM technique will be given. Subsequently, the theory of the fs DFWM process will be presented together with the detailed description of the simulation of fs DFWM spectra. In the second part of this chapter the two different ways of preparing a gas phase sample for fs DFWM experiments will be discussed.

2.2.2 Technique

Conceptually the fs DFWM technique may be explained in the context of a transient grating evolution. Two femtosecond laser pulses, acting as a pump, are overlapped at zero time within a molecular sample. The laser fields of the two pulses interfere with each other creating a grating-like intensity pattern. The polarization of the molecules in the region will follow the intensity, leading to the formation of a polarization grating in the sample (**Fig. 2.2-1**, left). A third probe fs pulse scattered at this grating in the direction defined by the Bragg condition, is utilized for observing this polarization structure (**Fig. 2.2-1**, right).

Due to molecular rotation the polarization grating will be destroyed soon after creation. Thus, if the probe comes at this time, no scattering will be detected. However, according to rotational coherence effect, all molecules after some time come into the same orientations as they were at zero time. Therefore, the polarization grating will rise again and can be detected by the probe pulse. By varying the time delay between pump and probe pulses the time evolution of this grating can be monitored. The grating re-appearing shows up as signal recurrences. The recurrences period is related to the moments-of-inertia of the species under study.

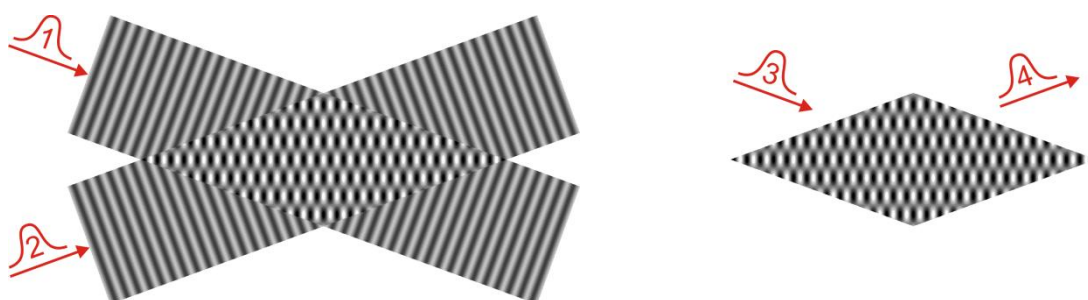


Fig. 2.2-1 Left: Formation of a polarization grating by two femtosecond laser pulses (pump). Right: Probing the grating with the third femtosecond pulse (probe). The fourth pulse (signal) is a Bragg scattering of the third probe pulse at the polarization grating.

The energetic diagram of the fs DFWM process is depicted in **Fig. 2.2-2**. Two pump pulses **1** and **2** excite the molecule via a non-resonant Raman process within a rotational manifold of the

vibronic ground state. After a certain time delay pulse **3** probes the coherently excited rotational levels resulting in scattered signal pulse **4**.

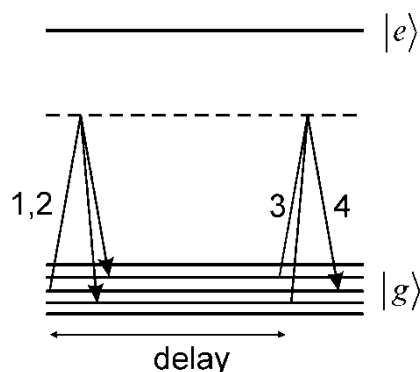


Fig. 2.2-2 The energy diagram of the femtosecond pump-probe non-resonant degenerate four-wave mixing. $|g\rangle$ is the rotational manifold of the vibronic ground state. The pump pulses **1** and **2** are coinciding in time, as well as probe pulse **3** and signal **4**.

The complete optical scheme of the fs DFWM experiment is depicted in **Fig. 2.2-3**. The femtosecond laser pulses are divided into three isoenergetic parts, **pu1**, **pu2** and **pr**, by means of beamsplitters **bs1** and **bs2**. The delay stage **ds2** is utilized for overlapping the two pump pulses **pu1** and **pu2** in time. The computer controlled delay stage **ds1** determines the delay between pump and probe pulses. Three laser pulses, **pu1**, **pu2** and **pr**, are focused by the lens **l1** into the sample. This beam arrangement is called a folded boxcar [36]; it provides phase matching and allows for the separation of the diffracted coherent four-wave mixing signal beam **s**. In order to collimate this signal beam the second lens **l2** is employed. Several apertures on the path of the signal beam serve as spatial filters, allowing for significant improvement of the signal-to-noise ratio.

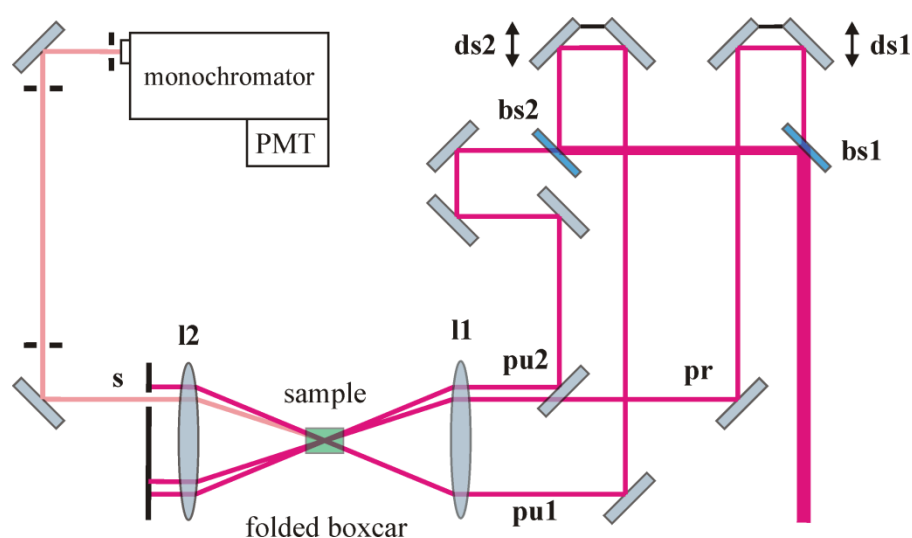


Fig. 2.2-3 The optical scheme of the fs DFWM experiment.

2.2.3 Theory of the pump-probe non-resonant degenerate four wave mixing signal

The DFWM signal intensity resulting from the interaction between the three incident laser pulses and the sample medium can be evaluated by [37]:

$$I_{DFWM} \propto \int_{-\infty}^{+\infty} |P^{(3)}(t)|^2 dt, \quad (2.2-1)$$

Where $P^{(3)}(t)$ is the third order nonlinear polarization. $P^{(3)}(t)$ depends parametrically on the time delay t_d between the pump and probe pulses, which determines the time dependence of the signal. Since the laser frequency is usually not in resonance with any electronic transition of the molecule under study, the third order polarization may be expressed as follows [37, 38]:

$$P^{(3)}(t) = E_{pr}(t) \int_{-\infty}^{+\infty} |E_{pu}(\tau)|^2 \chi_{NR}^{(3)}(t-\tau) d\tau, \quad (2.2-2)$$

where $E_{pu}(t)$ and $E_{pr}(t)$ are the envelopes of the pump and the probe fields, respectively. Non-resonant part of the susceptibility tensor $\chi_{NR}^{(3)}(t)$ in turn may be expressed as the ensemble average of the temporal antisymmetrized autocorrelation function of the operator of molecular polarizability $\alpha(t)$ [37, 39]:

$$\chi_{NR}^{(3)}(t) = \left\langle \frac{i}{\hbar} [\alpha(t), \alpha(0)] \right\rangle, \quad \alpha(t) \equiv \sum_{m,n=x,y,z} \alpha_{mn}(t) e_m e_n, \quad (2.2-3)$$

$$[\alpha(t), \alpha(0)] \equiv \alpha(t)\alpha(0) - \alpha(0)\alpha(t)$$

Here e_m is the unit vector along the polarization of the pump and probe fields which, for simplicity, are assumed to be polarized along the same direction. α_{mn} can be decomposed into two parts: the isotropic part $\sum_{k=x,y,z} \alpha_{kk} / 3$ and anisotropic part $\alpha_{mn} - \delta_{mn} \sum_{k=x,y,z} \alpha_{kk} / 3$. The isotropic term depends neither on the orientational motion (rotation) nor on the vibration of a molecule. It does not contribute to I_{DFWM} , except for an instantaneous response near time-zero ($t_d \sim 0$) [37]. The anisotropic contribution to the susceptibility, $\chi_{NR,ANISO}^{(3)}(t)$, can conveniently be rewritten in terms of the components $\alpha_0^{(2)}$ of the irreducible operator of the polarizability tensor:

$$\chi_{NR,ANISO}^{(3)}(t) = \frac{i}{2\hbar} \langle [\alpha_0^{(2)}(t), \alpha_0^{(2)}(0)] \rangle \quad (2.2-4)$$

Due to molecular rotation, the Heisenberg operator $\alpha_0^{(2)}(t)$ is time-dependent. To make this time-dependence explicit, it is convenient to transform it to the molecular fixed coordinate frame as follows [38]:

$$\alpha_0^{(2)}(t) = \sum_{l=-2}^2 D_{0l}^{2*}(t) T_l^{(2)} \quad (2.2-5)$$

Here D_{0l}^2 is the Wigner rotation operator [40] and the components of the irreducible tensor $T_k^{(2)}$ are constructed from its Cartesian components α_{mn} as follows [41]:

$$\begin{aligned} T_2^{(2)} &= (\alpha_{xx} - \alpha_{yy})/2 + i\alpha_{xy} \\ T_1^{(2)} &= -\alpha_{xz} - i\alpha_{yz} \\ T_0^{(2)} &= (2\alpha_{zz} - \alpha_{xx} - \alpha_{yy})/\sqrt{6} \\ T_{-1}^{(2)} &= \alpha_{xz} - i\alpha_{yz} \\ T_{-2}^{(2)} &= (\alpha_{xx} - \alpha_{yy})/2 - i\alpha_{xy} \end{aligned} \quad (2.2-6)$$

Let H be the rotational Hamiltonian. Then time-dependent Wigner rotation operator can be explicitly written:

$$D_{0l}^{(2)}(t) \equiv \exp\left(\frac{i}{\hbar} Ht\right) D_{0l}^{(2)} \exp\left(\frac{-i}{\hbar} Ht\right) \quad (2.2-7)$$

The eigenvalues E_a , eigenfunctions $|a\rangle$, and eigenfrequencies ω_{ab} of Hamiltonian H can be introduced as follows:

$$H|a\rangle = E_a|a\rangle, \quad \omega_{ab} = (E_a - E_b)/\hbar \quad (2.2-8)$$

Then, inserting eq. (2.2-5) into eq. (2.2-4), using definition of the commutator (2.2-3), and employing eq. (2.2-7) one gets:

$$\begin{aligned}
\chi_{NR,ANISO}^{(3)}(t) &= \frac{i}{2\hbar} \sum_{l,l'} T_l^{(2)} T_{l'}^{(2)} \sum_{a,b} \rho_a \left\{ \langle a | D_{0l}^{(2)} | b \rangle \langle b | D_{0l'}^{(2)} | a \rangle \exp(i\omega_{ab}t) - \right. \\
&\quad \left. - \langle a | D_{0l}^{(2)} | b \rangle \langle b | D_{0l'}^{(2)} | a \rangle \exp(i\omega_{ba}t) \right\} \equiv \\
&\equiv \frac{1}{\hbar} \sum_{l,l'} T_l^{(2)} T_{l'}^{(2)} \sum_{a,b} \rho_a \langle a | D_{0l}^{(2)} | b \rangle \langle b | D_{0l'}^{(2)} | a \rangle \sin(\omega_{ab}t) \equiv \\
&\equiv \frac{1}{\hbar} \sum_{a,b} \rho_a |X|^2 \sin(\omega_{ab}t); \quad X \equiv \sum_l T_l^{(2)} \langle a | D_{0l}^{(2)} | b \rangle
\end{aligned} \tag{2.2-9}$$

Here

$$\rho_a \equiv Z^{-1} \exp\left(\frac{-E_a}{k_B T}\right), \quad Z = \sum_a \exp\left(\frac{-E_a}{k_B T}\right) \tag{2.2-10}$$

is the equilibrium rotational distribution, $|a\rangle$ and $|b\rangle$ are all possible rotational states of Hamiltonian H and $\langle a | D_{0l}^{(2)} | b \rangle$ is determined through the Clebsch-Gordan coefficients.

Eq. (2.2-9) is nothing else as the sine transformation of the frequency domain rotational Raman spectrum.

2.2.4 Simulation of fs DFWM spectra

According to eqs. (2.2-1), (2.2-2) and (2.2-9), the simulation of fs DFWM spectra of a single species in a semirigid rotor approximation consists of the following steps. (1) The rotational energy level structure is obtained according to a chosen rotational Hamiltonian. (2) The rotational Raman spectrum in the frequency domain is constructed from the energy level structure and the appropriate selection rules. (3) Subsequently, the frequency domain spectrum is converted into the time domain spectrum by the Fast Fourier Transformation (FFT). (4) The time-domain spectrum is transformed into a fs DFWM spectrum utilizing a response function of a DFWM process (see eqs. (2.2-1) and (2.2-2)). In the following the detailed description of these steps will be given.

1. The exact analytical calculations of the rotational levels are only possible for the simple cases, such as linear and symmetric rigid rotors. In order to calculate the rotational levels in the most general case of a non-rigid asymmetric rotor, we adopt the Watson A-reduced parameterization of the rotational molecular Hamiltonian H , which can be written in a perturbation treatment as a

sum of the rigid rotor Hamiltonian, H_0 , and the centrifugal distortion (CD)-induced part, H_{CD} [42]:

$$H = H_0 + H_{CD}, \quad (2.2-11)$$

The total Hamiltonian H possesses the D_2 symmetry. The D_2 group (which is frequently referred to as V -group) is made up of four elements: three operators $C_2(a)$, $C_2(b)$, $C_2(c)$ which describe rotation by the angle π around the axes a , b , c and the identity operator, E . Therefore, the eigenfunctions $\Psi^{(k)}$ of the Hamiltonian H can be classified according to the irreducible representations ($k=A, B_a, B_b, B_c$ according to Mulliken designation [43]) of the D_2 group. Namely, the eigenfunctions $\Psi^{(A)}$ are invariant upon two-fold rotation about any of the principal axes of inertia. $\Psi^{(B_i)}$ are invariant upon the rotation $C_2(i)$ about the i 's axis but change their sign under the other two rotations.

Using the King-Hainer-Cross notation of asymmetric top energy levels K_{-1}, K_1 , ($= K_a, K_c$) species of the D_2 group can be also labeled as ee, eo, oo, oe [44]. The first letter indicates the parity (even/odd) of K_{-1} (K_a), the second the parity of K_1 (K_c). The two notations are connected through: $A=ee, B_a=eo, B_b=oo, B_c=oe$.

The Schrödinger equation corresponding to Hamiltonian (2.2-11) is written as follows:

$$\hat{H}\Psi(J, \tau, M) = E\Psi(J, \tau, M), \quad (2.2-12)$$

The solution of eq. (2.2-12) is commonly expressed as a linear combination of the Wang functions $S(J, K, M, \gamma)$, which, in turn, belong to the D_2 symmetry group as well [43, 45]:

$$\Psi(M, J, \tau) = \sum_{K, \gamma} a_{K\gamma}^{J\tau} S(M, J, K, \gamma), \quad K = 0, \dots, J, \quad \gamma \in 0, 1 \quad (2.2-13)$$

K and γ define the symmetry of a Wang function. The relationship between a set of K , γ and aforementioned symmetry notations (shown in **Table 2.2-1**) depends on the way the molecular-fixed coordinate system (x, y, z) associates with the inertial axis system (a, b, c). There are six different representations, however the most frequently used are only two of them: I^R ($a=z, b=x, c=y$) and III^L ($a=y, b=x, c=z$). The representation I^R is commonly the choice for the case of near-prolate tops, while the representation III^L for near-oblate ones.

Table 2.2-1 Symmetry classification of rotational levels in the D_2 group.

D_2	E	$C_2(a)$	$C_2(b)$	$C_2(c)$	K_{-1}, K_1	$K, \gamma (\Gamma^R)$	$K, \gamma (\Pi^L)$
A	1	1	1	1	ee	ee	ee
B_a	1	1	-1	-1	eo	eo	oe
B_b	1	-1	1	-1	oo	oo	oo
B_c	1	-1	-1	1	oe	oe	eo

The Wang functions are constructed from the symmetric rotor wavefunctions in the following way:

$$S(M, J, K, \gamma) = \frac{1}{\sqrt{2}} [\psi(M, J, K) + (-1)^\gamma \psi(M, J, -K)], \quad K > 0, \quad \gamma \in 0, 1, \quad (2.2-14)$$

$$S(M, J, 0, 0) = \psi(M, J, 0)$$

The solution $\Psi(M, J, \tau)$ of the Schrödinger equation (2.2-12) may be as well expressed by an expansion of symmetric rotor wavefunctions:

$$\Psi(M, J, \tau) = \sum_K c_K^{J\tau} \psi(M, J, K), \quad K = -J, \dots, 0, \dots, J, \quad (2.2-15)$$

Taking (2.2-13) into account the Schrödinger equation (2.2-12) can be rewritten:

$$\sum_{K, \gamma} \sum_{K', \gamma'} a_{K\gamma}^{J\tau} a_{K'\gamma'}^{J\tau} \langle S(M, J, K, \gamma) | \hat{H} | S(M, J, K', \gamma') \rangle = E^{J\tau}, \quad (2.2-16)$$

After the reassignment: a set of $K, \gamma \rightarrow i$ and $K', \gamma' \rightarrow j$ eq. (2.2-16) will have a form:

$$\sum_{i, j} a_i^{J\tau} a_j^{J\tau} H_{ij} = E^{J\tau}, \quad i, j \in 1, \dots, 2J + 1, \quad (2.2-17)$$

where

$$H_{ij} = \langle S(M, J, i) | \hat{H} | S(M, J, j) \rangle, \quad i, j \in 1, \dots, 2J + 1 \quad (2.2-18)$$

The eq. (2.2-17) can be rewritten in a matrix form:

$$\mathbf{a}^T \mathbf{H} \mathbf{a} = E, \quad (2.2-19)$$

This eigenvalue problem can be solved numerically, which will yield the energies $E^{J\tau}$ of rotational levels in a chosen J manifold and the corresponding sets of coefficients $\mathbf{a}^{J\tau}$ from the expansion (2.2-14).

2. Raman type transitions are allowed between rotational manifolds with $|\Delta J| = 0, 1, 2$. According to Platzek's polarizability theory of the Raman effect [46], the intensity of the transition $i \rightarrow f$ between two rotational states described by wavefunctions $|i\rangle$ and $|j\rangle$ for a gaseous sample at thermal equilibrium with temperature T can be evaluated as follows [47]:

$$I_{i \rightarrow f} \propto \left(\frac{\pi}{\varepsilon_0} \right)^2 (\nu_0 - \nu)^4 g_{ns} \frac{e^{-E_i/kT}}{Z(T)} |\langle f | \alpha | i \rangle|^2, \quad (2.2-20)$$

where ε_0 is the permittivity of vacuum, E_i is the energy of the i state, ν_0 is the frequency of an exciting photon, $\nu = (E_f - E_i)/hc$ is the frequency of the rotational transition $i \rightarrow f$, g_{ns} is the nuclear spin degeneracy of the initial state i , $Z(T)$ is the total partition function, and $\langle f | \alpha | i \rangle$ is the transition moment of the polarizability tensor, which is given [41]:

$$\begin{aligned} |\langle f | \alpha | i \rangle|^2 = & (2J^i + 1) \left(\sum_K c_K^i c_K^{f*} C(J^i 2J^f; K0) T_0^{(2)} + \right. \\ & \left. + \sum_K c_K^i c_{K+2}^{f*} C(J^i 2J^f; K2) (T_2^{(2)} + T_{-2}^{(2)}) \right)^2, \end{aligned} \quad (2.2-21)$$

where $T_x^{(y)}$ are the irreducible spherical tensor components given in (2.2-6), $C(J^i 2J^f; Kx)$ are Clebsh-Gordan coefficients, the coefficients c_K are introduced in (2.2-15) and can be evaluated from coefficients $\mathbf{a}^{J\tau}$ obtained in the first step. The term $(2J^i + 1)$ is the degeneracy of rotational states in the magnetic quantum number M when there are no external electric or magnetic fields.

3. Transformation of the obtained rotational Raman spectrum from the frequency into the time domain is done by means of the sine transformation, which is a part of the Fast Fourier Transformation (FFT) algorithm.

$$I(\tau) = \sum_i I(\omega_i) \sin(\omega_i \tau) \quad (2.2-22)$$

We have used the FFT routines which are implemented in the AMD Core Math Library (ACML) in order to have a high performance on AMD64 platform processors.

4. On the fourth step of simulation the time-domain signal is processed by the response function of degenerate four-wave mixing process, which may be written as follows:

$$I_{DFWM}(\tau) = g * (g * I)^2, \quad (2.2-23)$$

where I is the time-domain spectrum $I(\tau)$ evaluated by (2.2-22), g is a temporal function of fs pulses and $*$ denote convolution. This equation is a consequence of the eqs (2.2-1) and (2.2-2).

The simulation is incorporated into a nonlinear fitting routine in order to find the optimal simulation parameters that correspond to the minimal difference between the calculated and experimental spectra. Commonly this difference is defined as a *chi*-square:

$$\chi^2(\mathbf{\alpha}) = \sum_{i=1}^n \frac{[s_i(\mathbf{\alpha}) - e_i]^2}{\sigma_i^2}, \quad (2.2-24)$$

where $\mathbf{\alpha}$ is the vector of simulation parameters being fitted, $s_i(\mathbf{\alpha})$ is a simulation and σ_i are the uncertainties of the individual measurements e_i . The fit utilizes two optimization approaches: Differential Evolution [48] and the gradient based methods that are implemented in the MINUIT optimization package [49]. The former approach allows for finding a global minimum of a *chi*-square function, while the latter one is worth for the fine optimization in the global minimum region and for the error analysis of the fitted parameters $\mathbf{\alpha}$.

2.2.5 Preparation of the gas phase sample

The rotational coherence effect can be observed only in the absence of collisions, when molecular rotational motion is underdamped. This requirement is only fulfilled in not too dense gases. The gas phase sample preparation is traditionally done either in a gas cell or in a molecular beam. In the following these two approaches will be considered in detail.

2.2.5.1 Gas cell with the heat-pipe principle

Fs DFWM experiments imply a preparation of an isolated gas phase sample, which concentration lies usually in the range of 10^{22} - 10^{24} molecules·m⁻³. This is not a problem when at room temperature the sample is a gas or a liquid that has a high vapour pressure; in this case the

usual gas cell constructions can be exploited. However, a special design, which employs heating, has to be utilized for substances with low vapour pressure such as solid state compounds and some liquids.

We have adopted a gas cell construction that is based on the heat-pipe principle [50-52]. This is shown in **Fig. 2.2-4**. It consists of the central and side parts of cylindrical shape, which are sealed in joints by means of rubber o-rings. The central part of this heat-pipe gas cell is heated by two heating elements, which temperature can be controlled by an external electronic device. The water cooling rings are utilized in order to keep the ends of the central part cold. A metallic wire netting, serving as a capillary, is introduced into the central part of the cell. The ends of the side parts of the gas cell are closed with the lenses, one of which focuses the three laser beams, **pu1**, **pu2** and **pr**, into the sample region (in the centre), and the other lens collimates the resulting signal beam as shown in **Fig. 2.2-3**.

The operation principle of the heat-pipe is as follows. Initially the cell is filled up with the inert gas at low pressure of about several mbar. Heating the central part causes the substance under investigation, which is placed there, to evaporate. Note, that under these conditions the temperature of the substance will not exceed the temperature at which the vapor pressure of this substance equals or is just higher than that of the inert gas, no matter how high the temperature of the heating elements is. Therefore, by controlling the pressure of the inert gas the desired temperature/concentration of the sample can be set. The substance vapor diffuses from the hot central zone towards the colder ends of the cell, where it condenses. Ideally, the condensed, liquid sample should be driven back to the center by the capillary force arising in the metallic wire netting [50].

The heat-pipe has several advantages over the conventional gas cell constructions. First, there is no lens contamination since the inert gas confines the substance vapor to the central part of the cell. The second advantage is that due to the sample circulation the well-known conditions can be maintained in the cell over a long period of time. This makes the heat-pipe cell ideal for spectroscopic studies. It was extensively exploited by Hering and coworkers in the frequency domain CARS and DFWM experiments [53-55].

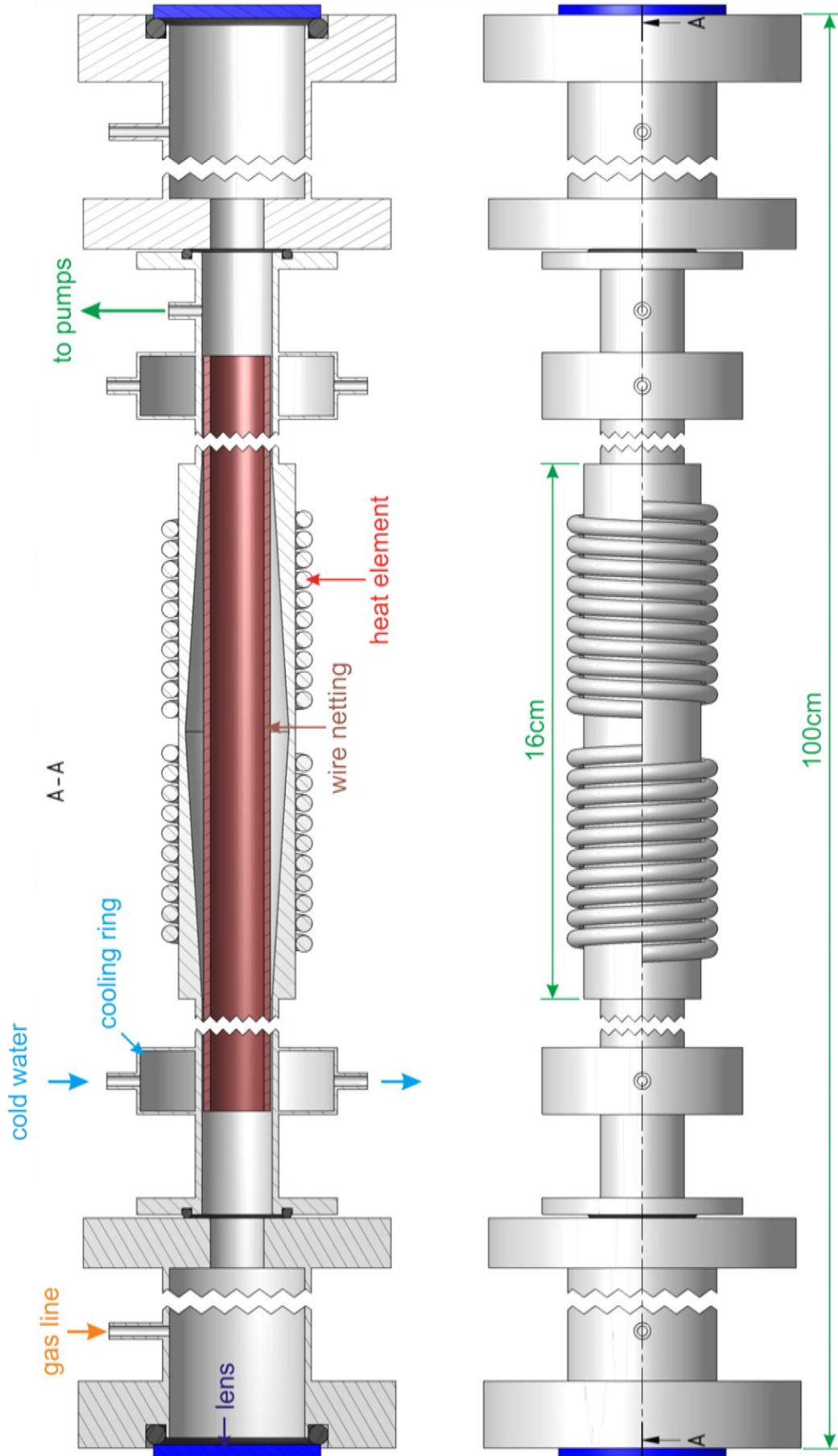


Fig. 2.2-4 Vapour cell based on the heat-pipe principle.

2.2.5.2 Molecular beams

Isolation of the molecules for investigation in a fs DFWM experiment can be done as well by the supersonic beam technique [56, 57]. A supersonic beam is produced by a supersonic expansion of molecules from a high pressure zone into a low pressure region (vacuum) through a nozzle with a tiny orifice. In this way the rotational and vibrational cooling of molecules is achieved. This allows for studying the molecular system under different conditions, and thus gaining information on the conformational preferences.

In order to produce the supersonic beam for fs DFWM experiments two types of nozzle were employed. The first type is a continuous nozzle with a slit orifice [58] with dimensions of 0.1x3 mm. Under the low-concentration conditions of a supersonic expansion, a slit nozzle provides a much better signal-to-noise ratio than a round orifice of the same cross section. This is due to the fact that a four-wave mixing signal depends on the square of the interaction length of the laser beams. The second type of nozzle used in the experiments is a pulsed Even-Lavie valve [59] with a round orifice of 0.2 mm in diameter, which was specially designed to work at high temperature/pressure/repetition rate. The use of a pulsed nozzle allows a significant reduction of the sample consumption as well as lower requirements for the pump capacity.

Better cooling conditions can be achieved by mixing the sample vapor with a carrier gas, for instance Helium or Argon. Mixing is usually done by either bubbling the carrier gas through a liquid sample or blowing the gas over a heated solid-state sample. Molecular collisions during the expansion result in an efficient energy transfer from the internal to the translational degrees of freedom, resulting in cold molecules [56, 57].

There is always a compromise between the rotational and vibrational cooling rate of molecules and their concentration in a supersonic expansion, since these two parameters have an opposite dependence on the distance from an orifice. The farther downstream the molecules are, the colder their internal degrees of freedom, but also the lower their concentration. Therefore, in order to provide sufficient molecular concentration for the fs DFWM experiments, the molecules are usually probed at a distance of approximately 1-2 mm from the nozzle orifice.

2.3 Vibrational analysis of molecular clusters by IR/fsMPI

2.3.1 Introduction

Molecular clusters are perfect archetypical systems for a molecular-scale understanding of solute-solvent interactions in aqueous solution [60-65] and weak van der Waals interactions, which determine the progress of many relevant biological processes. Since the molecular clusters are produced in a supersonic expansion, they are isolated from many perturbative factors like collisions, many-body interactions *etc.* This reduces the complexity of the system under study, allowing a comparison with the results obtained by high-level *ab initio* quantum chemistry calculations; in that way the accuracy of the theoretical approach can be experimentally verified.

Several different spectroscopic methods were applied for studying molecular clusters. Among others are laser-induced fluorescence [56], microwave [66], Raman [67] and direct IR absorption [68-70] spectroscopies. One of the most favorable methods of vibrational analysis of hydrogen-bonded molecular clusters is infrared depletion - resonant two photons ionization (IR/R2PI) spectroscopy [16-19]. This technique has the definite advantage of being mass- and isomer selective and allows for recording vibrational spectra in the region of X-H (X=C, O, N) stretches.

It was shown that the X-H (X=C, O, N) stretch absorption provides an important diagnostic of X-H...Y hydrogen bonds. When the hydrogen bond is intermolecular, the strength of the hydrogen bond is reflected in [19, 63, 71]:

- (1) the magnitude of the frequency shift of the X-H stretch absorption,
- (2) an increase in the integrated absorption intensity of the band (often by a factor of 5 or more),
- (3) an increase in the breadth of the X-H stretch absorption.

Molecules which incorporate an intramolecular X-H...Y hydrogen bond typically show a large red shift in the X-H stretch frequency (i.e., toward lower frequency), but only a modest increase in the intensity of the transition [71]. Thus by studying the X-H stretch transitions in a molecular cluster, the similarities and differences of intermolecular and intramolecular hydrogen bonds can be probed.

Additionally to characterization of hydrogen bonds in molecular clusters, their structures can be determined by comparing the experimental vibrational spectra with those calculated by *ab initio* quantum chemistry methods.

2.3.2 Conventional ns IR/R2PI

The energetic scheme of the conventional nanosecond IR/R2PI method is depicted in **Fig. 2.3-1**. The method is based on the detection of the ion current, which is produced by resonant two photons ionization (R2PI) of sample molecules. This process is shown in **Fig. 2.3-1** by two photons: **ph2** and **ph3**. The wavelength of photon **ph2** is tuned to be in resonance with the $S_1 \leftarrow S_0$ transition of the molecule. For a wide range of substances this transition is higher than half of ionization potential, what means that a photon with the same wavelength used for excitation can also be utilized for ionization of the molecule from its S_1 excited state (**ph3**). The ion current is detected by means of TOF spectrometry, allowing mass selection of the produced ions.

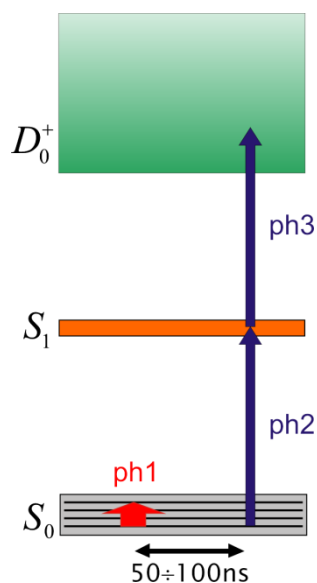


Fig. 2.3-1 Energetic diagram of the conventional nanosecond IR/R2PI method.

Since all the molecules are in their electronic ground state due to efficient cooling in a supersonic expansion, the ion current resulting from the absorption of **ph2** and **ph3** photons in the R2PI process can be quite significant. However, if about 100 ns prior to R2PI the molecular ensemble is irradiated by infrared photons **ph1**, the frequency of which is in resonance with any vibrational state of this system, a change is observed in the magnitude of the ion current for the corresponding mass channel.

There are several reasons for the IR induced change of the ion current. In case of the monomer, intramolecular vibrational energy redistribution (IVR), which follows the vibrational excitation, produces a different population of vibrational states in the molecular ensemble, which, in turn, alters the efficiency of the R2PI process. In case of a molecular cluster, IVR leads to dissociation of the cluster, which shows up as a depletion of ion signal in the corresponding mass channel. Thus, monitoring of the ion current while scanning the wavelength of the infrared radiation it is possible to determine the vibrational pattern of the molecular cluster under study.

2.3.3 IR/fsMPI principle

The essential condition for the “classical” IR/R2PI depletion method is the existence of an electronically excited state of the cluster, halfway to the ionization potential, which can be excited resonantly and lives long enough to be able to ionize the species by non-resonant absorption of a second photon of the same energy. However, if this intermediate state is short-lived ($\ll 1$ ns) due to a fast proton or electron transfer or internal conversion, the ion yield of the R2PI process, observed with nanosecond lasers, goes to zero. This means that the IR/R2PI cannot be applied for many interesting photoreactive biological systems such as nucleobases, their microsolvates or molecular systems exhibiting excited state proton and electron transfer.

In order to extend the applicability range of the method towards short-lived excited state systems, we have recently proposed a new approach which is based on utilization of femtosecond pulses for the ionization step (**ph2** and **ph3** in **Fig. 2.3-1**). This modification of IR/R2PI was termed infrared depletion-femtosecond multiphoton ionization (IR/fsMPI) spectroscopy.

An instructive example is given in **Fig. 2.3-2**, where mass spectra of 1*H*-pyrrolo[3,2-*h*]quinoline (PQ, see chapter **3.2.1**) with methanol were recorded for comparison, exploiting nanosecond and femtosecond laser pulses of the same wavelength (267 nm). It is obvious that in the spectrum acquired using nanosecond pulses the molecular aggregates of PQ with methanol are missing, due to their short excited state lifetime. From the displayed mass spectra it is evident that if one is interested in vibrational investigation of the PQ:methanol aggregates, this can only be achieved by fs multi-photon ionization (fsMPI).

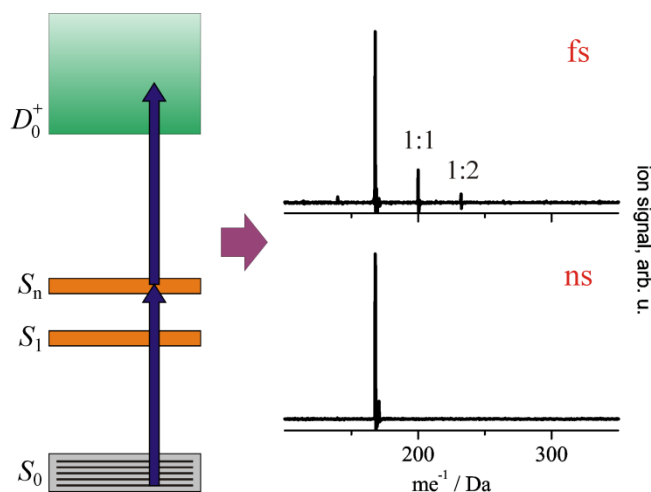


Fig. 2.3-2 One-color (267 nm) two-photon ionization scheme of PQ:methanol (left) and corresponding mass spectra obtained with the femtosecond and nanosecond laser pulses under the same experimental conditions (right).

2.3.4 Experimental IR/fsMPI setup

The experimental setup of IR/fsMPI is shown in **Fig. 2.3-3**. The third harmonic (267 nm) of the CPA fundamental output is utilized in the MPI process. This femtosecond laser beam is spatially overlapped with a counter-propagating nanosecond IR-OPO (Optical Parametric Oscillator) beam in the ionization region of the time-of-flight spectrometer. Both laser beams cross perpendicularly a molecular beam collimated from a pulsed supersonic expansion of a carrier gas enriched with the substance under study.

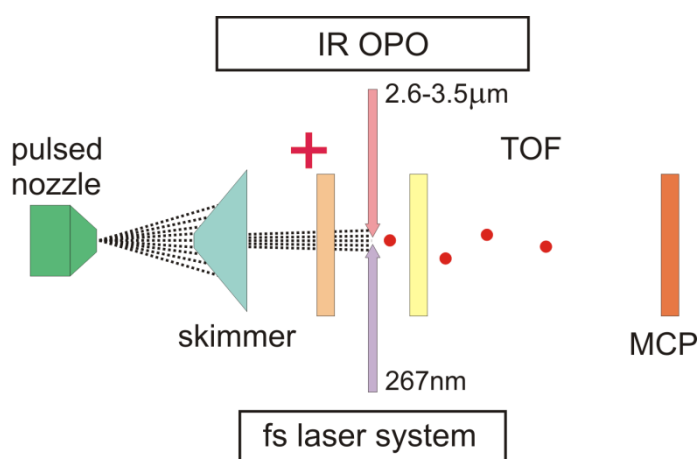


Fig. 2.3-3 Experimental setup of IR/fsMPI.

Since the maximum repetition rate at which the pulsed nozzle (General Valve) and the IR-OPO can operate is 10 Hz, they should be by some means synchronized to the femtosecond laser system running at 1 kHz.

The synchronization was achieved employing a digital delay generator (DG535, Stanford Research Systems) as shown in Fig. 2.3-4. Initially, the generator is triggered by an arbitrary femtosecond laser pulse (“trigger” pulse, see Fig. 2.3-4) from the kHz sequence. One of the delay channels (Fig. 2.3-4, red) is set to 95 ns, which prevent the generator to be triggered by the next 99 pulses from the kHz sequence. In that way the kHz repetition rate of the laser system can be divided by 100, resulting in 10 Hz. Thus, not each fs laser pulse is utilized for fsMPI, but only every 100th one. The second channel of the generator (Fig. 2.3-4, green) starts the pulsed nozzle so that the gas pulse is in the ionization region of the mass spectrometer when the ionization laser pulse is coming. The third channel starts the IR-OPO laser in order to deliver the IR pulse into the ionization region about 50-100 ns before the arrival of the ionization fs pulse. The TOF zero time is also synchronized to the ionization laser pulse.

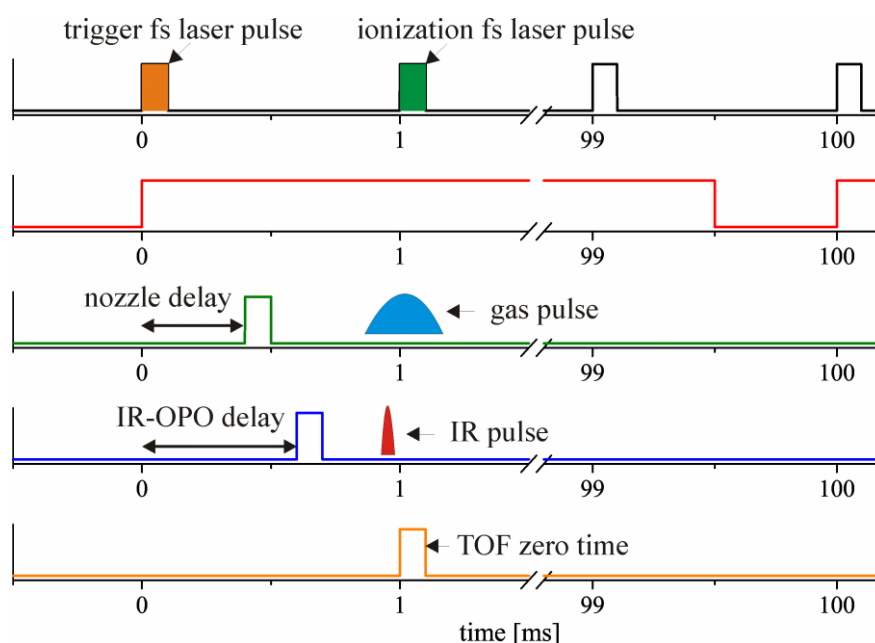


Fig. 2.3-4 Synchronization in the IR/fsMPI experiment.

Thus, the IR/fsMPI experiment progresses as follows. The molecules in the gas pulse are initially irradiated by IR radiation. If the IR wavelength is in resonance with a vibrational transition, the molecules undergo vibrational excitation, which is followed by IVR. After about 50-100 ns, which is necessary for IVR to be completed, the femtosecond laser pulse ionizes the vibrationally relaxed molecules *via* two-photon absorption. The efficiency of this ionization process is different without and with IVR, which results in the change of the ion current, when the IR wavelength is in resonance with a molecular transition.

2.3.5 The source of infrared radiation

Following Byer's definitive study [72] the tunable sources of infrared radiation are conventionally based on the angle tuned LiNbO₃ Optical Parametric Oscillator (OPO). Naturally the OPO generates a radiation with a relatively broad frequency spectrum ($\Delta\nu=20\text{ cm}^{-1}$), precluding the direct use of such a device for high resolution spectroscopy. In order to make the bandwidth narrower two approaches are commonly used. The first one is to introduce frequency selecting components such as gratings and etalons into the OPO cavity [73, 74]. This approach however has the severe drawbacks of increasing the threshold for laser action and reducing the overall efficiency. The alternative way of forcing the OPO to oscillate in the narrow frequency range, is seeding it with an external narrow-bandwidth radiation [75]. This technique, referred to as injection seeding, is utilized in the IR-OPO laser, which was developed in our lab by Dr. Hans-Dieter Barth. Essentially it consists of the two parts: the OPO and the seeder (Fig. 2.3-5) [75, 76].

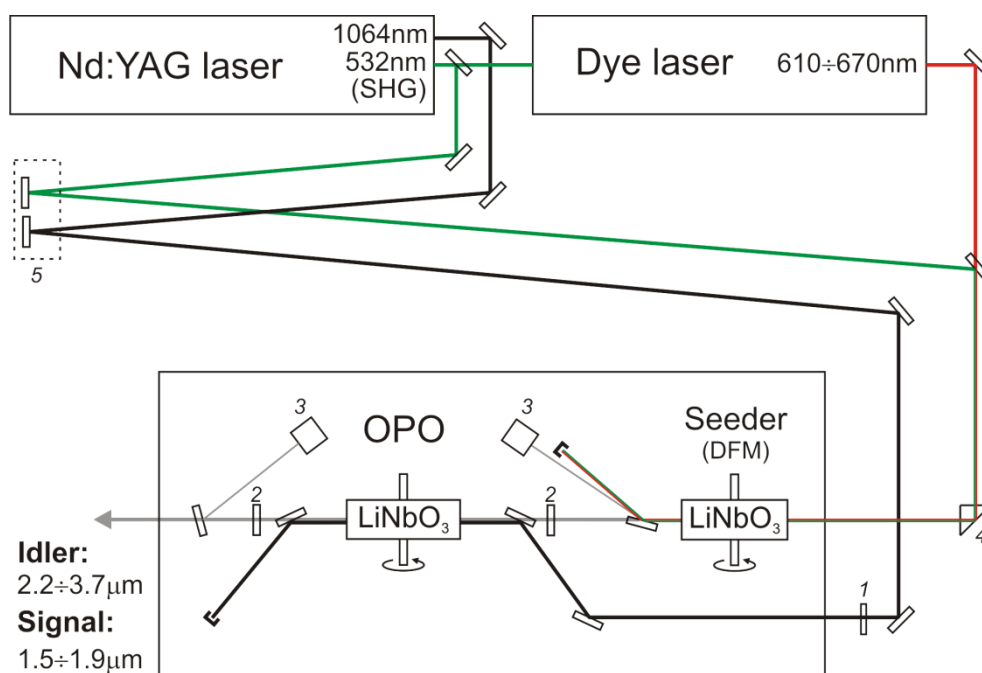


Fig. 2.3-5 The IR-OPO laser: 1 – polarizer, 2 – OPO resonator, 3 – pyroelectric detectors, 4 – prism, 5 – delay stage.

The OPO is based on the nonlinear crystal (LiNbO₃), which is confined within the resonator **2**. The optical parametric generation ($\chi^{(2)}$ nonlinearity) in the crystal is used to convert an input pump wave (shown in black) into two waves, called signal and idler. The energy conservation gives rise to the following relations between these three waves:

$$\frac{1}{\lambda_{pump}} = \frac{1}{\lambda_{signal}} + \frac{1}{\lambda_{idler}} \quad (2.3-1)$$

Since the fundamental output (1064nm) of the Nd:YAG (Continuum NY 81) laser serves as the pump, the idler wave can be generated in the range from 2.2 to 3.7 μm . The signal and idler waves are further amplified in the resonator **2** by passing several times through the crystal.

The seed generation is based on the Difference Frequency Mixing (DFM) (Generation, $\chi^{(2)}$ nonlinearity) of two waves in the LiNbO₃ crystal. One of the waves is the second harmonic (532 nm) of the Nd:YAG laser. The other one is the output of the dye laser (Continuum ND 60, dye DCM), which can be continuously tuned in the range from 610 to 670 nm. These two waves are introduced into the DFM crystal by means of a full reflection in the prism **4**. As a result the third wave with the wavelength in the infrared region is generated. The energy conservation of the process is given by the following formula:

$$\frac{1}{\lambda_{DFM}} = \frac{1}{\lambda_{532}} - \frac{1}{\lambda_{dye}} \quad (2.3-2)$$

The spectral bandwidth of the seed can be estimated using eq. (2.3-3). It depends on the bandwidths of both laser radiations used in the DFM and is in the range of about 0.2 cm^{-1} . Seeding the OPO resonator with such a narrow linewidth radiation causes the OPO to oscillate in the same narrow frequency range.

$$(\Delta\nu_{DFM})^2 = (\Delta\nu_{532})^2 + (\Delta\nu_{dye})^2 \quad (2.3-3)$$

The delay stage **5** is utilized for overlapping in time of the second harmonic of YAG and the dye laser radiation prior to entering the DFM crystal. Wavelength tuning is performed by a computer controlled change of the dye laser wavelength together with the angular tuning of both LiNbO₃ crystals.

The OPO efficiency of about 7-8% allows for achieving output energies of up to 10mJ/pulse when pumping with an energy of 120-140 mJ. However, in order to avoid saturation effects in the depletion experiments, the OPO output energy is usually maintained below 1-2 mJ/pulse. The energies of the seed and OPO radiations are monitored by pyroelectric detectors **3**.

The OH⁻ ions inside the LiNbO₃ crystal absorb at 3485 cm^{-1} , causing a significant reduction of the OPO power in the range of 3460-3510 cm^{-1} .

Calibration of the IR frequency was accomplished by measuring the wavelengths λ_{dye} and λ_{532} by means of a commercially available lambda-meter ATOS LM-007. Using eq. (2.3-2) λ_{IR} can be evaluated. This calibration procedure ensures an accuracy of $\pm 1 \text{ cm}^{-1}$ in the frequency region of 2800-3800 cm^{-1} .

2.3.6 Nozzle source

The nozzle source used for production of the supersonic beams in the IR/R2PI and IR/fsMPI experiments should fulfil certain requirements. Time-of-flight spectrometry, used in these experiments as a detection method, requires high vacuum conditions, which can be achieved either by using powerful vacuum pumps or a nozzle source with a pulsed regime of operation. The latter approach is, however, more favorable since it has an additional advantage of sparing sample consumption. The second requirement for the nozzle design originates from the fact that many solid state substances have a rather high melting temperature. For instance, in order to get a sufficient vapor pressure of some nucleobases, they should be heated up to about 300°C. Therefore, the nozzle should allow the heating of a sample reservoir to such high temperatures.

Taking these two requirements into account, we have developed a new nozzle source. It is depicted in **Fig. 2.3-6**. The nozzle consists of three main parts: a heated sample chamber with an orifice (on the left), a heatsink (in the center) and a modified pulsed valve (General Valve 9 Series), shown on the right. The valve is made up of a metal body with a solenoid, a plunger and a return spring. When the voltage is not applied to the solenoid, the return spring presses on the metal stick with a polymer tip on its end, closing the orifice outlet. When voltage is applied, the plunger tends to minimize the gap between them and the valve body, moving against the return spring. The metal stick follows the plunger, opening the orifice, thus the mixture of the sample vapor and the carrier gas collected in the sample chamber expand into the vacuum.

The end part of the nozzle with the sample chamber is heated by a heating element (wire). In order to maintain the desired temperature of a sample, the temperature is monitored at different points of the chamber. Based on these temperature readings, an electronic heating control unit supplies an appropriate voltage to the heating wire. To prevent heating of the valve, which would cause the damage of the solenoid, there is a heatsink between the sample chamber and the valve. The heatsink is connected directly to the flange of the vacuum apparatus, providing an efficient heat withdrawal from the central part of the nozzle. As polymer material for the sealing tip, called poppet, Vespel SP-1 was used, since it can withstand temperatures up to 300°C.

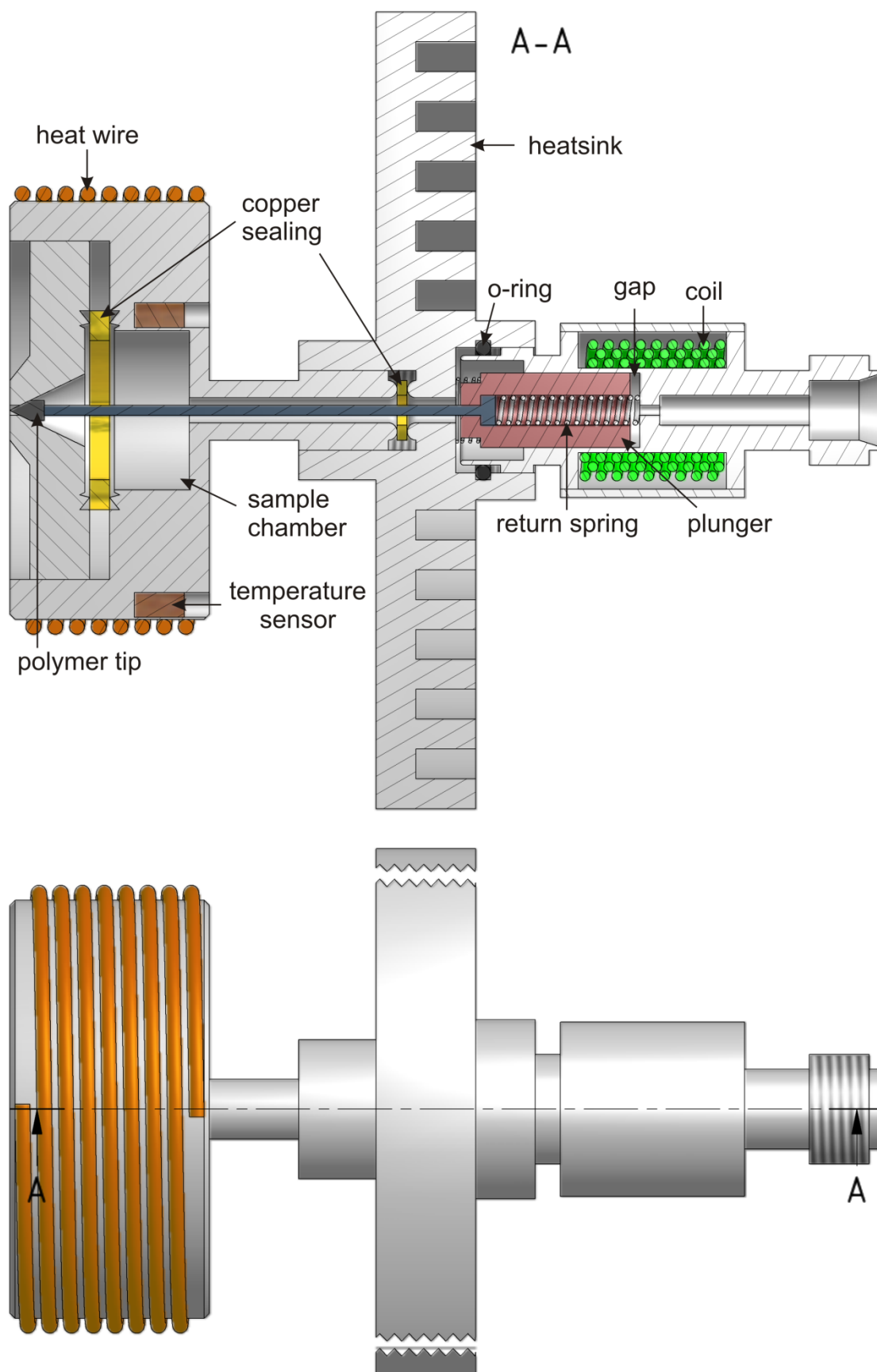


Fig. 2.3-6 Nozzle source construction.

Minimization of the pulse duration and thus the duty cycle (the ratio of the pulse duration to the period of a pulse sequence) has two advantages. First, it allows for improving the vacuum condition without increasing the pumping capacity. Second, it results in reduction of the sample consumption. Therefore, the goal is always to get a gas pulse as short as possible. However, a reduction of the gas pulse duration is limited by fundamental and technical reasons. The fundamental limitation is imposed by the fluid dynamics of the gas itself [57, 77]. Thus, for instance, some time is required for the acceleration of the molecule to the same stream velocity as in a continuous steady-state expansion. This time depends on the molecule's size and is in a range of tens of microseconds [77].

The technical obstacles in designing fast solenoid nozzles stem from the magnetic nature of the pulling force. In first approximation this force can be written for an electromagnet with the non-magnetic gap $d_{gap} > 0$ as follows:

$$F_{em} = \frac{B^2 S}{2\mu_0}, \quad (2.3-4)$$

Here B is the magnetic field in the gap, S is the cross-section of the plunger. However, all ferromagnetic materials are saturated at a value of the B field about 1.6 teslas. This provides the higher limit for F_{em} (more precisely F_{em}/S , see (2.3-4)), and, as a consequence, results in the lower limit of the opening time of the solenoid nozzle.

Another limitation is related to the fact that the force F_{em} cannot be set instantaneously, but some time is required for the field B in a solenoid to reach a desired magnitude. If the voltage U is applied to the solenoid with the number of turns N , this build-up time can be calculated as follows:

$$t_{build-up} = \frac{BNS}{U} \quad (2.3-5)$$

Thus, the build-up time can be shortened by either reducing the number of turns in the solenoid or by increasing the voltage applied to a solenoid. Taking this into account, the original solenoid of the valve was modified by reducing the number of turns by about ten times. Furthermore, a special solenoid driver has been developed, which is capable of providing a 30 μ s electric pulses with an amplitude of 160V and a current of 200A.

Since the closing time is only determined by the return spring, the original spring was replaced by a stronger one.

The dependence of ion signals of two monomers, 9-methyl-adenine and thymine, as well as their hetero-dimer and the 9-methyl-adenine-water cluster on the time delay between the nozzle opening and the ionization laser pulse is depicted in **Fig. 2.3-7**. According to the ion signals of monomers, the gas pulse duration is 260 μs (FWHM); that is about 3-4 times shorter than that achieved with the original General Valve design and the standard pulsed driver.

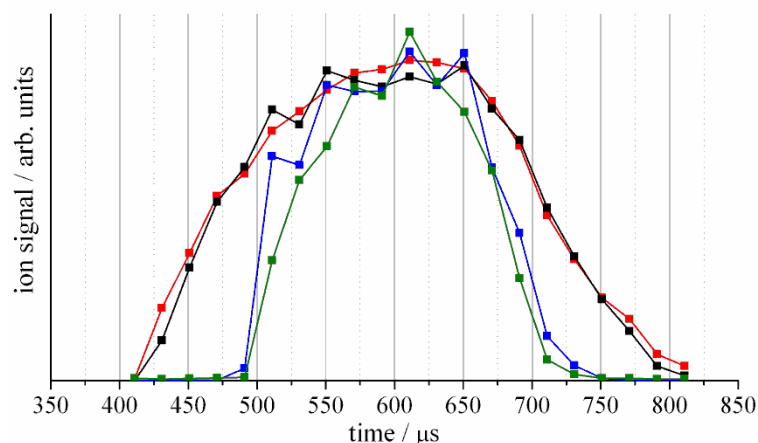


Fig. 2.3-7 The normalized ion signals of two monomers and two clusters: 1Me-Adenine (red), Thymine (black), (1Me-Adenine)-(H₂O) complex (blue) and (1Me-Adenine)-(Thymine) hetero-dimer (green).

From **Fig. 2.3-7** it can be seen that molecular clusters are preferably produced in the middle of the gas pulse. This can be explained by the highest rate of molecular collisions at this time, which means better cooling favouring the cluster formation process.

2.3.7 Dual beam technique

The signal-to-noise of the original IR/fsMPI method is in some cases rather poor due to several factors such as pulse-to-pulse stability of the laser and the nozzle. Averaging over a high number of laser shots is time demanding and not so efficient when long time fluctuations are present. In order to improve the signal-to-noise we have adopted the dual beam technique introduced by Lee and coworkers [16]. The principle of this technique is visualized in **Fig. 2.3-8**. Not one, but two UV laser beams are introduced into the ionization region (i) of the TOF spectrometer in the way to be about 4 mm apart from each other along the direction of the molecular beam. The beam that is downstream of the molecular beam is overlapped with the infrared beam and served as the signal, whereas the second one acts as a reference. The ion signals originated from these two UV beams are separated in time by about 90 ns by choosing an appropriate magnitude of the electric

field between the two plates of the ionization region (i). As an example, the time-of-flight spectrum of adenine (Ade) and the 1:1 adenine:water cluster (Ade+W) is shown on the right of **Fig. 2.3-8**. Each mass channel is made up of two peaks: signal (S) and reference (R).

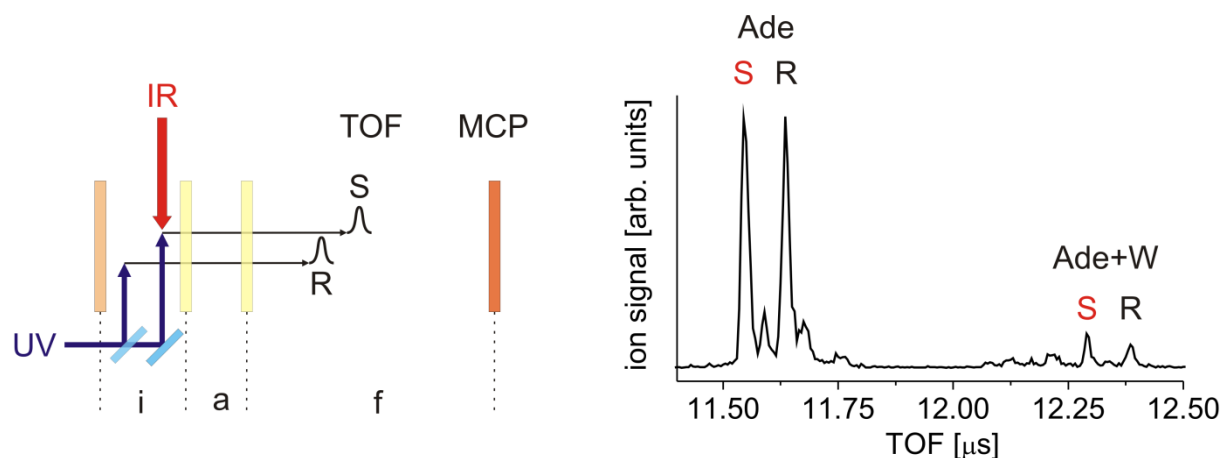


Fig. 2.3-8 Left: Principle of the dual beam technique; Right: the corresponding TOF spectrum of adenine with water.

The improvement of the quality of the spectra, which resulted from employing the dual beam technique, can be illustrated by an example of adenine monomer, the IR/fsMPI spectrum of which is shown in **Fig. 2.3-9**. It is clearly seen that the quality of the spectrum (b), which is constructed as the ratio of the signal to reference, is much better than that of the separate single spectra (S or R). In the shown IR region adenine has only one band at 3452 cm^{-1} (NH_2 symmetric stretch).

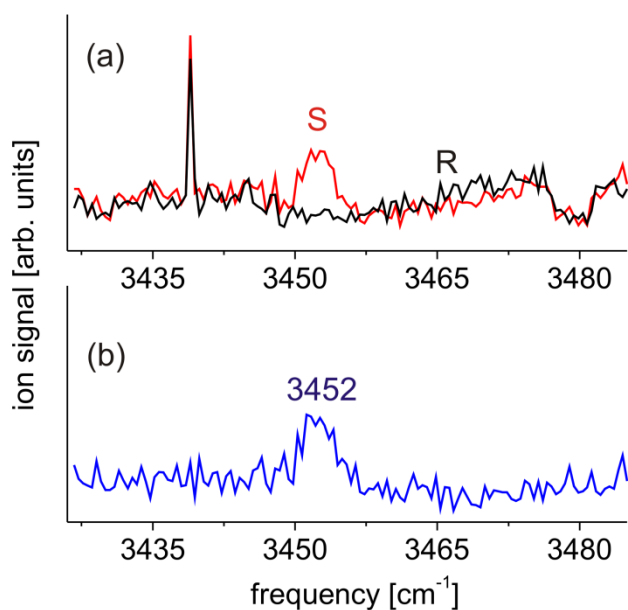


Fig. 2.3-9 The IR/fsMPI spectra of adenine: (a) ion signal of S and R peaks, (b) the ratio of the signal to reference.

2.4 Pump-probe Resonant Excitation Multiphoton Ionization

The energy provided to a molecule by an electronic excitation can be transferred and distributed by different relaxation mechanisms. Thus, if the excited electronic state neither crosses nor is coupled to others (adjacent) electronic states, the excitation energy is redistributed over all vibrational modes of this electronic state by means of vibrational coupling; this is called intramolecular vibrational energy redistribution (IVR). If there is a coupling with another electronic state, an internal conversion (IC) process may take place, resulting in the energy transfer from the initially excited electronic state to the vibrational modes of the coupled electronic state. The excited state energy can also be deactivated through conical intersection (CI), i.e. by crossing of two electronic states, to a different electronic state of the molecule.

Electronic excitation can also lead to various types of photochemical reactions such as photo-induced structural change (photoisomerization) and hydrogen or proton transfer inside the molecule or molecular cluster.

By studying the dynamics of the excited state population of molecular systems, it is possible to gain insight into the fundamental processes described above. For this purpose a straightforward approach, called femtosecond pump-probe resonant excitation multiphoton ionization (fs REMPI), can be utilized. The energetic diagram of the method is depicted in [Fig. 2.3-10](#). The pump femtosecond laser pulse **ph1**, the wavelength of which is in resonance with the $S_n \leftarrow S_0$ transition, excites a molecular ensemble into the electronic state S_n . The evolution of the excited state population is subsequently probed by two photon ionization (**ph2** and **ph3**).

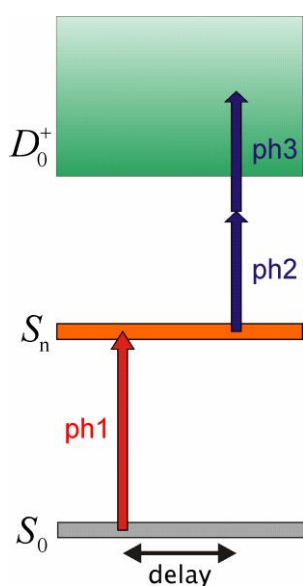


Fig. 2.3-10 The energetic diagram of the fs pump-probe REMPI.

3 Results

In this chapter the most important results are collected, which were obtained in the course of my PhD work by three aforementioned methods: fs DFWM, IR/fsMPI, fs pump-probe REMPI. All these results are either published or submitted for publication, therefore, for more details the references will be given to the corresponding articles. The quantum chemistry calculations were carried out by Dr. P. Tarakeshwar (pyrrolidine), Dr. S. Knippenberg and Prof. Dr. A. Dreuw (cyclopentene), Alexander Kyrychenko (*1H*-pyrrolo[3,2-*h*]quinoline-methanol/water clusters) and Philipp H. P. Harbach (adenine and 9-methyladenine hydrates).

This chapter is divided into two parts. The first part (3.1) is devoted to an application of fs DFWM for studying the structure and dynamics of molecules in their electronic ground state. In the second part (3.2) the structure and excited state dynamics of photoreactive molecules and molecular clusters are studied by means of IR/fsMPI and fs pump-probe REMPI.

3.1 Femtosecond Degenerate Four-Wave Mixing experiments

This chapter consists of two parts. In the first part (3.1.1), the influence of nuclear spin statistics (NSS) on fs DFWM spectra will be discussed. As will be shown, NSS effect can be very pronounced in some special cases, leading to the appearance of completely new recurrences in a fs DFWM spectrum. Thus, understanding of the nuclear spin statistics manifestation in fs DFWM spectra and subsequently taking it into account in the simulation procedure is indispensable, allowing for extending the scope of the fs DFWM method towards that of high-resolution spectroscopy.

Originally the time-resolved rotational fs DFWM spectroscopy was intended for the structural (rotational constants) investigation of non-polar molecules in their electronic ground state. Recently we have applied this method for studying the dynamics of large amplitude intramolecular motions, such as puckering in cyclic five-membered ring compounds. This new approach will be considered in the second part (3.1.2) of the current chapter.

3.1.1 Missing levels lead to additional lines: the influence of nuclear spin statistics on femtosecond degenerate four wave mixing spectroscopy of polyatomic systems

C. Riehn, M.I. Kunitski, V.V. Matylitsky, M.F. Gelin, and B. Brutschy, *Missing levels lead to additional lines: the influence of nuclear spin statistics on femtosecond degenerate four wave mixing spectroscopy of polyatomic systems*, *Physical Chemistry Chemical Physics*, 2005, **7**(23): p. 3955-3962.

The effects of nuclear spin statistics (NSS) on fs DFWM spectra has been described in the literature for diatomic and linear molecules such as O₂, N₂ and CO₂ [12, 37, 78]. There, the analysis is straightforward since the simulation of fs DFWM spectra can be done in an analytical form. However, it is by no means trivial to predict the NSS influence on a time-resolved spectrum in the general case of polyatomic non-linear molecules.

Here the effect of NSS on the fs DFWM spectra of sulphur dioxide (SO₂), nitrogen dioxide (NO₂) and nitromethane (CH₃NO₂) will be discussed (**Fig. 3.1-1**). All these molecules exhibit new types of rotational recurrences, which were successfully reproduced by the incorporation of NSS into the fs DFWM simulation-fitting code. The subsequent theoretical analyses uncovered the appearance mechanisms of these new spectral features. The NSS is shown to have a profound effect on fs DFWM spectra of asymmetric top species, notably with several zero spin nuclei.

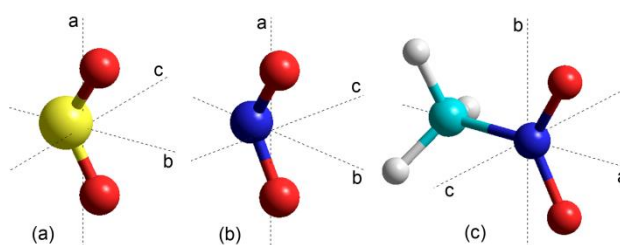


Fig. 3.1-1 a), b) and c) Schematic view of sulphur dioxide (SO₂), nitrogen dioxide (NO₂) and nitromethane (CH₃NO₂) molecules, respectively, with principal axes of inertia.

It was shown in chapter 2.2.4 that rotational levels of asymmetric top can be classified according to their symmetry towards two-fold (90°) rotation (C_2 operation) about any of the principal axes of inertia x , where x is a , b or c (**Table 2.2-1**). According to this classification there are only four possible kinds of rotational levels, which make up the D_2 group. The first one is a totally symmetric rotational level (designated as A); the wavefunction of this level is invariant upon C_2 operation about every one of three principal axes of inertia. The other three types of levels are designated as B_a , B_b , B_c , where the subscript indicates the principal axis of inertia, the two-fold rotation about which does not change the sign of the rotational wavefunction. Upon C_2 operation about two others principal axes of inertia the sign of the rotational wavefunction changes (see **Table 2.2-1**).

If a molecule possesses two identical nuclei, which can be exchanged during the two-fold rotation about, for instance, the principal axis of inertia a , the rotational levels which are symmetric to this rotation (A , B_a) will have different statistical weights than the antisymmetric ones (B_b , B_c). This difference in statistical weights depends on the spin of the nuclei. In the limiting case, when the nuclei have zero spin, the statistical weights of antisymmetric rotational levels are zero, meaning that these rotational levels do not exist. As a consequence, the rotational transitions between the antisymmetric levels do not exist as well. Therefore, the rotational spectrum becomes diluted if compared to that of a molecule with the non-zero spin nuclei.

This effect can be shown by considering the simplest case of a diatomic molecule. For such a system the rotational Raman selection rules are $\Delta J=0, \pm 2$. Therefore, the rotational spectrum in the frequency domain consists of equidistant lines spaced by $4B$ (B is the rotational constant of the molecule), as shown on the top of Fig. 3.1-2. The Fourier transformation of the frequency spectrum results in the time-domain spectrum, which also appears as the sequence of peaks with the inverted period of $1/4B$. In the case of two *identical zero spin* nuclei, only symmetric rotational levels (even J) exist, resulting in the spacing in the frequency spectrum twice as long, namely $8B$, as shown on the bottom of Fig. 3.1-2. The corresponding time-domain spectrum acquires twice shorter period of $1/8B$, if compared to that of a molecule having two *non-identical* nuclei but the same rotational constant B (Fig. 3.1-2, bottom).

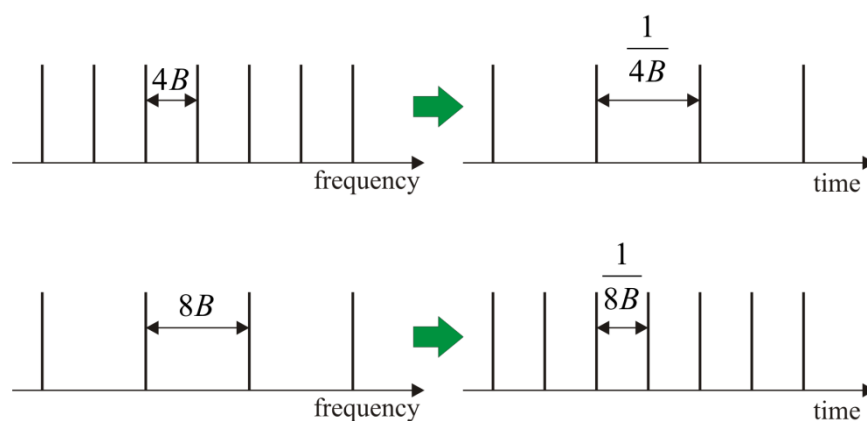


Fig. 3.1-2 The frequency and corresponding time-domain spectra of two diatomic molecules having the same rotational constant B : top – with two *non-identical* nuclei, bottom – with the *identical zero spin* nuclei.

Thus, in case of a diatomic molecule the NSS effect causes the new recurrences in the time-domain spectrum to appear. Such an influence was however not expected for the more general case of an asymmetric rotor, with all three rotational constants A , B and C being different. The frequency spectrum of an asymmetric rotor is usually much more complicated than that of a

diatomic (linear) molecule, and lacks for a transparent frequency pattern. Nevertheless, it was shown that even in this case NSS can lead to appearance of new recurrences.

A short introduction should be given to the assignment and classification of rotational recurrences in the time-domain RCS spectra. There are several types of recurrences; they originate from different rotational transitions. The most abundant rotational recurrences (at least for nearly symmetric tops) are the so-called J -type recurrences, with a period of $1/[2(A+B)]$ and $1/[2(B+C)]$ for nearly oblate and prolate tops, respectively. For slightly asymmetric tops the asymmetry rotational recurrences of A - or C -type with the corresponding periods $1/(4A)$ and $1/(4C)$ can occur. They dominate the spectrum for highly asymmetric species. Thus the recurrences in fs DFWM spectra will be denoted by $X(1), X(2), \dots, X(n)$, where integer $n=1, 2, \dots$ numbers the recurrence peaks and $X=J, A, C$ stands for the recurrence type. The recurrences induced by the NSS appear in between the integer recurrences and therefore will be referred to as $X(n/2)$.

In **Fig. 3.1-3** the fs DFWM spectra of three asymmetric top molecules, SO_2 , NO_2 , CH_3NO_2 , are presented. Thus, taking into account the NSS in the simulation of the fs DFWM spectra of the SO_2 and NO_2 molecules, it is possible to reproduce half integer recurrences $J(n/2)$, which were observed previously in the experiments by Frey et al. [79] and Pastirk et al. [80] The same approach was used for the simulation of the fs DFWM spectrum of nitromethane, which was experimentally measured in our lab. In this case two identical oxygen nuclei, situated about the principal axis of inertia a (see **Fig. 3.1-1**), cause the half integer asymmetry recurrence $A(3/2)$, having the highest intensity, to appear in the fs DFWM spectrum. Additionally, there is a very weak $A(1/2)$ recurrence at the time delay of 9.5 ps.

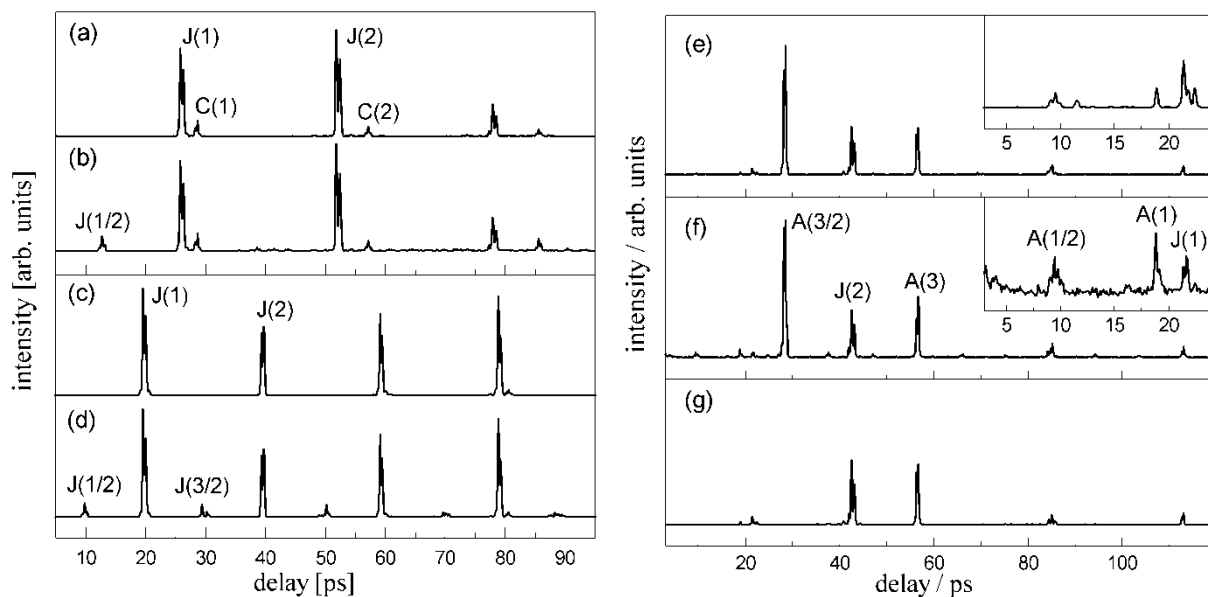


Fig. 3.1-3 Left: Simulations of the fs DFWM spectra of SO_2 and NO_2 . **a)** and **b)** - SO_2 , **c)** and **d)** - NO_2 without/with consideration of nuclear spin statistics. Right: Experimental and simulated fs DFWM spectra of nitromethane: **e)** Fitted simulation of the spectrum using nuclear spin statistics, **f)** Experimental fs DFWM spectrum (this work), **g)** Simulation of the spectrum without consideration of nuclear spin statistics. For assignment of rotational recurrences see text.

In order to gain insight into the origin of these half integer recurrences, the frequency-domain spectra were considered. It turned out that in the cases of sulphur and nitrogen dioxides the NSS, “forbidding” a part of the rotational transitions, cause a special pattern to occur in the frequency domain to occur. This pattern is made up of equidistant clusters of frequency lines. The period of this cluster sequence is $4(B+C)$, which corresponds to the period of a half integer J -type recurrence in the time-domain.

Fig. 3.1-4 presents the simulation of the partial frequency spectrum of nitromethane, where only the rotational transitions with $\Delta J=2$ and $\Delta \tau=+2$ are considered (τ designates the rotational energy levels within a J -manifold). These transitions contribute to the A -type asymmetry recurrences. The NSS makes the period of the frequency pattern longer, namely $8A/3$, resulting in the recurrence period of $3/8A$, which, according to the assignment given above, corresponds to the recurrence $A(3/2)$.

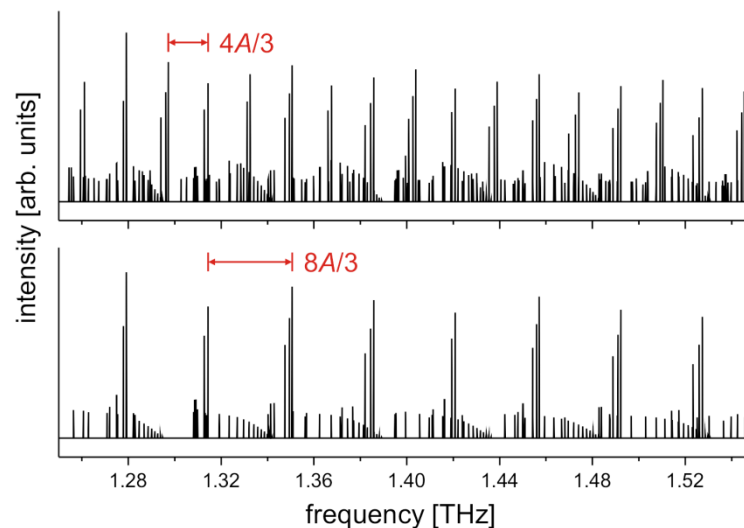


Fig. 3.1-4 Simulations of the rotational quantum beat frequency spectrum of nitromethane. Only $\Delta J=2$, $\Delta \tau=+2$ transitions are taken into account. All J manifolds contribute, without/with consideration of nuclear spin statistics, respectively.

Three molecules that have been considered have two identical zero spin nuclei. However not only *zero* spin nuclei, but also two identical *non-zero* spin nuclei might induce half integer recurrences in fs DFWM spectra. In this case the rotational levels of different symmetry have different but non-zero statistical weights. This can lead to an intensity modulation pattern of the frequency spectrum, and subsequently cause the ‘doubling’ of rotational recurrences. The simulation of the fs DFWM spectrum of the CF_2 radical provided evidence for weak $J(n/2)$ recurrences. This molecular top is very similar to SO_2 and NO_2 , apart from the ^{19}F nuclei, which has the spin of $1/2$. Here, the antisymmetric levels and symmetric levels have statistical weights of 3 and 1, respectively. This leads to an intensity modulated periodic pattern in the frequency spectrum, similar to SO_2 and NO_2 . Hence, the occurrence of extra rotational recurrences is not limited to cases where rotational energy levels do not exist (zero statistical weight), but the additional features can also be expected in the more general case of non-zero statistical weighting factors.

Conclusions

i) In the spectra of polyatomic molecules nuclear spin statistical effects might provide extra rotational recurrences with strongly varying intensity and persistence, which cannot be simply ‘extrapolated’ from the well-known behavior of diatomic and linear molecules.

ii) The occurrence of these RRs and their origin can be investigated by spectral simulations for general asymmetric molecular tops based on a symmetry classification of their rotational energy levels. By this way also the influence of different NSS weighting factors on the fs DFWM spectra can be explored.

iii) Thus, numerical simulations for the complete spectra based on a comprehensive model for fs DFWM spectroscopy are indispensable for a quantitative analysis, i. e. the extraction of molecular parameters from the experimental spectra. Moreover, these detailed data obtained from fs DFWM spectra extends the scope of the time-resolved approach towards that of high-resolution spectroscopy.

3.1.2 Large amplitude intramolecular motions studied by fs DFWM: pyrrolidine and cyclopentene molecules

M. Kunitski, C. Riehn, V.V. Matylitsky, P. Tarakeshwar, and B. Brutschy, *Pseudorotation in pyrrolidine: rotational coherence spectroscopy and ab initio calculations of a large amplitude intramolecular motion*, Physical Chemistry Chemical Physics, 2010, **12**: p. 72-81.

M. Kunitski, S. Knippenberg, M. Gelin, C. Riehn, A. Dreuw, and B. Brutschy, *Ring-puckering motion in cyclopentene studied by time-resolved rotational coherence spectroscopy and ab initio calculations*, Physical Chemistry Chemical Physics, 2010, **12**: p. 8190-8200.

Large amplitude intramolecular motions that cause a change in chemical constitution are of special interest to chemists and biochemists since they take place in a wide range of naturally occurring compounds [81-83]. One example of such a motion is the ring puckering in saturated five-membered ring compounds which are constituents of a wide range of biomolecules such as the deoxyribose/ribose of DNA/RNA, the amino acid proline and the drug nicotine. Pyrrolidine and cyclopentene being the simplest among these compounds were chosen as archetypical systems for studying ring puckering dynamics.

A five-membered ring has $5-3=2$ out-of-plane skeletal modes consisting of a bend and a twist. These two modes are shown in [Fig. 3.1-5](#)

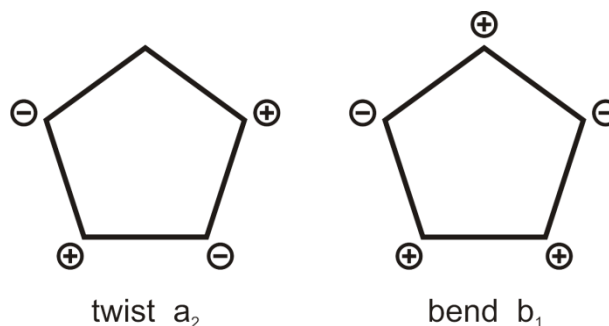


Fig. 3.1-5 Two out-of-plane modes of a five-membered ring.

The character of these two modes is different in pyrrolidine and cyclopentene molecules. In pyrrolidine the ring is relatively flexible, since all five bonds of the ring are saturated. The approximate two dimensional potential of the skeletal motion of the pyrrolidine ring is shown in [Fig. 3.1-6](#).

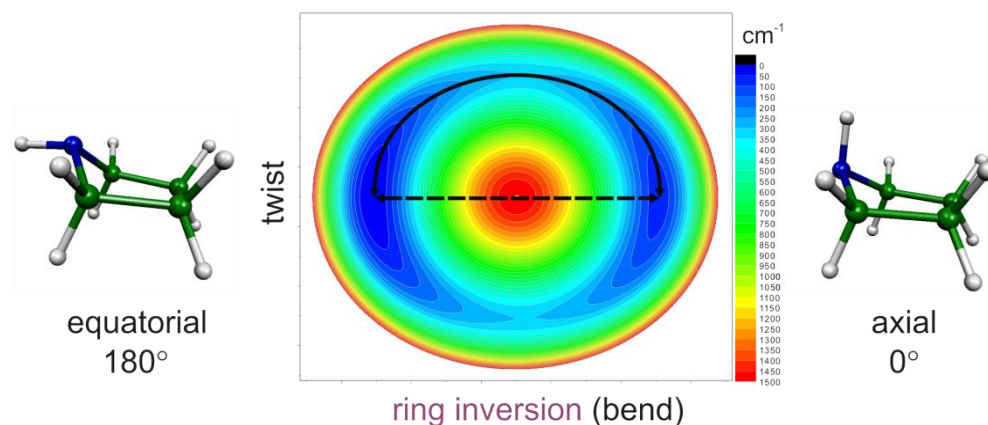


Fig. 3.1-6 The two dimensional potential of the skeletal motion of pyrrolidine and two minima energy structures of pyrrolidine: equatorial and axial. Two ways of going from the equatorial to the axial conformers are shown by arrowed lines: dashed – ring inversion, solid – pseudorotation.

The centre corresponds to the planar structure and has the highest energy of about 1500 cm^{-1} . Of the two minima energy structures, equatorial and axial (see **Fig. 3.1-6**), the former is the global minimum. Interconversion of these two conformers can be done either by crossing the central barrier (ring inversion) or by going along the potential valley (pseudorotation). Pseudorotation is the energetically most favorable path, since its energy barrier is about five times lower than that of ring inversion.

The name “pseudorotation” was chosen due to the appearance of this motion: the ring atoms move in such a way that the phase of the puckering rotates around the ring [84]. The half of the pseudorotational cycle is shown in **Fig. 3.1-7**. Since pseudorotation corresponds to a motion in a circle on the potential surface, it is convenient to use an angle (ϕ) as the pseudorotational coordinate.

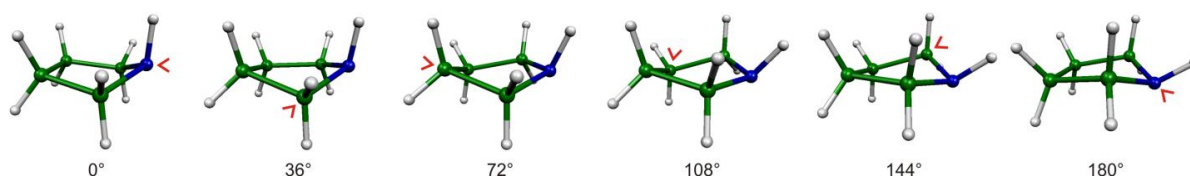


Fig. 3.1-7 The envelope structures of pyrrolidine and corresponding pseudorotational angles ϕ . In all these structures four atoms of the ring are in one plane, while the fifth one (indicated by a red arrow) is not. This pucker rotates around the ring during pseudorotation.

The situation is different in cyclopentene, where one double bond is present. This makes the twist mode energetically not favorable, therefore only the bending mode (ring inversion) is active at room temperature. In this case the two dimensional potential of the ring vibration looks like as shown in **Fig. 3.1-8**. Therefore, the interchange of two mirrored minimum energy structures, shown on both sides of the potential in **Fig. 3.1-8**, is accomplished by ring inversion through the planar ring structure.

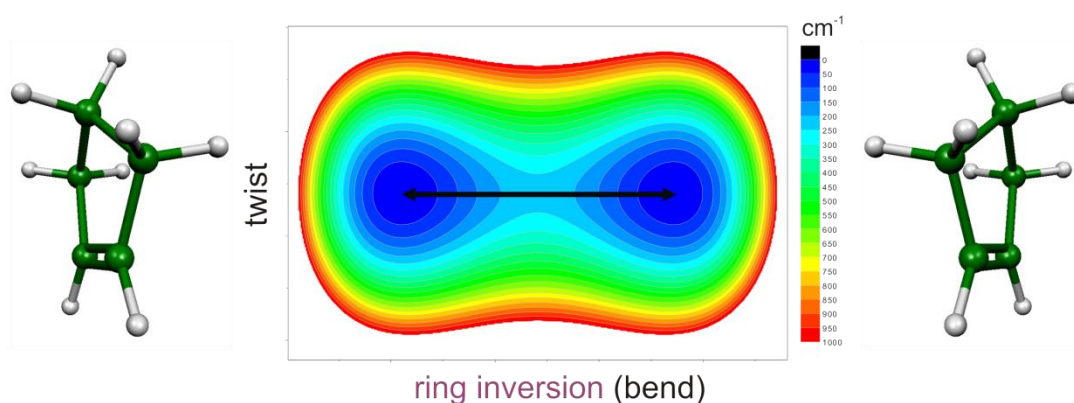


Fig. 3.1-8 The two dimensional potential for the skeletal motion of cyclopentene. The arrowed line shows the ring inversion path.

Both ring motions, pseudorotation in pyrrolidine and ring inversion in cyclopentene, are of large amplitude, highly anharmonic and are accompanied with significant changes in molecular geometry. Therefore, the fs DFWM spectroscopy, which is sensitive to the structure, was thought to be applicable for studying these large amplitude intramolecular motions. And indeed, the measured fs DFWM spectrum of pyrrolidine at room temperature was found to be much more complex as if it was originated from a single rigid molecule. Moreover, it could in no way be explained by the superposition of two structures: the axial and equatorial ones, which are shown in **Fig. 3.1-6**.

Pyrrolidine

In order to gain insight into the experimental fs DFWM spectrum of pyrrolidine the one-dimensional quantum mechanical model for pseudorotation was adopted. The model implies a one-dimensional potential for pseudorotation, which consists of two minima, corresponding to the equatorial and axial conformers of pyrrolidine, and the barrier in between, as shown on the left of **Fig. 3.1-9**. The model provides the pseudorotational (vibrational) energy levels and corresponding wavefunctions, which depend on the shape of the potential.

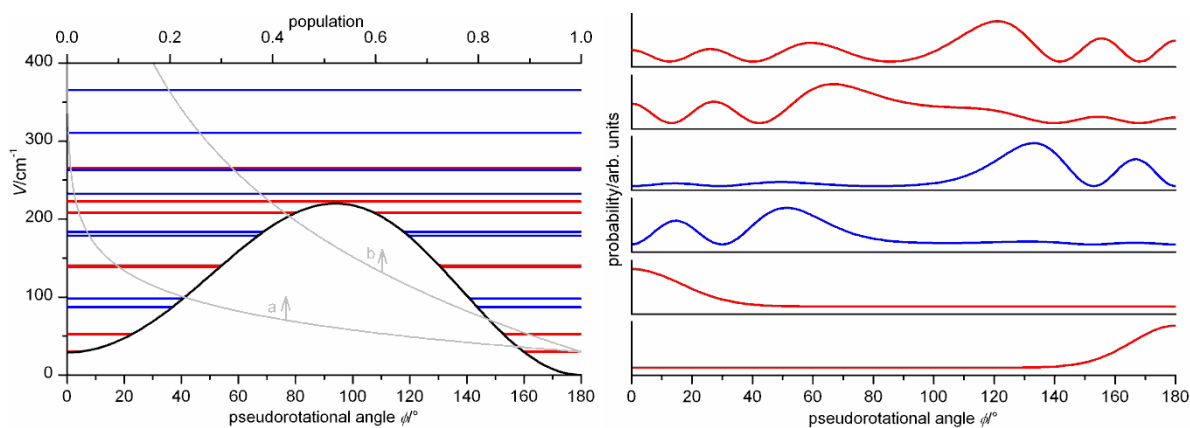


Fig. 3.1-9 Left: Pseudorotational potential and corresponding levels with their relative Boltzmann populations at temperatures of 68K (a) and 298K (b). Right: The probability density functions of the first six pseudorotational levels. The parity of levels is shown by red (even) and blue (odd) colors.

As one can see from the wavefunctions on the right of **Fig. 3.1-9**, the first two pseudorotational states relate to the equatorial and axial conformers of pyrrolidine, the structures that occupy two energy minima of the potential at the pseudorotational angles of 180° and 0° , respectively. The higher the state the more delocalized is the molecule on the pseudorotational path.

As follows from **Fig. 3.1-9**, with a given pseudorotational potential many pseudorotational levels are populated at room temperature, and, consequently contribute the experimental observations. This contribution can be understood as follows. The pseudorotational levels have different vibrationally averaged molecular properties, such as, for instance, rotational constants (structure), which may be evaluated using the pseudorotational model. Thus the complete fs DFWM spectrum is expected to originate from a mixture of different species (levels) that have different molecular properties. The contribution of each species is proportional to the Boltzmann population of the corresponding pseudorotational level.

Hence, the simulation of the fs DFWM spectra of a molecule, undergoing pseudorotation, consists of the following steps. First the pseudorotational levels are calculated relying on an assumed pseudorotational potential. Next the expectation values of the molecular properties required for the simulation are evaluated. With these data the fs DFWM spectra are generated for each pseudorotational state in the way as for a single species using the semirigid rotor approximation (see chapter 2.2.4). A coherent superposition of all individual fs DFWM spectra weighted by the Boltzmann population of the corresponding pseudorotational levels yields the complete fs DFWM spectrum. By means of a fitted simulation, the energetic (pseudorotational potential) and structural (rotational constants) parameters of pseudorotation can be obtained.

The fs DFWM spectrum of pyrrolidine at room temperature and its fitted simulation based on the one-dimensional model for pseudorotation are shown in **Fig. 3.1-10**.

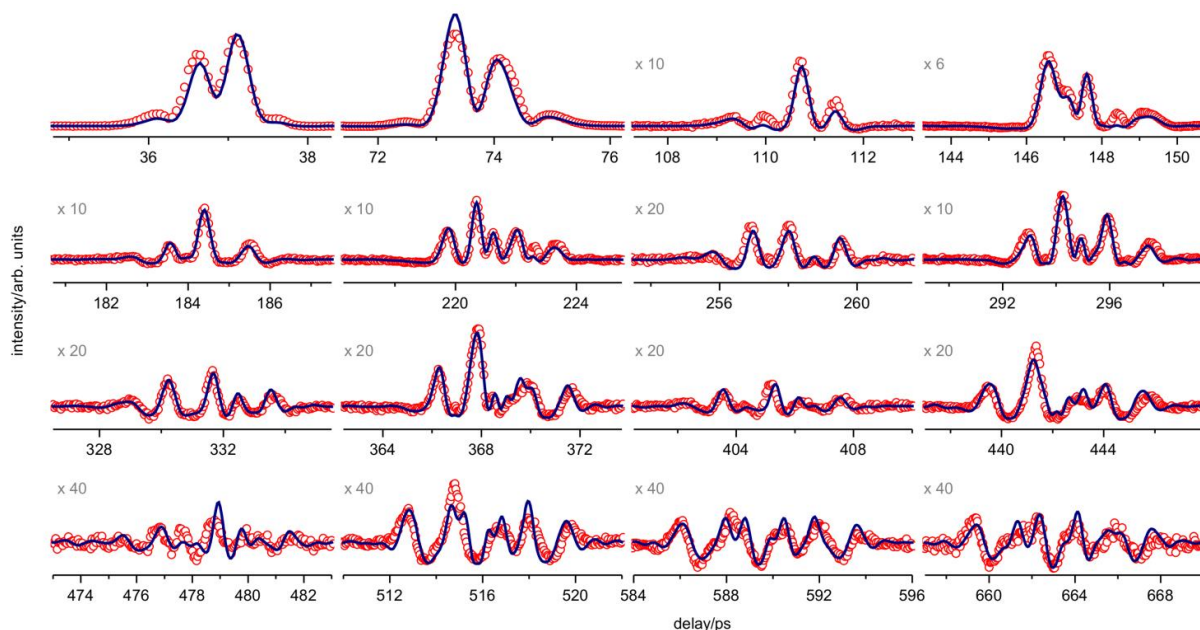


Fig. 3.1-10 The experimental fs DFWM spectrum (red) of pyrrolidine at room temperature (298K) and the fitted simulation (blue), using the one-dimensional model for pseudorotation.

The pseudorotational potential and the dependence of rotational constants on the pseudorotational angle obtained from the fit are depicted in **Fig. 3.1-11**. For comparison, quantum chemistry optimizations of various points along the pseudorotational path were performed using Synchronous Transit-Guided Quasi-Newton (STQN) method. The calculated pseudorotational potential as well as the rotational constants A and B are shown in **Fig. 3.1-11**.

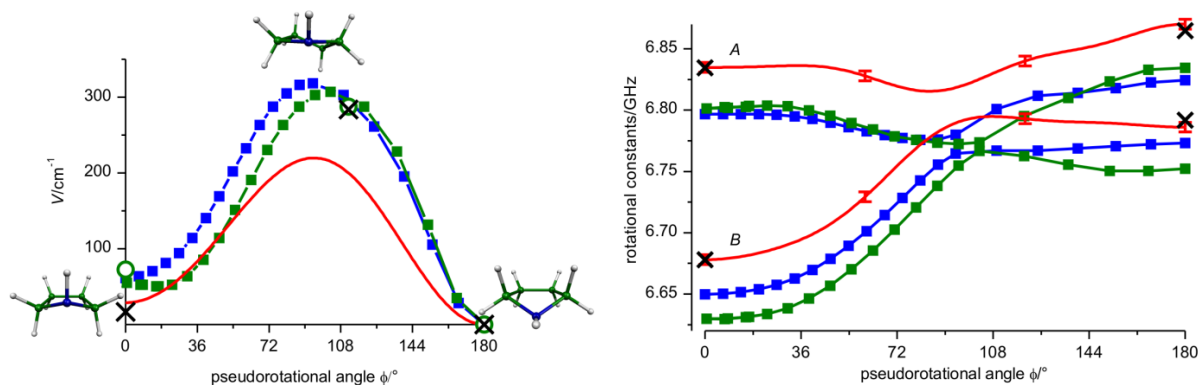


Fig. 3.1-11 The energy potential and the rotational constants A and B of pyrrolidine along the pseudorotational path: red – from the fitted simulation of fs DFWM spectrum at room temperature; blue and green – calculated with the aug-cc-pVDZ basis set at both the B3LYP and MP2 levels of theory. The MP2/aug-cc-pVTZ calculations are shown by green circles. These geometries were further used for single point CCSD(T)/aug-cc-pVTZ calculations (black crosses).

As follows from the fitted simulation of the room temperature fs DFWM spectrum of pyrrolidine, the equatorial conformer (180°) of pyrrolidine is stabilized by 29 cm^{-1} relative to the axial one (0°). The same finding was also reported in the microwave spectroscopic study [85].

However, it should be noted that microwave spectroscopy was not capable for deducing information about the complete pseudorotational path in pyrrolidine. This failure is explained by the very low dipole moment of the conformations with pseudorotational angles close to 180° .

From the fit of the fs DFWM spectrum of pyrrolidine the barrier for pseudorotation turned out to be 220cm^{-1} . This value and the energy difference between the axial and equatorial conformers of 29cm^{-1} are lower than those calculated with the aug-cc-pVDZ basis set at both the MP2 and B3LYP levels of theory (**Fig. 3.1-11**). However, the higher basis sets and levels of theory (CCSD(T)) tend to lower these values. Thus, the energy difference between the axial and equatorial conformers was found to be 17cm^{-1} at single point CCSD(T)/aug-cc-pVDZ calculations carried out on the MP2/aug-cc-pVTZ geometries (**Fig. 3.1-11**).

The results above give rise to new questions, concerning the energetic of pyrrolidine conformations. What is the reason for the barrier for pseudorotation in pyrrolidine to be much higher when compared to that in analogous five-membered saturated ring compounds such as cyclopentane [86] ($<25\text{cm}^{-1}$) and tetrahydrofuran [87] ($\sim 30\text{cm}^{-1}$)? Another question: Why is the equatorial form of pyrrolidine energetically more preferable than the axial one?

Apparently, in order to understand these peculiarities of the pyrrolidine molecule one should gain insight into the nature of its pseudorotational potential. Several factors controlling the conformation in saturated cyclic compounds are known. The main among others are ring angle strains and the torsional forces associated with the rotation about a single ring bond [81]. While the former effect tends to keep the ring planar, the latter favors the pucker of the ring. The torsional forces in cyclopentane and tetrahydrofuran as well as in pyrrolidine are dominant leading to the ring being puckered.

The angle and torsional strains of the ring are manifestation of two electronic effects: steric repulsion and hyperconjugation stabilization. It is however difficult to determine which of these two effects has the greater contribution. In the last decade there were several debates about the nature of the torsional strain in the ethane molecule, which hinder the internal rotation by a barrier of about 1000cm^{-1} . Pophristic and Goodman [88] showed that the energetic of this rotation is to a great extent explained by hyperconjugation, while the subsequent studies [89, 90] concluded steric repulsion to have a major impact. Thus, additional theoretical investigations are required in order to gain insight into the nature of the pseudorotational energetics of pyrrolidine.

Cyclopentene

Though the puckering motion of the cyclopentene ring is different from pseudorotation in pyrrolidine, the same approach can be utilized for gaining insight into its dynamics. Since the twist vibration of the cyclopentene ring is quite energetic, the two-dimensional motion can be reduced into the one-dimensional one, which consists of the single ring bending mode, or ring inversion, as shown in **Fig. 3.1-8** by the arrowed line. This bending mode is also referred to as the ring-puckering vibration. As seen from **Fig. 3.1-8** the ring-puckering potential in case of cyclopentene is of double minima nature with the central barrier corresponding to the planar ring structure. The ring-puckering vibration is usually described either by a dihedral angle ϕ or a distance x , as shown in **Fig. 3.1-12**. However, in mathematical calculations it is more convenient to use a dimensionless reduced ring-puckering coordinate Z .

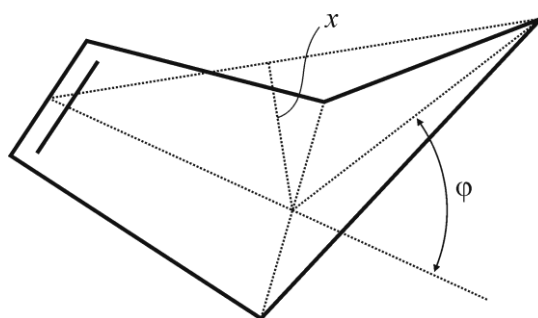


Fig. 3.1-12 Two geometric parameters, an angle ϕ and a distance x , which are usually used for the description of the ring-puckering vibration.

The fs DFWM spectrum of cyclopentene, measured in the gas cell at room temperature is shown in **Fig. 3.1-13** (red). The fitted simulation based on the one-dimensional model for the ring-puckering vibration (**Fig. 3.1-13**, blue) is in good agreement with the experimental spectrum.

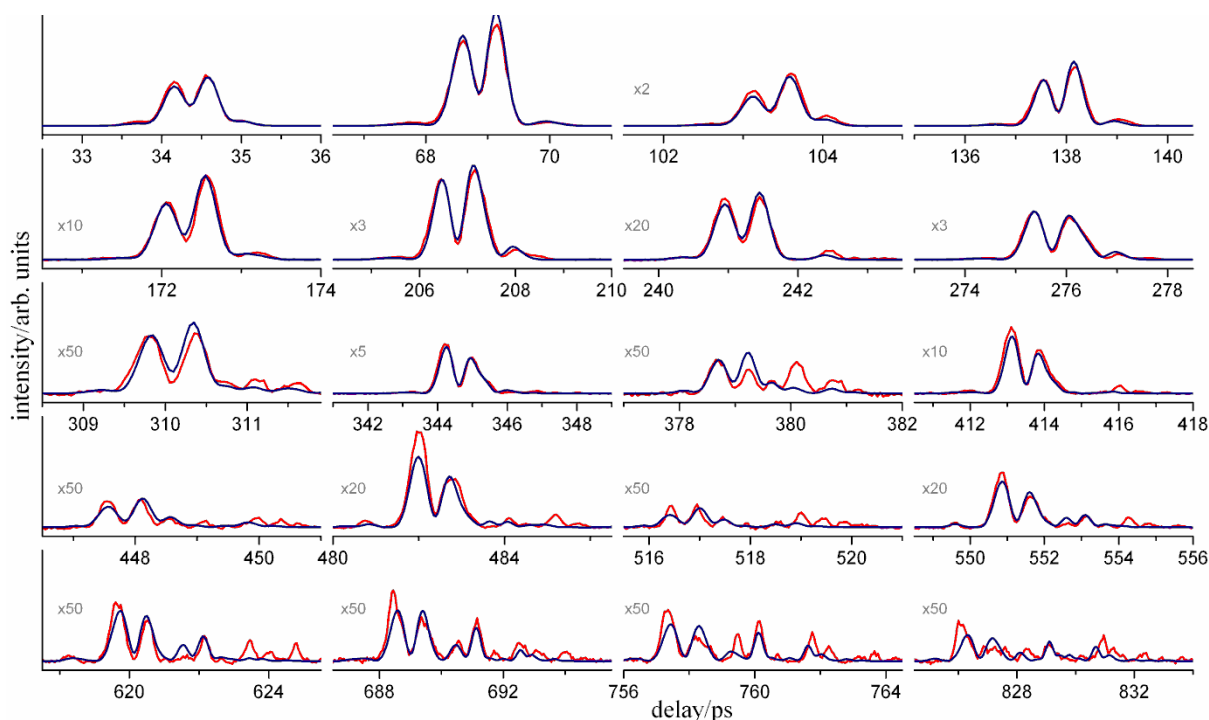


Fig. 3.1-13 Fs DFWM spectra of cyclopentene in the gas cell at room temperature: red - experimental, blue - fitted simulation based on the one-dimensional model for the ring-puckering vibration.

From the fit the double-minima potential of the ring-puckering motion in cyclopentene was obtained together with the rotational constants. Thus, the barrier to ring inversion (corresponding to the planar ring structure) was found to be 274 cm^{-1} , which is somewhat higher than the previously determined value of $232 \pm 5 \text{ cm}^{-1}$ [91-93]. A value of 1.769 was derived for the reduced puckering coordinate Z corresponding to the potential minimum. The relationship between the coordinate Z and the puckering angle φ was evaluated by quantum chemistry calculations. From this relation and the Z value of 1.769 the puckering angle φ corresponding to the potential minimum was found to be 24.3° ($\varphi/Z \approx 13.75$). The previous estimations of this angle lie in the wide range: $22\text{-}30^\circ$.

The rotational constants A and B as functions of the dimensionless reduced puckering coordinate Z as obtained from the fit are depicted in **Fig. 3.1-14** (green). For comparison the calculated rotational constants and those found in the MW studies [93, 94] are also shown. Our results are in excellent agreement with the rotational constants from the MW work of Lopez et al. [94] (**Fig. 3.1-14**, blue dashes).

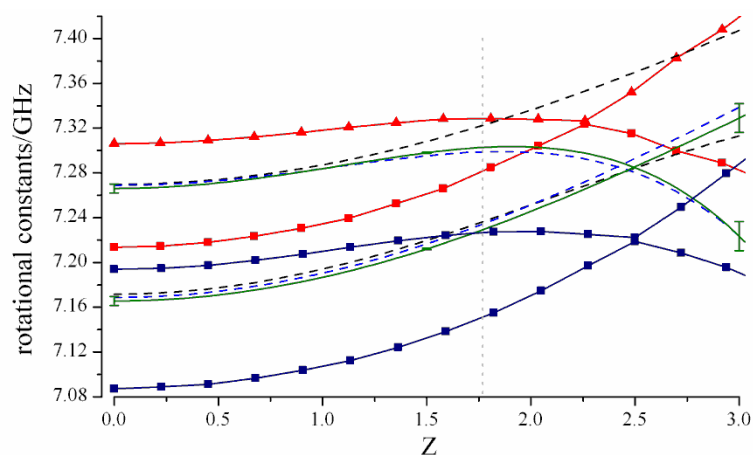


Fig. 3.1-14 Dependence of the rotational constants A and B on the reduced puckering coordinate Z : red - calculated at B3LYP/cc-pVTZ; dark blue squares - calculated at SOSMP2/cc-pVDZ; green - derived from the fitted simulation of the experimental fs DFWM spectrum of cyclopentene at room temperature (standard deviation is shown by error bars); blue dashes - taken from the MW work of Lopez et al. [94]; black dashes - taken from the MW work of Scharpen [93] The dashed vertical line indicates the equilibrium reduced puckering coordinate Z_{min} deduced from the fit. $\varphi/Z \approx 13.75$.

Conclusions

- i) Large amplitude motions such as pseudorotation in pyrrolidine and the ring-bending vibration in cyclopentene were investigated by a new approach based on fs rotational degenerate four-wave mixing spectroscopy.
- ii) The energetic and structural aspects of pseudorotation in pyrrolidine were revealed for the first time. Thus, the barrier to pseudorotation was found to be 220 cm^{-1} . The obtained pseudorotational potential provides evidence for the energetic preference of the equatorial conformer over the axial one. This is in line with the finding of microwave spectroscopy, where only two mentioned structures were assigned. The low dipole moment of the pyrrolidine conformations makes microwave spectroscopy not applicable for study pseudorotation in this molecule.
- iii) Hence, the high structural sensitivity together with good energetic evaluation makes fs DFWM spectroscopy an attractive tool for the investigation of large amplitude intramolecular motions. The method is particularly interesting for molecules lacking or possessing only a small dipole moment, where far-infrared and microwave spectroscopy cannot be applied.

3.2 Structure and Dynamics of short-lived excited state molecules and clusters

3.2.1 Structural characterization of 1*H*-pyrrolo[3,2-*h*]quinoline microhydrates with ultrashort-lived electronically excited states

Y. Nosenko, M. Kunitski, R.P. Thummel, A. Kyrychenko, J. Herbich, J. Waluk, C. Riehn, and B. Brutschy, *Detection and structural characterization of clusters with ultrashort-lived electronically excited states: IR absorption detected by femtosecond multiphoton ionization*, *Journal of the American Chemical Society*, 2006, **128**(31): p. 10000-10001.

Y. Nosenko, M. Kunitski, C. Riehn, R.P. Thummel, A. Kyrychenko, J. Herbich, J. Waluk, and B. Brutschy, *Separation of different hydrogen-bonded clusters by femtosecond UV-ionization-detected infrared spectroscopy: 1*H*-pyrrolo[3,2-*h*]quinoline·(H₂O)_(n=1,2) complexes*, *Journal of Physical Chemistry A*, 2008, **112**(6): p. 1150-1156.

The progress in chemical kinetics makes it clear that the so-called “elementary” reactions, such as proton or electron transfer are, in fact, multidimensional processes, involving not only intramolecular degrees of freedom, but also those of the environment. The microsolvated 1*H*-pyrrolo[3,2-*h*]quinoline (PQ) constitutes an important model system for understanding the mechanism and dynamics of intermolecular excited state double proton transfer (ESDPT), which leads to tautomerization, a key reaction for chemical mutagenesis of DNA. PQ belongs to the group of bifunctional (H-bonding donor/acceptor) azaaromatics.

The dual fluorescence for PQ in protic solutions was observed and attributed to an ESDPT process. Fluorescence transient measurements with the femtosecond resolution yielded two time constants, fast and slow, indicating the presence of two kinds of solute-solvent complexes. The fast decay in a subpicosecond range was ascribed to a complex that exhibits intermolecular ESDPT, while the one of hundreds picosecond was assigned to the non ESDPT solute-solvent complex [95]. The subsequent gas phase study showed different photophysical properties of PQ upon stepwise solvation by methanol. Namely, no laser-induced fluorescence (LIF) of the jet-cooled 1:1 cluster was observed, while that of the 1:2 and larger complexes was quite strong upon S₁←S₀ excitation. The absence of fluorescence indicates a fast relaxation channel, therefore, the assignment can be made that the 1:1 cluster is the one that exhibits intermolecular ESDPT. Our goal is to investigate in detail the structure of such photoreactive complexes in order to shed light on their excited state reaction mechanism. For this purpose, their IR spectra in the NH, OH stretch region have to be recorded. Because of the ultrashort life-time of the excited state, the conventional nanosecond double resonant IR depletion technique or LIF is not applicable, and thus IR/fsMPI is the method of choice.

1:1 and 1:2 PQ-methanol hydrates.

The IR spectra in the region 3150-3450 cm^{-1} measured by IR/fsMPI for the PQ:methanol_{n=1,2} clusters are depicted in **Fig. 3.2-1**. The ascription of an experimental spectrum to a structure is performed by comparison with theoretically calculated spectra. The relevant structures of the 1:1 and 1:2 complexes of PQ with methanol are shown in **Fig. 3.2-1** together with their stick spectra calculated at the B3LYP/6-31G** level.

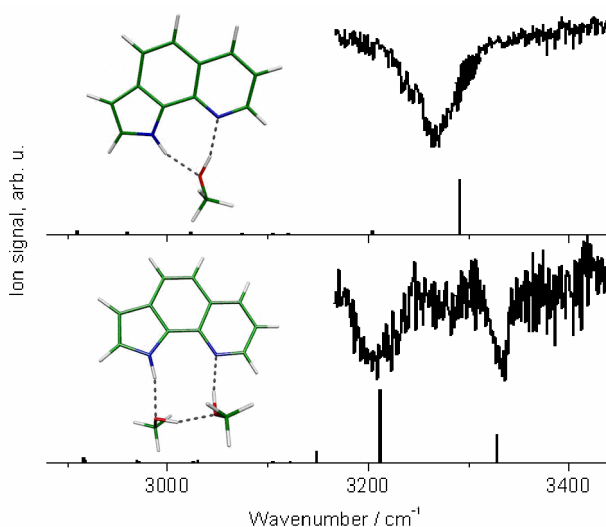


Fig. 3.2-1 IR/fsMPI spectra measured for PQ:methanol_{1,2} mass channels. The calculated IR spectra (B3LYP/6-31G**) are plotted with bars. Relevant cluster structures are inserted.

The strongest band of the 1:1 aggregate, calculated at 3291 cm^{-1} (measured at 3268 cm^{-1}), is readily identified as the coupled anti-phase stretch of the OH group of methanol and the NH of the pyrrole unit of PQ. Due to the strong double H-bond interaction ($E_{\text{binding}} \approx 10$ kcal/mol [96]) in this cyclic complex the local oscillator modes no longer exist. Similarly, for the 1:2 aggregate the most intense mode calculated at 3212 cm^{-1} is the anti-phase stretch of the pyrrole NH and pyridine bound OH. The vibration predicted at 3328 cm^{-1} is mainly the methanol dimer OH stretching, mixed, however, with elongations of the OH and NH bonds within the H-bond cycle.

The cyclic NH...OH...N bridge of the 1:1 aggregate was suggested as an intermediate for fast ESDPT in solution which gives rise to the anomalous fluorescence and quenches the normal one [97]. After photoexcitation, the protons involved in the H-bonds undergo a concerted, albeit asynchronous, transfer. In principle such a process is also possible in the 1:2 aggregate, but since there the “proton wire” is longer, a higher barrier or a higher chance for dissipative side processes or of disturbances along the way is also conceivable.

It should be emphasized that under the employed experimental conditions, i.e., fixed fs laser wavelength at 266 nm, no spectral selection of a specific cluster size by its UV fingerprints is possible. Therefore, the obtained mass spectra of clusters can be contaminated by signals from larger clusters due to their fragmentation. This, however, can be usually avoided by choosing appropriate expansion conditions, either by changing the vapour pressure of the solvent or by ionizing different segments of the gas pulse containing different cluster sizes.

1:1 and 1:2 PQ-water hydrates.

The similar situation was observed for PQ-water clusters, namely of the two complexes, 1:1 and 1:2, only the latter showed a LIF spectrum in the gas phase, indicating a fast relaxation channel for the 1:1 complex. This is in line with the study of PQ in water solution, where it was found that ESDPT occurs in cyclic 1:1 complexes [98].

FDIR and IR/fsMPI spectra of PQ-water clusters are shown in **Fig. 3.2-2**. The FDIR spectrum was recorded upon excitation of the transition at 28061 cm^{-1} , which was found to be the vibrational origin of the smallest PQ-water cluster exhibiting fluorescence. This spectrum resembles very closely the IR/fsMPI, recorded for the 1:2 mass channel (**Fig. 3.2-2**, $n=2$), thus indicating the fast relaxation mechanism in excited 1:1 cluster.

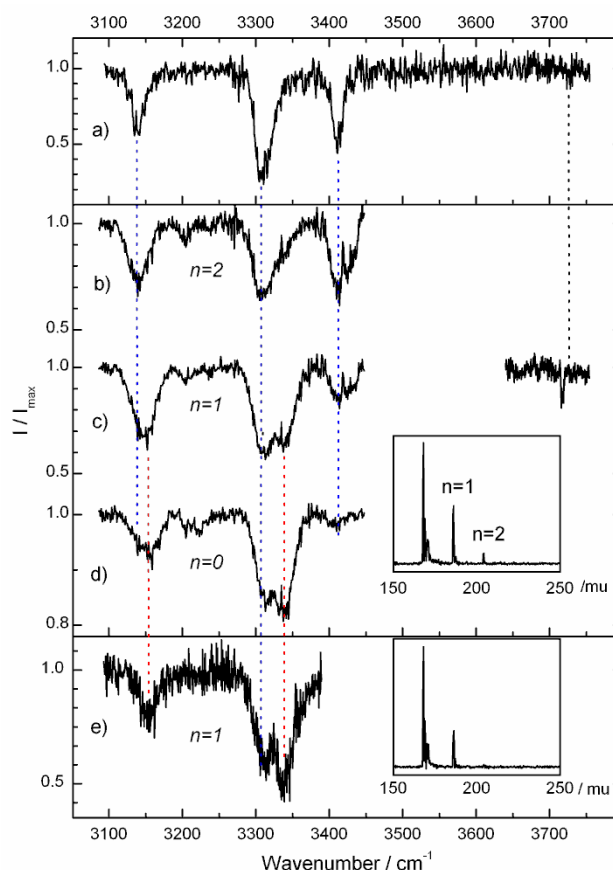


Fig. 3.2-2 A comparison of the FDIR spectrum (a) measured upon excitation of the transition at 28061 cm^{-1} with the IR/fsMPI spectra recorded in (b) $1^+{:}2$, (c, e) $1^+{:}1$, and (d) $1^+{:}0$ cluster channels. The spectrum e) was recorded at lower water concentration than the c) one. The inserted mass spectrum shows the corresponding cluster ion distribution. The dotted lines indicate: blue – bands of 1:2 clusters; red – bands of the 1:1 cluster; dark - free OH stretch.

As seen from **Fig. 3.2-2** (b and c), the bands at 3310 and 3411 cm^{-1} are common for the spectra of the $1^+{:}1$ and $1^+{:}2$ ion mass channels. This provides evidence for the fragmentation of the $1^+{:}2$ complex by loss of one water molecule. In contrast to the PQ-methanol case, it was not possible to find expansion conditions under which only a 1:1 PQ-water complex was formed. In order to deduce the vibrational features of the 1:1 cluster from the contaminated spectrum, the contributions of higher clusters should be determined. This was done by comparing the $1^+{:}1$ channel spectra recorded at different water pressures and thus at different cluster distributions. Upon reduction of the content of the 1:2 complex the intensity of the band at 3310 cm^{-1} decreases relative to that at 3341 cm^{-1} (see **Fig. 3.2-2**, c and e), indicating the relation between this band and the complex. Thus, it turned out that bands at 3155 and 3341 cm^{-1} stems from the 1:1 PQ-water cluster. The bands at 3140 , 3310 and 3411 cm^{-1} were ascribed to the 1:2 water complexes.

The assignment of the experimental bands and the deduction of structures that correspond to them is accomplished by comparing an experimental vibrational spectrum with one calculated

theoretically. The experimental spectra of PQ-water clusters as well as the calculated ones for the depicted cluster structures are shown in **Fig. 3.2-3**.

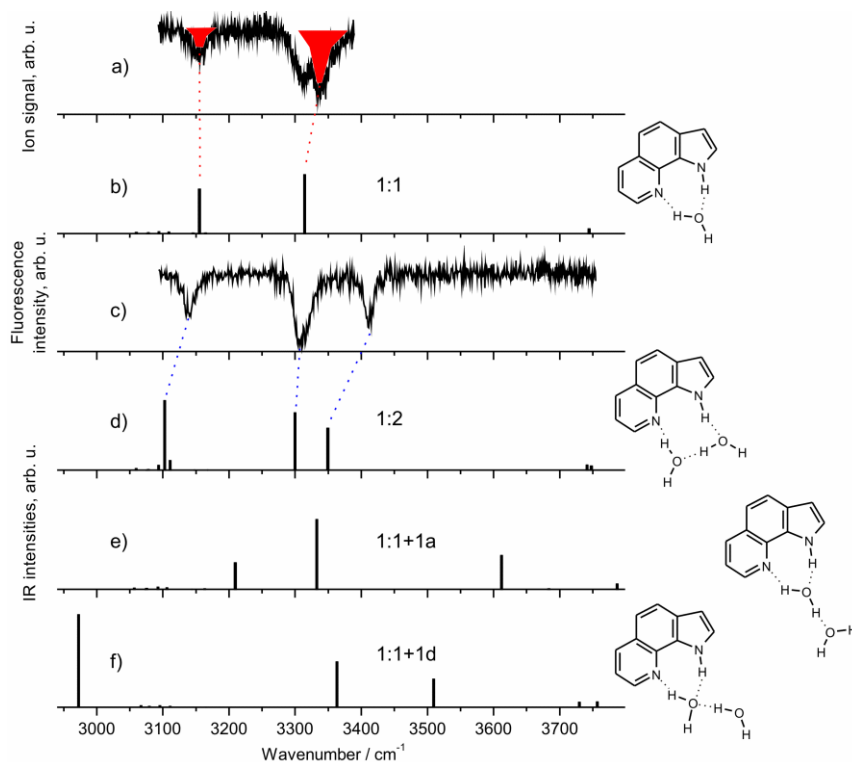


Fig. 3.2-3 The ground state vibrational spectra of the 1:1 (a, red) and 1:2 (c) complexes. The “IR fingerprints” of the relevant cluster structures, calculated at the B3LYP/cc-pVDZ level of theory, are depicted by the stick spectra (b, d-f).

Two bands of 1:1 PQ-water complex at 3155 and 3341 cm^{-1} agree very well with those calculated at 3155 and 3314 cm^{-1} , which indicates that the cyclic 1:1 complex (**Fig. 3.2-3**, b) is observed in the experiment. This structure was previously found to be the one in which ESDPT occurs [98], which explains a short life-time of its excited state. On the basis of the theoretical spectrum the experimental bands at 3155 and 3341 cm^{-1} are readily identified as simultaneous in-phase and out-of-phase stretches, respectively, of the hydrogen-bonded NH and OH groups (**Fig. 3.2-4**, a and b). In-phase stretch at 3155 cm^{-1} is a promoting mode of the ESDPT process.

Several relevant geometries of the 1:2 PQ-water aggregate together with the corresponding theoretical spectra are shown in **Fig. 3.2-3** (d-f). The calculated spectrum of the cyclic 1:2 complex (**Fig. 3.2-3**, d) resembles the experimental spectrum (**Fig. 3.2-3**, c) most closely indicating the presence of this complex under our experimental conditions. The two other complexes, 1:1+1a and 1:1+1d can be ruled out since they have spectral features not observed in the experimental spectrum. These clusters are by several kcal/mol less stable than the cyclic 1:2 complex, as follows from the calculated binding energies. Hence, the bands at 3411, 3310 and 3140 cm^{-1} are assigned to the donor OH stretch of the water dimer (**Fig. 3.2-4**, c), the out-of-

phase $\text{NH}\cdots\text{O}\&\text{OH}\cdots\text{N}$ (Fig. 3.2-4, d) and the in-phase “proton transfer” (Fig. 3.2-4, e) vibrational modes, respectively.

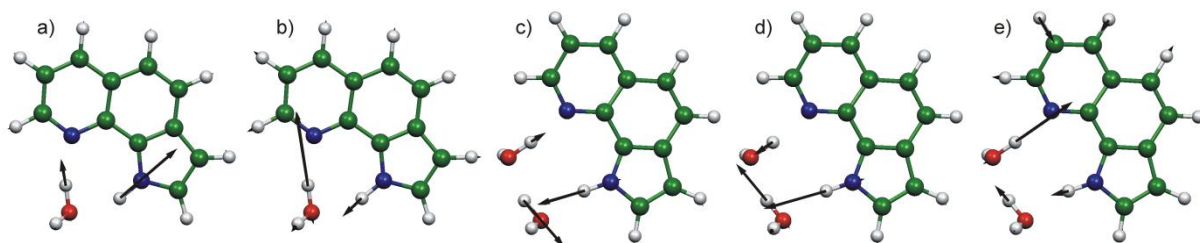


Fig. 3.2-4 Normal modes showing H-bonded NH and OH stretching motions, calculated for the 1:1 and 1:2 PQ/water complexes: a) 3314 cm^{-1} , b) 3155 cm^{-1} , c) 3349 cm^{-1} , d) 3300 cm^{-1} , e) 3103 cm^{-1} .

Comparison of PQ-methanol and PQ-water clusters.

By comparing the relative shifts of the vibrational bands of PQ-methanol and PQ-water clusters it is possible to deduce information about the relative strength of the H-bonds in these systems. The 3341 cm^{-1} band of the 1:1 complex with water is by 73 cm^{-1} higher than in the corresponding complex with methanol (3268 cm^{-1}). Similarly, the 3310 cm^{-1} and 3411 cm^{-1} vibrations of the 1:2 complex with water also exhibit blue shifts of 105 and 79 cm^{-1} in comparison with the 3205 and 3332 cm^{-1} bands, observed with methanol. This indicates that H-bonds in the 1:1 and 1:2 PQ-methanol clusters are stronger than those in PQ-water clusters. The finding is in good agreement with the calculated binding energies, which are larger for the methanol complexes.

Conclusions

The vibrational spectra of the isolated 1:1 and 1:2 clusters of PQ with methanol and water were recorded by IR/fsMPI spectroscopy in the region of hydrogen-bonded NH and OH stretch vibrations. Both PQ-methanol and PQ-water aggregates reveal the same excited state dynamics: whereas the 1:2 hydrate exhibits fluorescence upon $S_1\leftarrow S_0$ excitation, the 1:1 cluster does not fluoresce, which is a manifestation of a short lifetime of the electronically excited state. The fast excited state deactivation in the 1:1 complex was previously ascribed to ESPT followed by a nonradiative relaxation of the vibrationally excited tautomer. A short-lived excited state is the main obstacle for investigation of a 1:1 complex by conventional IR/R2PI spectroscopy. This however can be overcome by the proposed IR/fsMPI technique using femtosecond laser pulses at the ionization step, although by sacrificing of size and isomer selectivity.

The structures of the 1:1 and 1:2 clusters are assigned to species in which the solvent molecule(s) form a hydrogen-bonded bridge between aromatic NH group and quinoline nitrogen of PQ. Both 1:1 and 1:2 PQ-water complexes reveal weaker hydrogen bonding than the analogous clusters with methanol.

3.2.2 Proton transfer with a twist? Femtosecond dynamics of 7-(2'-pyridyl)indole in supersonic jets

Y. Nosenko, G. Wiosna-Salyga, M. Kunitski, I. Petkova, A. Singh, W.J. Buma, R.P. Thummel, B. Brutschy, and J. Waluk, *Proton transfer with a twist? Femtosecond dynamics of 7-(2'-pyridyl)-indole in condensed phase and in supersonic jets*, *Angewandte Chemie-International Edition*, 2008, **47**(32): p. 6037-6040.

7-(2'-pyridyl)indole (7PyIn) is another member of the group of bifunctional (H-bonding donor/acceptor) azaaromatics. This compound can exist in *syn* and *anti* rotameric forms as shown in **Fig. 3.2-5**.

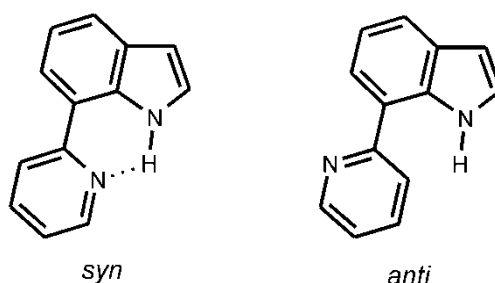


Fig. 3.2-5 The two rotameric structures of 7-(2'-pyridyl)indole.

Ab initio calculations [99] predict that the *syn* form is the dominant species being about 5 kcal/mol (CC2/cc-pVDZ) more stable than the *anti* rotamer. The higher stability of the *syn* form can be rationalized by the presence of an intramolecular H-bond between the azine group of indole and the nitrogen atom of the pyridine ring in this tautomer. The calculations also predict that along this intramolecular hydrogen bond of the *syn* form a barrierless excited state proton transfer should take place.

The theoretical findings are corroborated by the experimental study of 7PyIn in solutions [100]. Namely, only very weak and indeed unexpected fluorescence was observed and ascribed to a small fraction of *anti* rotamers. Subsequent investigation of 7PyIn in different solvents by transient absorption spectroscopy provided a very short excited state lifetime of 1.0 ± 0.2 ps, which can be attributed to the dominant *syn* form. The explanation for this rapid decay of the excited electronic state is an excited state proton transfer followed by a radiationless deactivation process.

In order to gain insight into the excited state dynamics of 7PyIn we performed a pump-probe REMPI experiment on the molecules isolated in a supersonic molecular beam. The pump-probe ion signal profiles are presented in **Fig. 3.2-6** for normal and N-deuterated species of 7PyIn.

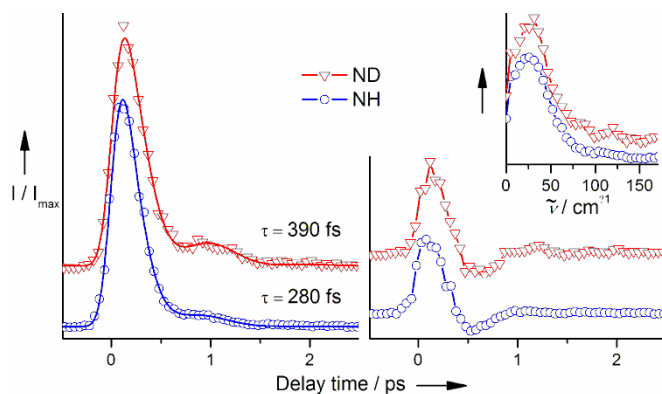


Fig. 3.2-6 Left: pump-probe REMPI spectra (\circ) obtained in a supersonic jet for normal and its N-deuterated analogue (∇); solid lines are the results of the fitting procedure. Right: oscillatory components of the data and their Fourier transforms (inset).

Interestingly, the decay is not monotonic: a second small maximum is observed at about 1 ps after excitation and its intensity is higher in the deuterated molecule. Convolution of a Gaussian function with a harmonically modulated mono-exponential decay:

$$I(t) = (1 + a \cdot \cos(\omega t + \varphi))e^{-t/\tau},$$

provided a satisfactory fit to the experimental data. Different time decays of 280 fs and 390 fs were extracted for the normal and N-deuterated 7PyIn, respectively. The cosine frequency was about 34 cm^{-1} in both cases.

The observation that the photoexcited population of 7PyIn decays in an isolated molecule much faster than in a solvated one may seem at first rather odd. However, it can be rationalized on the basis of *ab initio* calculations. Analysis of the excited state potential energy profile obtained at the CC2/cc-pVDZ level reveals a barrierless hydrogen transfer coupled to the indole-pyridine torsional coordinate [99]. Namely, after excitation of the nearly planar *syn* rotamer, transfer of the hydrogen to the pyridine ring occurs. The formed new structure relaxes through a torsion around the C-C bond towards the energy minimum corresponding to an indole-pyridine angle of 33° . At this minimum energy geometry, the S_1 - S_0 energy difference is only about 1 eV. At the dihedral angle close to 90° a conical intersection of the S_1 and S_0 states was found. Finally, the relaxation on the S_0 surface is also predicted to be barrierless [99].

Thus, coupling of hydrogen transfer with twisting implies that tautomerization should be sensitive to changes in torsional potential. In the condensed phase, solvent molecules hinder the torsion, thus slowing down the reaction (1 ps vs. 280 fs). The barrierless character of

tautomerization in a jet-isolated molecule is suggested by the deuterium isotope effect ($390/280=1.39$), which is equal, within experimental accuracy, to the square root of two.

The torsional vibration of the two moieties of the 7PyIn was calculated to be 29 cm^{-1} at the B3LYP/6-31G(d,p) level. This value is very close to that observed in the experiment for the oscillations of the pump-probe ion signal (34 cm^{-1} , or a period of about 1 ps, see **Fig. 3.2-6**). It is therefore tempting to associate these oscillations with the torsional vibration, which is responsible for a partial reflection of the initial wave packet at the CI point back into the initially excited state.

In addition, the vibrational spectrum of 7PyIn was recorded by IR/fsMPI spectroscopy (**Fig. 3.2-7**). The NH-stretch at 3412 cm^{-1} is fairly strong red shifted relative to that of bare indole (3525 cm^{-1}). In our case this can only indicate the presence of an intramolecular hydrogen bond and, consequently, this band should be assigned to the *syn* form. The position of the NH stretch of the *anti* form should be close to that of bare indole, as for similar non-hydrogen-bonded systems (**Fig. 3.2-7**). Since no spectral features are found in this region it can be concluded that the *anti* form does not exist under the experimental conditions applied. This is in line with the quantum chemistry calculations, where the *anti* form of 7PyIn was found to be by 5.5 kcal/mol [99] less stable than *syn* rotamer.

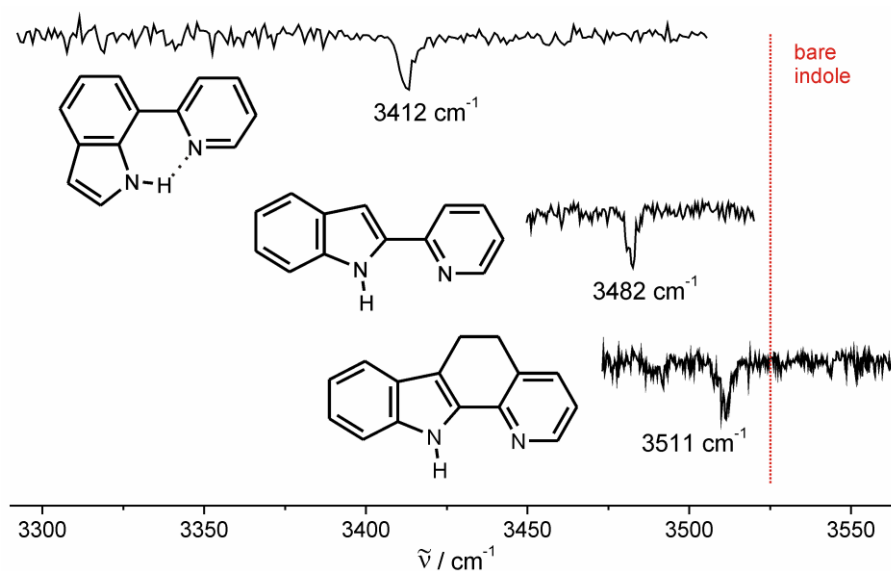


Fig. 3.2-7 The ionization-detected absorption of three pyridylindoles.

Conclusions

On the basis of theoretical and experimental findings it was concluded that of the two rotamers of 7-(2'-pyridyl)indole (7PyIn), the *syn* form is the most stable species.

The main conclusion however is that the phototautomerization in 7PyIn is coupled with a twisting of the molecule, and that the twisting provides an efficient channel for ultrafast radiationless excited state deactivation. Moreover, according to the observed isotope effect the tautomerization is barrierless in the lowest excited electronic singlet state. This pattern of excited-state tautomerization/deactivation might be quite general.

3.2.3 Structure of adenine monohydrates by femtosecond multiphoton ionization detected IR spectroscopy

Y. Nosenko, M. Kunitski, C. Riehn, P.H.P. Harbach, A. Dreuw, and B. Brutschy, *The structure of adenine monohydrates studied by femtosecond multiphoton ionization detected IR spectroscopy and quantum chemical calculations*, Physical Chemistry Chemical Physics, 2010, **12**: p. 863–870.

In recent years, the photophysics of DNA nucleobases has attracted a lot of attention. It turned out that all nucleobases can effectively dissipate the energy of absorbed UV radiation, a unique property that prevents photoreactions in DNA to happen upon irradiation with UV photons, thus leaving the genetic code intact. Of special interest are the paths by which the energy dissipation takes place and the role of the environment in these processes.

Thus, photostability of nucleobases originates from the very short excited state lifetimes of the isolated nucleobases, which are only of the order of several picoseconds [101-103], becoming even shorter upon microsolvation [104, 105]. This ultrafast excited state dynamics is the main obstacle for vibrational analysis of the Ade/9mAde monohydrates by means of the conventional size and isomer selective IR/R2PI depletion spectroscopy, exploiting ns laser pulses. Therefore, the modified version of this method, IR/fsMPI, was applied for acquiring the infrared spectra of monohydrates of Ade and 9mAde in the region of N-H and O-H vibrations.

Since methylation reduces the number of the possible hydration sites from three to two (**Fig. 3.2-8**), the 9mAde:water spectrum was thought to be helpful for the assignment of the vibrational bands of the Ade monohydrate.

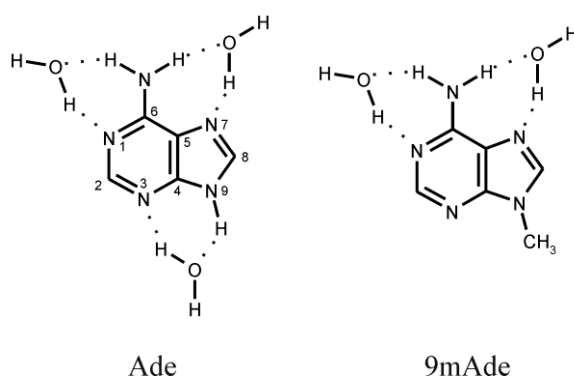


Fig. 3.2-8 Schematic primary hydration sites of 9H-adenine and 9-methyladenine.

In **Fig. 3.2-9** are shown the recorded IR/fsMPI spectra of 9mAde and Ade monohydrates as well as the calculated at the B3LYP/cc-pVTZ level of theory stick spectra of the possible cluster geometries.

Four cluster specific IR bands were observed at 3717, 3528, 3376 and 3326 cm^{-1} for the 9mAde monohydrate. Unfortunately, given the similarity of the calculated spectra for both 9mAde:water clusters, N1 and N7 (Fig. 3.2-9, left), and taking into account the fact that the IR/fsMPI method is not isomer selective, it is not possible to tell whether one or two isomers are present under experimental conditions applied.

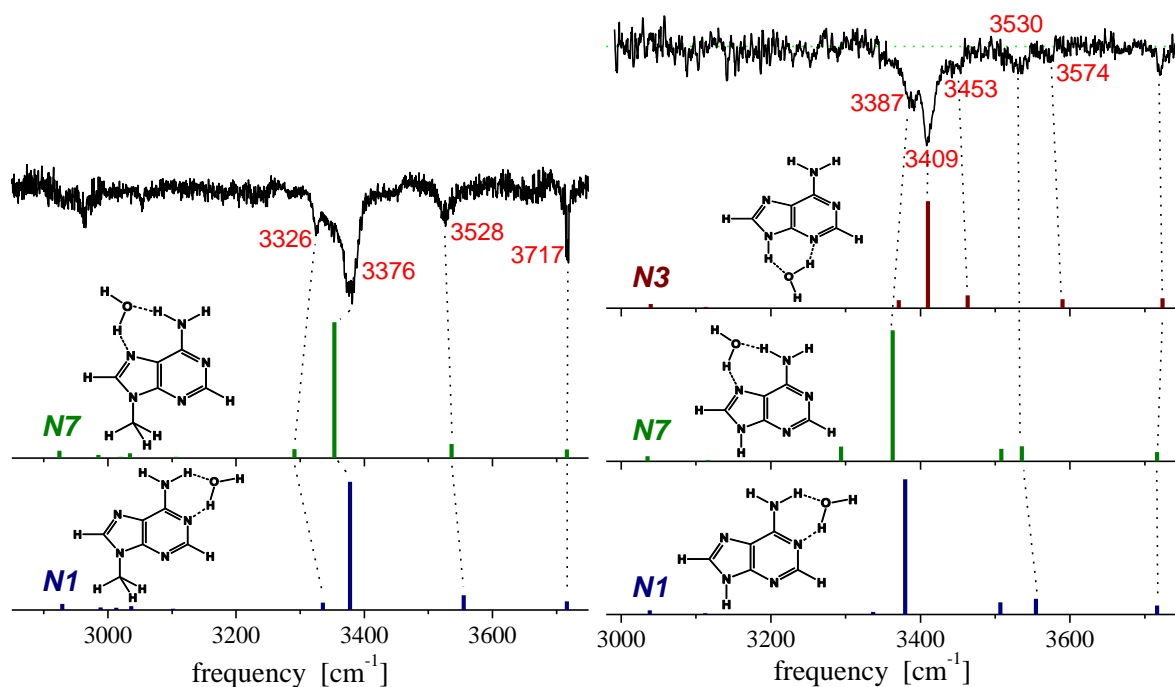


Fig. 3.2-9 IR/fsMPI spectra of the 9-methyladenine:water (left) and adenine:water (right) complexes compared to calculated stick spectra. The corresponding cluster geometries are shown as well.

Six IR bands were recorded for the monohydrate of Ade at 3720, 3574, 3530, 3453, 3409 and 3387 cm^{-1} . The vibration at 3530 cm^{-1} , being very close to the band at 3528 cm^{-1} of 9mAde monohydrates, is assigned to the stretching of non-bonded NH of the amino group. Thus, this band indicates the presence of the amino-bound hydrates, however, as was stated above, it is not possible to separate the individual contributions of N1 and N7 isomers.

Compared to 9mAde, one additional hydration site is available for Ade, involving the N9-H group as an H-bonding donor and the N3 atom as an acceptor. Indeed, weak but reproducible features at 3453 and 3574 cm^{-1} is the characteristic fingerprint of the free amino group of adenine, which indicates the presence of the N3 isomer under applied experimental conditions.

The issue of the relative stability of N3 and amino-bounded isomers of the Ade monohydrate was addressed as follows. The intensity of the 3409 cm^{-1} band, which is attributed to the N3 isomer, is twice higher than that of the amino-bound isomer at 3387 cm^{-1} , though the oscillator strength of the latter was calculated to be about by 20% more intense. Hence, assuming similar ionization cross sections for both isomers, the N3 bounded complex should be of higher

abundance than the amino-bound ones; this is consistent with quantum chemistry calculations, which give the N3 isomer to be the most stable structure.

In the course of acquiring the infrared spectra of monohydrates the ion signals in the monomer mass channels have been recorded as well. Interestingly, in contrast to the clusters, the monomer specific bands of Ade and 9mAde are shown up as an increase in the ion signal. This effect is not common and can have a twofold explanation. On the one hand, the signal enhancement might be caused by an IR induced increase of the Franck-Condon (FC) overlap for excitation or/and ionization steps, like for the 7-azaindole dimer [106], or by involvement of new excited or/and cationic states with appropriately higher transition dipole moments. On the other hand, vibrationally hot molecules may access the $\pi\pi^*$ (1L_a) electronic state with a large dipole moment [107], which is reflected as an increase of ionization yield.

Another interesting observation is the fragmentation pattern of Ade monohydrates in the monomer mass channel. Namely, the bands assigned to the amino-bound hydrate, for instance at 3387cm^{-1} , show a depletion in the $1^+{:}0$ channel, while that of the N3 bound (3409cm^{-1}) – rather an enhancement (Fig. 3.2-10, left). In order to explain this, the dynamics of the hydrates in the ground, electronically excited and cationic states have additionally to be taken into account, since dehydration of the complexes is energetically possible at all three stages of the photoionization process, as shown on the right of Fig. 3.2-10.

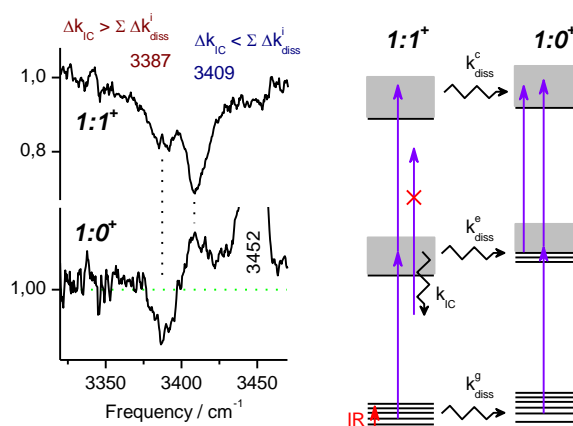


Fig. 3.2-10 The fragmentation pattern of the adenine hydrates in the monomer mass channel $1{:}0^+$ (left) and the energy diagram that shows possible dissociation paths in the ground, electronic excited and cationic states (right). Δk denotes change of a process rate after IR absorption.

The rate of direct dissociation of a hydrate in electronically excited and cationic states can only increase upon IR preexcitation. Dissociation of a hydrate in its neutral ground state is only possible after IR excitation. Since dissociation produces new monomer molecules ready for

ionization, or, if it occurs in the cationic state, new monomer ions, this will lead to an increase in the monomer ion signal.

There is however another process in the excited state, internal conversion (IC), which brings a hydrate back to its ground state, where it subsequently dissociates. Since this excited state relaxation happens in the middle of the fsMPI process, neither hydrate nor monomer can be ionized, which results in depletion of the ion signal in both mass channels.

Hence, the depletion of the ion signal at the specific band of amino-bound Ade hydrate (3387 cm^{-1}) indicates the prevalence of a fast IC mechanism over the dissociation of this complex. The opposite situation is observed for the N3 bound Ade hydrate with the IR induced enhancement of the fragmentation signal (**Fig. 3.2-10**, 3409 cm^{-1}). This means that IC is not as efficient as in the case of the amino-bound hydrates and dissociation is the dominant process.

The different fragmentation behavior of amino-bound and N3 bound monohydrates of Ade is consistent with their excited state dynamics observed in various pump-probe experiments. Two decay components of 110 fs and 1 ps were reported upon excitation by 267nm for 9mAde monohydrate, where only amino-bound isomers are possible [107]. The fast 110 fs process is associated with the $\pi\pi^*$ state relaxation by means of IC. This process is accompanied with the out-of-plane ring deformations, which are only weakly coupled with the in-plane dissociative intermolecular motion that would cause fragmentation.

The excited state dynamics of N3 monohydrate of Ade can be understood in terms of the $\pi\sigma^*$ state, associated with the N9-H group, which in this case makes a hydrogen bond with a water molecule. The $\pi\sigma^*$ state is dissociative by its nature; it can provide the dissipation path for the excitation energy to the intermolecular motion of the hydrate counterparts. Only a 80 fs decay was observed for the Ade-water complex in the pump-probe experiment with 130 fs laser pulses [105]. No sign of a 1 ps decay component, characteristic of the amino bound hydrates, was reported. Probably this component was too weak to be observed, which is justified by the fact that amino bound hydrates are less abundant than the N3 one.

Summarizing, based on the present IR/fsMPI results, the biexponential 0.1/1 ps decay has to be assigned to the amino bound hydrates, whereas the N3 complex should decay faster than 100 fs.

Conclusions

The IR spectra of Ade and 9mAde hydrates were measured for the first time utilizing femtosecond two-photon ionization detection. Observed vibrational bands for the 9mAde monohydrate can be assigned to two amino bound isomers, since they have similar vibrational fingerprints according to the quantum chemistry calculations. Moreover, we have identified two Ade hydrates, amino and N3 (N9-H) bound forms. These two isomers of the Ade monohydrate show different fragmentation patterns in the monomer mass channel, which implies different intermolecular dynamics of their excited states. In particular, for the N9-H bound hydrate excited state dissociation is more efficient than internal conversion (IC), whereas for the amino bound species, IC is dominant.

4 Overview and Future Perspectives

In the current PhD thesis the structure and dynamics of molecule and molecular aggregates were investigated by femtosecond spectroscopy. In particular, ultrafast large amplitude intramolecular motions in the electronically ground state of the non-rigid cyclic compounds were probed by rotational femtosecond degenerate four-wave mixing spectroscopy (fs DFWM). These motions, being of fundamental interest in chemistry and biology, were studied by far-infrared- and microwave spectroscopies over the last several decades. However, the conventional methods are not applicable for molecules lacking or possessing only a small dipole moment. For these cases fs DFWM spectroscopy is an attractive tool, since it is based on the Raman scattering, and, therefore, it is suitable for non-polar molecules. The fs DFWM approach was successfully tested on the two five-membered ring molecules: pyrrolidine and cyclopentene, which possess large amplitude ring-puckering vibrations.

The method is however not restricted by ring-puckering vibrations, but can be employed for studying other kinds of large amplitude intramolecular motions. Thus, we are going to apply fs DFWM spectroscopy for investigation of internal rotation in the 1-butene molecule. There is still controversy about the energy potential of the internal rotation in this molecule.

Another kind of ultrafast dynamics that takes place in the electronically excited state of molecules and molecular complexes (microsolvates) was studied by IR depletion detected by multiphoton ionization using femtosecond laser pulses (IR/fsMPI). This vibrational spectroscopic method in combination with quantum chemistry calculations allows for gaining information on structure of molecules and their microsolvates, which have electronically excited states with ultrashort lifetimes. Such systems cannot be studied by the conventional double resonance spectroscopic techniques, since their principles imply the existence of a long-lived intermediate state.

The ultrashort lifetimes is often the manifestation either of an “elementary” reaction, such as proton or electron transfer, which occurs in the excited state or of a fast non-radiative deactivation processes, such as internal conversion *via* conical intersection of the electronically excited and ground state. The pump-probe resonant excitation multiphoton ionization (fs REMPI) spectroscopy was utilized in order to probe the dynamics of such short-lived excited states. In this way the 7-(2'-pyridyl)indole molecules, which undergoes phototautomerisation followed by fast radiativeless relaxation channel, was investigated. The IR/fsMPI was applied

for study the following ultrashort-lived excited state aggregates: *1H*-pyrrolo[3,2-*h*]quinoline (PQ) with water/methanol as well as adenine- and 9-methyl-adenine-(water) clusters.

In future, employing the both IR/fsMPI and fs REMPI methods we are going to investigate the structure and excited state dynamics of the nucleobase pair adenine-thymine. It is known that all nucleobases can effectively dissipate the energy of absorbed UV radiation, a unique property that prevents photoreactions in DNA to happen upon the sun light, preventing the genetic code from damaging. Therefore, the photodynamics of the nucleobases pairs is of special interest.

5 Bibliography

- [1] A.H. Zewail, *Femtochemistry*, The Journal of Physical Chemistry, 1993, **97**(48): p. 12427-12446.
- [2] N.F. Scherer, J.L. Knee, D.D. Smith, and A.H. Zewail, *Femtosecond photofragment spectroscopy: the reaction $ICN \rightarrow CN + I$* , The Journal of Physical Chemistry, 1985, **89**(24): p. 5141-5143.
- [3] M. Dantus, M.J. Rosker, and A.H. Zewail, *Real-time femtosecond probing of transition-states in chemical-reactions*, Journal of Chemical Physics, 1987, **87**(4): p. 2395-2397.
- [4] M. Dantus, M.J. Rosker, and A.H. Zewail, *Femtosecond real-time probing of reactions. II. The dissociation reaction of ICN*, Journal of Chemical Physics, 1988, **89**(10): p. 6128-6140.
- [5] T.S. Rose, M.J. Rosker, and A.H. Zewail, *Femtosecond real-time observation of wave packet oscillations (resonance) in dissociation reactions*, Journal of Chemical Physics, 1988, **88**(10): p. 6672-6673.
- [6] M.J. Rosker, M. Dantus, and A.H. Zewail, *Femtosecond clocking of the chemical-bond*, Science, 1988, **241**(4870): p. 1200-1202.
- [7] L.R. Khundkar and A.H. Zewail, *Ultrafast molecular reaction dynamics in real-time - progress over a decade*, Annual Review of Physical Chemistry, 1990, **41**: p. 15-60.
- [8] A.H. Zewail, *Femtochemistry: Ultrafast dynamics of the chemical bond*. Vol. 1, 2. 1994, Singapore: World Scientific.
- [9] P.M. Felker and A.H. Zewail, eds. *in Femtochemistry*. ed. J. Manz and L. Wöste. Vol. 1. 1995, VCH: Weinheim.
- [10] M. Motzkus, S. Pedersen, and A.H. Zewail, *Femtosecond real-time probing of reactions .19. Nonlinear (DFWM) techniques for probing transition states of uni- and bimolecular reactions*, Journal of Physical Chemistry, 1996, **100**(14): p. 5620-5633.
- [11] M. Schmitt, G. Knopp, A. Materny, and W. Kiefer, *Femtosecond time-resolved four-wave mixing spectroscopy in iodine vapour*, Chemical Physics Letters, 1997, **280**(3-4): p. 339-347.
- [12] H.M. Frey, P. Beaud, T. Gerber, B. Mischler, P.P. Radi, and A.P. Tzannis, *Femtosecond nonresonant degenerate four-wave mixing at atmospheric pressure and in a free jet*, Applied Physics B-Lasers and Optics, 1999, **68**(4): p. 735-739.
- [13] M. Dantus, *Coherent nonlinear spectroscopy: From femtosecond dynamics to control*, Annual Review of Physical Chemistry, 2001, **52**: p. 639-+.

- [14] C. Riehn, *High-resolution pump-probe rotational coherencespectroscopy - rotational constants and structure of ground and electronically excited states of large molecular systems*, Chemical Physics, 2002, **283**(1-2): p. 297-329.
- [15] Y. Nosenko, M. Kunitski, R.P. Thummel, A. Kyrychenko, J. Herbich, J. Waluk, C. Riehn, and B. Brutschy, *Detection and structural characterization of clusters with ultrashort-lived electronically excited states: IR absorption detected by femtosecond multiphoton ionization*, Journal of the American Chemical Society, 2006, **128**(31): p. 10000-10001.
- [16] R.H. Page, Y.R. Shen, and Y.T. Lee, *Local modes of benzene and benzene dimer, studied by infrared-ultraviolet double-resonance in a supersonic beam*, Journal of Chemical Physics, 1988, **88**(8): p. 4621-4636.
- [17] C. Riehn, C. Lahmann, B. Wassermann, and B. Brutschy, *IR depletion spectroscopy - a method for characterizing a microsolvation environment*, Chemical Physics Letters, 1992, **197**(4-5): p. 443-450.
- [18] S. Tanabe, T. Ebata, M. Fujii, and N. Mikami, *OH stretching vibrations of phenol-(H₂O)_n (n=1-3) complexes observed by IR-UV double-resonance spectroscopy*, Chemical Physics Letters, 1993, **215**(4): p. 347-352.
- [19] R.N. Pribble and T.S. Zwier, *Size-specific infrared-spectra of benzene-(H₂O)_n clusters (n=1 through 7): evidence for noncyclic (H₂O)_n structures*, Science, 1994, **265**(5168): p. 75-79.
- [20] D. Strickland and G. Mourou, *Compression of amplified chirped optical pulses*, Optics Communications, 1985, **56**(3): p. 219-221.
- [21] P.A. Franken, G. Weinreich, C.W. Peters, and A.E. Hill, *Generation of optical harmonics*, Physical Review Letters, 1961, **7**(4): p. 118-&.
- [22] G. Pretzler, A. Kasper, and K.J. Witte, *Angular chirp and tilted light pulses in CPA lasers*, Applied Physics B-Lasers and Optics, 2000, **70**(1): p. 1-9.
- [23] Z. Sacks, G. Mourou, and R. Danielius, *Adjusting pulse-front tilt and pulse duration by use of a single-shot autocorrelator*, Optics Letters, 2001, **26**(7): p. 462-464.
- [24] M. Raghuramaiah, A.K. Sharma, P.A. Naik, and P.D. Gupta, *Simultaneous measurement of pulse-front tilt and pulse duration of a femtosecond laser beam*, Optics Communications, 2003, **223**(1-3): p. 163-168.
- [25] P.M. Felker, *Rotational coherence spectroscopy: studies of the geometries of large gas-phase species by picosecond time-domain methods*, The Journal of Physical Chemistry, 1992, **96**(20): p. 7844-7857.

- [26] P.M. Felker and A.H. Zewail, *Purely rotational coherence effect and time-resolved sub-Doppler spectroscopy of large molecules. I. Theoretical*, The Journal of Chemical Physics, 1987, **86**(5): p. 2460-2482.
- [27] T.C. Corcoran, L.L. Connell, G.V. Hartland, P.W. Joireman, R.A. Hertz, and P.M. Felker, *Ground-state rotational coherence spectroscopy of jet-cooled molecules by stimulated Raman-induced fluorescence depletion*, Chemical Physics Letters, 1990, **170**(2-3): p. 139-145.
- [28] M.J. Cote, J.F. Kauffman, P.G. Smith, and J.D. McDonald, *Picosecond fluorescence depletion spectroscopy. I. Theory and apparatus*, Journal of Chemical Physics, 1989, **90**(6): p. 2865-2874.
- [29] N.F. Scherer, L.R. Khundkar, T.S. Rose, and A.H. Zewail, *Sub-doppler measurement of excited-state rotational-constants and rotational coherence by picosecond multiphoton ionization mass-spectrometry*, Journal of Physical Chemistry, 1987, **91**(26): p. 6478-6483.
- [30] S.M. Ohline, J. Romascan, and P.M. Felker, *Time-resolved ionization depletion - a new picosecond method for molecular-beam studies*, Chemical Physics Letters, 1993, **207**(4-6): p. 563-568.
- [31] C. Riehn, A. Weichert, and B. Brutschy, *Mass-selective rotational coherence spectroscopy by (1+1') pump-probe photoionization*, Physical Chemistry Chemical Physics, 2000, **2**(9): p. 1873-1875.
- [32] A. Weichert, C. Riehn, and B. Brutschy, *High-resolution rotational coherence spectroscopy of the phenol dimer*, Journal of Physical Chemistry A, 2001, **105**(23): p. 5679-5691.
- [33] A. Weichert, C. Riehn, V.V. Matylitsky, W. Jarzeba, and B. Brutschy, *Time-resolved rotational spectroscopy of para-difluorobenzene•Ar*, Journal of Molecular Structure, 2002, **612**(2-3): p. 325-337.
- [34] M. Morgen, W. Price, L. Hunziker, P. Ludowise, M. Blackwell, and Y. Chen, *Femtosecond Raman-induced polarization spectroscopy studies of rotational coherence in O₂, N₂ and CO₂*, Chemical Physics Letters, 1993, **209**(1-2): p. 1-9.
- [35] M. Schmitt, G. Knopp, A. Materny, and W. Kiefer, *Femtosecond time-resolved coherent anti-Stokes Raman scattering for the simultaneous study of ultrafast ground and excited state dynamics: Iodine vapour*, Chemical Physics Letters, 1997, **270**(1-2): p. 9-15.
- [36] J.A. Shirley, R.J. Hall, and A.C. Eckbreth, *Folded BOXCARS for rotational Raman studies*, Opt. Lett., 1980, **5**(9): p. 380-382.
- [37] E.J. Brown, Q.G. Zhang, and M. Dantus, *Femtosecond transient-grating techniques: Population and coherence dynamics involving ground and excited states*, Journal of Chemical Physics, 1999, **110**(12): p. 5772-5788.

- [38] M. Morgen, W. Price, P. Ludowise, and Y. Chen, *Tensor analysis of femtosecond Raman induced polarization spectroscopy - application to the study of rotational coherence*, Journal of Chemical Physics, 1995, **102**(22): p. 8780-8789.
- [39] M.H. Cho, M. Du, N.F. Scherer, G.R. Fleming, and S. Mukamel, *Off-resonant transient birefringence in liquids*, Journal of Chemical Physics, 1993, **99**(4): p. 2410-2428.
- [40] R.N. Zare, *Angular Momentum*. 1988, New York: Wiley.
- [41] S. Brodersen, *High-Resolution Rotation-Vibrational Raman Spectroscopy*, in *Raman spectroscopy of gases and liquids (Topics in current Physics)*, Vol. 11, ed. A. Weber, 1979, Springer-Verlag: Berlin.
- [42] J.K.G. Watson, *Determination of Centrifugal Distortion Coefficients of Asymmetric-Top Molecules*, The Journal of Chemical Physics, 1967, **46**(5): p. 1935-1949.
- [43] R.S. Mulliken, *Species Classification and Rotational Energy Level Patterns of Non-Linear Triatomic Molecules*, Physical Review, 1941, **59**(11): p. 873.
- [44] G.W. King, R.M. Hainer, and P.C. Cross, *The Asymmetric Rotor I. Calculation and Symmetry Classification of Energy Levels*, The Journal of Chemical Physics, 1943, **11**(1): p. 27-42.
- [45] S.C. Wang, *On the Asymmetrical Top in Quantum Mechanics*, Physical Review, 1929, **34**(2): p. 243.
- [46] G. Placzek, in *Handbuch der Radiologie*, Vol. 6, part 2, ed. E. Marx, 1934, Akademische Verlagsgesellschaft: Leipzig. p. 205-374.
- [47] G. Avila, J.M. Fernández, B. Maté, G. Tejeda, and S. Montero, *Ro-vibrational Raman Cross Sections of Water Vapor in the OH Stretching Region*, Journal of Molecular Spectroscopy, 1999, **196**(1): p. 77-92.
- [48] K. Price and R. Storn, *Differential Evolution* (function optimization algorithm), <http://www.icsi.berkeley.edu/~storn/code.html>
- [49] M.R. F. James, MINUIT computer code; Program D-506, CERN, Geneva, 1977.
- [50] C.R. Vidal and J. Cooper, *Heat-Pipe Oven: A New, Well-Defined Metal Vapor Device for Spectroscopic Measurements*, Journal of Applied Physics, 1969, **40**(8): p. 3370-3374.
- [51] C.R. Vidal and F.B. Haller, *Heat Pipe Oven Applications. I. Isothermal Heater of Well Defined Temperature. II. Production of Metal Vapor-Gas Mixtures*, Review of Scientific Instruments, 1971, **42**(12): p. 1779-1784.

- [52] C.R. Vidal, in *Experimental Methods in the Physical Sciences*, Vol. 29B: Atomic, Molecular and Optical Physics, Atoms and Molecules, ed. F.B. Dunning and R. Hulet, 1996, Academic: New York. p. 67-83.
- [53] R.R.B. Correia, G. Pichler, S.L. Cunha, and P. Hering, *The role of nuclear spin in inelastic Na (3p) + H₂ collisions*, *Chemical Physics Letters*, 1990, **175**(4): p. 354-358.
- [54] G. Pichler, R.R.B. Correia, S.L. Cunha, K.L. Kompa, and P. Hering, *P-R doublet enhanced CARS lines of NaH*, *Optics Communications*, 1992, **92**(4-6): p. 346-354.
- [55] M. Motzkus, G. Pichler, K.L. Kompa, and P. Hering, *Vibrationally induced formation of NaH in the Na(3p) + H₂ collision system: Rate equation model and comparison with experimental results*, *The Journal of Chemical Physics*, 1998, **108**(22): p. 9291-9300.
- [56] D.H. Levy, *Laser Spectroscopy of Cold Gas-Phase Molecules*, *Annual Review of Physical Chemistry*, 1980, **31**(1): p. 197-225.
- [57] G. Scoles, ed. *Atomic and Molecular Beam Methods*. Vol. 1, 2. 1992, Oxford University Press: New York.
- [58] D.J. Nesbitt, *High-Resolution, Direct Infrared Laser Absorption Spectroscopy in Slit Supersonic Jets: Intermolecular Forces and Unimolecular Vibrational Dynamics in Clusters*, *Annual Review of Physical Chemistry*, 1994, **45**(1): p. 367-399.
- [59] U. Even, J. Jortner, D. Noy, N. Lavie, and C. Cossart-Magos, *Cooling of large molecules below 1 K and He clusters formation*, *The Journal of Chemical Physics*, 2000, **112**(18): p. 8068-8071.
- [60] B. Brutschy, *The Structure of Microsolvated Benzene Derivatives and the Role of Aromatic Substituents*, *Chemical Reviews*, 2000, **100**(11): p. 3891-3920.
- [61] D.H. Levy, *Van Der Waals Molecules*, in *Advances in Chemical Physics: Photoselective Chemistry*, Vol. 147 (Part 1), ed. J. Jortner, R.D. Levine, and S.A. Rice, 2007. p. 323-362.
- [62] J. Jortner, U. Even, A. Goldberg, I. Schek, T. Raz, and R.D. Levine, *Energetics and dynamics of molecular clusters*, *Surface Review and Letters*, 1996, **3**(1): p. 263-280.
- [63] A.W. Castleman and R.G. Keesee, *Clusters: Properties and Formation*, *Annual Review of Physical Chemistry*, 1986, **37**(1): p. 525-550.
- [64] A.W. Castleman and S. Wei, *Cluster Reactions*, *Annual Review of Physical Chemistry*, 1994, **45**(1): p. 685-719.
- [65] E.R. Bernstein, ed. *Chemical reactions in clusters*. 1996, Oxford University Press: New York, Oxford.

- [66] A.C. Legon, *Pulsed-Nozzle, Fourier-Transform Microwave Spectroscopy of Weakly Bound Dimers*, Annual Review of Physical Chemistry, 1983, **34**(1): p. 275-300.
- [67] P.M. Maxton, M.W. Schaeffer, and P.M. Felker, *Nonlinear Raman spectroscopy of intermolecular vibrations in benzene-(water)_n clusters*, Chemical Physics Letters, 1995, **241**(5-6): p. 603-610.
- [68] J.J. Scherer, J.B. Paul, A. O'Keefe, and R.J. Saykally, *Cavity Ringdown Laser Absorption Spectroscopy: History, Development, and Application to Pulsed Molecular Beams*, Chemical Reviews, 1997, **97**(1): p. 25-52.
- [69] R.E. Miller, *Infrared Laser Spectroscopy*, in *Atomic and Molecular Beam Methods*, Vol. 2, ed. G. Scoles, 1992, Oxford University Press: New York, Oxford.
- [70] U. Buck and F. Huisken, *Infrared Spectroscopy of Size-Selected Water and Methanol Clusters*, Chemical Reviews, 2000, **100**(11): p. 3863-3890.
- [71] R.K. Frost, F.C. Hagemester, C.A. Arrington, T.S. Zwier, and K.D. Jordan, *Fluorescence-dip infrared spectroscopy of tropolone and tropolone-OD*, The Journal of Chemical Physics, 1996, **105**(7): p. 2595-2604.
- [72] S.J. Brosnan and R.L. Byer, *Optical parametric oscillator threshold and linewidth studies*, Ieee Journal of Quantum Electronics, 1979, **15**(6): p. 415-431.
- [73] D.W. Michael, K. Kolenbrander, and J.M. Lisy, *New cavity design for a LiNbO₃ optical parametric oscillator*, Review of Scientific Instruments, 1986, **57**(6): p. 1210-1212.
- [74] T.K. Minton, S.A. Reid, H.L. Kim, and J.D. McDonald, *A scanning, single-mode, LiNbO₃, optical parametric oscillator*, Optics Communications, 1989, **69**(3-4): p. 289-293.
- [75] F. Huisken, A. Kulcke, D. Voelkel, C. Laush, and J.M. Lisy, *New infrared injection-seeded optical parametric oscillator with high-energy and narrow bandwidth output*, Applied Physics Letters, 1993, **62**(8): p. 805-807.
- [76] S. Djafari, G. Lembach, H.D. Barth, and B. Brutschy, *On the assignment of a size specific, intracuster ion/molecule reaction with IR-depletion spectroscopy*, Zeitschrift Fur Physikalische Chemie-International Journal of Research in Physical Chemistry & Chemical Physics, 1996, **195**: p. 253-272.
- [77] K.L. Saenger and J.B. Fenn, *On the time required to reach fully developed flow in pulsed supersonic free jets*, The Journal of Chemical Physics, 1983, **79**(12): p. 6043-6045.
- [78] L. Bruno, F. Olivier, M. Mike, and C. Roland, *Analysis of femtosecond Raman-induced polarization spectroscopy (RIPS) in N₂ and CO₂ by fitting and scaling laws*, Journal of Raman Spectroscopy, 2000, **31**(1-2): p. 77-83.

- [79] H.M. Frey, P. Beaud, T. Gerber, B. Mischler, P.P. Radi, and A.P. Tzannis, *Determination of rotational constants in a molecule by femtosecond four-wave mixing*, Journal of Raman Spectroscopy, 2000, **31**(1-2): p. 71-76.
- [80] I. Pastirk, M. Comstock, and M. Dantus, *Femtosecond ground state dynamics of gas phase N_2O_4 and NO_2* , Chemical Physics Letters, 2001, **349**(1-2): p. 71-78.
- [81] A.C. Legon, *Equilibrium conformations of four- and five-membered cyclic molecules in the gas phase: determination and classification*, Chemical Reviews, 1980, **80**(3): p. 231-262.
- [82] H.L. Strauss, *Pseudorotation - a Large-Amplitude Molecular-Motion*, Annual Review of Physical Chemistry, 1983, **34**: p. 301-328.
- [83] D.M. Leitner, M. Havenith, and M. Gruebele, *Biomolecule large-amplitude motion and solvation dynamics: modelling and probes from THz to X-rays*, International Reviews in Physical Chemistry, 2006, **25**(4): p. 553-582.
- [84] J.E. Kilpatrick, K.S. Pitzer, and R. Spitzer, *The Thermodynamics and Molecular Structure of Cyclopentane*, Journal of the American Chemical Society, 1947, **69**(10): p. 2483-2488.
- [85] W. Caminati, A. Dell' Erba, G. Maccaferri, and P.G. Favero, *Free Jet Absorption Millimeter Wave Spectrum of Pyrrolidine: Assignment of a Second, Equatorial, the Most Stable Conformer*, Journal of Molecular Spectroscopy, 1998, **191**(1): p. 45-48.
- [86] L.E. Bauman and J. Laane, *Pseudorotation of cyclopentane and its deuterated derivatives*, The Journal of Physical Chemistry, 1988, **92**(5): p. 1040-1051.
- [87] D.G. Melnik, S. Gopalakrishnan, T.A. Miller, and F.C. De Lucia, *The absorption spectroscopy of the lowest pseudorotational states of tetrahydrofuran*, The Journal of Chemical Physics, 2003, **118**(8): p. 3589-3599.
- [88] V. Pophristic and L. Goodman, *Hyperconjugation not steric repulsion leads to the staggered structure of ethane*, Nature, 2001, **411**(6837): p. 565-568.
- [89] F.M. Bickelhaupt and E.J. Baerends, *The case for steric repulsion causing the staggered conformation of ethane*, Angewandte Chemie-International Edition, 2003, **42**(35): p. 4183-4188.
- [90] Y.R. Mo and J.L. Gao, *Theoretical analysis of the rotational barrier of ethane*, Accounts of Chemical Research, 2007, **40**(2): p. 113-119.
- [91] J. Laane and R.C. Lord, *Far-Infrared Spectra of Ring Compounds. II. The Spectrum and Ring-Puckering Potential Function of Cyclopentene*, The Journal of Chemical Physics, 1967, **47**(12): p. 4941-4945.

- [92] L.E. Bauman, P.M. Killough, J.M. Cooke, J.R. Villarreal, and J. Laane, *Two-dimensional potential energy surface for the ring puckering and ring twisting of cyclopentene-d₀, -1-d₁, -1,2,3,3-d₄, and -d₈*, *The Journal of Physical Chemistry*, 1982, **86**(11): p. 2000-2006.
- [93] L.H. Scharpen, *Rotation-Vibration Interaction and Barrier to Ring Inversion in Cyclopentene*, *The Journal of Chemical Physics*, 1968, **48**(8): p. 3552-3556.
- [94] J.C. López, J.L. Alonso, M.E. Charro, G. Wlodarczak, and J. Demaison, *The millimeter-wave spectrum of cyclopentene*, *Journal of Molecular Spectroscopy*, 1992, **155**(1): p. 143-157.
- [95] D. Marks, H. Zhang, P. Borowicz, J. Waluk, and M. Glasbeek, *(Sub)picosecond Fluorescence Upconversion Studies of Intermolecular Proton Transfer of Dipyrido[2,3-a:3',2'-i]carbazole and Related Compounds*, *The Journal of Physical Chemistry A*, 2000, **104**(31): p. 7167-7175.
- [96] A. Kyrychenko, Y. Stepanenko, and J. Waluk, *Molecular Dynamics and DFT Studies of Intermolecular Hydrogen Bonds between Bifunctional Heteroazaaromatic Molecules and Hydroxylic Solvents*, *The Journal of Physical Chemistry A*, 2000, **104**(42): p. 9542-9555.
- [97] A. Kyrychenko, J. Herbich, M. Izydorzak, F. Wu, R.P. Thummel, and J. Waluk, *Role of Ground State Structure in Photoinduced Tautomerization in Bifunctional Proton Donor-Acceptor Molecules: 1H-Pyrrolo[3,2-h]quinoline and Related Compounds*, *Journal of the American Chemical Society*, 1999, **121**(48): p. 11179-11188.
- [98] M. Kijak, A. Zielinska, R.P. Thummel, J. Herbich, and J. Waluk, *Photoinduced double proton transfer in water complexes of 1H-pyrrolo[3,2-h]quinoline and dipyrido[2,3-a:3',2'-i]carbazole*, *Chemical Physics Letters*, 2002, **366**(3-4): p. 329-335.
- [99] A.L. Sobolewski and W. Domcke, *Computational Studies of the Photophysics of Hydrogen-Bonded Molecular Systems*, *The Journal of Physical Chemistry A*, 2007, **111**(46): p. 11725-11735.
- [100] G. Wiosna, I. Petkova, M.S. Mudadu, R.P. Thummel, and J. Waluk, *Intra- and intermolecular fluorescence quenching in 7-(pyridyl)indoles*, *Chemical Physics Letters*, 2004, **400**(4-6): p. 379-383.
- [101] H. Kang, K.T. Lee, B. Jung, Y.J. Ko, and S.K. Kim, *Intrinsic Lifetimes of the Excited State of DNA and RNA Bases*, *Journal of the American Chemical Society*, 2002, **124**(44): p. 12958-12959.
- [102] H. Satzger, D. Townsend, M.Z. Zgierski, S. Patchkovskii, S. Ullrich, and A. Stolow, *Primary processes underlying the photostability of isolated DNA bases: Adenine*, *Proceedings of the National Academy of Sciences*, 2006, **103**(27): p. 10196-10201.
- [103] C. Canuel, M. Mons, F. Piuzzi, B. Tardivel, I. Dimicoli, and M. Elhanine, *Excited states dynamics of DNA and RNA bases: Characterization of a stepwise deactivation pathway in the gas phase*, *The Journal of Chemical Physics*, 2005, **122**(7): p. 074316-6.

- [104] H. Kang, K.T. Lee, and S.K. Kim, *Femtosecond real time dynamics of hydrogen bond dissociation in photoexcited adenine-water clusters*, Chemical Physics Letters, 2002, **359**(3-4): p. 213-219.
- [105] H.H. Ritze, H. Lippert, E. Samoylova, V.R. Smith, I.V. Hertel, W. Radloff, and T. Schultz, *Relevance of $\pi\sigma^*$ states in the photoinduced processes of adenine, adenine dimer, and adenine-water complexes*, The Journal of Chemical Physics, 2005, **122**(22): p. 224320-9.
- [106] M. Sakai, S. Ishiuchi, and M. Fujii, *Picosecond time-resolved nonresonant ionization detected*, Eur. Phys. J. D, 2002, **20**(3): p. 399-402.
- [107] C. Canuel, M. Elhanine, M. Mons, F. Piuzzi, B. Tardivel, and I. Dimicoli, *Time-resolved photoelectron and photoion fragmentation spectroscopy study of 9-methyladenine and its hydrates: a contribution to the understanding of the ultrafast radiationless decay of excited DNA bases*, Physical Chemistry Chemical Physics, 2006, **8**(34): p. 3978-3987.

6 Summary

Large amplitude intramolecular motions in non-rigid molecules are a fundamental issue in chemistry and biology since they take place in a wide range of relevant biomolecules such as deoxyribose/ribose of DNA/RNA, the amino acid proline or the drug nicotine. The conventional approaches for study these motions by far-infrared and microwave spectroscopy are not applicable when the molecule is non-polar. Therefore, in the current thesis an alternative approach for the investigation of large amplitude intramolecular motions was developed and tested. This new method is based on femtosecond time-resolved rotational spectroscopy.

Another important subject is the photophysics of molecules and molecular clusters which have an ultrashort lifetime of the electronically excited state (photoreactivity). These ultrashort lifetimes often represent a protective mechanism causing photostability. The photoreactivity is usually the manifestation either of an “elementary” reaction, such as proton or electron transfer, which occurs in the excited state or of a fast non-radiative deactivation processes, such as internal conversion via conical intersection of the electronically excited and ground state. In these mechanisms solvent plays an important role, which implies additional requirements on the investigational method. Taking all requirements into account, a new vibrational spectroscopic approach was proposed for studying the structure of photoreactive microsolvated molecules.

Large amplitude intramolecular motions

The method for investigation of large amplitude intramolecular motions in non-rigid molecules is based on femtosecond rotational degenerate four-wave mixing spectroscopy (fs DFWM). This approach was successfully tested on two molecules, pyrrolidine and cyclopentene, which belong to the group of five-membered-ring cycloalkenes. Because of non-aromatic character, the ring of these molecules lacks in rigidity, which results in low frequency large amplitude out-of-plane skeletal vibrations.

Fs DFWM can be employed as rotational spectroscopy for the observation of rotational coherence phenomena. This technique is based on a Raman scattering, which makes it applicable for obtaining structural information on *non-polar* molecules. During a large amplitude motion there are noticeable changes in the structure of the molecule. The structural sensitivity of fs DFWM as rotational spectroscopy makes it possible to detect geometrical changes, and, subsequently, to acquire information on the intramolecular dynamics that causes these changes. Gaining the dynamical information of the large amplitude motion is done by comparison the

experimental fs DFWM spectrum with that simulated according to a chosen quantum mechanical model for this motion.

Pyrrolidine has two out-of-plane large amplitude ring-puckering modes consisting of a bend and a twist, which cause the ring atoms to move in such a way that the phase of the puckering rotates around the ring. This motion was termed pseudorotation. During pseudorotation the exchange between two conformers of pyrrolidine, axial and equatorial, occurs. In the analogous systems cyclopentane and tetrahydrofuran pseudorotation is almost unhindered, with barriers of only 25 cm^{-1} and 30 cm^{-1} , respectively. Using fs DFWM spectroscopy and a one-dimensional quantum model for pseudorotation the complete potential and rotational constants along pseudorotation of pyrrolidine were obtained for the first time with high precision. It turned out that the barrier for pseudorotation in pyrrolidine is 220 cm^{-1} , which is significantly larger than in cyclopentane and tetrahydrofuran. According to the obtained potential the equatorial conformer is by 29 cm^{-1} more stable than the axial one. This is a refinement of the microwave spectroscopic findings, where the energy difference between two conformer of pyrrolidine was estimated to be lower than 220 cm^{-1} . It should be noted that pyrrolidine is a particularly difficult system for microwave and infrared spectroscopy because of its low dipole moment. Only the axial and equatorial conformers, the two end points on pseudorotational path, were detected by microwave spectroscopy so far.

Cyclopentene has a different kind of ring-puckering motion. Because of the presence of the double bond in the ring the twisting mode of cyclopentene ring has a relatively high frequency (386 cm^{-1}), therefore at room temperature mainly the bending mode (ring inversion) is active. This motion can be described using a one-dimensional double minima potential with a barrier corresponding to the planar ring structure. From the fs DFWM spectrum of cyclopentene, this barrier was found to be 274 cm^{-1} , which is somewhat higher than the value of 232 cm^{-1} obtained by far-infrared spectroscopy. However, the derived rotational constants along the ring-bending vibration are in excellent agreement with those determined by microwave spectroscopy.

Thus, the high structural sensitivity together with good energetic evaluation of the transition path makes the fs DFWM spectroscopy an attractive tool for the investigation of large amplitude intramolecular motions. The method is particularly interesting for molecules lacking or possessing only a small dipole moment, where far-infrared and microwave spectroscopy cannot be applied.

Structure and dynamics of photoreactive molecules and molecular clusters

The second method, infrared depletion detected by femtosecond multiphoton ionization (IR/fsMPI), was developed in our lab for vibrational study of molecule and molecular clusters, which have ultrashort excited state lifetimes, in the X-H (X=C, O, N) stretch region. The positions of X-H stretches carry valuable information about intra- and intermolecular hydrogen bonds of the molecules and microsolvates. Furthermore, by comparing the experimental and theoretical spectra, the structure of the molecular aggregate can be unequivocally deduced. Since the cluster formation implies supersonic expansion conditions, not many techniques are applicable for such a vibrational analysis. One of the most widely used is the conventional IR depletion detected by resonance two-photon ionization spectroscopy (IR/R2PI), first applied for microsolvates in our lab. The working principle can be briefly explained as follows. The molecular system is affected by tunable IR radiation, and then resonantly ionized through the first excited singlet state using two UV photons. A so-produced ion current is detected by a time-of-flight spectrometer. If the IR radiation is in resonance with any molecular vibration, the efficiency of the second, ionization step will change, thus altering the ion current. In this way a vibrational spectrum can be acquired by tuning the IR laser.

However, the conventional IR/R2PI spectroscopy, which employs nanosecond laser pulses, is not applicable to the molecular aggregates with a short lived excited state. The reason for this is that the efficiency of the R2PI process drops significantly with decreasing the life-time of the intermediate excited state. Therefore, the conventional approach was modified by adopting femtosecond laser pulses for the two photon ionization. In this new technique the ionization of the molecules is done by femtosecond multiphoton ionization (fsMPI).

IR/fsMPI spectroscopy was applied for investigation of the following aggregates: 1*H*-pyrrolo[3,2-*h*]quinoline (PQ) with water/methanol as well as adenine- and 9-methyl-adenine-(water) clusters.

PQ belongs to the group of bifunctional azaaromatics, which implies that a molecule possesses both H-bonding donor and acceptor sites. At these sites solvent molecules may be bound forming so called microsolvates of typ 1:n (solute:solvent). The structures of 1:1 and 1:2 clusters are assigned to species in which the solvent molecule(s) form a hydrogen-bonded bridge between aromatic NH group (donor) and quinoline nitrogen (acceptor) of PQ. Both PQ-methanol and PQ-water aggregates reveal the same excited state dynamics: whereas the 1:2 complex exhibits fluorescence upon $S_1 \leftarrow S_0$ excitation and is thus relatively long-lived, the 1:1 cluster does not

fluoresce due to a short excited state lifetime. The fast excited state deactivation in the 1:1 aggregate was previously ascribed to an excited state proton transfer followed by a nonradiative relaxation of the vibrationally excited tautomer. Both 1:1 and 1:2 PQ-water complexes reveal weaker hydrogen bonding than the analogous clusters with methanol.

Vibrational bands observed by IR/fsMPI for the 9-methyladenine monohydrate can be assigned to two amino bound isomers, since they have similar vibrational fingerprints according to the quantum chemical calculations. In addition, the adenine (Ade) hydrates were identified as amino and N3 (N9-H) bound forms. These two isomers of the Ade monohydrate show different fragmentation patterns in the monomer mass channel, which implies a different excited state intermolecular relaxation dynamics. In particular, for the N9-H bound hydrate excited state dissociation is more efficient than internal conversion (IC), whereas for the amino bound species, IC is dominant.

The excited state dynamics of another bifunctional azaaromatic molecule 7-(2'-pyridyl)indole (7PyIn) was studied by femtosecond pump-probe resonance excitation multiphoton ionization technique (fs REMPI). This molecule has donor and acceptor sites close to each other and connected by intramolecular H-bond. Under electronic excitation this results in a fast proton transfer (phototautomerization) followed by radiationless excited state deactivation process. As determined by fs pump-probe REMPI measurements, this relaxation process occurred in 280 fs and 390 fs for normal and N-deuterated 7PyIn, respectively. The modulation of the fs pump-probe spectra leads to the conclusion that the phototautomerization in 7PyIn is coupled with a twisting of the molecule, and that the twisting provides an efficient channel for ultrafast radiationless excited state deactivation. Moreover, according to the observed isotope effect the tautomerization is barrierless in the lowest excited electronic singlet state. This pattern of excited-state tautomerization/deactivation might be quite general.

Thus, the combination of IR/fsMPI and fs pump-probe REMPI is an attractive tool for investigation of structure and excited state dynamics of photoreactive molecules and molecular aggregates.

7 Zusammenfassung

Intramolekulare Bewegungen mit großer Amplitude

Intramolekulare Bewegungen mit großer Amplitude in nicht-starren Molekülen im elektronischen Grundzustand sind von fundamentalem Interesse in Chemie und Biologie, da sie in einer Vielzahl von Biomolekülen wie der DNA/RNA, der Aminosäure Prolin sowie in Nikotin stattfinden. Konventionelle Methoden um diese molekularen Bewegungen spektroskopisch zu untersuchen wie Ferninfrarot- und Mikrowellenspektroskopie sind auf polare Moleküle begrenzt. Deshalb wurde in der vorliegenden Arbeit eine alternative Methode auf Basis der zeitaufgelösten Femtosekunden-Rotationsspektroskopie entwickelt und getestet.

Die neue spektroskopische Methode zur Untersuchung von intramolekularen Bewegungen mit großer Amplitude in nicht-starren Molekülen basiert auf der Femtosekunden-Rotationsspektroskopie mit Hilfe der Entarteten-Vier-Wellen-Mischung (fs DFWM). Sie konnte erfolgreich für zwei Moleküle, Pyrrolidin und Cyclopentan, welche zur Gruppe der fünf-Ring Zyklopentane zählen, demonstriert werden. Aufgrund des nicht-aromatischen Charakters der Moleküle liegt eine geringere Starrheit des Molekülrings vor, die zu niederfrequenten out-of-plane Schwingungen mit großer Amplitude des Molekülgerüsts führt.

Die Femtosekunden-Rotations-DFWM Spektroskopie kann zur Untersuchung von Rotationskohärenzphänomenen eingesetzt werden. Die Technik basiert auf der Raman-Spektroskopie und kann damit auch auf Strukturuntersuchung von nicht-polaren Molekülen angewendet werden. Während der Bewegungen mit großer Amplitude treten merkliche Änderungen in der Molekülstruktur auf. Die hohe Empfindlichkeit der Femtosekunden-Rotations-DFWM Spektroskopie gegenüber strukturellen Änderungen ermöglicht es, Informationen über die zugrunde liegende intramolekulare Dynamik zu erhalten. Um die Dynamik zu bestimmen, wird das experimentelle Spektrum mit einer Simulation, basierend auf einem quantenmechanischen Modell der jeweiligen Bewegung, verglichen.

Der Pyrrolidin-Ring besitzt zwei Schwingungsmoden großer Amplitude: bei der der Ring eine Verbiegung (bend mode) bzw. eine Verdrillung (twist mode) vollführt. Dies hat zum Ergebnis, dass die Phase, mit der die ausgelenkten Ringatome sich bewegen, um den Ring herum umläuft. Diese Bewegung wurde deshalb Pseudorotation genannt. Während der Pseudorotation wechselt Pyrrolidin zwischen dem axialen und dem äquatorialen Konformer. In den analogen Systemen Cyclopentan und Tetrahydrofuran ist die Pseudorotation nahezu ungehindert, was sich in den

energetischen Barrieren von nur 25 cm^{-1} beziehungsweise 30 cm^{-1} widerspiegelt. Anhand der Femtosekunden-Rotations-DFWM Spektroskopie und einem eindimensionalen quantenmechanischen Modell der Pseudorotation konnten zum ersten Mal das Potential und die Rotationskonstanten der Pseudorotation von Pyrrolidin mit hoher Genauigkeit bestimmt werden. Es hat sich gezeigt, dass die Barriere der Pseudorotation in Pyrrolidin 220 cm^{-1} beträgt, was merklich höher ist als in Cyclopentan und Tetrahydrofuran. Gemäß dem experimentell bestimmten Potential ist das äquatoriale Konformer um 29 cm^{-1} stabiler als das axiale Konformer. Diese Energiedifferenz der beiden Konformere des Pyrrolidin ist eine deutliche Verbesserung der durch Mikrowellenspektroskopie erhaltenen Abschätzung von weniger als 220 cm^{-1} . Aufgrund seines geringen Dipolmomentes stellt Pyrrolidin ein besonders schwer zu untersuchendes System für die Mikrowellen- und die Infrarotspektroskopie dar. Bis heute konnten nur die beiden Konformere, die zwei Endpunkte der Pseudorotation, mittels Mikrowellenspektroskopie nachgewiesen werden.

Cyclopenten zeigt eine andere Art der Ringbewegung. Die Anwesenheit der Doppelbindung im Ring führt zu einer relativ hohen Frequenz der Ring-Verdrehung von 386 cm^{-1} . Bei Raumtemperatur ist demnach hauptsächlich die Biege-Mode (Ringinversion) aktiv. Diese Bewegung kann durch ein Doppelminimum Potential mit einer Barriere entsprechend der planaren Ringstruktur beschrieben werden. Mit Hilfe der Femtosekunden-Rotations-DFWM Spektroskopie wurde für diese Barriere ein Wert von 274 cm^{-1} bestimmt, was etwas höher ist, als der mit Fern-Infrarotspektroskopie gefundene Wert von 232 cm^{-1} . Die abgeleiteten Rotationskonstanten der Biegeschwingung des Ringes zeigen jedoch eine hervorragende Übereinstimmung mit Werten, die mit Mikrowellenspektroskopie gefunden wurden.

Somit ist die Femtosekunden-Rotations-DFWM Spektroskopie, dank der hohen Empfindlichkeit gegenüber strukturellen Änderungen und der guten energetischen Darstellung der Bewegungspfade, ein attraktives Werkzeug für die Untersuchung von intramolekularen Bewegungen großer Amplitude. Diese Methode ist besonders interessant für das Studium von Molekülen ohne oder mit nur sehr kleinem Dipolmoment, da sowohl Ferninfrarotspektroskopie als auch Mikrowellenspektroskopie bei solchen Molekülen nicht anwendbar sind.

Struktur und Dynamik photoreaktiver Moleküle und molekularer Cluster

Ein weiterer wichtiger Aspekt ist die Photophysik von Molekülen und molekularen Clustern mit ultrakurzen Lebensdauern ihrer elektronisch angeregten Zustände. Diese sind oft Schutzmechanismen in Bezug auf die Photostabilität der Moleküle. Die sogenannte

Photoreaktivität manifestiert sich in Elementarreaktionen wie Protonen- oder Elektronentransfer in angeregten Zuständen oder schnellen strahlungslosen Deaktivierungsprozessen, wie interner Konversion oder sie läuft über konische Durchschneidungen des elektronisch angeregten Zustandes mit dem elektronischen Grundzustand. Innerhalb dieser Mechanismen spielen Lösungsmittel oft eine wichtige Rolle, was eine zusätzliche Komplexität und somit eine Herausforderung an die Untersuchungsmethode darstellt. Unter Berücksichtigung all dieser Anforderungen wurde in der vorliegenden Arbeit eine neue spektroskopische Methode zur Strukturuntersuchung von photoreaktiven molekularen Aggregaten und zu zeitaufgelösten Relaxationsstudien entwickelt.

Die zweite Methode ist die Infrarot-Depletion, nachgewiesen mittels Femtosekunden-Multiphotonen-Ionisation (IR/fsMPI). Diese Methode wurde in unserem Labor entwickelt, um Schwingungsstudien im Bereich der X-H Streckschwingungen ($X=C, O, N$) an Molekülen und molekularen Clustern durchzuführen, welche eine extrem kurze Lebensdauer im angeregten Zustand besitzen. Die Positionen der X-H Streckschwingungen beinhalten wichtige Informationen über intra- und intermolekulare Wasserstoffbrücken von Molekülen und deren Mikrosolvaten. Darüber hinaus können durch Vergleich von experimentellen mit theoretischen Spektren die Strukturen molekularer Aggregate eindeutig abgeleitet werden. Da die Clusterbildung Überschallexpansion-Bedingungen voraussetzt, sind nur wenige Methoden für solch eine Schwingungsanalyse geeignet. Eine weit verbreitete Methode ist die Infrarot-Depletion, nachgewiesen mittels resonanter Zwei-Photonen-Ionisation (IR/R2PI), welche in unserem Labor erstmalig auf Mikrosolvate angewendet wurde. Das Prinzip lässt sich vereinfacht wie folgt beschreiben. Das molekulare System wird mit abstimmbarer IR Strahlung bestrahlt und anschließend über den ersten angeregten Singulettzustand mit zwei UV Photonen resonant ionisiert. Die entstandenen Ionen werden mit einem Massenspektrometer nachgewiesen. Ist die IR Strahlung in Resonanz mit einem Schwingungsübergang im Molekül, dann ändert sich die Effizienz des Ionisationsschrittes und somit der Ionenstrom im Massenspektrometer. Auf diese Weise können Schwingungsspektren bei Abstimmen des IR Lasers aufgenommen werden.

Die konventionelle IR/R2PI Methode, die Nanosekunden Laserpulse verwendet, ist jedoch nicht anwendbar auf Moleküle in elektronisch angeregten Zuständen mit sehr kurzer Lebensdauer. Der Grund dafür ist, dass die Effizienz des R2PI Prozesses mit abnehmender Lebensdauer des angeregten Zustandes merklich sinkt. Daher wurde der konventionelle Ansatz um Femtosekunden Laserpulse erweitert. In dieser neuen Technik wird die Ionisation der Moleküle mittels Femtosekunden-Multiphoton-Ionisation realisiert.

Anhand der IR/fsMPI Spektroskopie wurden folgende Aggregate untersucht:

1*H*-pyrrolo[3,2-*h*]quinoline (PQ) mit Wasser/Methanol sowie Adenin- und 9-Methyl-Adenin-(Wasser) Cluster.

PQ gehört zu der Gruppe der bifunktionalen Azaaromaten, die sowohl H-Bindung Donoren als auch Akzeptoren besitzen. An diesen Stellen können Lösungsmittelmoleküle gebunden werden, wobei sie sogenannte Mikrosolvate des Typs 1:n (Molekül:Lösungsmittel) bilden. Die Strukturen der 1:1 und 1:2 Aggregate werden Spezies zugeordnet, in denen die Lösungsmittelmoleküle eine Wasserbrücke zwischen der aromatischen NH-Gruppe (Donor) und dem Quinolin-Stickstoff (Akzeptor) eingehen. Sowohl PQ-Methanol als auch PQ-Wasser Aggregate zeigen dieselbe Dynamik im angeregten Zustand: Während die 1:2 Aggregate unter $S_1 \leftarrow S_0$ Anregung fluoreszieren und daher relativ langlebig sind, zeigen die 1:1 Aggregate aufgrund eines nur sehr kurzlebigen angeregten Zustandes keine Fluoreszenz. Die schnelle Deaktivierung des angeregten Zustandes in den 1:1 Aggregaten wurde bereits früher einem Protonentransfer im angeregten Zustand (ESPT) zugeschrieben, gefolgt von einer strahlungslosen Relaxation des schwingungsangeregten Tautomers. Sowohl die 1:1 als auch die 1:2 PQ-Wasser Komplexe zeigen eine schwächere Wasserstoffbrückenbindung als die analogen Komplexe mit Methanol.

Die mit IR/fsMPI Spektroskopie beobachteten Schwingungsbanden für das 9-Methyladenin Monohydrat können zwei Amino-gebundenen Isomeren zugeordnet werden, da diese, gemäß quantenchemischen Berechnungen, ähnliche Schwingungsfingerabdrücke aufweisen. Die Adenin Hydrate wurden als Amino- und N3 (N9-H) gebundene Isomere identifiziert. Die beiden Isomere des Adenin Monohydrates zeigen verschiedene Fragmentationsmuster im Monomerenkanal des Massenspektrometers, was eine unterschiedliche intermolekulare Relaxationsdynamik des angeregten Zustandes voraussetzt. Insbesondere für das N9-H gebundene Hydrat ist die Dissoziation des angeregten Zustandes effizienter als die interne Konversion (IC), hingegen für die Aminogebundene Spezies ist die IC dominant.

Die Dynamik im angeregten Zustand eines anderen bifunktionalen Azaaromaten, 7-(2'-pyridyl)indol (7PyIn), wurde mit Femtosekunden-Resonant-Excitation-Multiphoton-Ionization (fsREMPI) untersucht. Dieses Molekül besitzt dicht beieinander liegende Donor- und Akzeptorgruppen, die über eine intramolekulare Wasserstoffbrücke verbunden sind. Als Folge davon findet nach elektronischer Anregung ein schneller Protonentransfer (Phototautomerisierung) gefolgt von einem strahlungslosen Deaktivierungsprozess statt. Mit Hilfe von fs REMPI Messungen konnte gezeigt werden, dass dieser Relaxationsprozess bei

normalem ${}^7\text{PyIn}$ in 280 fs und bei deuteriertem ${}^7\text{PyIn}$ in 390 fs abläuft. Die Spektren führen zu der Schlussfolgerung, dass die Phototautomerisierung in ${}^7\text{PyIn}$ an eine Verdrillung des Moleküls gekoppelt ist und dass diese Verdrillung einen effizienten Kanal für die strahlungslose Deaktivierung bietet. Darüber hinaus ist die Tautomerisierung gemäß dem beobachteten Isotopeneffekt im niedrigsten angeregten elektronischen Singulettzustand barriereelos. Dieses Muster der Tautomerisierung im angeregten Zustand und der Deaktivierung ist womöglich allgemeingültig.

Somit ist die Kombination aus IR/fsMPI und fs REMPI eine attraktive Methode, die Dynamik im angeregten Zustand und die Struktur von photoreaktiven Molekülen und molekularen Komplexen zu untersuchen.

8 Personal contribution to the papers

"Missing levels lead to additional lines: the influence of nuclear spin statistics on femtosecond degenerate four wave mixing spectroscopy of polyatomic systems"

C. Riehn, M.I. Kunitski, V.V. Matylitsky, M.F. Gelin, and B. Brutschy

Physical Chemistry Chemical Physics, 2005, **7**(23): p. 3955-3962.

My contribution to this paper consisted in an implementation of nuclear spin statistics into the simulation of fs DFWM spectra. Furthermore, I performed all simulations and analysis of the spectral features.

"Pseudorotation in pyrrolidine: rotational coherence spectroscopy and ab initio calculations of a large amplitude intramolecular motion"

M. Kunitski, C. Riehn, V.V. Matylitsky, P. Tarakeshwar, and B. Brutschy

Physical Chemistry Chemical Physics, 2010, **12**: p. 72-81.

"Ring-puckering motion in cyclopentene studied by time-resolved rotational coherence spectroscopy and ab initio calculations"

M. Kunitski, S. Knippenberg, M. Gelin, C. Riehn, A. Dreuw, and B. Brutschy

Physical Chemistry Chemical Physics, 2010, **12**: p. 8190-8200.

My contribution to these two papers is the following. I have done all fs DFWM experiments and developed the simulation code by taking into account large amplitude intramolecular motions. In addition, I adopted the population based optimization algorithm (Differential Evolution) for fitting the simulated fs DFWM spectra to the experimental ones.

"Detection and structural characterization of clusters with ultrashort-lived electronically excited states: IR absorption detected by femtosecond multiphoton ionization"

Y. Nosenko, M. Kunitski, R.P. Thummel, A. Kyrychenko, J. Herbich, J. Waluk, C. Riehn, and B. Brutschy

Journal of the American Chemical Society, 2006, **128**(31): p. 10000-10001.

"Separation of different hydrogen-bonded clusters by fs UV-ionization-detected infrared spectroscopy: 1H-pyrrolo[3,2-h]quipoiline •(H₂O)_(n=1,2) complexes"

Y. Nosenko, M. Kunitski, C. Riehn, R.P. Thummel, A. Kyrychenko, J. Herbich, J. Waluk, and B. Brutschy

Journal of Physical Chemistry A, 2008, **112**(6): p. 1150-1156.

"The structure of adenine monohydrates studied by femtosecond multiphoton ionization detected IR spectroscopy and quantum chemical calculations"

Y. Nosenko, M. Kunitski, C. Riehn, P.H.P. Harbach, A. Dreuw, and B. Brutschy

Physical Chemistry Chemical Physics, 2010, **12**: p. 863-870.

The femtosecond aspect of IR/fsMPI experiments was relied on me. Moreover, I took part in the development of the nozzle source for the production of supersonic molecular beams.

"Proton transfer with a twist? Femtosecond dynamics of 7-(2'-pyridyl)-indole in condensed phase and in supersonic jets"

Y. Nosenko, G. Wiosna-Salyga, M. Kunitski, I. Petkova, A. Singh, W.J. Buma, R.P. Thummel, B. Brutschy, and J. Waluk

Angewandte Chemie-International Edition, 2008, **47**(32): p. 6037-6040.

My contribution to this work was the performance of the pump-probe REMPI experiments and the subsequent analysis of the obtained spectra. For this purpose I developed the code, which allows the fitted simulation of experimental REMPI spectra.

9 Publications

9.1 Missing levels lead to additional lines: the influence of nuclear spin statistics on femtosecond degenerate four wave mixing spectroscopy of polyatomic systems

Missing levels lead to additional lines: the influence of nuclear spin statistics on femtosecond degenerate four wave mixing spectroscopy of polyatomic systems†

C. Riehn,*^a M. I. Kunitski,^a V. V. Matytilsky,^a M. F. Gelin‡^b and B. Brutschy^a

^a Johann Wolfgang Goethe-University Frankfurt/M., Institute of Physical and Theoretical Chemistry, Marie-Curie-Str. 11, D-60439 Frankfurt/M, Germany. E-mail: riehn@chemie.uni-frankfurt.de

^b Department of Chemistry & Biochemistry, University of Maryland, 0107 Chemistry Building, College Park, MD, 20742-4454, USA

Received 21st July 2005, Accepted 12th September 2005

First published as an Advance Article on the web 23rd September 2005

We present the results of comprehensive experimental and theoretical studies of the effect of nuclear spin statistics on the structure of rotational recurrences in femtosecond degenerate four-wave mixing (fs DFWM) spectra of asymmetric top molecules. New recurrences of *J*-type with a period of $1/[4(B + C)]$ are identified in fs DFWM spectra of near-prolate tops SO₂ [H. M. Frey, P. Beaud, T. Gerber, B. Mischler, P. P. Radi and A. P. Tzannis, *J. Raman Spectrosc.*, 2000, **31**, 71] and NO₂ [I. Pastirk, M. Comstock and M. Dantus, *Chem. Phys. Lett.*, 2001, **349**, 71]. Our measurements of the asymmetric oblate-like top CH₃NO₂ revealed new recurrences of *A*-type with a period of $1/(8A)$, *A*, *B* and *C* being the rotational constants. The incorporation of nuclear spin statistics into the fs DFWM simulation-fitting code allowed us to successfully reproduce all these new features and the subsequent theoretical analyses uncovered mechanisms of their appearance. The nuclear spin statistics is shown to have a profound effect on fs DFWM spectra of asymmetric top species, notably with several zero spin nuclei.

1. Introduction

Recently, femtosecond time-resolved degenerate four-wave mixing (fs DFWM) has been introduced as a new technique for high-resolution molecular spectroscopy.^{1,2,3} It represents an ultrafast pump-probe implementation of rotational coherence spectroscopy (RCS) pioneered by Baskin, Felker and Zewail in 1986.⁴

In general, RCS is based on coherent excitation of molecular rotational energy levels employing ultrashort laser pulses in order to generate a rotational wavepacket from an ensemble of molecules.^{5,6} The periodic movement of this wavepacket on the picosecond timescale is probed *via* a vector property ('antenna'), like the transition dipole moment or the axis of maximum polarizability. The obtained spectral features, so-called rotational recurrences (RRs), can be understood qualitatively by the picture of a classically spinning top, which exhibits periodic realignments that are directly related to its moments-of-inertia at fixed rotational energy.

In this work we have applied fs DFWM for generating and probing of rotational coherence. This is a non-resonant technique based on rotational Raman excitation. It can be employed to investigate a sample under the low-temperature environment of a supersonic expansion as well as at elevated temperatures in a gas cell. No particular chromophore and no permanent dipole moment is required. From a fs DFWM spectrum several molecular parameters can be obtained. The positions of RRs in the time domain are related to the inverse of the rotational constants of the molecule under study. Thus,

structural information is accessible which is particularly interesting for large molecules or molecular systems such as clusters where the frequency domain techniques are not applicable due to spectral congestion. Femtosecond DFWM spectroscopy also allows for the precise determination of centrifugal distortion (CD) constants and delivers information on the anisotropy of the polarizability tensor (PT).

In order to extract these pieces of information a theoretical model for quantitative reproduction of the experimental spectra is necessary. In this way a quantum mechanical approach based on perturbation theory was developed by Felker *et al.*⁵ for rigid asymmetric tops. Gelin *et al.*⁷ investigated the RRs of asymmetric tops by a semiclassical analysis of the quantum orientational correlation function. For the general case of a non-rigid asymmetric rotor the numerical simulation of the corresponding spectra is indispensable. We have developed a numerical simulation procedure that is based on Felker's original approach but generalizes it towards non-rigid asymmetric tops and includes also the anisotropy of the PT.⁸ Here we will describe and demonstrate a further extension of our spectral simulation model in order to incorporate nuclear spin statistics (NSS) effects.

The spectral signature induced by NSS has been described in the literature for diatomic and linear systems.¹ There, the analysis is straightforward since the energy levels can be obtained in an analytical form and the well-behaved regular rotational level structure simplifies the symmetry assignment. For example the spectra of O₂, N₂ and CO₂ have been analyzed in this way.^{1,2,9} However, the NSS effects for polyatomic non-linear molecules in fs DFWM spectroscopy have up to now not been elucidated and it is by no means trivial to predict the exact influence of NSS on fs DFWM spectra as we will show in the following.

In particular, we provide data and discuss the influence of NSS on the energy level structure, the quantum beat frequency

† Electronic supplementary information (ESI) available: Experimental and simulated fs DFWM spectra of nitromethane. See DOI: 10.1039/b510363k

‡ On leave from the Institute of Molecular and Atomic Physics, Skaryna Avenue 70, Minsk 220072, Belarus.

spectra and, finally, on the time-resolved spectra obtained by fs DFWM. We present numerical simulations of the spectra for the near-symmetric tops sulfur dioxide (SO₂) and nitrogen dioxide (NO₂) which have been measured by Frey *et al.*¹⁰ and Pastirk *et al.*,¹¹ respectively (Fig. 1). Additionally, we have recorded new fs DFWM spectra for the asymmetric top nitromethane (CH₃NO₂), which are also discussed in the framework of our spectral simulation model. All molecules exhibit new types of rotational recurrences, which can be nicely reproduced by the numerical simulations with our model. Thus, the incorporation of NSS into the general spectral simulation model is necessary for further developing RCS towards high-resolution spectroscopy.

2. Theoretical background

2.1 Rotational Hamiltonian

In order to calculate the DFWM signal in the most general case of a non-rigid asymmetric rotor, we adopt the Watson A-reduced parameterization of the molecular Hamiltonian \hat{H} , which can be written in a perturbation treatment as a sum of the rigid rotor Hamiltonian, \hat{H}_0 , and the centrifugal distortion (CD)-induced part, \hat{H}_{CD} :¹²

$$\hat{H} = \hat{H}_0 + \hat{H}_{CD} \quad (1)$$

The total Hamiltonian \hat{H} possesses the D_2 symmetry. The D_2 group (which is frequently referred to as V -group) consists of four elements: three operators $C_2(a)$, $C_2(b)$, $C_2(c)$ which describe rotation by the angle π around the axes a , b , c and the identity operator, E . Therefore, the eigenfunctions $\Psi^{(k)}$ of the Hamiltonian \hat{H} can be classified according to the irreducible representations ($k = A, B_a, B_b, B_c$ according to Mulliken designation) of the group D_2 . Namely, the eigenfunctions $\Psi^{(A)}$ are invariant upon two-fold rotation about any of the principal axes of inertia. $\Psi^{(B)}$ are invariant upon the rotation $C_2(i)$ about the i 's axis but change their sign under the other two rotations.

Using the King–Hainer–Cross notation of asymmetric top energy levels K_{-1}, K_1 , ($=K_a, K_c$) species of the D_2 group can be also labeled as ee, eo, oo, oe .¹³ The first letter indicates the parity (even/odd) of K_{-1} (K_a), the second the parity of K_1 (K_c). The two notations are connected through: $A = ee$, $B_a = eo$, $B_b = oo$, $B_c = oe$.

2.2 Implementation of nuclear spin statistics

Molecular symmetry is significant in determining selection rules for various spectra.^{14,15} In the context of rotational coherence spectroscopy (RCS), a crucial role is played by the nuclear spin statistics (NSS), provided the molecule under study possesses several identical nuclei (notably with zero spin).

Since interaction of nuclear spins with molecular electrons is negligibly small, the total (coordinate \times spin) molecular wave function is independent of projections of nuclear spins on a certain space-fixed axis and is thus degenerate. If a molecule possesses identical nuclei, an exchange of any pair of them results in the multiplication of the total wave function by $+1$ (symmetric) or -1 (antisymmetric wave function), depending on whether the nuclei have an integer spin (bosons) or a half-integer spin (fermions). All possible exchanges of identical nuclei realize a certain reducible representation of the molecular point group in the spin space. Decomposing this reducible representation into irreducible parts gives the weighting factors which tell us how many times a certain irreducible representation enters the reducible one. As a result, the coordinate (electronic \times vibrational \times rotational) part of the molecular wavefunction acquires certain statistical weights. On the other hand, the ground vibronic state of a molecule is

Table 1 Symmetry classification and nuclear spin statistical weights

D_2	K_{-1}, K_1 K_a, K_c	SO ₂ , NO ₂	CH ₃ NO ₂
A	ee	1	1
B _a	eo	0	1
B _b	oo	1	0
B _c	oe	0	0

normally totally symmetric with respect to all transformations of its point group. In this case, the symmetry of the coordinate wavefunction with respect to these transformations coincides with the symmetry of its rotational part. Thus the statistical weights deliver the “oscillator strengths” for various rotational transitions, which affect RCS transients.

It is generally believed that the influence of NSS on RCS signals is substantial for diatomics and linear triatomics, but is negligible for polyatomic molecules. The aim of the present paper is to demonstrate that the NSS is of crucial importance for polyatomic (asymmetric top) molecules possessing two identical nuclei with zero spin. In that case, the mechanism and extent of the influence of NSS on RRs is very similar for both asymmetric top and linear molecules. Namely, a part of the rotational transitions becomes forbidden.

Indeed, suppose that a molecule possesses two identical nuclei with spin s , which are situated symmetrically with respect to a certain principal axis of inertia. Let us denote this axis by x and the remaining two axes by y and z . The rotational wave functions $\Psi^{(A)}$ and $\Psi^{(B_x)}$ are thus invariant upon the operation $C_2(x)$, while $\Psi^{(B_y)}$ and $\Psi^{(B_z)}$ change their signs. Since the total (coordinate \times spin) molecular wave function is multiplied by $+1$ (-1) upon the exchange of two identical bosonic (fermionic) nuclei, it is straightforward to demonstrate,^{14,15} that the wavefunctions $\Psi^{(k)}$ acquire the appropriate statistical weights ζ_k . Namely, $\zeta_A = \zeta_{B_x} = s + 1$ (for an integer s) and s (for a half-integer s). *Vice versa*, $\zeta_{B_y} = \zeta_{B_z} = s$ (for an integer s) and $s + 1$ (for a half-integer s). Thus, the smaller the nuclear spin, the stronger is its effect on the ratio of the statistical weights. If the nuclei have zero spin, then $\zeta_{B_y} = \zeta_{B_z} = 0$ and the corresponding energy levels do not exist.

As a result of the discussion above the nuclear spin statistical weights for the molecular species of this investigation have been obtained and summarized together with their symmetry assignments in Table 1.

2.3 Spectral simulations

The rotationally-sensitive part of a general fs DFWM signal is expressed through the third order molecular susceptibility $\chi(t)$ as follows^{16,17}

$$S(t) = I(t) \otimes |I(t) \otimes \chi(t)|^2 e^{-t/\tau}, \quad (2)$$

$$\chi(t) \sim \text{Im} \sum_{ij=a,b,c} \langle [\beta_{ij}, \beta_{ji}(t)] \rangle$$

Here $I(t)$ is the intensity of the laser pulses, τ is a phenomenological decay time, the indices label the axes of the principal moments of inertia, the angular brackets denote the thermal averaging,

$$\beta_{ij}(t) = \exp\{-i\hat{H}t/\hbar\} \beta_{ij} \exp\{i\hat{H}t/\hbar\}$$

\hat{H} being the total molecular Hamiltonian, eqn (1). β_{ij} is the imaginary part of the traceless polarizability tensor (PT) of a ground vibronic state. Normally, the diagonal components of the PT are much larger than the off-diagonal ones (see, *e.g.*, ref. 18). Throughout the present paper we therefore neglect the off-diagonal components and parametrize the diagonal components of the traceless PT by a single angle $-\pi/2 \leq \varphi \leq \pi/2$:¹⁹

$$\beta_{AA} = r\cos(\varphi), \beta_{BB} = r\sin(\varphi), \beta_{CC} = -r(\cos(\varphi) + \sin(\varphi)), \quad (3)$$

$r \equiv 1/\sqrt{2 + \sin(2\varphi)}$ being the normalization constant ($(\beta_{AA})^2 + (\beta_{BB})^2 + (\beta_{CC})^2 = 1$).

To evaluate the fs DFWM signal *via* eqn. (2), we have incorporated the effect of the NSS into our computer code, which has been described in more detail elsewhere.^{§¶} In short, the simulation procedure consists of several steps. (i) The rotational energy level structure is obtained according to a chosen Hamiltonian. (ii) The rotational frequency domain spectrum is constructed from the energy level structure and the appropriate selection rules. (iii) This frequency domain spectrum is converted into the time-domain spectrum by the Fast Fourier Transformation (FFT). (iv) The time-domain spectrum is convoluted with temporal shapes of the laser pulses. The simulation is incorporated into a nonlinear fitting routine, so that all steps (i–iv) are repeated until the difference between the calculated and experimental spectra reaches the desirable accuracy or until the difference cannot be decreased any further.

The NSS is implemented within the first step. Namely, the asymmetric top eigenfunctions $\Psi^{(k)}$ belonging to a particular irreducible representation of the group D_2 ($k = A, B_a, B_b, B_c$) are constructed as the linear combinations of the symmetrized and antisymmetrized eigenfunctions $\psi_{JKM}^{\pm} = (\psi_{JKM} \pm \psi_{J-KM})/\sqrt{2}$ of the rigid symmetric rotor Hamiltonian,^{14,15}

$$\Psi_{J\tau M}^{(k)} = \sum_{K,\pm} a_{\tau JK M}^{(k)} \psi_{JKM}^{\pm}$$

The matrix elements of the Hamiltonian (1) with respect to ψ_{JKM}^{\pm} are computed analytically. For any irreducible representation k of the group D_2 and for any magnitude (J) and projection (M) of the angular momentum on the axis of the laboratory frame, the finding of the coefficients $a_{\tau JK M}^{(k)}$ is reduced to the eigenvalue problem for the corresponding $N \times N$ matrix, which is solved numerically (if $k = A$, then $N = J/2 + 1$ and $(J - 1)/2$ for even and odd J , respectively; if $k = B_a, B_b, B_c$, then $N = J/2$ and $(J + 1)/2$ for even and odd J , respectively). After the asymmetric top eigenvalues and eigenfunctions are obtained, the latter acquire the appropriate NSS weights ξ_k , that is $\Psi_{J\tau M}^{(k)} \rightarrow \xi_k \Psi_{J\tau M}^{(k)}$ ($k = A, B_a, B_b, B_c$). Note that the energy levels within a J -manifold of an asymmetric top are labelled by τ , with $\tau = -J, \dots, 0, \dots, J$, $\tau = K_{-1} - K_1$.

2.4 Nomenclature of RRs

The assignment and classification of RRs in time-domain RCS spectra has been discussed in several reviews.^{5,6,20} The most abundant RRs (for nearly symmetric tops) are the so-called J -type RRs, with the period $t_J = 1/[2(B + C)]$. For slightly asymmetric tops the asymmetry RRs of A - or C -type with the period $t_A = 1/(4A)$ and $t_C = 1/(4C)$ can occur. They dominate the spectrum for highly asymmetric species. Hereafter, RRs in fs DFWM spectra will be denoted by $X(1), X(2), \dots, X(n)$, where $n = 1, 2, \dots$ numbers the RR peaks and ($X = J, A, C$) stands for the RR type.

The influence of the NSS on fs DFWM spectra of polyatomic molecules SO_2 , NO_2 and CH_3NO_2 is discussed and exemplified in sections 4 and 5. They are shown to exhibit extra RRs with the period $t_J/2$ and $t_A/2$, which will be referred to as $J(n/2)$ and $A(n/2)$.

§ Our simulation program is based on the code developed by P. M. Felker (UCLA, Los Angeles, USA) for computing ground-state RCS transients for rigid asymmetric tops. We are grateful to him for providing us with this code.

¶ The simulation software described and applied here can be obtained upon request from the corresponding author (CR).

3. Experimental

The femtosecond degenerate four-wave mixing measurements on nitromethane have been performed with an experimental setup described recently in detail.^{20,21} Briefly, the laser setup consists of an Ar-ion laser (Coherent, Innova 310) pumped Ti:sapphire oscillator (Coherent, Mira Basic) and a chirped-pulse amplification system (Quantronix, 4800 Series). The output of this femtosecond laser apparatus (wavelength of 800 nm, 1 kHz pulse repetition rate, pulse duration is 200 fs [fwhm autocorrelation], energy up to 800 $\mu\text{J pulse}^{-1}$) is divided into three beams: two pump and one probe beam of identical linear polarization and energy. The probe beam is directed over a computer controlled translational stage for scanning the time delay up to 4 ns. All three beams are combined in a forward boxcar arrangement in order to provide phase matching and allow for the separation of the diffracted coherent four-wave mixing signal beam.²²

The fs DFWM measurements on nitromethane have been performed in a gas cell at room temperature at a pressure of *ca.* 40 mbar. The energy of the pump and probe laser beams was *ca.* 70 $\mu\text{J pulse}^{-1}$. The time delay scanning step size was 0.1 ps and 500 laser shots were averaged per delay line position. Only the first 200 ps of the spectrum have been scanned. Nitromethane was obtained from Riedel-de Haën (purity 99%) and was used without further purification. The fs DFWM spectra for SO_2 and NO_2 were taken from the literature.^{10,11} They have been obtained with similar experimental setups as described here.

4. Results

4.1 Simulation of sulfur dioxide (SO_2) and nitrogen dioxide (NO_2) spectra

The fs DFWM spectra for SO_2 and NO_2 are reported in the literature.^{10,11} So, we will give here only spectral simulations which emphasize NSS induced features of these spectra that have not been discussed so far.

SO_2 and NO_2 molecules are near-prolate tops (Ray's asymmetry parameter $\kappa = (2B - A - C)/(A - C) = -0.942$ and -0.994 , respectively) and belong to the point group C_{2v} . The rotational constants and other molecular parameters of these tops used in the simulations are listed in Table 2. The rotational constants are precisely known from microwave and rotationally resolved IR experiments.^{23,24} The centrifugal distortion for NO_2 was not considered here. The PT for both molecules was used in a parameterized form (3). Computed data from the literature²⁵ on SO_2 give a PT of 'prolate-like' type, *i.e.*, the largest polarizability is found along the a -axis (prolate top axis). For the simulations we assume the same PT parameterization for NO_2 since no data from the literature were found.

Both molecules have two zero spin nuclei of oxygen ($s(^{16}\text{O}) = 0$) symmetrically situated about the b -axis (Fig. 1(a), (b)). Hence, as described in section 2.2, energy levels of symmetry B_a (*eo*) and B_c (*oe*) do not exist. This NSS weighting results in the simulated spectra depicted in Fig. 2(b), (d). For comparison the traces of Fig. 2(a), (c) were simulated without consideration of the NSS.

In the spectra of Fig. 2(b), (d) extra recurrences appear, assigned as $J(1/2), J(3/2)$ *etc.*, which match exactly half of the time interval of a J -type recurrence, *i.e.*, $t(n) = n/[4(B + C)]$, $n = 1, 2, \dots$. The decay of these new recurrences is very fast for SO_2 (only $J(1/2)$ can be clearly seen), whereas in the case of NO_2 at least five recurrences of this type are seen. Additionally, for SO_2 asymmetry recurrences of C -type are visible. Finally, we state that the simulated fs DFWM spectra of SO_2 and NO_2 including the NSS are in good agreement with the experimental data.^{10,11}

Table 2 Molecular data used for simulation of fs DFWM spectra of SO₂, NO₂ and CH₃NO₂

Parameter	SO ₂	NO ₂	Nitromethane (CH ₃ NO ₂)	
			Fitted simulation, this work	Ref. 26
<i>A</i> /GHz	60.778 549 82(32) ^a	239.904 516(6) ^b	13.335(3)	13.341 881(30)
<i>B</i> /GHz	10.318 073 532(54)	13.002 2006(4)	10.543(7)	10.544 375(30)
<i>C</i> /GHz	8.799 703 384(49)	12.304 7551(4)	5.96(2)	5.875 760(29)
<i>A_J</i> /kHz	6.612 203(126)	— ^c	6.9(6)	6.14(62)
<i>A_{JK}</i> /kHz	−116.949 69(213)	—	−29(4)	17.75(37)
<i>Δ_K</i> /kHz	2590.3156(77)	—	−9(15)	−7.54(40)
<i>δ_J</i> /kHz	1.701 1290(123)	—	2.467	2.467(44)
<i>δ_K</i> /kHz	25.36986(115)	—	15.75	15.75(19)
<i>κ</i>	−0.942	−0.994	+0.243	+0.251
Temperature/K	300	300	300	
Parametrized polarizability <i>φ</i> /rad	−0.292 ^d	−0.292 ^e	+1.57	+1.53 ^f

^a Rotational and CD constants taken from ref. 23. ^b Rotational constants taken from ref. 24. ^c No centrifugal distortion constants used for the simulation. ^d Calculated from ref. 25. ^e Value fixed to the one for SO₂, implying a 'prolate-like' polarizability tensor. ^f Calculated from ref. 18.

4.2 Measurement and simulation of nitromethane (CH₃NO₂) spectrum

Nitromethane (CH₃NO₂) is a very asymmetric (*κ* = +0.25) oblate-like top which belongs to the C_s point group (with one of the H atoms in the ONO plane) or otherwise, to the C₁ point group. The molecule has two zero spin nuclei of oxygen, which are symmetrically situated about the *a*-axis (Fig. 1(c)). Thus, the rotational levels of B_{*b*} (*oo*) and B_{*c*} (*oe*) symmetry do not exist. With the account of this effect the experimental fs

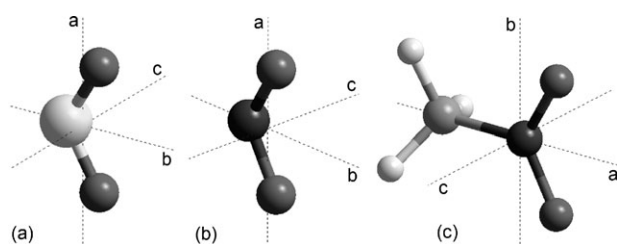


Fig. 1 (a), (b) and (c) Schematic view of sulfur dioxide (SO₂), nitrogen dioxide (NO₂) and nitromethane (CH₃NO₂) molecules, respectively, with principal axes of inertia.

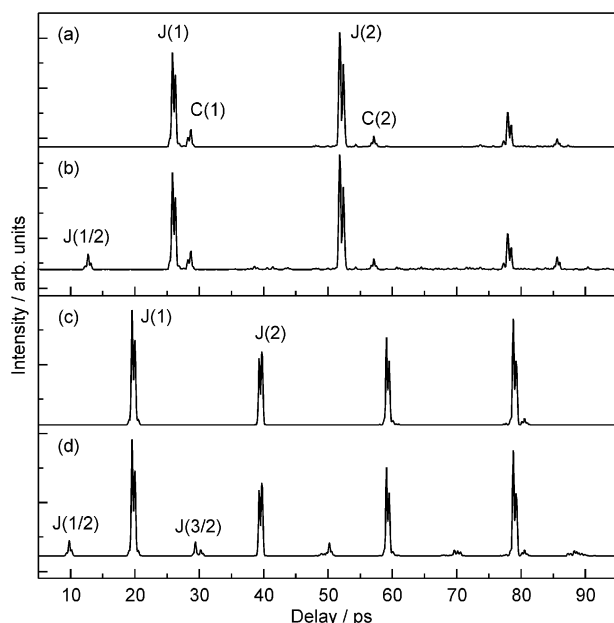


Fig. 2 Simulations of the fs DFWM spectra of SO₂ and NO₂. (a) and (b) SO₂, (c) and (d) NO₂ without/with consideration of nuclear spin statistics, respectively. For assignment of rotational recurrences see text.

DFWM spectrum of nitromethane (Fig. 3(b)) can be reproduced by a fitted simulation (Fig. 3(a)). In order to focus the discussion on the main peaks we have depicted the spectrum in Fig. 3 only up to 120 ps. The spectrum up to 200 ps and the result of the fitted simulation are given as electronic supplementary information (ESI).[†] During this fitting the rotational and CD constants of nitromethane were varied and the resulting values are given in Table 2 together with reference data from microwave spectroscopy.²⁶ For the simulations the influence of the internal rotor of the methyl group on the energy level structure was neglected.

One can see that, as in the case of SO₂ and NO₂, besides 'classical' transients of *A*- and *J*-type, extra recurrences appear. However, for nitromethane the NSS induces only the 'doubling' of *A*-type (asymmetry) recurrences, while no 'doubling' of *J*-type recurrences is observed. These extra RRs possess the period of *t_A*/2 and are assigned as *A*(1/2) and *A*(3/2). The simulation without considering NSS (depicted in Fig. 3(c)) does not reproduce the experimental spectrum, especially the strongest recurrence *A*(3/2). Another remarkable feature of the spectra of Fig. 3(a), (b) is that the *A*-type recurrences show an

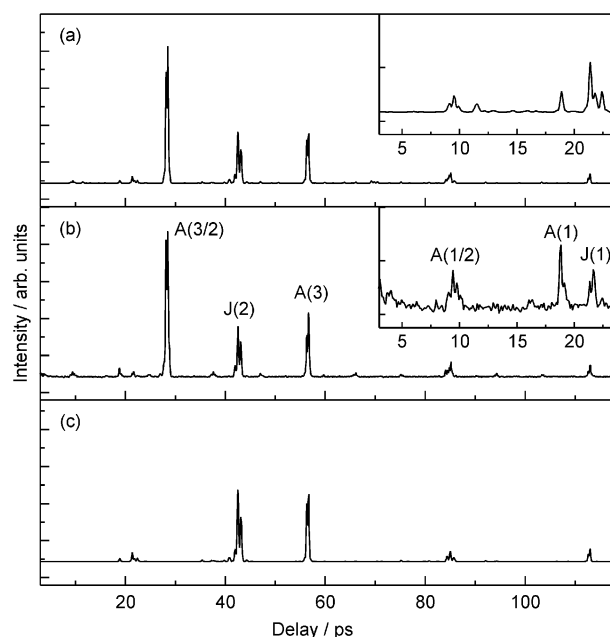


Fig. 3 Experimental and simulated fs DFWM spectra of nitromethane. (a) Fitted simulation of the spectrum using nuclear spin statistics. (b) Experimental fs DFWM spectrum (this work). (c) Simulation of the spectrum without consideration of nuclear spin statistics. For assignment of rotational recurrences see text.

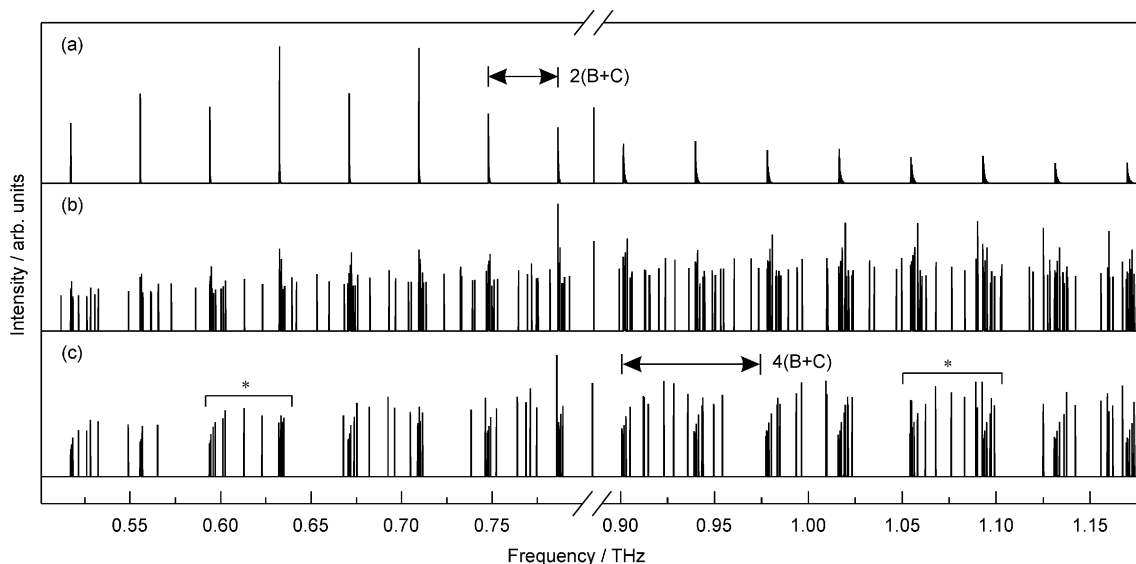


Fig. 4 Simulations of the fs DFWM quantum beat frequency spectrum of SO_2 . Only the following transitions are taken into account: (a) $\Delta J = 2$, $\Delta\tau = -2$, $\tau > 0$ (the J -type frequency sequence). (b) and (c) $\Delta J = 2$, $\Delta\tau = -2$, all τ , without/with consideration of nuclear spin statistics, respectively.

additional structure, *i.e.*, a modulation in intensity over the complete spectrum, such that every third recurrence ($A(3)$, $A(6)$ *etc.*) is very strong. Similarly, this behavior is also seen for the NSS extra recurrences.

5 Discussion

5.1. The near-symmetric top case: SO_2 and NO_2

In order to understand the influence of the NSS on the fs DFWM spectra we have undertaken extensive numerical simulations and examined the resulting rotational energy levels and quantum beat frequency domain patterns.

By these computer experiments on the SO_2 and NO_2 molecules it was worked out that only transitions obeying the selection rules $\Delta J = 2$, $\Delta\tau = -2$ ($\tau_{J+2} - \tau_J = -2$) contribute to the extra recurrences with the period of $t_J/2$. For an asymmetric prolate-like top these transitions are also involved in the C -type²⁷ and J -type recurrence generation. To be specific, transitions between lower τ ($\tau \approx -J$) correspond to C -type and higher τ ($\tau \approx J$) to J -type recurrences. For a better understanding of the origin of these extra recurrences, we switch to the frequency domain. Since only certain transitions

take part in the generation of extra recurrences the spectral simulations will be restricted to $\Delta J = 2$, $\Delta\tau = -2$ transitions. The resulting quantum beat frequency spectra are given in Fig. 4 and 5. The NSS demand that antisymmetric rotational eigenstates and the corresponding transitions do not exist. For example, for SO_2 this changes the rotational quantum beat frequency spectrum from Fig. 4(b) (without NSS) to the regular pattern of frequency clusters Fig. 4(c) (with NSS, clusters are marked by *). A similar effect is observed for the spectra of the more symmetric NO_2 as depicted in Fig. 5(a).

In order to reveal the origin of $t_J/2$ recurrences the following numerical experiment was performed. Using the additional restriction of $\tau > 0$ for the transitions, the simulation of the quantum beat frequency spectrum of SO_2 leads to the sequence plotted in Fig. 4(a), where regular frequency intervals of $\Delta f_J = 2(B + C) = 38$ GHz can be observed. These transitions obviously contribute to the regular J -type recurrences ($t_J(n) = n/2(B + C) = n \cdot 26$ ps, $n = 1, 2, \dots$). By comparison of the traces of Fig. 4(a) and Fig. 4(c), one can see that the frequencies that appear in Fig. 4(c), where all τ levels are considered, are grouped in clusters of sequence $2\Delta f_J$. Thus, such a frequency pattern leads to a rotational recurrence of $t_J/2$ in the time domain.

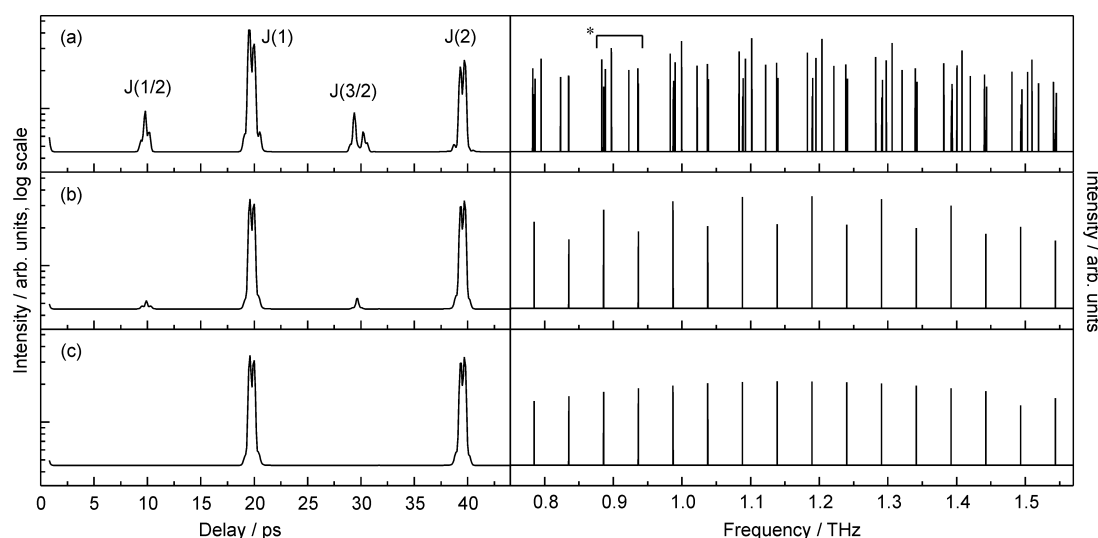


Fig. 5 Simulation of the fs DFWM spectrum and corresponding quantum beat frequency spectrum of NO_2 . Only $\Delta J = 2$, $\Delta\tau = -2$ transitions are taken into account. Please note the logarithmic ordinate scale which was chosen in order to emphasize the extra recurrences at $J(n/2)$. (a) NO_2 ($\kappa = -0.994$). (b) and (c) Artificial prolate top ($\kappa = -1$) with/without consideration of nuclear spin statistics, respectively.

Since the arrangement and intensity of lines within each of the frequency cluster varies strongly, the corresponding rotational recurrence is rather weak and does not persist for a long time (*cf.* Fig. 2(b), where $J(n/2)$ appears only once in the spectrum for SO₂ with appreciable intensity).

For a perfect symmetric prolate top the frequency groups collapse into lines of J -type frequency. In order to demonstrate this case, we have considered an artificial molecule derived from NO₂ with new rotational constants $B' = C' = (B + C)/2$, where B and C are the NO₂ constants. The resulting frequency spectra are plotted in Fig. 5(b) and (c) with and without NSS, respectively. The simulation with NSS (Fig. 5(b)) exhibits an intensity modulation of the frequencies, which gives rise to weak time-domain recurrences of $J(1/2)$ -type. This interpretation is confirmed by comparison with the simulation in Fig. 5(c), where the NSS have been omitted. Thus in the case of symmetric tops the NSS can also result in extra recurrences.

As far as intensity modulation of a frequency spectrum can lead to extra recurrences we have explored the idea that not only zero spin, but also non-zero spin nuclei might induce such an effect. If they are symmetrically situated in a C_{2v} geometry, the NSS leads to different statistical weights for rotational levels which are classified as antisymmetric and symmetric with respect to rotation about the C_{2v} axis. Thus, different weights can lead to an intensity modulation pattern of the quantum beat frequencies, and this could also cause the 'doubling' of rotational recurrences. In order to prove this suggestion, we have chosen the CF₂ radical as a model. It was found that the simulated fs DFWM spectrum (not shown here) exhibits weak $J(n/2)$ recurrences. This molecular top is prolate-like, as well as SO₂ and NO₂, with an asymmetry parameter of $\kappa = -0.96$. The two nuclei of F ($s(^{19}\text{F}) = 1/2$) are situated symmetrically about the b -axis and thus the antisymmetric levels (species B_a and B_c) and symmetric levels (A and B_b) have statistical weights of 3 and 1, respectively. This leads to an intensity modulated periodic pattern in the frequency spectrum, similar to SO₂ and NO₂. Hence, the occurrence of extra rotational recurrences is not limited to cases where rotational energy levels do not exist (zero statistical weight), but the additional features can also be expected in the more general case of non-zero statistical weighting factors.

Such effects have also been found for diatomic and linear molecules.^{1,2,9} In those cases the rotational energy structure is described by only one quantum number J and analytical expressions are obtained which allow for a comparably simple analysis. For instance, the oxygen atoms in linear tops O₂ and CO₂ have zero spin, the NSS weights $\xi_{B_b} = \xi_{B_c} = 0$ and the odd- J levels are thus forbidden. Therefore every second line in the frequency spectrum does not exist and the RR period is shortened by a factor of two, $1/(8B)$. For N₂ the ratio of the statistical weights of symmetric and antisymmetric levels is 2 : 1 (for ¹⁴N, $s = 1$). This results in the alternating intensity modulation in the frequency domain spectrum and shows up as additional RRs with twice shorter period in the time-domain.

5.2 The asymmetric top case: CH₃NO₂

We have confirmed by numerical experiments that the observed extra rotational recurrences in the case of nitromethane arise from transitions between the highest ($\tau \approx J$) rotational eigenstates with $\Delta J = 2$ and $\Delta \tau = +2$ ($\tau_{J+2} - \tau_J = +2$). This differs from a prolate-like top, for which $\Delta \tau = -2$.

In Fig. 6 the upper ($\tau \geq 0$) rotational energy level structure of two specific manifolds $J = 27, 29$ is depicted. Symmetric and antisymmetric (according to $C_2(a)$) levels are shown with solid and dashed lines, respectively. The upper levels are labelled, according to the King-Hainer-Cross notation of asymmetric top energy levels, by K_{-1}, K_1 ($\tau = K_{-1} - K_1$) and according to their D_2 group species. The transitions between two energy

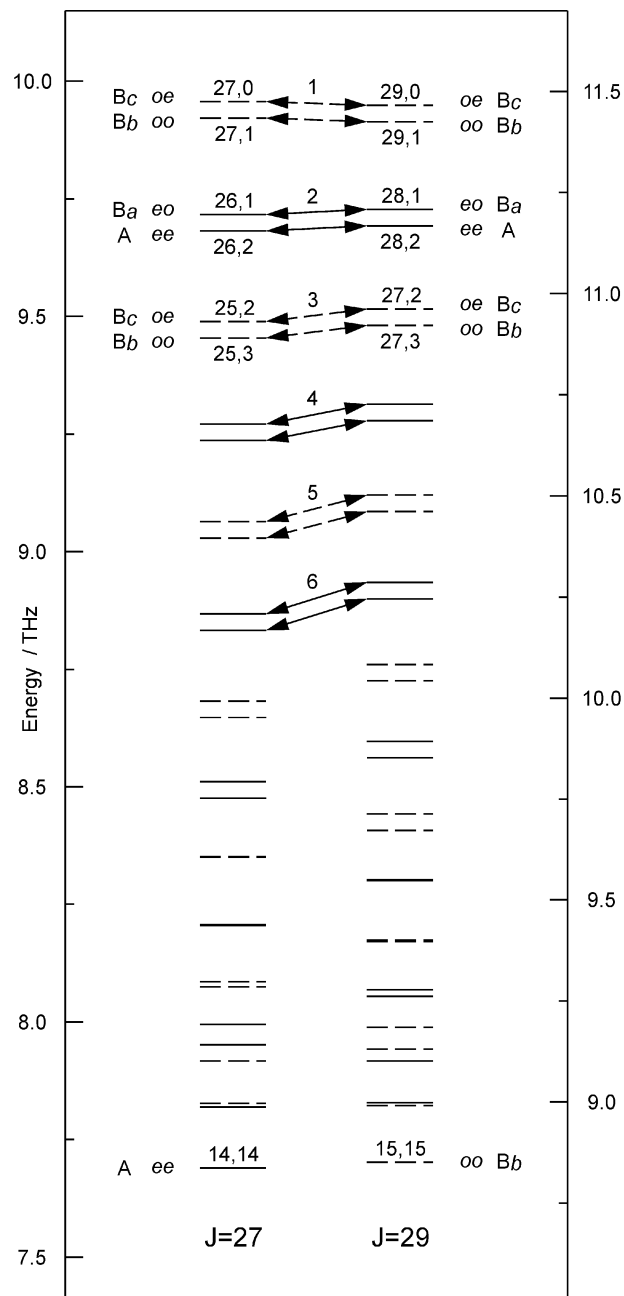


Fig. 6 Rotational energy level sub-structure of $J' = 27$ and $J'' = 29$ manifolds of nitromethane ($\tau \geq 0$). Levels drawn with dashed lines are antisymmetric with respect to $C_2(a)$ and therefore not occupied upon consideration of nuclear spin statistics. Assignment of energy levels is given in K_{-1}, K_1 and D_2 group notation. Transitions are indicated by arrows. Dashed arrows indicate lost transitions due to nuclear spin statistics. The numbering of transitions is the same as that of Fig. 7.

levels of the two manifolds are marked with arrows. The energy levels on the top of this structure show a small asymmetry splitting. For the sake of clarity the separation of lines within each pair is drawn enlarged. All $\Delta \tau = +2$ transitions between the J -manifolds 27 and 29 result in the frequency spectrum given in Fig. 7(a), so that the frequencies of lines 1, 2, 3... of Fig. 7(a) correspond to the transitions 1, 2, 3... of Fig. 6 *etc.* Moreover, one can clearly see that the pairs of antisymmetric (according to $C_2(a)$) rotational levels do not exist as well as the corresponding frequency lines (Fig. 7(b)), so that only the 'symmetric' frequencies 2, 4, 6... remain.

The spectrum in Fig. 7(c) represents an extension of the one in Fig. 7(a). Here the $\Delta \tau = +2$ transitions between *all* J manifolds differing by $\Delta J = 2$ have been considered. The distance between the frequency groups of the evolving periodic

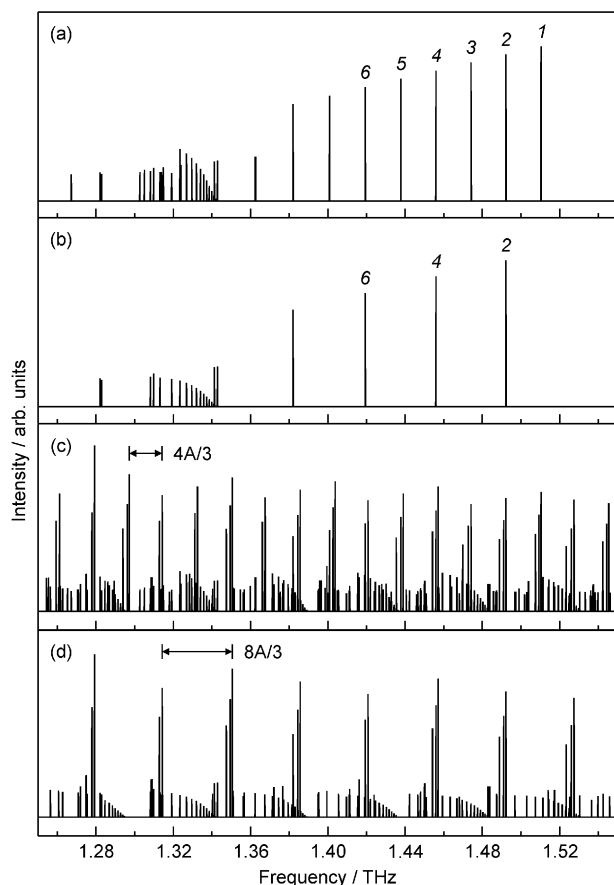


Fig. 7 Simulations of the rotational quantum beat frequency spectrum of nitromethane. Only $\Delta J = 2$, $\Delta \tau = +2$ transitions are taken into account. (a) and (b) Only between $J' = 27$ and $J'' = 29$ manifolds, without/with consideration of nuclear spin statistics, respectively. (c) and (d) All J manifolds contribute, without/with consideration of nuclear spin statistics, respectively. The frequency line marked 1 corresponds to two transitions: $J'_{27} \leftrightarrow J''_{29}$ and $J'_{26} \leftrightarrow J''_{28}$; frequency line 2 to $J'_{25} \leftrightarrow J''_{27}$ and $J'_{24} \leftrightarrow J''_{26}$ and so on. In general: $J'_\tau \leftrightarrow J''_{\tau+2}$.

pattern is given by $4A/3$, so that the corresponding rotational recurrence period equals $3/(4A)$. Upon consideration of the NSS the spectrum is clearly modified as depicted in Fig. 7(d). The corresponding time period of the recurrences becomes twice shorter ($3/(8A)$). That explains the appearance of the extra recurrence $A(3/2)$ in the experimental spectrum.

Another peculiar pattern in the nitromethane fs DFWM spectrum is the observed intensity modulation of the A -type recurrences. Every third RR of A -type was found to be strong. This behaviour is not caused by NSS and can be rationalized as follows.⁷ In general, an asymmetric top molecule possesses two rotational frequencies. One of them is responsible for the RR of a certain asymmetry type while the other, which is much smaller, induces intensity modulation of the corresponding RRs. For A -type RRs, the ratio of the two frequencies is $A/\sqrt{(A-C)(A-B)}$. This equals $2.94 (\approx 3)$ for nitromethane, which confirms nicely the experimental observation. In an earlier investigation we have found an A -type modulation period of ≈ 7 for the case of pyridine,²⁸ which can also be obtained from the corresponding rotational constants applying the above formula.

5. Conclusions

We have presented extensive numerical simulations on fs DFWM spectra of polyatomic molecules subject to pronounced nuclear spin statistical (NSS) effects in the rotational energy level manifold. The chosen molecular systems covered the near-symmetric prolate-like tops of sulfur dioxide (SO_2)

and nitrogen dioxide (NO_2) as well as the very asymmetric oblate-like top of nitromethane (CH_3NO_2). The numerical spectral simulations agree very well with the experimental spectra reported in the literature for SO_2 and NO_2 ^{10,11} and also with the new spectrum measured by us for CH_3NO_2 . The appearance of new rotational recurrences (RRs), their position in time, shape and persistence is reproduced very well. The origin of the extra RRs induced by NSS was revealed by inspection of the rotational energy level and quantum beat frequency pattern, both obtained through the numerical simulations.

For the near-symmetric prolate-like tops a regularly spaced frequency cluster can be observed in the quantum beat frequency spectrum at twice the frequency spacing of the 'classical' J -type recurrences. This means that features at half of the 'classical' J -type period are expected in the time domain which was experimentally observed for both SO_2 and NO_2 . For the asymmetric top molecule CH_3NO_2 another dominating type of rotational recurrence, namely of A -type, was found. Here a very regular pattern was revealed by the numerical simulations for the rotational energy levels corresponding to $\tau \approx J$. Furthermore, the NSS symmetry analysis of those levels demonstrated that every second of the level pairs does not exist. This gives rise to a similar doubling in the frequency domain as observed for the near-symmetric top case, but now for the asymmetric recurrences of A -type with a period of $1/(8A)$.

In a simplified picture of rotational coherence spectroscopy the *full rephasing of the original orientation* of an ensemble of (diatomic) molecules occurs at times that are related to the minimum increment of the rotational speed ($\omega/2\pi \approx 2BJ$) between the different rotational energy levels. The *rephasing of alignment* occurs at half of this time. If every second rotational level does not exist as due to the influence of NSS, the minimum speed increment is doubled and thus the rephasing occurs at half of the former time periods. In this work we have demonstrated that a similar mechanism is operative for asymmetric top molecules and that depending on their degree of asymmetry a different type of rotational recurrence is affected.

In summary, the following conclusions can be drawn from our results:

(i) In the spectra of polyatomic molecules nuclear spin statistical effects might provide extra rotational recurrences with strongly varying intensity and persistence, which cannot be simply 'extrapolated' from the well-known behavior of diatomic and linear molecules.

(ii) The occurrence of these RRs and their origin can be investigated by spectral simulations for general asymmetric molecular tops based on a symmetry classification of their rotational energy levels. By this way also the influence of different NSS weighting factors on fs DFWM spectra can be explored.

(iii) Thus, numerical simulations for complete spectra based on a comprehensive model for fs DFWM spectroscopy are indispensable for a quantitative analysis, *i.e.* the extraction of molecular parameters from the experimental spectra. Moreover, these detailed data obtained from fs DFWM spectra extends the scope of the time-resolved approach towards that of high-resolution spectroscopy. The simulations also provide valuable information for the design of dynamic molecular alignment experiments by strong laser fields, especially for the challenge of aligning asymmetric top systems.^{29,30}

Acknowledgements

We gratefully acknowledge the Johann Wolfgang Goethe-Universität Frankfurt/M. and the Fonds der Chemie for financial support. We are grateful to the Adolf Messer Stiftung (Königstein, Germany) and the Vereinigung von Freunden und Förderern der Johann Wolfgang Goethe-Universität for

their generous support. This work was also partially supported by an INTAS collaboration project (Ref. Nr. 03-50-5765).

References

- H.-M. Frey, P. Beaud, T. Gerber, B. Mischler, P. P. Radi and A. P. Tzannis, *Appl. Phys. B: Lasers Opt.*, 1999, **68**, 735.
- E. J. Brown, Q. Zhang and M. Dantus, *J. Chem. Phys.*, 1999, **110**, 5772.
- W. Jarzēba, V. V. Matylitsky, A. Weichert and C. Riehn, *Phys. Chem. Chem. Phys.*, 2002, **4**, 451.
- J. S. Baskin, P. M. Felker and A. H. Zewail, *J. Chem. Phys.*, 1986, **84**, 4708.
- P. M. Felker and A. H. Zewail, in *Femtochemistry*, ed. J. Manz and L. Wöste, VCH, Weinheim, 1995, **vol. 1**, ch. 5.
- P. M. Felker, *J. Phys. Chem.*, 1992, **96**, 7844.
- M. F. Gelin, V. A. Tolkahev and A. P. Blokhin, *Chem. Phys.*, 2000, **255**, 111.
- C. Riehn, V. V. Matylitsky and M. F. Gelin, *J. Raman Spectrosc.*, 2003, **34**, 1045.
- L. Lavorel, O. Faucher, M. Morgen and R. Chauv, *J. Raman Spectrosc.*, 2000, **31**, 77.
- H. M. Frey, P. Beaud, T. Gerber, B. Mischler, P. P. Radi and A. P. Tzannis, *J. Raman Spectrosc.*, 2000, **31**, 71.
- I. Pastirk, M. Comstock and M. Dantus, *Chem. Phys. Lett.*, 2001, **349**, 71.
- J. K. G. Watson, *J. Chem. Phys.*, 1967, **46**, 1935.
- G. W. King, R. M. Hainer and P. C. Cross, *J. Chem. Phys.*, 1943, **11**, 27.
- G. Herzberg, *Infrared and Raman Spectra of Polyatomic Molecules*, Krieger Publishing Co, Malabar, FL, 1991, p. 52.
- L. D. Landau and E. M. Lifshitz, *Quantum Mechanics: Non-relativistic Theory*, Pergamon Press, New York, 3rd edn, 1977.
- M. Morgen, W. Price, P. Ludowise and Y. Chen, *J. Chem. Phys.*, 1995, **102**, 8780.
- M. Cho, M. Du, N. F. Scherer, G. R. Fleming and S. Mukamel, *J. Chem. Phys.*, 1993, **94**, 2410.
- L. Jensen, P. O. Åstrand, A. Osted, J. Kongsted and K. V. Mikkelsen, *J. Chem. Phys.*, 2002, **116**, 4001.
- V. V. Matylitsky, C. Riehn, M. F. Gelin and B. Brutschy, *J. Chem. Phys.*, 2003, **119**, 10553.
- C. Riehn, *Chem. Phys.*, 2002, **283**, 297.
- V. V. Matylitsky, W. Jarzēba, C. Riehn and B. Brutschy, *J. Raman Spectrosc.*, 2002, **33**, 877.
- P. H. Vaccaro in *Nonlinear Optical Spectroscopy for Molecular Structure and Dynamics*, ed. H. Hirota, R. W. Field, J. P. Maier and S. Tsuchiya, Blackwell Scientific, London, 1997, ch. 4, p. 75.
- H. S. P. Muller, J. Farhoomand, E. A. Cohen, B. Brupbacher-Gatehouse, M. Schäfer, A. Bauder and G. Winnewisser, *J. Mol. Spectrosc.*, 2000, **201**, 1–8.
- Y. Liu, X. Liu, H. Liu and Y. Guo, *J. Mol. Spectrosc.*, 2000, **202**, 306–308.
- D. Xenides and G. Maroulis, *J. Chem. Phys.*, 2001, **115**, 7953.
- F. Rohart, *J. Mol. Spectrosc.*, 1975, **57**, 301.
- P. W. Joireman, L. L. Connell, S. M. Ohline and P. M. Felker, *J. Chem. Phys.*, 1992, **96**, 4118.
- W. Jarzēba, V. V. Matylitsky, C. Riehn and B. Brutschy, *Chem. Phys. Lett.*, 2003, **368**, 680.
- H. Stapelfeldt and T. Seideman, *Rev. Mod. Phys.*, 2003, **75**, 543.
- M. D. Poulsen, E. Péronne, H. Stapelfeldt, C. Z. Bisgaard, S. S. Viftrup, E. Hamilton and T. Seideman, *J. Chem. Phys.*, 2004, **121**, 783.

9.2 Pseudorotation in pyrrolidine: rotational coherence spectroscopy and ab initio calculations of a large amplitude intramolecular motion

Pseudorotation in pyrrolidine: rotational coherence spectroscopy and *ab initio* calculations of a large amplitude intramolecular motion†

Maksim Kunitski,^a Christoph Riehn,^b Victor V. Matyilitsky,^a Pilarisetty Tarakeshwar*^c and Bernhard Brutschy*^a

Received 22nd August 2009, Accepted 8th October 2009

First published as an Advance Article on the web 9th November 2009

DOI: 10.1039/b917362e

Pseudorotation in the pyrrolidine molecule was studied by means of femtosecond degenerate four-wave mixing spectroscopy both in the gas cell at room temperature and under supersonic expansion. The experimental observations were reproduced by a fitted simulation based on a one-dimensional model for pseudorotation. Of the two conformers, axial and equatorial, the latter was found to be stabilized by about $29 \pm 10 \text{ cm}^{-1}$ relative to the former one. The barrier for pseudorotation was determined to be $220 \pm 20 \text{ cm}^{-1}$. In addition, quantum chemical calculations of the pseudorotational path of pyrrolidine were performed using the synchronous transit-guided quasi-Newton method at the MP2 and B3LYP levels of theory. Subsequent CCSD(T) calculations yield the energy preference of the equatorial conformer and the barrier for pseudorotation to be 17 and 284 cm^{-1} , respectively.

1. Introduction

Paths presenting low energy barriers to conformational change are of special interest because they govern the progress of many important processes in chemistry and biology.^{1–3} Amongst the several factors controlling the conformation of molecules, pseudorotation (PR) is one of the most widely invoked but least understood intramolecular motions.^{1,2,4,5} Though more than 60 years have elapsed since Kilpatrick *et al.*⁴ put forward the concept of PR to explain the anomalously high entropy of cyclopentane, little is known about its energetic relevance in complex molecular systems.

PR is an inherent property of saturated five-membered rings. It is an out-of-plane ring-puckering vibration that causes the ring atoms to move in such a way that the phase of the puckering rotates around the ring. Since it is a periodic motion it is convenient to use an angle (ϕ) as the pseudorotational coordinate. An important aspect of PR is that it represents a lower energy path between molecular conformations as compared to ring inversion.⁶ This is illustrated in

Fig. 1 at the example of the pyrrolidine molecule. PR plays an important role in a wide range of biomolecules such as the deoxyribose/ribose of DNA/RNA,⁷ the amino acid proline, nicotine and numerous drugs containing the 5-membered thiazolidine ring, such as penicillin. For instance a recent study has shown that the side-chain flexibility of the proline residue, which largely arises from PR, is coupled to the backbone conformation of a protein.⁸

Pyrrolidine (PYR) was chosen as an archetypical system for studying PR since it is an essential component of several biologically important molecules and the relatively sparse experimental information available about PR in this molecule.

Several experimental techniques have been utilized for studying ring-puckering vibration and PR.^{1,2} Vibrational spectroscopy¹ is used to investigate energetical but not structural aspects of PR. Concerning PYR, however, only one vibrational mode corresponding to PR was reported so far, but it was not sufficient for gaining information about the energetics of PR in this molecule.^{9,10} Nuclear magnetic

^a Institut für Physikalische und Theoretische Chemie, Goethe-Universität Frankfurt am Main, Max-von-Laue-Straße 760438 Frankfurt am Main Germany. E-mail: brutschy@chemie.uni-frankfurt.de; Fax: +49 (0)69 798 29560; Tel: +49 (0)69 798 29424

^b Department of Chemistry, Technische Universität Kaiserslautern, Erwin-Schrödinger-Straße 52, 67663 Kaiserslautern, Germany

^c Department of Chemistry, University of Nevada Las Vegas, 4505 Maryland Parkway, Las Vegas, NV 89154, USA. E-mail: tarakesh@unlv.nevada.edu

† Electronic supplementary information (ESI) available: A flash movie with pseudorotation in pyrrolidine; further details on the fitted simulation of the fs DFWM spectrum; calculated dependences of the maximum pseudorotational amplitude q on the pseudorotational angle ϕ ; the energy difference between the axial and equatorial conformers of pyrrolidine calculated with different methods and basis sets; the experimental and calculated rotational constants of the axial and equatorial conformers of pyrrolidine; SCRF calculations of the pseudorotational pathway of pyrrolidine. See DOI: 10.1039/b917362e

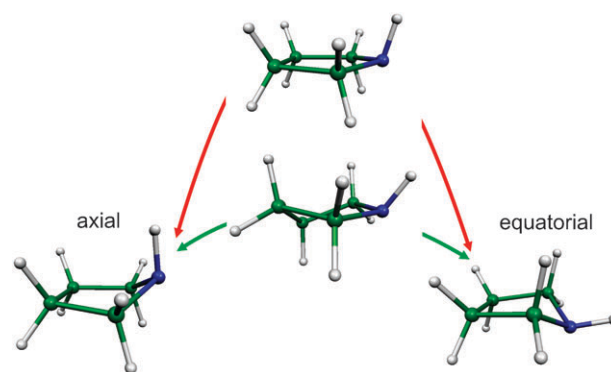


Fig. 1 Two ways of interconversion of the axial ($\phi = 0^\circ$) and equatorial ($\phi = 180^\circ$) conformers of pyrrolidine: pseudorotation (green, $< 300 \text{ cm}^{-1}$) and ring inversion (red, $\sim 1500 \text{ cm}^{-1}$).⁶

resonance¹¹ and electron diffraction (ED)^{11,12} enable the determination of energetic preferences and structures of lower pseudorotational states, however, information about the complete pseudorotational potential usually remains beyond their scope. The gas-phase ED study of the conformational preferences in pyrrolidine in conjunction with *ab initio* calculations indicated that the axial conformer is energetically the most stable one,¹³ an assignment which was revised later by microwave spectroscopy.¹⁴ However it was conceded that the signal intensity was not very sensitive to the conformation.¹³ Microwave spectroscopy (MW) is a straightforward approach for precise determination of both potential energy and structural changes along a pseudorotational pathway^{15,16} but is not suitable for molecules lacking or possessing a small dipole moment. This was the reason why the equatorial conformer of PYR was not observed in early microwave investigations¹⁷ and as a consequence, the axial conformer was assumed to be the most stable structure. Only later under better cooling conditions in a free jet experiment the equatorial conformer turned out to be the most stable structure.^{14,18} The energy difference between the axial and equatorial minima was estimated to be lower than 220 cm⁻¹.¹⁴

High resolution rotationally resolved infrared spectroscopy was shown to be applicable for studying ring puckering in four-membered ring compounds.^{19–21} The assignment of the spectra however is not an easy task, mainly due to their congestion. To the best of our knowledge, no high resolution infrared spectra of molecules undergoing PR have been reported so far. Recently single molecule vibrational spectroscopy²² was exploited for studying a pyrrolidine molecule attached to the Ag(001) surface at a temperature of 9 K. The frequency of 298 cm⁻¹ was reported and assigned to the barrier for PR. This mode however may be also attributed to ring inversion, as shown in several other vibrational studies.^{6,9,10}

In a recent theoretical study on PYR Carballeira *et al.*⁶ revised the previous findings²³ and showed that the calculated energy difference between the axial and equatorial conformers strongly depends both on the quantum chemistry method and the basis set. The pseudorotational path of pyrrolidine was also modeled by constrained optimization of several points along the pseudorotational path. Subsequent single point calculations yielded the energy barrier for pseudorotation of 248 cm⁻¹ at MP2 and 236 cm⁻¹ at B3LYP levels of theory with the 6-311 + + G(3df,3pd) basis set. It was also stated that explicit inclusion of electron correlation and zero-point energies corrections would lower the estimated barrier for PR down to 150 cm⁻¹. The barrier to ring inversion was estimated to be around 1500 cm⁻¹.

Femtosecond degenerate four-wave mixing (fs DFWM), an ultrafast pump-probe laser technique, enables in its many different implementations to study different kinds of molecular dynamics.^{24–27} In the scheme utilized in rotational coherence spectroscopy, which is used in the present study, fs DFWM allows for the time-domain observation of the coherent rotation of a molecular ensemble. Being a Raman type spectroscopy, fs DFWM has proven to be a powerful tool for investigating the structure of large molecular systems at thermal equilibrium, even if they do not possess a permanent dipole moment.^{28,29} Recently fs DFWM was applied to obtain

accurate rotational constants for several lower vibrational states of cyclobutane³⁰ and cyclooctatetraene.³¹

In this work fs DFWM spectroscopy was applied for the first time to study such a large amplitude intramolecular motion as PR at example of the pyrrolidine molecule. The interpretation of the experimental fs DFWM spectra was done by means of the simulation based on a one-dimensional quantum mechanical model for PR. This allowed for determination of the energy potential and the rotational constants along the pseudorotational path. The experimental findings were additionally supplemented by unrestrained high level quantum chemistry calculations.

The paper is organized as follows. We initially discuss the theoretical background of PR in five-membered ring compounds. Then follows the description of experimental details, the simulation procedure and the quantum chemical methods utilized in the current work. Subsequently we discuss the results.

2. Theoretical framework

2.1 Pseudorotation

The theory of ring puckering in five-membered saturated rings was developed by Harris *et al.*³² For such a system there are 5–3 = 2 out-of-plane skeletal modes consisting of a bend and a twist. Assuming that rotation and other vibrations may be separated from these two modes, the Hamiltonian may be written as follows:

$$H(x_1, x_2) = \frac{P_1^2}{2m_1} + \frac{P_2^2}{2m_1} + V(x_1, x_2) \quad (1)$$

where $V(x_1, x_2)$ is a two-dimensional potential of ring puckering vibrations, P_1 and P_2 are momentum operators, m_1 and m_2 are the reduced masses of the two modes.

The Hamiltonian (1) may also be written in polar coordinates in the way that the radial coordinate expresses the amplitude of the ring puckering and the angular coordinate relates to the puckering phase. While the motion in the radial coordinate is nothing else than ring inversion, the puckering phase motion was termed pseudorotation.^{4,32} In PYR the barrier for inversion through the planar ring is much higher than the barrier for PR.⁶ Therefore, the puckering amplitude mode can be separated from the puckering phase mode. Then, PR alone can be described with the following one-dimensional Hamiltonian:³²

$$H(\phi) = B_p P_\phi^2 + V(\phi) \quad (2)$$

where B_p is the pseudorotational constant, P_ϕ is an angular momentum operator, ϕ is the pseudorotational coordinate (angle) and $V(\phi)$ is the pseudorotational potential. During pseudorotation, the motion of the j th atom of the five-membered ring can be expressed in the first approximation by the displacement perpendicular to the mean plane:³³

$$z_j = q \cos\left(\phi + \frac{4\pi}{5}(j-1)\right) \quad (3)$$

where q is the maximum amplitude of the displacement, which, in general, depends on the pseudorotational angle. Thus the

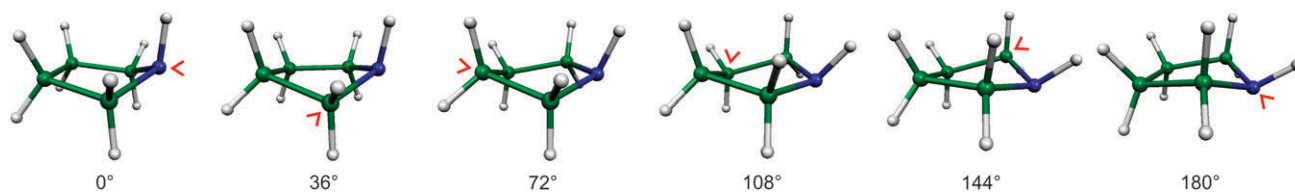


Fig. 2 The envelope structures of pyrrolidine and the corresponding pseudorotational angles ϕ . In all these structures four atoms of the ring are in one plane, while the fifth one (indicated by a red arrow) is not. This pucker rotates around the ring during pseudorotation.

pseudorotational angle ϕ , or reaction coordinate of PR, describes the phase of puckering rather than the geometrical amplitude of the distortion.¹⁵ Using formula (3) the approximate structures of the pyrrolidine ring during pseudorotation may be obtained. The envelope structures of PYR with the corresponding pseudorotational angles for half of the pseudorotational path are shown in Fig. 2. Without loss of generality the 0° angle is chosen to correspond to the axial conformer of PYR. In this assignment the equatorial conformer has the pseudorotational angle of 180° . The intermediate structures are called twisted.

The solution of the Schrödinger equation that corresponds to Hamiltonian (2) can be numerically obtained in the free rotor basis set.³⁴ For this purpose the potential $V(\phi)$ can be parameterized in the following way:

$$V(\phi) = \frac{1}{2} \sum_{i=1}^N V_i (1 - \cos i\phi) \quad (4)$$

The solution yields the energies and wavefunctions of the pseudorotational levels. The wavefunctions $\Psi_l(\phi)$ may subsequently be used for determination of the average value of a molecular property of interest $R(\phi)$ for each pseudorotational level l :

$$R_l = \langle \Psi_l^*(\phi) | R(\phi) | \Psi_l(\phi) \rangle \quad (5)$$

Since the pseudorotational wavefunctions were obtained in the free rotor basis set, the calculation of integrals in (5) may be simplified if the dependence of a molecular property on the pseudorotational angle ϕ is expressed by a Fourier series:

$$R(\phi) = \sum_{n=0}^N R_n \cos(n\phi) \quad (6)$$

Depending on the shape of the potential and temperature, various pseudorotational levels may have a significant Boltzmann population and consequently contribute to the experimental observation. This contribution can be understood as follows. Since pseudorotation is a large amplitude, highly anharmonic out-of-plane vibration it is usually accompanied with significant changes in molecular geometry. Therefore it is plausible to assume that pseudorotational levels have different vibrationally averaged molecular properties, which may be evaluated using eqn (5). Thus, the complete fs DFWM spectrum is expected to originate from a mixture of different species (levels) that have different molecular properties. The contribution of each species is proportional to the Boltzmann population of the corresponding pseudorotational level.

2.2 Pseudorotational potential

Previous studies on PYR^{6,14} favor a shape of the pseudorotational potential where two energetically non-identical minima (the axial and equatorial forms) are separated by a barrier (Fig. 3). The energy difference of the two minima was experimentally estimated to be lower than 220 cm^{-1} .¹⁴ The analysis of the solutions of the one-dimensional model for PR indicated that depending on the barrier height two limiting cases may be observed in experiment. The first one occurs when the barrier for PR is rather high (related to the thermal energy), so that only a few of the lowest pseudorotational states are populated. The average geometries of these states are very close to those of the axial and equatorial conformers, since the molecule is localized in the regions of the two minima, namely close to the pseudorotational angles of 0° and 180° . Therefore the spectrum will appear mainly as a superposition of the spectra of two structures. The second case is when the barrier for pseudorotation is low. In this case, a

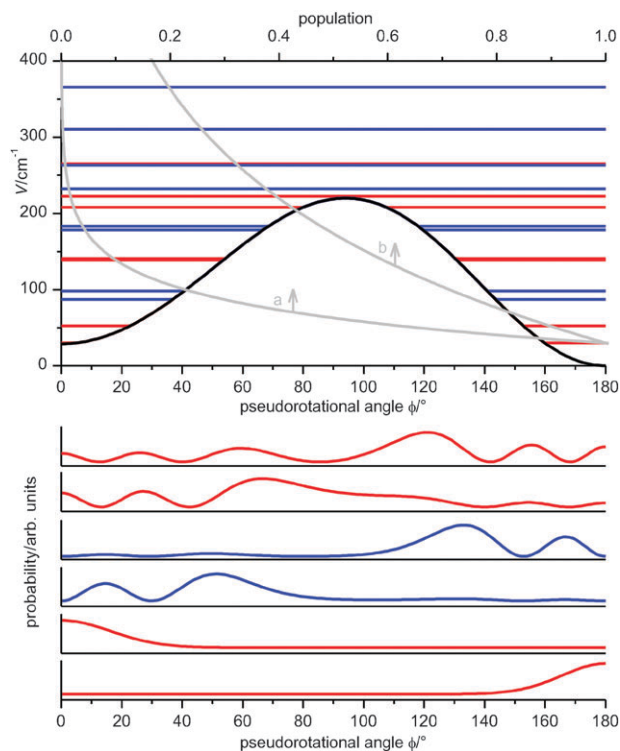


Fig. 3 Top: Pseudorotational potential and corresponding levels with their relative Boltzmann populations at temperatures of 68 K (a) and 298 K (b). Bottom: The probability density functions of the first six pseudorotational levels. The parity of levels is shown by red (even) and blue (odd) colors. The levels above 300 cm^{-1} are doubly degenerated.

number of pseudorotational levels will be populated and contribute to the experimental spectrum.

These two limiting cases can be illustrated by considering a potential with a barrier height of 220 cm^{-1} and the energy difference between the axial and equatorial conformers of 29 cm^{-1} (these values will be obtained below from the fitted simulation of the room-temperature fs DFWM spectrum of PYR, see Table 2). The calculated pseudorotational energy levels and their populations at two temperatures 68 K and 298 K are shown on the top of Fig. 3. On the bottom the probability density functions of the first six pseudorotational states are depicted. As one can see the higher the state the more delocalized is the molecule on the pseudorotational path. Thus at low temperatures (about 68 K and below) only the structures close to 0° and 180° will be observed in experiment. With increase of the temperature more and more conformations along the pseudorotational path will contribute to the spectrum.

2.3 Simulation of the fs DFWM spectrum

Simulation of the fs DFWM spectrum of a single species in the semirigid rotor approximation has been previously discussed in detail.^{28,29,35} Briefly, the typical time-resolved fs DFWM spectrum of a single species consists of equidistant signal peaks called transients or recurrences. The period of such a transient sequence relates to the rotational constants (structural parameters) of the molecule under investigation. Quantitative simulation of the fs DFWM spectrum requires the following molecular properties to be known: rotational constants, centrifugal distortion constants, rotational temperature and anisotropy of the polarizability tensor. In order to reduce the number of parameters in the simulation, the following approximations were made. Only two terms of quartic centrifugal constants Δ_J , Δ_{JK} were included, since the other terms have a negligible influence on the spectrum in case of a nearly symmetric top and, in particular, when no K-type transients are observed.²⁸ Only diagonal elements of the polarizability tensor were considered, which is justified by the fact that the off-diagonal elements are usually much smaller. The diagonal components of the tensor might be further parameterized by only one parameter φ .³⁵ Therefore, in total, seven parameters are required for the simulation of a fs DFWM spectrum of a single species.

A fs DFWM spectrum of a mixture of several species or of one species with several low-frequency vibrations may be constructed as a coherent superposition of the individual contributions with certain weights, which in the latter case correspond to the Boltzmann populations of the vibrational states.^{26,30,31}

As was already mentioned, pseudorotation causes significant changes in the molecular structure and therefore the rotation of the molecule cannot be described within the scope of a semirigid rotor approximation. In order to consider pseudorotation in the simulation each pseudorotational level is considered as a single species with its own set of averaged molecular properties such as rotational constants, polarizability, centrifugal distortion constants. Thus the complete simulation procedure consists of the following steps. First the

pseudorotational levels are calculated relying on the pseudorotational potential and the kinetic term constant B_p . Next the expectation values of the rotational constants, centrifugal distortion constants and polarizability parameter φ are evaluated using eqn (5). With these data the fs DFWM spectra are generated for each pseudorotational state in the way as for a single species using a semirigid rotor approximation. A coherent superposition of all individual fs DFWM spectra weighted by the Boltzmann population of the corresponding pseudorotational levels yields the complete fs DFWM spectrum.

The above discussion is not limited to the case of PR, but may be applicable to other kinds of intramolecular motions such as ring-puckering in four-membered ring compounds or rotation around a central bond in *n*-butane-like molecules. For further details see Supp. Inf.

3. Methods and material

3.1 Experimental

The femtosecond degenerate four-wave mixing spectra of PYR were recorded using an experimental setup that has been previously described in detail.^{28,29} The vapour pressure of PYR in the gas cell was about 65 mbar at a temperature of 298 K. The supersonic expansion was produced by a slit nozzle of dimensions: $0.1 \times 3\text{ mm}$. Under the low-concentration conditions of a supersonic expansion, a slit nozzle provides a much better signal-to-noise ratio than a round orifice of the same cross section. This is due to the fact that a four-wave mixing signal depends on the square of the interaction length of the laser beams. Helium at 0.4 bar stagnation pressure was bubbled through liquid PYR and expanded adiabatically into a vacuum chamber at a background pressure of 10^{-4} bar. The interaction region of the three laser beams was located at a distance of approximately 2mm from the nozzle. PYR (=98.0%, purum grade) was obtained from Fluka and used without further purification.

3.2 Quantum chemistry calculations

The synchronous transit-guided quasi-Newton (STQN) method^{36,37} was applied for generating various points along the pseudorotational pathway of PYR. Compared to previous simulations of the pseudorotational barrier,⁶ the STQN approach enables a more detailed following the pseudorotational pathway without resorting to artificial geometric constraints. The STQN calculations were carried out at both the second order Møller–Plesset perturbation (MP2) and density functional (B3LYP) levels of theory using the aug-cc-pVXZ (X = D,T) basis sets. Additionally, CCSD(T) calculations^{38,39} with aug-cc-pVD(T)Z basis sets were performed. The energy difference between the axial and equatorial conformers of PYR was also calculated at the MP2 level of theory with (aug)-cc-pCVXZ (X = D,T,Q) basis sets.

4. Results and discussion

4.1 Experimental fs DFWM spectra of pyrrolidine

The fs DFWM spectra of PYR were recorded both in the gas cell (298 K) and in the supersonic expansion. Sixteen

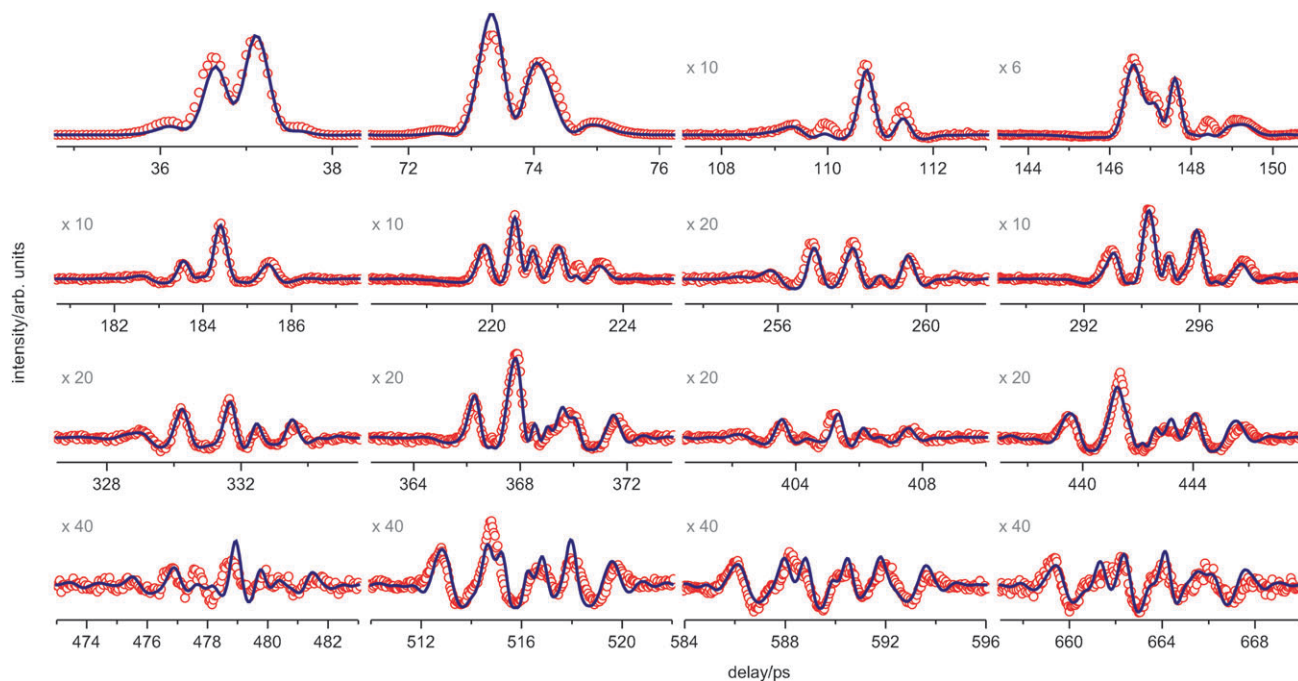


Fig. 4 The experimental fs DFWM spectrum (red) of PYR at room temperature (298 K) and the fitted simulation (blue) using the one-dimensional model for PR. The magnification factor of some weak recurrences is given.

recurrences of the room temperature spectrum and ten of the supersonic expansion spectrum are shown in Fig. 4 and 5.

One can clearly see that the supersonic jet spectrum (Fig. 5) contains a permanent signal component, which results in the negative signal modulations (relative to the background level). This occurs at higher laser intensity, which had to be employed to increase the signal under the conditions of the supersonic expansion. A very small permanent signal component is present in the cell spectrum as well. This can be recognized on the late recurrences, which are of rather small intensity (Fig. 4, $\times 20$ and $\times 40$). It can be explained by non-linear field effects, formation of an ion grating or a plasma and additional scattering thereof.^{40,41} In the first approximation these high field effect can be satisfactorily described by means of a local

field oscillator,^{28,42} which was also included in the simulation procedure.²⁸

The shapes of the rotational recurrences of the experimental spectra appear to be much more complex than those of a single rigid molecule. Therefore the first attempt to explain the experimental observations was based on the assumption that the spectra result from a mixture of two conformers, axial and equatorial, as identified in previous studies.^{6,13,14,17} As shown in Fig. 5 (green) the spectrum measured under supersonic expansion conditions can be satisfactorily fitted with two structures. The obtained rotational constants A and B (Table 1) are in good agreement (within their error bars) with the ones assigned to the axial and equatorial conformers in previous MW studies.^{14,17,18} Since PYR is a nearly oblate top,

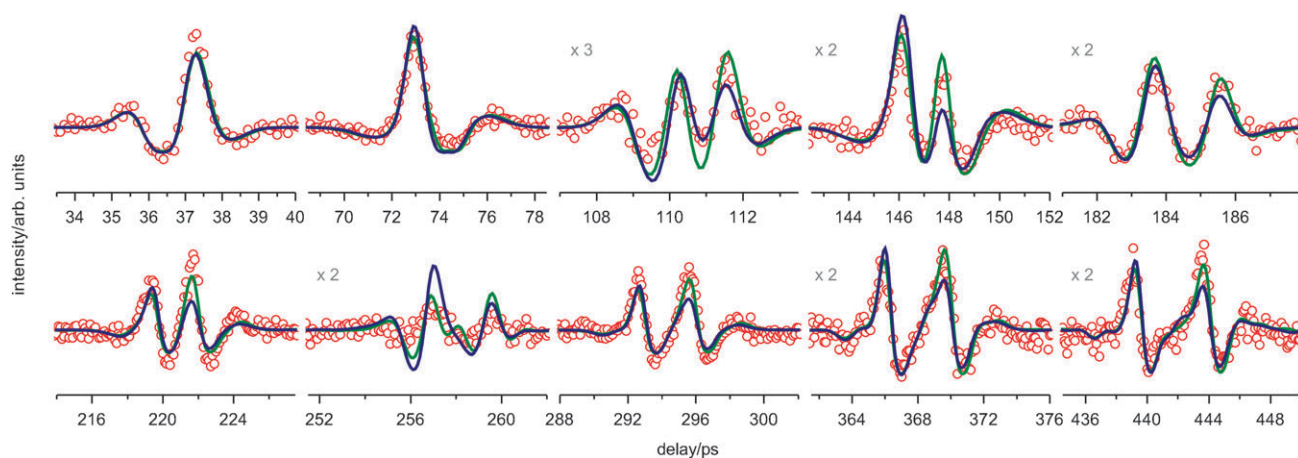


Fig. 5 The experimental fs DFWM spectrum (red) of PYR measured under supersonic expansion and the fitted simulations: green—using only 2 conformers, blue—using the pseudorotational model with parameters taken from the fit of the room-temperature spectrum. The magnification factor of some weak recurrences is given.

Table 1 Rotational constants and relative population of the axial (ax) and equatorial (eq) conformers of PYR

	Supersonic expansion ^a		Cell ^b		MW spectroscopy ¹⁸	
	eq	ax	eq	ax	eq	ax
A/GHz	6.864(5)	6.837(5)	6.866(4)	6.835(4)	6.864704(6)	6.834536(8)
B/GHz	6.788(5)	6.680(5)	6.787(4)	6.682(4)	6.791908(5)	6.677856(8)
C/GHz	3.9004 ^c	3.888062 ^c	3.895 ^c	3.895 ^c	3.9004(42)	3.888062(8)
Rotational <i>T</i> /K	66(9)		298 ^c		10	
Relative population (ax/eq)	1.6(3)		0.9 ^d		< 1.0	

^a Fitted using two conformers. ^b Fitted using the pseudorotational model; the equatorial and axial conformers correspond to the first and second pseudorotational levels (see Fig. 3). ^c Fixed in the fit. ^d Calculation based on the obtained pseudorotational potential.

the fs DFWM signal is only slightly sensitive to the rotational constant *C*. Therefore, this constant was fixed in all fits.

However, the two conformers fit yields one inconsistency, namely, that the axial conformer has a greater contribution to the simulated spectrum than the equatorial one (Table 1). This indicates an energetic preference of the axial conformer over the equatorial one, which is in qualitative disagreement to the assignment reported in the literature.¹⁴

The room temperature spectrum of pyrrolidine can in no way be reproduced by a simulation using only the axial and equatorial conformers (Fig. 6). As was discussed above this is evidence that the barrier for pseudorotation is not very high—presumably below 1000 cm⁻¹—since the signals of more than two structures are superimposed in the room temperature spectrum.

4.2. Vibrational analysis in the low frequency region

In order to gain insights into the experimental spectra we proceed with the identification of vibrations that are populated at room temperature and consequently contribute to the spectrum.^{30,31} The infrared and Raman spectra of PYR were reported by Billes *et al.*⁹ and El-Gogary *et al.*¹⁰ The normal mode assignment of the spectral lines was based on scaled quantum mechanical force fields.^{6,9,10} The lowest frequency reported by Billes *et al.*⁹ at 65 cm⁻¹ in the infrared spectrum (gas phase) and 71 cm⁻¹ in the Raman spectrum

(liquid) was attributed to PR.⁶ El-Gogary *et al.*¹⁰ measured the infrared and Raman spectra of liquid PYR. The lowest frequency they reported was 162 cm⁻¹, which was not detected by Billes and coworkers.⁹ This mode was assigned to an out-of-plane twist of the ring, which is commonly attributed to PR.^{1,32} The next higher frequency of 299 cm⁻¹ reported in both works^{9,10} was assigned to the ring bending mode, in other words to ring inversion. All other frequencies were measured to be higher than 580 cm⁻¹ and therefore they are omitted from our discussion. The main conclusion from this analysis is that only two vibrations assigned to PR and ring inversion may have an influence on the room temperature fs DFWM spectrum. However, in the following, we will consider only PR on the ground state of the ring inversion vibration. This can be justified by two arguments. The first one is that the population of the first excited ring inversion state (299 cm⁻¹) at room temperature amounts to only about 24% of the ground state. The second argument is that the pseudorotational motion on the first excited ring inversion state should not differ too much from the one in the ground state, since the barrier to ring inversion is rather high so that this vibration at the bottom of its potential minima may be considered as harmonic, which means that the ring puckering amplitude *q* (see eqn (3)) remains almost the same in the ground and the first excited state of ring inversion. Therefore, the contribution of the state at 299 cm⁻¹ is very similar to that of the ground state, but much weaker in intensity and thus should affect mainly amplitude of the spectrum, but not its structure.

4.3. Quantum chemistry calculations

The STQN method³⁶ was applied for optimization of 21 and 19 points along the pseudorotational path of PYR with the aug-cc-pVDZ basis set at the B3LYP and MP2 levels of theory, respectively. Additionally, the 3 points STQN optimization was carried out at the MP2 level of theory using the aug-cc-pVTZ basis set. The obtained geometries were further used for single point CCSD(T)/aug-cc-pVTZ calculations. The pseudorotational angle ϕ and the maximum puckering amplitude *q* (see eqn (3)) were constructed for each calculated structure using the procedure described by Cremer and Pople³³ (for the dependence of *q* on ϕ see Fig. S1 of Supp. Inf.). The calculated potential energy along the pseudorotational path is depicted in Fig. 7. Despite the shift of the potentials both methods yield very similar barrier heights with the aug-cc-pVDZ basis set, namely 318 cm⁻¹ (B3LYP) and 307 cm⁻¹ (MP2). The MP2 optimization with aug-cc-pVTZ basis set and subsequent single point CCSD(T) calculations

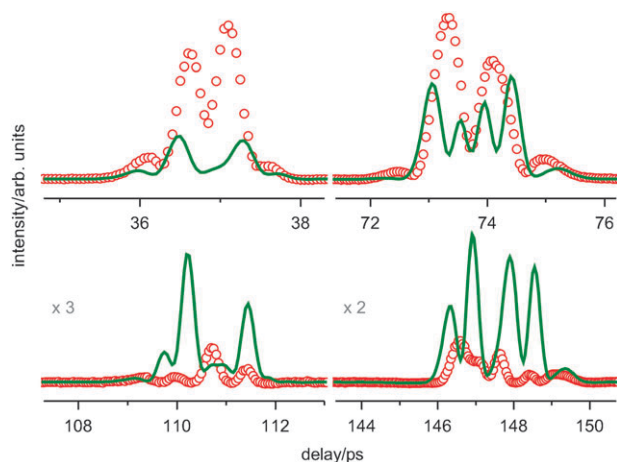


Fig. 6 The first four recurrences of fs DFWM spectrum of pyrrolidine at room temperature: red—experimental, green—fitted simulation by only two conformers: axial and equatorial, the rotational constants are taken from microwave spectroscopy.¹⁸

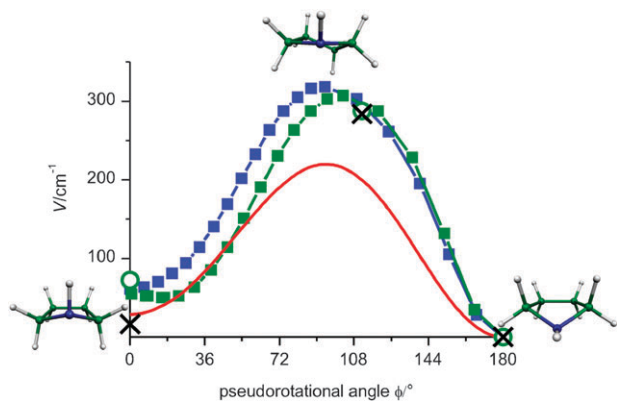


Fig. 7 Potential energy of PR: calculated using aug-cc-pVDZ at B3LYP (blue) and MP2 (green squares). The MP2/aug-cc-pVTZ calculations are shown by green circles. Single point CCSD(T)/aug-cc-pVTZ calculations on the MP2/aug-cc-pVTZ geometries are shown by black crosses. The potential obtained from the fitted simulation of the fs DFWM cell spectrum at room temperature is plotted in red. The structures shown are those optimized at the B3LYP level.

give a smaller value of about 285 cm^{-1} . The structure with the highest energy on the pseudorotational path at B3LYP/aug-cc-pVDZ corresponds to the pseudorotational angle of 94° and is the twisted form (Fig. 7, top). The energetically highest structure at MP2/aug-cc-pVDZ relates to 104° , which is very close to the envelope form at 108° , shown in Fig. 2. The MP2 calculations with a larger basis set (aug-cc-pVTZ) yield the potential maximum being shifted even further towards the equatorial conformer, at a pseudorotational angle of about 112° . Both the MP2 and B3LYP methods give the equatorial conformer being stabilized by about $55\text{--}70\text{ cm}^{-1}$ with respect to the axial one. It has been noted earlier that most current theoretical methods are able to reproduce the relative experimental conformer energy differences within about 100 cm^{-1} .⁴³

However, since the size of the basis set was found to be crucial for the energy calculation,⁶ we have determined the energy difference between axial and equatorial conformers at different basis sets and levels of theory (see Table 2, Fig. S2 of ESI†).

The MP2 calculations with larger basis sets progressively favor the equatorial form, converging at a value of about 90 cm^{-1} (Fig. S2 of the ESI†). The CCSD(T) optimization with the aug-cc-pVDZ basis set indicates a significantly smaller stabilization (only by 7 cm^{-1}) of the equatorial conformer

Table 2 The energetic parameters of pseudorotation in pyrrolidine

	$\phi_{\text{max}}/^\circ$	$V_{\text{max}}/\text{cm}^{-1}$	$\Delta V_{\text{ax-eq}}/\text{cm}^{-1}$
Fitted simulation	94.5(2)	220(20)	29(10)
B3LYP/aug-cc-pVDZ	94	318	61
MP2/aug-cc-pVDZ	104	307	55
MP2/aug-cc-pVTZ	112	288	72
MP2/aug-cc-pVQZ	—	—	84
CCSD(T)/aug-cc-pVDZ	—	—	7
CCSD(T)/aug-cc-pVTZ ^a	112 ^a	284	17

^a Single point calculations on geometries optimized at MP2/aug-cc-pVTZ.

over the axial one. This energetic preference became 17 cm^{-1} at single point CCSD(T)/aug-cc-pVTZ calculations, carried out on the MP2/aug-cc-pVTZ geometries.

According to the MP2 calculations with the aug-cc-pVDZ basis set (Fig. 7), the energy minimum on the left side of the barrier does *not* correspond to the axial form (0° , C_s symmetry, envelope), but rather to the pseudorotational angle of 18° (C_1 symmetry, twist). This outcome of the MP2 calculations was also reported by Carballeira *et al.*⁶ This is not the case when larger basis sets are used (Fig. S2 of the ESI† starting from aug-cc-pCVTZ), giving the left minimum to be exactly at the pseudorotational angle of 0° . However the lowest frequency of 16 cm^{-1} indicates that this minimum is rather flat.

The calculated rotational constants A and B are shown in Fig. 8. They are systematically lower than those obtained in MW studies. Thus, both theoretical methods, MP2 and B3LYP, overestimate the bond lengths at the aug-cc-pVDZ basis set. An enlargement of the basis set increases the magnitude of rotational constants, whereas consideration of higher order correlation and anharmonic effects in calculations tends to decrease it (see Table S2 of the ESI† and ref. 44). Thus, one can expect a better agreement between calculated and experimental values when larger basis sets are used and higher order correlation along with anharmonic effects are taken into account.

Additionally we calculated the barrier for ring inversion (the structure with a planar ring) using the aug-cc-pVDZ basis set at the B3LYP and MP2 levels of theory. The calculations yield the values of 1422 cm^{-1} (B3LYP) and 1634 cm^{-1} (MP2). These results are in agreement with those reported by Carballeira *et al.*⁶ Thus the barrier for ring inversion in PYR is indeed about five times larger than that for PR.

4.4 Fitted simulation of the fs DFWM spectra with consideration of pseudorotation

The one-dimensional model for PR was incorporated into the simulation of the fs DFWM spectrum as described heretofore. In order to obtain an initial guess of the rotational constants we have scaled the calculated dependencies of rotational constants (Fig. 8) by normalizing their values at 0 and 180°

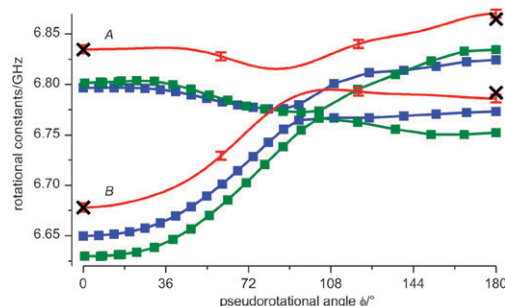


Fig. 8 Rotational constants A and B of PYR as functions of the pseudorotational angle ϕ : calculated at B3LYP/aug-cc-pVDZ (blue) and MP2/aug-cc-pVDZ (green); obtained from the fitted simulation of the fs DFWM cell spectrum at room temperature (red). MW values for the axial and equatorial conformers¹⁸ are shown with black crosses (at $\phi = 0^\circ$ and $\phi = 180^\circ$).

close to those of the axial and equatorial conformers earlier determined by fitted simulation of the supersonic jet spectrum (Table 1). The fitted simulation of the fs DFWM spectrum of pyrrolidine at room temperature is depicted in Fig. 4. It shows very good agreement with the experimental spectrum. The energetic parameters of PR obtained from both the fitted simulation and quantum chemistry calculations are collected in Table 2 (see also Table S1 of the ESI).† The pseudorotational potential found from the fit is depicted in Fig. 7 (red). It indicates that the equatorial form of PYR is stabilized by 29 cm^{-1} with respect to the axial one. This value is smaller than those calculated at the MP2 and B3LYP levels of theory ($55\text{--}92\text{ cm}^{-1}$). However, as was pointed out above, the calculated energetic stabilization of the equatorial conformer decreases when the calculations are carried out using higher levels of correlation. We believe that CCSD(T) calculations using larger basis sets might yield energetics which are in better agreement with experiment.

The energetical preference of the equatorial form over the axial one, though being small, could be understood in terms of two electronic effects: steric repulsion and hyperconjugation stabilization. It is however difficult to determine which of these two effects has the greater contribution. Natural bond orbital analysis on the HF/6-31G** wavefunctions²³ showed that the hyperconjugation interactions were greater than steric repulsion in the equatorial conformer of PYR, what consequently favored this conformer over the axial one. We also believe that the nitrogen lone pair plays an important role in the stabilization of the equatorial conformer because SCRF calculations of PYR carried out in the presence of polar solvent like water reverses the energetical order of the conformers (see Fig. S3 of the ESI).† Additionally, the enhanced dipole moment of the axial conformer as compared to the equatorial one can also explain its lower energy in polar solutions.

The fitted simulation yields the pseudorotational barrier height of 220 cm^{-1} , which is lower by about 100 cm^{-1} than that derived from the calculations with the aug-cc-pVDZ basis set at the MP2 and B3LYP levels of theory. This discrepancy however becomes smaller (64 cm^{-1}) when the MP2 method with a larger basis set, aug-cc-pVTZ, is used. The twisted conformation at the pseudorotational angle of about 94° was found to have the highest energy on the pseudorotational path. This value is very close to the one obtained in the calculation at the B3LYP level of theory.

It should be pointed out that the barrier for PR in PYR is higher than that in analogous five-membered saturated ring compounds such as cyclopentane (CYC, $<25\text{ cm}^{-1}$)⁴⁵ and tetrahydrofuran (THF, $\sim 30\text{ cm}^{-1}$).⁴⁶ This difference is related to the subtle interplay of steric repulsion and hyperconjugation, whose contributions depend sensitively on the individual molecular structure and electronic configuration. Thus, we cannot give a simple explanation for this observation. The ongoing debate on the origin of the torsional barrier of ethane demonstrates that this analysis is a demanding task.^{47,48}

The pseudorotational constant B_p was found to be $3.8 \pm 0.1\text{ cm}^{-1}$, which is also higher than those reported for CYC (2.9 cm^{-1})⁴⁵ and THF (3.2 cm^{-1}).⁴⁶

The fitted rotational constants A and B as functions of the pseudorotational coordinate are presented in Fig. 8. They show a similar dependence on the pseudorotational angle as the calculated ones, especially those of the MP2 level of theory, being however systematically shifted to higher values. The rotational constant C was fixed in the fit to the value of 3.895GHz (see the ESI)† since, as was stated above, its influence on the fs DFWM spectrum of PYR was found to be insignificant.

Using the fitted parameters we calculated the average values of rotational constants for the first two pseudorotational states, which correspond to the equatorial and axial conformers (see Fig. 3). These constants are collected in Table 1. They are in good agreement with the values obtained from the two-structure-fit of the spectrum measured under supersonic expansion and also close to those of previous MW studies.¹⁸

Next we checked whether the simulation based on the pseudorotational model can reproduce the experimental fs DFWM spectrum measured under supersonic expansion. All parameters required for the simulation, with the exception of the vibrational and rotational temperatures, were taken from the fit of the room-temperature spectrum. The resulting fitted simulation is shown in Fig. 5 (blue). Although the root mean-square deviation (chi-square) of this fit is higher than that using only two conformers (Fig. 5, green), the agreement with the experimental spectrum is still good. Moreover, the energetic preference of the equatorial conformer, as follows from the obtained pseudorotational potential (Fig. 7, red), is consistent with the finding of MW spectroscopy.¹⁴ This was not the case when only two structures have been considered (Table 1). From the fitted simulation the rotational and vibrational temperatures under supersonic expansion were found to be roughly the same and equal to about 68 K . This is very close to the value of 66 K obtained in the foregoing two-structure-fit (Table 1).

Thus, the invoked model for PR in PYR supported by *ab initio* calculations was successfully applied to the analysis and simulation of the experimental fs DFWM transients measured in a supersonic expansion and in a gas cell.

5. Conclusions

The key findings of this study may be summarized as follows. Femtosecond degenerate four-wave mixing (fs DFWM, a pump-probe rotational coherence spectroscopic scheme) was applied successfully to the characterization of pseudorotation (PR) in gaseous pyrrolidine (PYR). The structural and energetic implications of this large amplitude motion were deduced from the detailed analysis of the fs DFWM spectra at different temperatures. It turned out that a mixture of two conformers (axial and equatorial) is definitely not sufficient to explain the fs DFWM spectrum of PYR at room temperature. Hence, it is pertinent to consider the energetics and dynamics of PR in terms of its potential and the evolution of the rotational constants (structure) along the pseudorotational path. These data were obtained by means of fitted simulations of the experimental fs DFWM spectra. Thus, the equatorial conformer of PYR was found to be by $29 \pm 10\text{ cm}^{-1}$ more stable than the axial one. The barrier for PR was determined

to be $220 \pm 20 \text{ cm}^{-1}$. As a consequence we have confirmed the results of former experimental studies on the relative stability of the axial and equatorial conformers with an independent spectroscopic method. However, clear differences and significant refinements in the quantitative analysis give evidence that the energy difference between both conformers is much smaller than estimated in previous experimental studies. Moreover, for the first time we provide for PYR the pseudorotational path, including its barrier, deduced from the fitted simulation of experimental data. Our experimental findings are in satisfactory agreement with results from high level quantum chemistry calculations, namely, the stabilization of the equatorial conformer and the pseudorotational barrier were calculated to be 17 cm^{-1} and 284 cm^{-1} , respectively (single point CCSD(T)/aug-cc-pVTZ on the MP2/aug-cc-pVTZ geometries).

Thus we have with fs DFWM a method at hand that allows for the analysis of conformational transformations of molecules possessing no dipole moment even under the spectroscopically often inaccessible condition of a high temperature equilibrium. The method outlined here may be applied in addition to PR for studying the wide range of large amplitude intramolecular motions, such as the puckering inversion in four-membered rings or the internal rotation along the central bond in bithiophene- and n-butane-like molecules.

Acknowledgements

M.K. and C.R. thank the Deutsche Forschungsgemeinschaft (DFG RI 749/5-1) and the Goethe University Frankfurt for financial support and M. Gelin for lots of discussions. The authors gratefully acknowledge support by the Frankfurt Centre for Scientific Computing as well as the donations of the “Messer-Foundation” and of the “Friends and Sponsors of the Goethe University”.

References

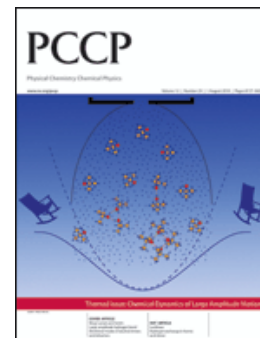
- 1 A. C. Legon, *Chem. Rev.*, 1980, **80**, 231–262.
- 2 H. L. Strauss, *Annu. Rev. Phys. Chem.*, 1983, **34**, 301–328.
- 3 D. M. Leitner, M. Havenith and M. Gruebele, *Int. Rev. Phys. Chem.*, 2006, **25**, 553–582.
- 4 J. E. Kilpatrick, K. S. Pitzer and R. Spitzer, *J. Am. Chem. Soc.*, 1947, **69**, 2483–2488.
- 5 A. F. Sax, *Chem. Phys.*, 2008, **349**, 9–31.
- 6 L. Carballeira, I. Perez-Juste and C. Van Alsenoy, *J. Phys. Chem. A*, 2002, **106**, 3873–3884.
- 7 W. K. Olson and J. L. Sussman, *J. Am. Chem. Soc.*, 1982, **104**, 270–278.
- 8 B. K. Ho, E. A. Coutsas, C. Seok and K. A. Dill, *Protein Sci.*, 2005, **14**, 1011–1018.
- 9 F. Billes and E. Geidel, *Spectrochim. Acta, Part A*, 1997, **53**, 2537–2551.
- 10 T. M. El-Gogary and M. S. Soliman, *Spectrochim. Acta, Part A*, 2001, **57**, 2647–2657.
- 11 G. V. Girichev, N. I. Giricheva, A. Bodi, P. I. Gudnason, S. Jonsdottir, A. Kvaran, I. Arnason and H. Oberhammer, *Chem.–Eur. J.*, 2007, **13**, 1776–1783.
- 12 H. Oberhammer, G. V. Girichev, N. I. Giricheva, A. V. Krasnov and U. Klingebiel, *Inorg. Chem.*, 2004, **43**, 3537–3542.
- 13 G. Pfaffertott, H. Oberhammer, J. E. Boggs and W. Caminati, *J. Am. Chem. Soc.*, 1985, **107**, 2305–2309.
- 14 W. Caminati, A. Dell’Erba, G. Maccaferri and P. G. Favero, *J. Mol. Spectrosc.*, 1998, **191**, 45–48.
- 15 G. G. Engerholm, A. C. Luntz, W. D. Gwinn and D. O. Harris, *J. Chem. Phys.*, 1969, **50**, 2446–2457.
- 16 A. K. Mamleev, L. N. Gunderova, R. V. Galeev and A. A. Shapkin, *J. Struct. Chem.*, 2004, **45**, 960–965.
- 17 W. Caminati, H. Oberhammer, G. Pfaffertott, R. R. Filgueira and C. H. Gomez, *J. Mol. Spectrosc.*, 1984, **106**, 217–226.
- 18 B. Velino, A. Millemaggi, A. Dell’Erba and W. Caminati, *J. Mol. Struct.*, 2001, **599**, 89–93.
- 19 H. Li, C. C. Miller and L. A. Philips, *J. Chem. Phys.*, 1994, **100**, 8590–8601.
- 20 G. Moruzzi, M. Kunzmann, B. P. Winnewisser and M. Winnewisser, *J. Mol. Spectrosc.*, 2003, **219**, 152–162.
- 21 T. A. Blake, E. A. Glendening, R. L. Sams, S. W. Sharpe and S. S. Xantheas, *J. Phys. Chem. A*, 2007, **111**, 11328–11341.
- 22 J. Gaudioso and W. Ho, *J. Am. Chem. Soc.*, 2001, **123**, 10095–10098.
- 23 L. Carballeira and I. Perez-Juste, *J. Chem. Soc., Perkin Trans. 2*, 1998, 1339–1345.
- 24 M. Motzkus, S. Pedersen and A. H. Zewail, *J. Phys. Chem.*, 1996, **100**, 5620–5633.
- 25 H. M. Frey, P. Beaud, T. Gerber, B. Mischler, P. P. Radi and A. P. Tzannis, *Appl. Phys. B: Lasers Opt.*, 1999, **68**, 735–739.
- 26 M. Dantus, *Annu. Rev. Phys. Chem.*, 2001, **52**, 639–679.
- 27 C. Riehn, *Chem. Phys.*, 2002, **283**, 297–329.
- 28 V. V. Matyilitsky, W. Jarzaba, C. Riehn and B. Brutschy, *J. Raman Spectrosc.*, 2002, **33**, 877–883.
- 29 V. V. Matyilitsky, C. Riehn, M. F. Gelin and B. Brutschy, *J. Chem. Phys.*, 2003, **119**, 10553–10562.
- 30 D. S. Kummli, H. M. Frey and S. Leutwyler, *J. Phys. Chem. A*, 2007, **111**, 11936–11942.
- 31 D. S. Kummli, S. Lobsiger, H. M. Frey, S. Leutwyler and J. F. Stanton, *J. Phys. Chem. A*, 2008, **112**, 9134–9143.
- 32 D. O. Harris, G. G. Engerholm, C. A. Tolman, A. C. Luntz, R. A. Keller, H. Kim and W. D. Gwinn, *J. Chem. Phys.*, 1969, **50**, 2438–2445.
- 33 D. Cremer and J. A. Pople, *J. Am. Chem. Soc.*, 1975, **97**, 1354–1358.
- 34 J. D. Lewis, T. B. Malloy, T. H. Chao and J. Laane, *J. Mol. Struct.*, 1972, **12**, 427–449.
- 35 C. Riehn, V. V. Matyilitsky and M. F. Gelin, *J. Raman Spectrosc.*, 2003, **34**, 1045–1050.
- 36 P. Y. Ayala and H. B. Schlegel, *J. Chem. Phys.*, 1997, **107**, 375–384.
- 37 M. J. Frisch, G. W. Trucks, H. B. Schlegel, G. E. Scuseria, M. A. Robb, J. R. Cheeseman, J. Montgomery, J. A. T. Vreven, K. N. Kudin, J. C. Burant, J. M. Millam, S. S. Iyengar, J. Tomasi, V. Barone, B. Mennucci, M. Cossi, G. Scalmani, N. Rega, G. A. Petersson, H. Nakatsuji, M. Hada, M. Ehara, K. Toyota, R. Fukuda, J. Hasegawa, M. Ishida, T. Nakajima, Y. Honda, O. Kitao, H. Nakai, M. Klene, X. Li, J. E. Knox, H. P. Hratchian, J. B. Cross, V. Bakken, C. Adamo, J. Jaramillo, R. Gomperts, R. E. Stratmann, O. Yazyev, A. J. Austin, R. Cammi, C. Pomelli, J. W. Ochterski, P. Y. Ayala, K. Morokuma, G. A. Voth, P. Salvador, J. J. Dannenberg, V. G. Zakrzewski, S. Dapprich, A. D. Daniels, M. C. Strain, O. Farkas, D. K. Malick, A. D. Rabuck, K. Raghavachari, J. B. Foresman, J. V. Ortiz, Q. Cui, A. G. Baboul, S. Clifford, J. Cioslowski, B. B. Stefanov, G. Liu, A. Liashenko, P. Piskorz, I. Komaromi, R. L. Martin, D. J. Fox, T. Keith, M. A. Al-Laham, C. Y. Peng, A. Nanayakkara, M. Challacombe, P. M. W. Gill, B. Johnson, W. Chen, M. W. Wong, C. Gonzalez and J. A. Pople, *GAUSSIAN 03, Revision C.02*, Gaussian, Inc., Wallingford CT, 2004.
- 38 J. F. Stanton, J. Gauss, M. E. Harding and P. G. Szalay, *CFOUR, Coupled-cluster techniques for computational chemistry*, a quantum-chemical program package with contributions from A. A. Auer, R. J. Bartlett, U. Benedikt, C. Berger, E. Bernholdt, Y. J. Bomble, O. Christiansen, M. Heckert, O. Heun, C. Huber, T.-C. Jagau, D. Jonsson, J. Jusélius, K. Klein, W. J. Lauderdale, D. A. Matthews, T. Metzroth, D. P. O’Neill, D. R. Price, E. Prochnow, K. Ruud, F. Schiffmann, S. Stopkowitz, J. Vázquez, F. Wang and J. D. Watts and the integral packages/MOLECULE/(J. Almlöf and P. R. Taylor)/PROPS/(P. R. Taylor)/ABACUS/(T. Helgaker, H. J. Aa. Jensen, P. Jørgensen and J. Olsen), and ECP routines by A. V. Mitin and C. van Wüllen; M. E. Harding, T. Metzroth, J. Gauss and A. A. Auer, *J. Chem. Theory Comput.*, 2008, **4**, 64.

- 39 J. F. Stanton, J. Gauss, J. D. Watts, M. Nooijen, N. Oliphant, S. A. Perera, P. G. Szalay, W. J. Lauderdale, S. A. Kucharski, S. R. Gwaltney, S. Beck, A. Balkov, D. E. Bernholdt, K. K. Baeck, P. Rozyczko, H. Sekino, C. Hober and R. J. Bartlett, *ACES II is a program product of the Quantum Theory Project*, University of Florida, pp. Integral packages included are VMOL (J. Alml and P. R. Taylor); VPROPS (P. Taylor) ABACUS; (T. Helgaker, H. J. Aa. Jensen, P. Jørgensen, J. Olsen, and P. R. Taylor). J. F. Stanton, J. Gauss, M. E. Harding and P. G. Szalay, *ACES II*.
- 40 V. G. Stavros, E. Harel and S. R. Leone, *J. Chem. Phys.*, 2005, **122**, 064301.
- 41 A. Rouzee, V. Renard, S. Guerin, O. Faucher and B. Lavorel, *J. Raman Spectrosc.*, 2007, **38**, 969–972.
- 42 V. G. Stavros and S. R. Leone, *Chem. Phys. Lett.*, 2008, **452**, 33–37.
- 43 K. B. Wiberg and Y. G. Wang, *J. Comput. Chem.*, 2004, **25**, 1127–1132.
- 44 C. Riehn, V. V. Matylitsky, W. Jarzeba, B. Brutschy, P. Tarakeshwar and K. S. Kim, *J. Am. Chem. Soc.*, 2003, **125**, 16455–16462.
- 45 L. E. Bauman and J. Laane, *J. Phys. Chem.*, 1988, **92**, 1040–1051.
- 46 D. G. Melnik, S. Gopalakrishnan, T. A. Miller and F. C. De Lucia, *J. Chem. Phys.*, 2003, **118**, 3589–3599.
- 47 F. M. Bickelhaupt and E. J. Baerends, *Angew. Chem., Int. Ed.*, 2003, **42**, 4183–4188.
- 48 Y. R. Mo and J. L. Gao, *Acc. Chem. Res.*, 2007, **40**, 113–119.

9.3 Ring-puckering motion in cyclopentene studied by time-resolved rotational coherence spectroscopy and ab initio calculations

This paper is published as part of a *PCCP* themed issue on [chemical dynamics of large amplitude motion](#)

Guest editors: David J. Nesbitt and Martin A. Suhm



Editorial

[Chemical dynamics of large amplitude motion](#)

David J. Nesbitt and Martin A. Suhm, *Phys. Chem. Chem. Phys.*, 2010

DOI: [10.1039/c0cp90051f](https://doi.org/10.1039/c0cp90051f)

Papers

[The benefits of alternation and alkylation: large amplitude hydrogen bond librational modes of alcohol trimers and tetramers](#)

R. Wugt Larsen and M. A. Suhm, *Phys. Chem. Chem. Phys.*, 2010

DOI: [10.1039/b925578h](https://doi.org/10.1039/b925578h)

[Analysis of the FASSST rotational spectrum of NCNCS in view of quantum monodromy](#)

Brenda P. Winnewisser, Manfred Winnewisser, Ivan R. Medvedev, Frank C. De Lucia, Stephen C. Ross and Jacek Koput, *Phys. Chem. Chem. Phys.*, 2010

DOI: [10.1039/b922023b](https://doi.org/10.1039/b922023b)

[Ring-puckering motion in cyclopentene studied by time-resolved rotational coherence spectroscopy and *ab initio* calculations](#)

Maksim Kunitski, Stefan Knippenberg, Maxim Gelin, Christoph Riehn, Andreas Dreuw and Bernhard Brutschy, *Phys. Chem. Chem. Phys.*, 2010

DOI: [10.1039/b925388b](https://doi.org/10.1039/b925388b)

[Periodic bond breaking and making in the electronic ground state on a sub-picosecond timescale: OH bending spectroscopy of malonaldehyde in the frequency domain at low temperature](#)

Nils O. B. Lüttschwager, Tobias N. Wassermann, Stéphane Coussan and Martin A. Suhm, *Phys. Chem. Chem. Phys.*, 2010

DOI: [10.1039/c002345k](https://doi.org/10.1039/c002345k)

[Large-amplitude vibrations of an N–H... \$\pi\$ hydrogen bonded *cis*-amide–benzene complex](#)

Chantal Pfaffen, Hans-Martin Frey, Philipp Ottiger, Samuel Leutwyler, Rafa A. Bachorz and Wim Klopper, *Phys. Chem. Chem. Phys.*, 2010

DOI: [10.1039/c002056g](https://doi.org/10.1039/c002056g)

[Vibration–rotation–tunneling states of the benzene dimer: an *ab initio* study](#)

Ad van der Avoird, Rafa Podeszwa, Krzysztof Szalewicz, Claude Leforestier, Rob van Harreveld, P. R. Bunker, Melanie Schnell, Gert von Helden and Gerard Meijer, *Phys. Chem. Chem. Phys.*, 2010

DOI: [10.1039/c002653k](https://doi.org/10.1039/c002653k)

[Dissociation of nitric acid at an aqueous surface: Large amplitude motions in the contact ion pair to solvent-separated ion pair conversion](#)

Shuzhi Wang, Roberto Bianco and James T. Hynes, *Phys. Chem. Chem. Phys.*, 2010

DOI: [10.1039/c002299n](https://doi.org/10.1039/c002299n)

[Vibrational dynamics around the conical intersection: a study of methoxy vibrations on the \$^2X\tilde{E}\$ surface](#)

Jayashree Nagesh and Edwin L. Sibert, *Phys. Chem. Chem. Phys.*, 2010

DOI: [10.1039/c002593c](https://doi.org/10.1039/c002593c)

[Rotational study of carbon monoxide isotopologues in small \$^4\text{He}\$ clusters](#)

P. L. Raston, Y. Xu, W. Jäger, A. V. Potapov, L. A. Surin, B. S. Dumesch and S. Schlemmer, *Phys. Chem. Chem. Phys.*, 2010

DOI: [10.1039/c0cp00193g](https://doi.org/10.1039/c0cp00193g)

[Simulating ligand-induced conformational changes in proteins using a mechanical disassembly method](#)

Juan Cortés, Duc Thanh Le, Romain Iehl and Thierry Siméon, *Phys. Chem. Chem. Phys.*, 2010

DOI: [10.1039/c002811h](https://doi.org/10.1039/c002811h)

[Molecular dynamic simulations of OH-stretching overtone induced photodissociation of fluorosulfonic and chlorosulfonic acid](#)

Priyanka Gupta, Joseph R. Lane and Henrik G. Kjaergaard, *Phys. Chem. Chem. Phys.*, 2010

DOI: [10.1039/c003073m](https://doi.org/10.1039/c003073m)

[Vibrational specificity of proton-transfer dynamics in ground-state tropolone](#)

Daniel Murdock, Lori A. Burns and Patrick H. Vaccaro, *Phys. Chem. Chem. Phys.*, 2010

DOI: [10.1039/c003140b](https://doi.org/10.1039/c003140b)

[New insights into the photodynamics of acetylacetone: isomerization and fragmentation in low-temperature matrixes](#)

A. Trivella, T. N. Wassermann, J. M. Mestdagh, C. Manca Tanner, F. Marinelli, P. Roubin and S. Coussan, *Phys. Chem. Chem. Phys.*, 2010

DOI: [10.1039/c003593a](https://doi.org/10.1039/c003593a)

[Ab initio anharmonic vibrational frequency predictions for linear proton-bound complexes OC–H⁺–CO and N₂–H⁺–N₂](#)

Kasia Terrill and David J. Nesbitt, *Phys. Chem. Chem. Phys.*, 2010

DOI: [10.1039/c002774j](https://doi.org/10.1039/c002774j)

Ring-puckering motion in cyclopentene studied by time-resolved rotational coherence spectroscopy and *ab initio* calculations

Maksim Kunitski,^a Stefan Knippenberg,^a Maxim Gelin,^b Christoph Riehn,^c Andreas Dreuw^a and Bernhard Brutschy*^a

Received 2nd December 2009, Accepted 26th February 2010

First published as an Advance Article on the web 13th April 2010

DOI: 10.1039/b925388b

The ring-puckering vibration in cyclopentene was studied by rotational time-resolved femtosecond degenerate four-wave mixing (fs DFWM) spectroscopy. The fs DFWM spectra of cyclopentene were measured both in a supersonic expansion and in a gas cell at room temperature. The room temperature fs DFWM spectrum has been satisfactorily reproduced by a fitted simulation based on a one-dimensional model for the ring-puckering vibration. This has allowed for the determination of energetic parameters of the ring-puckering motion such as the energy barrier to ring inversion of $274(+12/-20)$ cm^{-1} and the equilibrium ring-puckering angle of 24.3° . The derived dependences of the rotational constants *A* and *B* on the puckering angle resemble very closely those obtained by microwave spectroscopy. In addition, previous theoretical estimates of the ring inversion barrier of cyclopentene were improved by performing high level *ab initio* calculations. Zero-point vibrational energy correction was found to be essential for an accurate evaluation of the puckering potential. Altogether, this study provides a proof-of-principle of the applicability of the fs DFWM technique for investigating large amplitude intramolecular motions.

1. Introduction

Low energy large amplitude intramolecular motions in cyclic compounds is a fundamental issue in chemistry, which has been extensively addressed by various experimental and theoretical methods over the last several decades.^{1–3} Recently, we have proposed a new experimental method for the investigation of this kind of motions. The method, based on Rotational Coherence Spectroscopy (RCS),^{4,5} was successfully applied for obtaining energetic and structural information on pseudorotation in pyrrolidine.⁶ In the present work, an application of this method for studying a ring bending vibration will be reported. In order to evaluate the accuracy of the method we have chosen the well studied five-membered ring molecule cyclopentene (CYC).

In general, *N*-membered rings have *N*-3 low frequency out-of-plane vibrations. Thus, in five-membered rings there are two such out-of-plane modes: a bend and a twist (Fig. 1, top). In saturated ring compounds such as cyclopentane and pyrrolidine these two modes are coupled, resulting in a ring motion, termed pseudorotation.⁷ Since CYC has one double bond in the ring, the twisting mode has a relatively high frequency (385 cm^{-1}).⁸ Therefore, at room temperature

mainly the bending mode, *i.e.* ring inversion, is active (Fig. 1). This property makes CYC similar to four-membered ring systems, where also only one low frequency out-of-plane mode is present. Due to this similarity, molecules like CYC were termed “pseudo-four-membered-ring” compounds. In these systems the ring bending mode is usually referred to as the ring-puckering vibration.

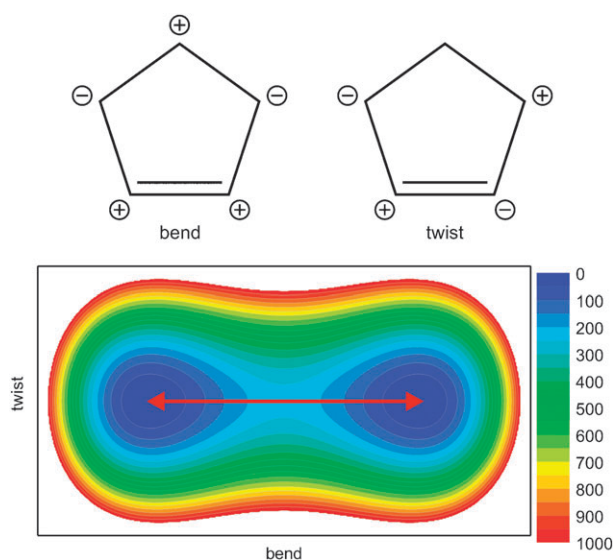


Fig. 1 The two out-of-plane skeletal modes of the cyclopentene ring and the corresponding approximate 2D potential energy surface. Scale is in cm^{-1} . The relevant ring-puckering vibration is shown by the red arrowed line. The 2D potential energy function was taken from ref. 15.

^a Institut für Physikalische und Theoretische Chemie, Goethe-Universität Frankfurt am Main, Max-von-Laue-Straße 7, 60438 Frankfurt am Main, Germany.

E-mail: brutschy@chemie.uni-frankfurt.de; Fax: +49 (0)69 798 29560; Tel: +49 (0)69 798 29424

^b Department of Chemistry, Technische Universität München, Lichtenbergstraße 4, 85747 Garching, Germany

^c Department of Chemistry, Technische Universität Kaiserslautern, Erwin-Schrödinger-Straße 52, 67663 Kaiserslautern, Germany

RCS^{4,5} allows for the time-domain observation of the coherent rotation of a molecular ensemble. In the present study a particular implementation of RCS, namely femto-second degenerate four-wave mixing (fs DFWM),^{9–12} is utilized. Being a Raman-type spectroscopy, fs DFWM has proven to be a powerful tool for the investigation of the structure of large molecular systems at thermal equilibrium, even if they do not possess a permanent dipole moment.^{13,14}

In this work the fs DFWM spectra of CYC recorded both in a gas cell and in a supersonic expansion will be reported. It will be shown that the room temperature fs DFWM spectrum can be reproduced by a fitted simulation based on a one-dimensional model for the ring-puckering vibration. The obtained results on this large amplitude vibration are compared with experimental and theoretical data on CYC available in the literature. In addition, a high level quantum chemical investigation of the ring-puckering minimum energy pathway in CYC has been carried out.

The paper is organized as follows. Chapter 2 reviews the available data on the ring-puckering vibration in CYC. Subsequently, the theoretical framework for the treatment of the ring-puckering motion and simulation of fs DFWM spectra is presented (chapter 3). Chapter 4 describes the experimental setup and provides necessary details about our quantum chemical calculations. The paper proceeds with the discussion of the experimental and theoretical results (chapter 5). The main conclusions are summarized in chapter 6.

2. Previous studies on cyclopentene

2.1 Experimental works

Being a representative molecule of “pseudo-four-membered-ring” compounds, CYC was thoroughly studied by different experimental and theoretical methods.^{15–36} The ring bending mode is usually considered as a one-dimensional vibration along a coordinate that corresponds to either a dihedral angle φ or a distance x , as shown in Fig. 2.

It is known that the ring of CYC is puckered by an angle of about 22–30° in its equilibrium geometry (Fig. 2). Therefore, the ring-puckering potential is of double-minimum nature with the central barrier corresponding to the planar ring structure (Fig. 1).

The ring-puckering potential can be derived from the vibrational pattern, measured either directly by means of far-infrared spectroscopy¹⁸ or as combination and difference bands in the mid-infrared region.¹⁹ In this way the energy barrier to ring inversion was found to be 232–244 cm⁻¹ and the puckering

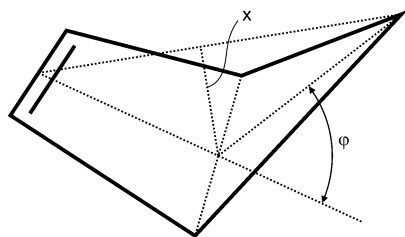


Fig. 2 Two geometric parameters, an angle φ and a distance x , which are usually used for the description of the ring-puckering vibration.

angle of the equilibrium structure of 22.1–23.3° was obtained. A two-dimensional analysis of the far-infrared and Raman spectra of CYC gave a barrier of 232 cm⁻¹ and an equilibrium puckering angle of 26°.¹⁵

Microwave spectroscopy (MW) is very often well suited for obtaining both energetic and structural information about out-of-plane ring vibrations. In the first MW study on CYC¹⁶ the rotational constants of the first two vibrational states of the puckering mode were determined and utilized to estimate the puckering angle (*ca.* 22°). On the basis of intensity measurements, the energies of several lower puckering vibrational states were estimated, from which an inversion barrier of 232 cm⁻¹ was deduced. Butcher *et al.*¹⁷ found for the lowest inversion doublets a splitting of 0.91 cm⁻¹. Using this value, the inversion barrier was estimated to be about 250–400 cm⁻¹. Scharpen²⁰ examined the coupling between the ring bending vibration and rotation and suggested a correction for the rotational constants of the two lowest vibrational states. The barrier to ring inversion was derived to be 232 ± 5 cm⁻¹, which is in excellent agreement with the results obtained in the far-infrared studies.^{15,18} Additionally, it was noted that consideration of more sophisticated potential functions in the one-dimensional ring-puckering model should not change the estimated barrier height substantially.

For the explanation of MW spectra, Lopez and co-workers³³ adopted a more complex semi-rigid vibrational Hamiltonian and considered the vibration–rotation coupling for the first two puckering states. On this basis an inversion barrier of 236 ± 5 cm⁻¹ was derived.

The molecular structure of CYC was also determined by gas-phase electron diffraction.³⁶ The equilibrium puckering angle was estimated to be 29 ± 2.5°.

Additionally, the ring-puckering motion of liquid CYC was studied by ¹³C NMR relaxation.³⁷ Comparing the exchange rate between its two equivalent bent conformations at different temperatures it was concluded that the activation energy of this process should be rather low. The bent conformation was found to have a puckering angle of 25–30°.

Thus, most of the published experimental values for the ring inversion barrier lie near 232 cm⁻¹. The proper estimation of the puckering angle that corresponds to the minimum on the potential energy surface is more difficult, since it requires some assumptions on the geometry of the molecule. The reported values for this angle are in the range from 22 to 30°.

2.2 Theoretical works

A number of theoretical studies were devoted to the structure and vibrations of CYC (see ref. 8, 31, 34, 35 and references therein). Performing extensive *ab initio* calculations on CYC, Allen and coworkers³¹ found that large basis sets and high-level treatments of electron correlation are indispensable to obtain reliable values for both the inversion barrier and the equilibrium puckering angle. Combining the results of MP4/TZ(d,p) and MP2/PZ(3d2f,2p1d) calculations, they derived a value of 235 ± 20 cm⁻¹ for the inversion barrier. However, in order to compare this calculated value with that derived experimentally, it should be corrected for zero-point vibrational energy (ZPVE) yielding a barrier height of *ca.* 260 cm⁻¹.

Their computed value for the puckering angle was 23.6° at the theoretical level of MP2/DZ(d).

Nevis *et al.*³⁴ performed molecular mechanics calculations employing the MM4 force field and reported values of 266 cm^{-1} and 24.6° for the inversion barrier and the equilibrium puckering angle, respectively. Leong and coworkers³⁵ optimized the geometry of CYC at MP2/6-31G* and obtained a puckering angle of 26.3° .

Recently Al-Saadi *et al.*⁸ compared results obtained by *ab initio* and density functional theory (DFT) methods employing various different basis sets. DFT with the B3LYP hybrid exchange–correlation functional underestimates both the barrier height ($40\text{--}80\text{ cm}^{-1}$) and the puckering angle ($19\text{--}20^\circ$) even when the relative large basis sets 6-311 + G(d,p) and cc-pVTZ are used. The small puckering angle is a result of the tendency of B3LYP to favour planar structures, which stems from an incomplete description of long-range non-bonding interactions.³⁸ Nevertheless, B3LYP is usually considered as being superior to MP2 in predicting geometrical parameters like bond lengths and angles, which are not influenced by non-bonding interactions.^{38,39} Indeed, as will be shown below, rotational constants calculated at B3LYP/cc-pVTZ optimized geometries resemble most closely those obtained experimentally when constraints are imposed on the puckering angle.

In the same work Al-Saadi and co-workers⁸ reported MP2/cc-pVTZ calculated values of 247 cm^{-1} and 26° for the ring inversion barrier and the equilibrium puckering angle of CYC, respectively. It turned out that the value of 247 cm^{-1} was obtained after taken into account the complete ZPVE correction (see Table 1 below). However, for proper comparison of theoretical and experimental barriers the contribution of the ring-puckering mode should be removed from the complete ZPVE correction,⁴⁰ which will increase the value above by about 90 cm^{-1} , yielding 337 cm^{-1} , which is about 100 cm^{-1} higher than the experimentally derived barrier.

To finally yield converged theoretical *ab initio* results for the barrier to ring inversion and the equilibrium puckering angle of CYC, we have performed a new set of quantum chemical calculations far beyond the level of previously reported computations.

3. Theoretical framework

3.1 Ring-puckering vibration

The ring-puckering vibration in “pseudo-four-membered-ring” compounds is usually treated as a one-dimensional motion in a double minimum potential using a model Hamiltonian of the following form:^{18,41}

$$H_V(\varphi) = -B_\varphi P_\varphi^2 + V(\varphi), \quad V(\varphi) = a\varphi^4 - b\varphi^2 \quad (1)$$

Here B_φ is the puckering kinetic constant, which is, for the sake of simplicity, treated here as being independent of the puckering angle φ , and $V(\varphi)$ is the double minimum ring-puckering potential. It is more convenient, however, to transform Hamiltonian (1) to the reduced form:^{18,42}

$$H_V(Z) = A_Z(-P_Z^2 + Z^4 - B_Z Z^2) \quad (2)$$

The relationship between the puckering angle φ and the reduced puckering coordinate Z is given by the expression:

$$Z = \left(\frac{A_Z}{B_\varphi}\right)^{1/2} \varphi \quad (3)$$

The barrier to ring inversion V_{barrier} and the equilibrium puckering coordinate Z_{min} can be easily evaluated from the ring-puckering potential in Hamiltonian (2):

$$Z_{\text{min}} = \sqrt{\frac{B_Z}{2}}, \quad V_{\text{barrier}} = A_Z \frac{B_Z^2}{4} \quad (4)$$

The Schrödinger equation corresponding to Hamiltonian (2) can be solved numerically in the harmonic oscillator basis set.^{42,43} The solution provides both the energy levels E , and the wavefunctions $\Psi_\nu(Z)$ of the ring-puckering vibration. The averaged molecular property M_ν (e.g., a rotational constant) in the ring-puckering state ν is evaluated as:

$$M_\nu = \langle \Psi_\nu^*(Z) | M(Z) | \Psi_\nu(Z) \rangle \quad (5)$$

3.2 Simulation of an fs DFWM spectrum

Simulation of an fs DFWM spectrum of a single species in the semi-rigid rotor approximation has been previously discussed in detail.^{13,44,45} Briefly, a typical time-resolved fs DFWM spectrum of a single species consists of equidistant double-peak signals called transients or recurrences. The period of such a transient sequence is closely related to rotational constants (structural parameters) of the molecule under investigation. Quantitative simulation of the fs DFWM spectrum, however, requires the rotational Raman spectrum to be calculated.⁴⁵ This is usually done within a semi-rigid rotor approximation using a Watson A reduction of the rotational Hamiltonian.⁴⁶

In case of a large amplitude intramolecular motion such as the ring-puckering vibration the semi-rigid rotor approximation fails and a more general, vibration–rotation Hamiltonian should be considered:^{41,47,48}

$$H = H_R + H_V + H_{RV} \quad (6)$$

H_V is a vibration Hamiltonian of a large amplitude motion, H_R describes rotation of the molecule as a whole, and H_{RV} is the vibration–rotation coupling.

Provided the spacing between the vibrational states ν is much larger than that between the rotational states of H_R , a series of contact transformations can be applied to the non-rigid Hamiltonian (6). The so-obtained zero-order Hamiltonian for each vibrational state ν is simply given in analogy to eqn (5) as:

$$H_{R\nu}^{(0)} = \langle \Psi_\nu^*(Z) | H_R | \Psi_\nu(Z) \rangle \quad (7)$$

Subsequently, the vibration–rotation coupling can be taken into account by the centrifugal distortion (CD) perturbation term $H_{R\nu}^{\text{CD}}$, yielding the semi-rigid Watson A -reduced rotational Hamiltonian $H_{R\nu}$:⁴⁶

$$H_{R\nu} = H_{R\nu}^{(0)} + H_{R\nu}^{\text{CD}} \quad (8)$$

Two Watson quartic CD constants⁴⁶ Δ_J and Δ_{JK} turned out to be sufficient for the simulation of an fs DFWM spectrum of a

nearly symmetric top.¹³ In case of CYC the CD constants can be expressed as a sum of two terms, one of which originates from the ring puckering vibration while another one stems from all residual vibrations. Apparently, only the former term is different for each ring-puckering state ν and can be expressed in the instantaneous principal axes and the representation I' as follows:^{49,50}

$$A_J^{\nu} = -\frac{1}{8}(\tau_{bbbb}^{\nu} + \tau_{cccc}^{\nu}), \Delta_{JK}^{\nu} = \frac{3}{8}(\tau_{bbbb}^{\nu} + \tau_{cccc}^{\nu}) - \frac{1}{4}(\tau_{aabb}^{\nu} + \tau_{aacc}^{\nu} + \tau_{bbcc}^{\nu}) \quad (9)$$

Here the Kivelson and Wilson quartic centrifugal distortion constants⁵¹ are determined as:

$$\tau_{\alpha\alpha\beta\beta}^{\nu} = 4 \sum_{\nu \neq \nu'} \frac{\langle R_{\alpha} \rangle_{\nu\nu'} \langle R_{\beta} \rangle_{\nu\nu'}}{E_{\nu} - E_{\nu'}} \langle R_{\alpha} \rangle_{\nu\nu'} = \langle \Psi_{\nu}^*(Z) | R_{\alpha} | \Psi_{\nu'}(Z) \rangle$$

$$\alpha, \beta = a, b, c$$

and R_a , R_b , R_c are the rotational constants A , B and C , respectively.

The two lowest states of the ring-puckering vibration of CYC are separated by 0.91 cm^{-1} (27 GHz), which is already comparable with the energy spacing between the rotational states.^{17,33} In this case the vibration–rotation coupling cannot be taken into account by only the CD perturbation term. Several approaches were proposed for the treatment of the general vibration–rotation problem.^{47,48,52} In this work, we follow the suggestion by Sharpen²⁰ and account for the vibration–rotation coupling between the two lowest ring-puckering states by correcting the corresponding rotational constants.

In a simulation of a fs DFWM spectrum, each ring-puckering state ν is associated with a semi-rigid rotor described by Hamiltonian (8). Each ν -rotor has its unique set of averaged rotational constants, CD constants, and polarizabilities, which are used to calculate the rotational Raman spectrum for a specific ν . The complete spectrum is constructed as a superposition of the spectra of all vibrational states weighted by their Boltzmann populations. Ultimately, the rotational Raman spectrum is utilized for calculation of a fs DFWM spectrum.⁴⁵

The vibrationally averaged values of the rotational constants for each puckering state were evaluated by eqn (5). This requires the knowledge of the dependences of the rotational constants on the puckering coordinate, which were expressed in terms of a Taylor's expansion:

$$R_x(Z) = \sum_{n=0}^2 R_x^{(n)} Z^{2n}$$

Because the vibration is symmetric with respect to the puckering coordinate, only the coefficients at even powers of Z are non-zero. Since it is quite difficult to visualize the limits within which the coefficients $R_x^{(n)}$ should be varied in the fit, we used the values of $R_x(Z)$ at $Z = 0.0$, 1.5 and 3.0 as fitting parameters and re-calculated them into $R_x^{(n)}$ afterwards.

Another molecular property, which is necessary for the simulation of a fs DFWM spectrum, is the polarizability tensor. It was shown previously⁴⁴ that a fs DFWM signal is mainly sensitive to the anisotropy of the polarizability tensor,

which can be parameterized by a single parameter. For CYC this parameter is almost independent of the puckering angle. Therefore, the same value of the parameter was used in simulations for all puckering states.

In total, fourteen variable parameters were used in the fit of the experimental fs DFWM spectrum of CYC at room temperature. The global minimum of the chi-square function in this multi-dimensional parameter space was searched by means of the Differential Evolution minimization algorithm developed by R. Storn and K. Price.⁵³ The MINUIT optimization package⁵⁴ was further employed for the final precise optimization in the global minimum region.

4. Methods and materials

4.1 Experimental

The femtosecond degenerate four-wave mixing spectra of CYC were recorded using an experimental setup described previously.¹³ Briefly, the laser setup consists of a Ti:sapphire oscillator (Coherent, Mira Basic), which is pumped by a frequency-doubled diode-pumped laser (Coherent, Verdi V-5), and a chirped-pulse amplification system (Quantronix, 4800 Series). The fundamental output of this femtosecond laser apparatus (wavelength of 800 nm, 1 kHz pulse repetition rate, autocorrelation of 220 fs FWHM, energy of up to $800 \mu\text{J pulse}^{-1}$) is divided into three beams: two pumps and one probe of identical linear polarization and energy. The probe pulse is delayed with respect to the pump ones by a computer controlled translational stage, which allows for scanning the time delay up to 4 ns. All three laser beams are combined in a forward boxcar arrangement in order to provide phase matching and the separation of the diffracted coherent four-wave mixing signal beam.

In the gas cell experiment the vapour pressure of CYC was kept at *ca.* 10 mbar and the temperature was 298 K.

The supersonic expansion experiments were carried out by expanding a mixture of CYC and helium adiabatically into the vacuum by means of a pulsed Even–Lavie valve⁵⁵ working at a repetition rate of 1 kHz. Stagnation and background pressures were 2 bar and 10^{-4} bar, respectively. DFWM spectra were recorded in the expansion region located at a distance of approximately 2 mm from the nozzle orifice.

CYC (=96.0%, purum grade) was obtained from Fluka and used without further purification.

4.2 Quantum chemical calculations

Sixteen different geometries of CYC with constrained puckering angles in the range between 0° and 50° have been optimized using the B3LYP/cc-pVTZ level of theory. This approach is known to provide structural results of quality comparable to that achieved at a benchmark theoretical level^{56,57} of CCSD(T).⁵⁸

Energy differences among the chosen points on the potential energy surface were accurately evaluated by a Focal Point Analysis (FPA) similar to those carried out by Allinger *et al.*,⁵⁹ Salam *et al.*⁶⁰ and Huang *et al.*,³⁹ to determine the conformational energy differences or barriers of n-butane, n-pentane, and dimethoxymethane, respectively.

The main point of a FPA is to establish convergence of conformational energy differences at the limit of both the basis set and the correlation correction.⁵⁹ This is done by extrapolating the results of single point calculations at the HF, MP2, MP3, MP4, CCSD and CCSD(T) levels and basis sets of improving quality (cc-pVXZ, X = D, T, Q) to the benchmark CCSD(T)/cc-pV ∞ Z. FPA allows for the determination of conformational energy differences with an accuracy of ~ 0.05 kcal mol⁻¹ (~ 20 cm⁻¹).^{39,60}

In addition to FPA, sixteen points along the ring-puckering coordinate were optimized at the scaled-opposite-spin second order Møller–Plesset⁶¹ (SOSMP2) level of theory with Dunning's cc-pVDZ basis set. The energies at these optimized structures were subsequently refined by single point calculations at the CCSD/aug-cc-pVTZ level.

In order to accurately determine the inversion barrier and the minimum puckering angle from the calculated discrete ring-puckering potentials a number of points around the minimum were interpolated by a symmetric polynomial function with the highest power of eight.

Furthermore, MP2, MP4 and CCSD optimizations of the planar and puckered equilibrium configurations of CYC were performed using different basis sets. Optimized geometries were subsequently used for high level single point energy calculations.

The ZPVE correction for the evaluation of the ring-puckering potential was calculated by excluding the contribution of the ring-puckering vibration from the complete ZPVE correction.⁴⁰

The quantum chemical calculations were performed using the following program packages: Gaussian03⁶² (DFT, FPA), Q-Chem 3.0⁶³ (SOSMP2⁶¹) and MOLPRO⁶⁴ (MP2, MP4, CCSD).

5. Results and discussion

5.1 Quantum chemical calculations

The puckering potential of CYC obtained by FPA is shown in Fig. 3. The barrier to ring inversion was found to be 194 cm⁻¹ without taking ZPVE correction into account. However inclusion of the ZPVE correction calculated at the B3LYP/cc-pVTZ level of theory yields a barrier height of 229 cm⁻¹, which agrees very favourably with the obtained previously experimental value of 232 ± 5 cm⁻¹.^{15,18} The puckering angle that corresponds to the equilibrium structure, φ_{\min} , was determined to be 24.4° ($x_{\min} = 0.244$ Å).

In addition to FPA, the ring-puckering potential of CYC was also evaluated by single point CCSD/aug-cc-pVTZ calculations at SOSMP2/cc-pVDZ optimized geometries. Subsequently, the potential was corrected by ZPVE calculated at the SOSMP2/cc-pVDZ level, which results in an inversion barrier of 210 cm⁻¹ (Fig. 3, blue). If the ZPVE correction is not taken into account, the barrier height is about 23 cm⁻¹ smaller. These calculations yield an equilibrium puckering angle of 24.4°, which is exactly the value that was also found by FPA. Due to the different nature of the two employed methods, this perfect agreement is rather surprising and puts thus some confidence in that value.

To further corroborate the above findings, the planar and puckered structures of CYC have been optimized at different levels of theory and basis sets. High level single point

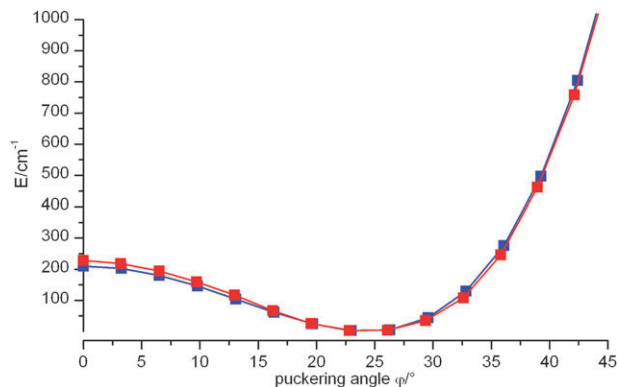


Fig. 3 Puckering potential of CYC obtained by FPA at B3LYP/cc-pVTZ optimized geometries (red) and the single point CCSD/aug-cc-pVTZ calculations at the geometries optimized with SOSMP2/cc-pVDZ (blue).

calculations (at the CCSD/aug-cc-pVTZ level of theory) were later applied to these geometries in order to accurately evaluate the barrier to ring inversion. The obtained results are collected in Table 1.

According to our results, inclusion of the ZPVE correction increases the ring inversion barrier by about 22–53 cm⁻¹, depending on the level of theory and the basis set employed. Thus, a ZPVE correction is indeed indispensable for an accurate evaluation of the conformational energy difference.

In summary, the best agreement with the experimentally determined value for the ring inversion barrier (232 ± 5 cm⁻¹)^{15,18,20} was found employing FPA at B3LYP optimized geometries (229 cm⁻¹) and by using CCSD/aug-cc-pVDZ for geometries and energies (243 cm⁻¹). Furthermore, these two methods predict the same value of 24.4° for the equilibrium puckering angle.

According to B3LYP/cc-pVTZ and SOSMP2/cc-pVDZ geometries the relationship between the puckering coordinate x and the puckering angle φ is linear with a coefficient of about 0.01 Å per degree.

On the basis of the B3LYP/cc-pVTZ and SOSMP2/cc-pVDZ structures the puckering kinetic constant B_φ (see eqn (1)) has been calculated as a function of the puckering angle (Fig. 4).⁴⁷ The constant B_φ does not change significantly in the region below 30°, where the molecule is mainly localized during the ring-puckering vibration. Therefore, the assumption that B_φ does not depend on the puckering angle in the one-dimensional ring-puckering Hamiltonian (1) is plausible. The average value of B_φ is taken to be 5.3×10^3 cm⁻¹.

5.2 fs DFWM spectra of cyclopentene

5.2.1 Supersonic expansion. The fs DFWM spectra of CYC were recorded both in a gas cell (298 K) and in a supersonic expansion at lower temperature. Seven recurrences of the supersonic expansion spectrum are shown in Fig. 5. The recurrences can be successfully reproduced by a fitted simulation using only one structure (Fig. 5, blue). The corresponding simulation parameters are collected in Table 2. Since CYC is a nearly oblate top, the fs DFWM signal is only slightly sensitive to the rotational constant C . Therefore, this constant was fixed in all fits to the values obtained by MW.³³

Table 1 Energetic and structural parameters of cyclopentene calculated at different levels of theory and basis sets

Geometry	$\varphi_{\min}/^\circ$	$x_{\min}/\text{\AA}$	SP	$E_{\text{barrier}}/\text{cm}^{-1a}$	$\Delta\text{ZPVE}/\text{cm}^{-1c}$	$\frac{1}{2}E_{\text{puck}}/\text{cm}^{-1d}$	$E_{\text{barrier}}^*/\text{cm}^{-1b}$
B3LYP/cc-pVTZ	24.4	0.244	FPA	194	—	—	229
SOSMP2/cc-pVDZ	24.4	0.244	CCSD/aug-cc-pVTZ	187	—	—	210
MP2/aug-cc-pVDZ	26.9	0.263	—	318	-38	+91	371
MP2/aug-cc-pVTZ	26.6	0.258	CCSD/aug-cc-pVTZ	164	—	—	217
			—	290	-43	+91	338
MP2/cc-pVTZ	26.2	0.255	CCSD/aug-cc-pVTZ	169	—	—	217
			—	290	-43	+91	338
MP4/aug-cc-pVDZ	25.6	0.251	—	251	-56	+93	288
			CCSD/aug-cc-pVTZ	180	—	—	217
CCSD/aug-cc-pVDZ	24.4	0.239	—	212	-54	+85	243
			CCSD/aug-cc-pVTZ	184	—	—	215

^a Without the ZPVE correction. ^b With the ZPVE correction. ^c The complete ZPVE correction (all normal modes are considered). ^d The contribution of the ring-puckering vibration to the ZPVE correction.

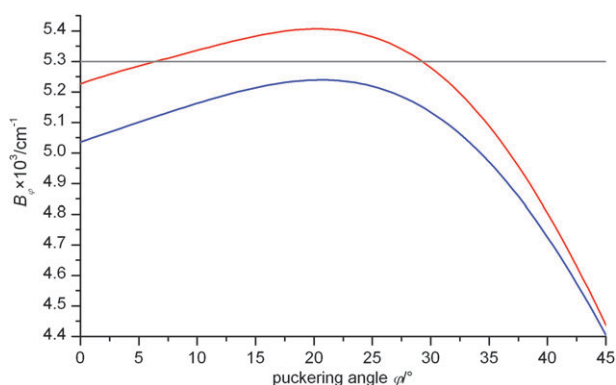


Fig. 4 The calculated dependence of the puckering kinetic constant B_φ on the puckering angle φ : red-B3LYP/cc-pVTZ geometries, blue-SOSMP2/cc-pVDZ geometries. The average value of B_φ , $5.3 \times 10^3 \text{ cm}^{-1}$ is shown by the horizontal line.

The rotational constants A and B obtained from the one-structure fit are slightly lower than those found by MW for the first two vibrational states of the puckering mode of CYC (see Table 5 below), but higher than those from the highest puckering states. The most probable explanation for this finding is that already under the conditions of a supersonic

Table 2 Parameters of two different fitted simulations of the fs DFWM spectrum of CYC recorded under supersonic expansion

	1 structure fit	5 structures fit
A/GHz	7.290(4)	— ^a
B/GHz	7.225(4)	— ^a
C/GHz	3.9494 ^a	— ^a
φ/rad	0.5(+0.7/-0.2)	0.6(+0.5/-0.2)
Δ_J/kHz	1.7(9)	1.9(9)
Δ_{JK}/kHz	-2(6)	0(6)
T_{rot}/K	114(10)	119(10)
T_{vib}/K	—	121(15)

^a Fixed to the MW values (see Table 5).

expansion not only the lowest two but more puckering states are populated.

In order to test this assumption a fit was performed taking the five lowest vibrational puckering states into account. The rotational constants were taken from MW spectroscopy³³ and were fixed in the fit. The contribution of each puckering state to the complete spectrum was calculated from its population assuming thermal equilibrium, *i.e.* a Boltzmann distribution. The distribution was characterized by a single vibrational temperature, which was varied in the fit. The puckering state energies were taken from far-infrared and Raman vibrational spectroscopy studies.¹⁵

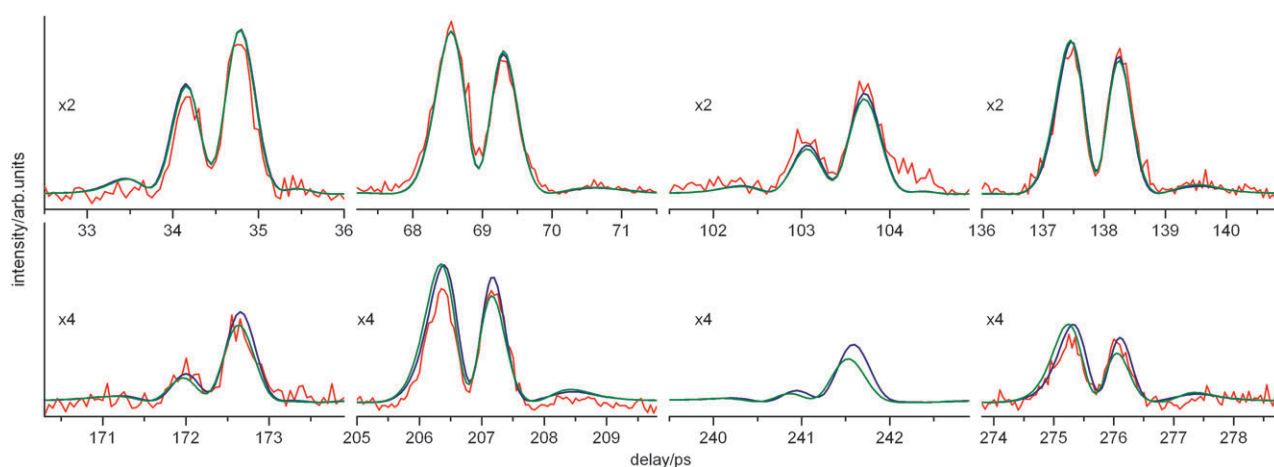


Fig. 5 fs DFWM spectra of cyclopentene under supersonic expansion: red—experimental, blue—fitted simulation using one structure, green—fitted simulation using five ring-puckering states (structures) with rotational constants taken from MW (see Table 5).

The resulting fitted simulation is shown in Fig. 5 (green). It is in good agreement with the experimental spectrum. Thus, indeed, several puckering states contribute to the supersonic expansion spectrum of CYC. But according to the obtained vibrational temperature of 121 K, the first two nearly degenerate puckering states have a dominant contribution of 81% to the fs DFWM spectrum.

The rotational temperature was found to be similar to the vibrational one. This can be justified⁶⁵ by the fact that the spacing between the puckering states is rather small, *i.e.* 25–130 cm^{-1} .¹⁵ The same was observed for pyrrolidine in a supersonic expansion experiment.⁶

5.2.2 Gas cell. Twenty recurrences of the fs DFWM spectrum of CYC measured in the gas cell at room temperature are shown in Fig. 6. This experimental spectrum cannot be reproduced by a fitted simulation using only one structure, as for the spectrum measured under supersonic expansion, which is not unexpected since at room temperature several ring-puckering vibrational states have significant population. Therefore, we carried out the fitted simulation based on a one-dimensional model for the ring-puckering vibration. Seven ring-puckering states of the ground state of the twist mode together with the lowest ring-puckering doublet of the first excited twist state¹⁵ at 385 cm^{-1} were considered in the fit.

The fitted simulation (Fig. 6, blue) is in good agreement with the experimental fs DFWM spectrum. The parameters of the ring-puckering vibration obtained from the fit are collected in Table 3 together with the experimental data available in literature. The reduced puckering coordinate corresponding to

the minimum energy structure, Z_{\min} , was found from the fit to be $1.769 + 0.009/-0.005$. The same value was derived in the MW study of Lopez *et al.*,³³ implying that the kinetic term of the ring-puckering Hamiltonian is independent of the puckering angle.

The experimentally derived barrier to ring inversion, V_{barrier} , of $274 + 12/-20 \text{ cm}^{-1}$ is somewhat higher than those found in the infrared and MW studies (Table 3). It should be noted, however, that of two potential parameters, Z_{\min} and V_{barrier} , only the former determines the wavefunctions of Hamiltonian (2), and therefore also the expectation values of the rotational constants for each ring-puckering state.^{20,33} The parameter V_{barrier} (more precisely A_z) is mainly a scaling factor²⁰ for the energies of the puckering states, and, thus, determines only the populations of these states and the centrifugal distortion constants. Therefore, the simulated spectra according to the adopted ring-puckering model are much more sensitive to the parameter Z_{\min} than to V_{barrier} . It was pointed out previously³³ that a more complex ring-puckering model, where the kinetic constant B_ϕ is treated as a function of the puckering angle, allows for a more precise determination of the barrier to ring inversion. The accuracy may also be improved by consideration of the vibration-rotation coupling for the two lowest ring-puckering states.

The equilibrium puckering angle ϕ_{\min} was calculated to be $24.3^\circ + 1.4/-0.7$ from the experimentally determined values for V_{barrier} and Z_{\min} (see eqn (3) and (4)) and the calculated average B_ϕ value of $5.3 \times 10^3 \text{ cm}^{-1}$ (Fig. 4). This semi-experimental value of the equilibrium puckering angle is very close to those obtained theoretically by FPA,

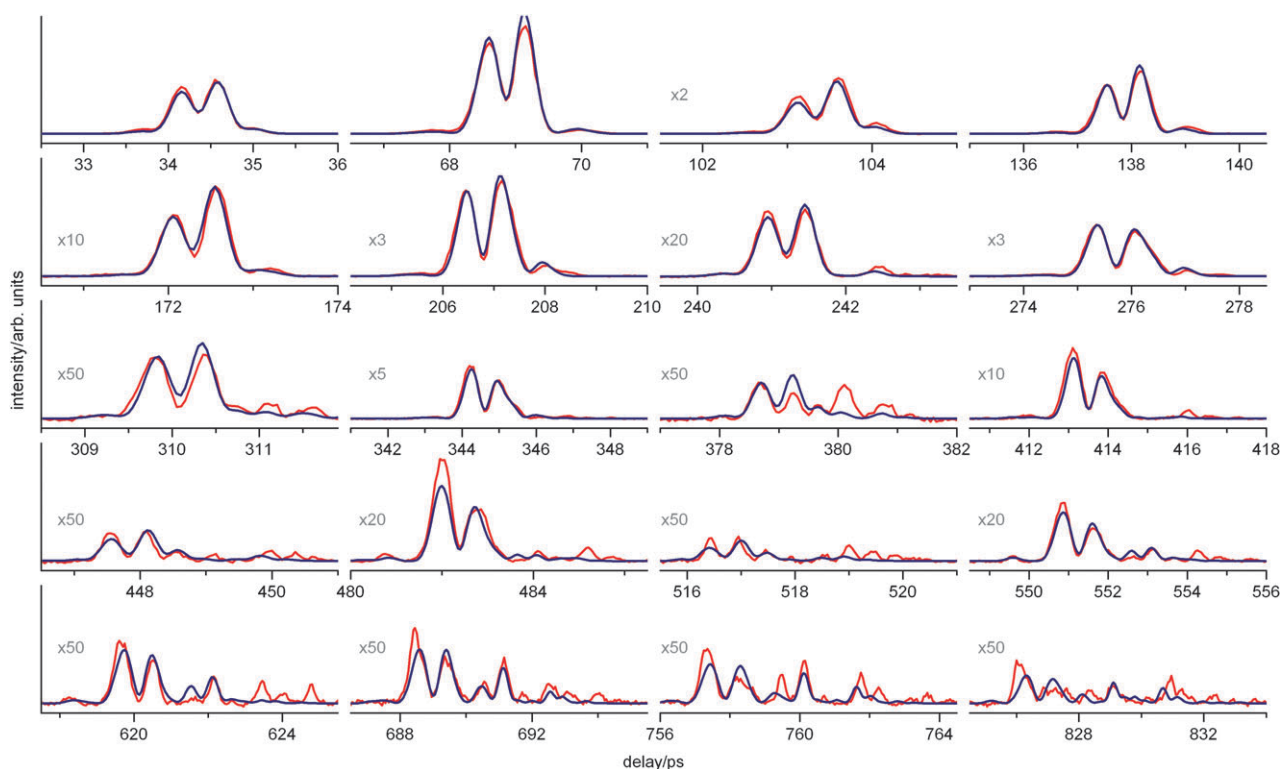


Fig. 6 fs DFWM spectra of cyclopentene in the gas cell at room temperature: red—experimental, blue—fitted simulation based on the one-dimensional model for the ring-puckering vibration.

Table 3 The parameters of the ring-puckering potential of CYC

	This work		Lopez <i>et al.</i> ³³		Laane <i>et al.</i> ¹⁸	Malloy ⁴³	Scharpen ²⁰	Ueda <i>et al.</i> ¹⁹
	Experiment	Theory	<i>a</i>	<i>b</i>				
$V_{\text{barrier}}/\text{cm}^{-1}$	274 + 12/−20	229	241.8	238.0	231.9	232	236/232	244.6
Z_{min}	1.769 + 0.009/−0.005	—	1.769	1.746	1.758	1.758	1.746	1.773 ^c
$\varphi_{\text{min}}/^\circ$	24.3 ^d	24.4	—	—	23.3	—	—	22.12
$x_{\text{min}}/\text{Å}$	0.243	0.244	—	—	0.234	0.264	—	0.214

^a From fixed reduced mass Hamiltonian $B_\varphi = \text{const.}$ ^b Semirigid Hamiltonian $B_\varphi = B_\varphi(\varphi)$. ^c Calculated by Leong and coworkers.³⁵ ^d Calculated from experimentally derived V_{barrier} , Z_{min} and the theoretical value of $B_\varphi = 5.3 \times 10^3 \text{ cm}^{-1}$ (see eqn (3) and (4)).

CCSD/aug-cc-pVDZ and the single point CCSD/aug-cc-pVTZ calculation on the SOSMP2/cc-pVDZ geometry (Table 1). The corresponding puckering coordinate x_{min} was found to be 0.243 Å from its relation to the puckering angle derived from B3LYP/cc-pVTZ and SOSMP2/cc-pVDZ structures.

The dependence of the rotational constants A and B on the puckering angle obtained from the fit are shown in Fig. 7 (green). They resemble closely those obtained by MW³³ (Fig. 7, blue dashes). Furthermore, the accuracy in the determination of the rotational constants A and B is about 1 MHz in the region close to Z_{min} (as shown by error bars at $Z = 1.5$ in Fig. 7), which corresponds to a relative error of better than 0.02%. This error increases for larger Z (> 2 , see error bars at $Z = 3.0$) because the probability of finding the system in this region is lower. Since the fs DFWM spectra in case of CYC are only slightly sensitive to the rotational constant C , its dependence on the puckering coordinate Z , was taken from MW³³ and fixed in the fit. Alternatively, this dependence may be taken from quantum chemical calculations.

The calculations at the B3LYP/cc-pVTZ level of theory yield rotational constants A and B that are systematically higher than the experimental ones. On the contrary, the rotational constants calculated at the SOSMP2/cc-pVDZ level

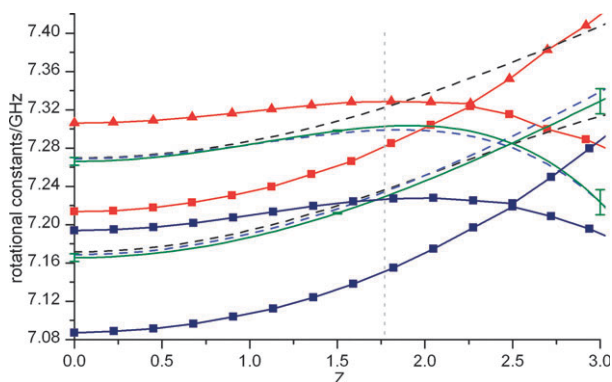


Fig. 7 Dependence of the rotational constants A and B on the reduced puckering coordinate Z : red—calculated at B3LYP/cc-pVTZ, the relationship between the puckering angle and the puckering coordinate Z is calculated according to eqn (3); dark blue squares—calculated at SOSMP2/cc-pVDZ; green—derived from the fitted simulation of the experimental fs DFWM spectrum of CYC at room temperature (standard deviation is shown by error bars); blue dashes—taken from the MW work of Lopez *et al.*³³ black dashes—taken from the MW work of Scharpen.²⁰ The dashed vertical line indicates the equilibrium reduced puckering coordinate Z_{min} deduced from the fit.

are lower than those derived from experiment. In order to find out how quantum chemical calculations can reproduce the rotational constants a number of optimizations of the CYC planar structure have been carried out using different combinations of theory levels and basis sets. The obtained results are collected in Table 4.

The smallest discrepancy of about 40 MHz between the experimentally determined and the calculated rotational constants was found for the B3LYP/cc-pVTZ optimized geometries. On the basis of Table 4 it can be concluded that an enlargement of the basis set increases the magnitude of rotational constants, whereas inclusion of higher order correlation in the calculations tends to decrease it. The same effects were previously found in calculations of the rotational constants of pyrrolidine.⁶ Moreover, it was shown that consideration of anharmonic effects should also decrease the magnitude of the rotational constants. Thus, better agreement between calculated and experimental values can be expected when CCSD with larger basis sets is employed and the anharmonic effects are taken into account, which is unfortunately currently not technically feasible. Hence, the results obtained by rotational fs DFWM spectroscopy can be used as a structural benchmark for *ab initio* calculations.

The experimentally derived ring-puckering potential and dependences of the rotational constants on the puckering coordinate can be used for calculation of vibrationally averaged values of the rotational constants A_v , B_v , C_v for each ring-puckering state v . These averaged values for the first seven ring-puckering states of CYC together with the CD constants A_v^J and A_v^K are collected in Table 5. The A_v and B_v values obtained in the current work deviate from the MW ones by +3 MHz and −5 MHz, respectively. The deviation of the parameter $(A_v + B_v)/2$, to which the fs DFWM signal is

Table 4 The rotational constants of the planar structure of CYC calculated at different levels of theory and derived experimentally in the present work

	A/GHz	B/GHz	C/GHz
Exp.	7.266(4)	7.166(4)	3.8642 ^a
B3LYP/cc-pVTZ	7.3062	7.2136	3.8874
MP2/aug-cc-pVDZ	7.2187	7.0877	3.8331
MP2/aug-cc-pVTZ	7.3312	7.2121	3.8951
SOSMP2/cc-pVDZ	7.1938	7.0871	3.8267
MP4/aug-cc-pVDZ	7.1551	7.0332	3.8011
CCSD/aug-cc-pVDZ	7.1756	7.0718	3.8171

^a Taken from the MW study of Lopez *et al.*³³

Table 5 Rotational constants for the first seven ring-puckering states of CYC

Puckering state ν	This work					From the MW work of Lopez <i>et al.</i> ³³				
	A/GHz	B/GHz	C/GHz^a	$\Delta_J^{\nu}/\text{kHz}^c$	$\Delta_{\text{JK}}^{\nu}/\text{kHz}^c$	A/GHz	B/GHz	C/GHz	$\Delta_J^{\nu}/\text{kHz}^c$	$\Delta_{\text{JK}}^{\nu}/\text{kHz}^c$
0	7.2967 ^d	7.2220	3.9497	0.25	-0.47	7.2936358(8)	7.2269160(9)	3.9493823(8)	0.225	-0.339
1	7.2970 ^d	7.2229	3.9510	0.23	-0.43	7.2939721(8)	7.2279943(9)	3.9510356(9)	0.197	-0.280
2	7.2817	7.1987	3.9159	0.25	-0.43	7.281364(1)	7.202949(1)	3.915786(1)	0.220	2.508
3	7.2874	7.2135	3.9398	0.15	-0.30	7.285844(4)	7.218342(4)	3.939766(4)	0.126	-2.671
4	7.2814	7.2066	3.9308	-0.09	0.06	7.280766(2)	7.211166(2)	3.930749(2)	-0.089	0.308
5	7.2837	7.2180	3.9506	0.05	-0.17	—	—	—	—	—
6	7.2824	7.2223	3.9597	0.03	-0.16	—	—	—	—	—
$0_{\text{T}}, 1_{\text{T}}^e$	7.273(4)	7.224(4)	3.945 ^b	—	—	—	—	—	—	—

^a The dependence of the rotational constant C on the puckering coordinate was taken from the MW work of Lopez *et al.*³³ ^b Fixed in the fit. ^c The CD constants originated from the rest of vibrations was found to be $\Delta_J^* = 1.2 \pm 0.1$ kHz and $\Delta_{\text{JK}}^* = 0.2 + 0.6/-0.4$ kHz. ^d The correction for the rotational constant A of the first two puckering states as suggested by Scharpen²⁰ was found to be $5.2 + 0.9/-0.3$ MHz. ^e The two first puckering states of the first excited state of the twist mode.

most sensitive in the case of CYC, is however less than -2 MHz.

It was previously reported by Lopez *et al.*³³ that the ring-puckering part Δ_J^{ν} of the complete CD constant Δ_J does not change much over the ring-puckering states. Indeed, it stays almost the same through the first three ring-puckering states and drops only slightly for the highest states (Table 5). Similarly, the other CD constant Δ_{JK}^{ν} shows only a weak dependence on the ring-puckering state, which is in contrast to the finding reported by Lopez and co-workers, where this constant changes significantly (by about 5 kHz from $\nu = 2$ to 3, Table 5). This discrepancy stems from the difference in the forms of the adopted rotation–vibration Hamiltonian. In the current work the rotation–vibration Hamiltonian is developed in the instantaneous principal axes system, whereas Lopez *et al.*³³ utilized the reduced axis system.⁴⁷

The energy splitting of the first two ring-puckering states was found from the fitted simulation to be 0.78 cm^{-1} , which is slightly smaller than the previously reported value of 0.91 cm^{-1} .⁴⁷

In addition, the rotational constants A and B for the lowest puckering doublet of the first excited twist state at 385 cm^{-1} were determined (Table 5). However, these constants should be considered with caution, since they can be somewhat affected by contributions from all higher ring-puckering states not included in the simulation.

6. Conclusions

In the present work rotational time-resolved fs DFWM spectroscopy has been successfully applied for the investigation of the large amplitude ring-puckering motion in gaseous cyclopentene. This well studied molecule was chosen in order to evaluate the accuracy of the fs DFWM technique in determination of energetic and structural parameters of such large amplitude motions.

The fs DFWM spectrum of CYC recorded at room temperature has been satisfactorily reproduced by a fitted simulation based on an one-dimensional quantum mechanical model for the ring-puckering motion. The fit yields the energetic parameters of the ring-puckering motion such as the barrier to ring inversion, V_{barrier} , of $274 + 12/-20$ cm^{-1} and the equilibrium

value of the reduced puckering coordinate Z_{min} of $1.769 + 0.009/-0.005$. Whereas the obtained inversion barrier is somewhat higher than the most frequently reported experimental value of 232 ± 5 cm^{-1} , Z_{min} is in line with previously derived values of $1.746-1.773$.

On the basis of these two energetic parameters (V_{barrier} , Z_{min}) an equilibrium puckering angle of 24.3° has been determined using the calculated puckering kinetic constant of 5.3×10^3 cm^{-1} . The dependences of the rotational constants A and B on the puckering angle obtained from fs DFWM are in excellent agreement with those obtained by microwave spectroscopy.³³

In addition, previous theoretical estimates of the inversion barrier in cyclopentene were improved by high level quantum chemical calculations. It turned out that inclusion of ZPVE correction increases the barrier to ring inversion by about $20-50$ cm^{-1} , depending on the level of theory and is thus relevant for an accurate comparison of theoretical and experimental potentials. Focal point analysis on B3LYP/cc-pVTZ geometries yields a barrier to ring inversion of 229 cm^{-1} , which is in excellent agreement with the experimental value of 232 ± 5 cm^{-1} . The puckering angle corresponding to the minimum on the potential energy surface has been calculated to be 24.4° , which is very close to the semi-experimental value of 24.3° determined by the analysis of the room-temperature fs DFWM spectrum in the current work.

Thus, the high structural sensitivity together with good energetic evaluation makes the fs DFWM spectroscopy in combination with high-level *ab initio* calculations an attractive tool for the investigation of large amplitude intramolecular motions. The method is particularly interesting for molecules lacking or possessing only a small dipole moment, where far-infrared and microwave spectroscopy cannot be applied.

Acknowledgements

The financial support by Deutsche Forschungsgemeinschaft, Goethe-University Frankfurt is gratefully acknowledged. S. K. is grateful to the Alexander von Humboldt foundation for his research grant. The authors also acknowledge the support by the Frankfurt Centre for Scientific Computing.

Notes and references

- 1 L. A. Carreira, R. C. Lord and T. B. Malloy, 1979, vol. 82, pp. 1–95.
- 2 A. C. Legon, *Chem. Rev.*, 1980, **80**, 231–262.
- 3 H. L. Strauss, *Annu. Rev. Phys. Chem.*, 1983, **34**, 301–328.
- 4 J. S. Baskin, P. M. Felker and A. H. Zewail, *J. Chem. Phys.*, 1986, **84**, 4708–4710.
- 5 P. M. Felker and A. H. Zewail, in *Femtochemistry*, ed. J. Manz and L. Wöste, VCH, Weinheim, 1995, vol. 1.
- 6 M. Kunitski, C. Riehn, V. V. Matyilitsky, P. Tarakeshwar and B. Brutschy, *Phys. Chem. Chem. Phys.*, 2010, **12**, 72.
- 7 J. E. Kilpatrick, K. S. Pitzer and R. Spitzer, *J. Am. Chem. Soc.*, 1947, **69**, 2483–2488.
- 8 A. A. Al-Saadi and J. Laane, *J. Mol. Struct.*, 2007, **830**, 46–57.
- 9 H. M. Frey, P. Beaud, T. Gerber, B. Mischler, P. P. Radi and A. P. Tzannis, *Appl. Phys. B: Lasers Opt.*, 1999, **68**, 735–739.
- 10 A. Materny, T. Chen, M. Schmitt, T. Siebert, A. Vierheilg, V. Engel and W. Kiefer, *Appl. Phys. B: Lasers Opt.*, 2000, **71**, 299–317.
- 11 M. Dantus, *Annu. Rev. Phys. Chem.*, 2001, **52**, 639–679.
- 12 C. Riehn, *Chem. Phys.*, 2002, **283**, 297–329.
- 13 V. V. Matyilitsky, W. Jarzba, C. Riehn and B. Brutschy, *J. Raman Spectrosc.*, 2002, **33**, 877–883.
- 14 V. V. Matyilitsky, C. Riehn, M. F. Gelin and B. Brutschy, *J. Chem. Phys.*, 2003, **119**, 10553–10562.
- 15 L. E. Bauman, P. M. Killough, J. M. Cooke, J. R. Villarreal and J. Laane, *J. Phys. Chem.*, 1982, **86**, 2000–2006.
- 16 G. W. Rathjens, *J. Chem. Phys.*, 1962, **36**, 2401–2406.
- 17 S. S. Butcher and C. C. Costain, *J. Mol. Spectrosc.*, 1965, **15**, 40–50.
- 18 J. Laane and R. C. Lord, *J. Chem. Phys.*, 1967, **47**, 4941–4945.
- 19 T. Ueda and T. Shimanou, *J. Chem. Phys.*, 1967, **47**, 5018–5030.
- 20 L. H. Scharpen, *J. Chem. Phys.*, 1968, **48**, 3552–3556.
- 21 T. H. Chao and J. Laane, *Chem. Phys. Lett.*, 1972, **14**, 595–597.
- 22 J. R. Durig and L. A. Carriera, *J. Chem. Phys.*, 1972, **56**, 4966–4969.
- 23 W. C. Harris and Ct. Longshor, *J. Mol. Struct.*, 1973, **16**, 187–204.
- 24 J. R. Villarreal, L. E. Bauman and J. Laane, *J. Phys. Chem.*, 1976, **80**, 1172–1177.
- 25 G. Dealti and P. Decleva, *J. Mol. Struct.*, 1977, **41**, 299–304.
- 26 D. F. Bocian, G. A. Schick and R. R. Birge, *J. Chem. Phys.*, 1981, **75**, 3215–3219.
- 27 M. Besnard, J. C. Lassegues, Y. Guissani and J. C. Leicknam, *Mol. Phys.*, 1984, **53**, 1145–1166.
- 28 J. Lascombe, D. Cavagnat, J. C. Lassegues, C. Rafilipomanana and C. Biran, *J. Mol. Struct.*, 1984, **113**, 179–190.
- 29 R. L. Rosas, C. Cooper and J. Laane, *J. Phys. Chem.*, 1990, **94**, 1830–1836.
- 30 R. Champion, P. D. Godfrey and F. L. Bettens, *J. Mol. Spectrosc.*, 1991, **147**, 488–495.
- 31 W. D. Allen, A. G. Csaszar and D. A. Horner, *J. Am. Chem. Soc.*, 1992, **114**, 6834–6849.
- 32 D. Cavagnat, R. M. Cavagnat, J. C. Cornut and S. Banisaeidvahedie, *J. Phys.: Condens. Matter*, 1992, **4**, 4205–4212.
- 33 J. C. Lopez, J. L. Alonso and M. E. Charro, *J. Mol. Spectrosc.*, 1992, **155**, 143–157.
- 34 N. Nevins, K. S. Chen and N. L. Allinger, *J. Comput. Chem.*, 1996, **17**, 669–694.
- 35 M. K. Leong, V. S. Mastryukov and J. E. Boggs, *J. Mol. Struct.*, 1998, **445**, 149–160.
- 36 M. I. Davis and T. W. Muecke, *J. Phys. Chem.*, 1970, **74**, 1104–1108.
- 37 M. Besnard, J. C. Lassegues, A. Lichanot and H. Nery, *J. Phys.*, 1984, **45**, 487–496.
- 38 S. P. Kwasniewski, L. Claes, J. P. Francois and M. S. Deleuze, *J. Chem. Phys.*, 2003, **118**, 7823–7836.
- 39 Y. R. Huang, S. Knippenberg, B. Hajgato, J. P. Francois, J. K. Deng and M. S. Deleuze, *J. Phys. Chem. A*, 2007, **111**, 5879–5897.
- 40 M. Villa, M. L. Senent and R. Dominguez-Gomez, *Chem. Phys. Lett.*, 2007, **436**, 15–18.
- 41 D. O. Harris, H. W. Harrington, A. C. Luntz and W. D. Gwinn, *J. Chem. Phys.*, 1966, **44**, 3467–3480.
- 42 S. I. Chan and D. Stelman, *J. Mol. Spectrosc.*, 1963, **10**, 278–299.
- 43 T. B. Malloy, *J. Mol. Spectrosc.*, 1972, **44**, 504–535.
- 44 C. Riehn, V. V. Matyilitsky and M. F. Gelin, *J. Raman Spectrosc.*, 2003, **34**, 1045–1050.
- 45 C. Riehn, M. I. Kunitski, V. V. Matyilitsky, M. F. Gelin and B. Brutschy, *Phys. Chem. Chem. Phys.*, 2005, **7**, 3955–3962.
- 46 J. K. G. Watson, *J. Chem. Phys.*, 1968, **48**, 4517–4524.
- 47 H. M. Pickett, *J. Chem. Phys.*, 1972, **56**, 1715–1723.
- 48 D. R. Lide, *J. Mol. Spectrosc.*, 1962, **8**, 142–152.
- 49 R. A. Creswell and I. M. Mills, *J. Mol. Spectrosc.*, 1974, **52**, 392–412.
- 50 J. C. López, A. G. Lesarri, D. G. Lister, J. L. Alonso, R. A. Shaw and H. Wieser, *Chem. Phys.*, 1990, **148**, 21–31.
- 51 D. Kivelson and J. E. B. Wilson, *J. Chem. Phys.*, 1953, **21**, 1229–1236.
- 52 J. E. B. Wilson, *J. Chem. Phys.*, 1936, **4**, 313–316.
- 53 K. Price and R. Storn, *Differential Evolution, Function Optimization Algorithm*, <http://www.icsi.berkeley.edu/~storn/code.html>.
- 54 M. R. F. James, *MINUIT computer code*, Program D-506, CERN, Geneva, 1977.
- 55 U. Even, J. Jortner, D. Noy, N. Lavie and C. Cossart-Magos, *J. Chem. Phys.*, 2000, **112**, 8068–8071.
- 56 J. M. L. Martin, J. El-Yazal and J.-P. Francois, *Mol. Phys.*, 1995, **86**, 1437–1450.
- 57 W. Koch and M. C. Holthausen, *Chemist's Guide to Density Functional Theory*, Wiley-VCH, Weinheim, 2001.
- 58 J. A. Pople, M. Head-Gordon and K. Raghavachari, *J. Chem. Phys.*, 1987, **87**, 5968–5975.
- 59 N. L. Allinger, J. T. Fermann, W. D. Allen and H. F. Schaefer III, *J. Chem. Phys.*, 1997, **106**, 5143–5150.
- 60 A. Salam and M. S. Deleuze, *J. Chem. Phys.*, 2002, **116**, 1296–1302.
- 61 Y. Jung, R. C. Lochan, A. D. Dutoi and M. Head-Gordon, *J. Chem. Phys.*, 2004, **121**, 9793–9802.
- 62 M. J. Frisch, G. W. Trucks, H. B. Schlegel, G. E. Scuseria, M. A. Robb, J. R. Cheeseman, J. A. Montgomery, Jr., T. Vreven, K. N. Kudin, J. C. Burant, J. M. Millam, S. S. Iyengar, J. Tomasi, V. Barone, B. Mennucci, M. Cossi, G. Scalmani, N. Rega, G. A. Petersson, H. Nakatsuji, M. Hada, M. Ehara, K. Toyota, R. Fukuda, J. Hasegawa, M. Ishida, T. Nakajima, Y. Honda, O. Kitao, H. Nakai, M. Klene, X. Li, J. E. Knox, H. P. Hratchian, J. B. Cross, V. Bakken, C. Adamo, J. Jaramillo, R. Gomperts, R. E. Stratmann, O. Yazyev, A. J. Austin, R. Cammi, C. Pomelli, J. Ochterski, P. Y. Ayala, K. Morokuma, G. A. Voth, P. Salvador, J. J. Dannenberg, V. G. Zakrzewski, S. Dapprich, A. D. Daniels, M. C. Strain, O. Farkas, D. K. Malick, A. D. Rabuck, M. Raghavachari, J. B. Foresman, J. V. Ortiz, Q. Cui, A. G. Baboul, S. Clifford, J. Cioslowski, B. B. Stefanov, G. Liu, A. Liashenko, P. Piskorz, I. Komaromi, R. L. Martin, D. J. Fox, T. Keith, M. A. Al-Laham, C. Y. Peng, A. Nanayakkara, M. Challacombe, P. M. W. Gill, B. G. Johnson, W. Chen, M. W. Wong, C. Gonzalez and J. A. Pople, *GAUSSIAN 03 (Revision D.01)*, Gaussian, Inc., Wallingford, CT, 2004.
- 63 Y. Shao, L. Fusti-Molnar, Y. Jung, J. Kusmann, C. Ochsenfeld, S. T. Brown, A. T. B. Gilbert, L. V. Slipchenko, S. V. Levchenko, D. P. O'Neill, R. A. Distasio Jr., R. C. Lochan, T. Wang, G. J. O. Beran, N. A. Besley, J. M. Herbert, C. Y. Lin, T. Van Voorhis, S. H. Chien, A. Sodt, R. P. Steele, V. A. Rassolov, P. E. Maslen, P. P. Korambath, R. D. Adamson, B. Austin, J. Baker, E. F. C. Byrd, H. Dachsel, R. J. Doerksen, A. Dreuw, B. D. Dunietz, A. D. Dutoi, T. R. Furlani, S. R. Gwaltney, A. Heyden, S. Hirata, C.-P. Hsu, G. Kedziora, R. Z. Khallilulin, P. Klunzinger, A. M. Lee, M. S. Lee, W. Liang, I. Lotan, N. Nair, B. Peters, E. I. Proynov, P. A. Pieniazek, Y. M. Rhee, J. Ritchie, E. Rosta, C. D. Sherrill, A. C. Simmonett, J. E. Subotnik, H. L. Woodcock III, W. Zhang, A. T. Bell, A. K. Chakraborty, D. M. Chipman, F. J. Keil, A. Warshel, W. J. Hehre, H. F. Schaefer III, J. Kong, A. I. Krylov, P. M. W. Gill and M. Head-Gordon, *Q-Chem Program Package*, 3.0 edn.

- 64 H.-J. Werner, P. J. Knowles, R. Lindh, F. R. Manby, M. Schütz, P. Celani, T. Korona, A. Mitrushenkov, G. Rauhut, T. B. Adler, R. D. Amos, A. Bernhardsson, A. Berning, D. L. Cooper, M. J. O. Deegan, A. J. Dobbyn, F. Eckert, E. Goll, C. Hampel, G. Hetzer, T. Hrenar, G. Knizia, C. Köppl, Y. Liu, A. W. Lloyd, R. A. Mata, A. J. May, S. J. McNicholas, W. Meyer, M. E. Mura, A. Nicklass, P. Palmieri, K. Pflüger, R. Pitzer, M. Reiher, U. Schumann, H. Stoll, A. J. Stone, R. Tarroni, T. Thorsteinsson, M. Wang and A. Wolf, MOLPRO, version 2008.3, a package of *ab initio* programs, Cardiff, UK, 2008.
- 65 I. Procaccia and R. D. Levine, *Chem. Phys. Lett.*, 1975, **33**, 5–10.

9.4 Detection and structural characterization of clusters with ultrashort-lived electronically excited states: IR absorption detected by femtosecond multiphoton ionization

Detection and Structural Characterization of Clusters with Ultrashort-Lived Electronically Excited States: IR Absorption Detected by Femtosecond Multiphoton Ionization

Yevgeniy Nosenko,^{†,§} Maksim Kunitski,[†] Randolph P. Thummel,[‡] Alexander Kyrychenko,[§] Jerzy Herbich,[§] Jacek Waluk,[§] Christoph Riehn,^{*,†} and Bernhard Brutschy^{*,†}

Institute of Physical and Theoretical Chemistry, University of Frankfurt, Max-von-Laue-Str. 7, 60438 Frankfurt/M, Germany, Department of Chemistry, University of Houston, Houston, Texas 77204-5641, and Institute of Physical Chemistry, Polish Academy of Sciences, Kasprzaka 44, 01-224 Warsaw, Poland

Received May 3, 2006; E-mail: brutschy@chemie.uni-frankfurt.de; riehn@chemie.uni-frankfurt.de

The progress in chemical kinetics makes it clear that the so-called “elementary” reactions, such as proton or electron transfer, are, in fact, multidimensional processes, involving not only intramolecular degrees of freedom but also those of the environment. Elucidating the intricacies of such phenomena requires techniques of high spectral, temporal, and structural resolution. These conditions can be simultaneously fulfilled by isolating the reactants in supersonic beams. Recent examples of successful applications of this methodology for proton transferring systems include studies of the cooperativity in excited state double proton transfer (ESDPT) in 7-azaindole dimers¹ or detection of *cis* and *trans* tautomeric species in alkylated porphycenes and the determination of tunneling splittings for both forms in the ground and lowest singlet electronic states.²

The investigation of gas phase molecular clusters formed in supersonic beams at ultralow temperature is a very active research field since it allows studying the structure of microsolvated molecules by vibrational spectroscopy in combination with density functional theory (DFT). The selection of species out of a distribution of clusters differing in size and structure is feasible by IR/UV double resonance spectroscopy combining IR predissociation with UV resonant two-photon ionization and mass spectrometric detection.³ This ultrasensitive IR/R2PI ion depletion method meanwhile finds widespread applications in the characterization of small biomolecules and their aggregates due to its size and isomer specificity.

We have chosen the 1-H-pyrrolo[3,2-*h*]quinoline (PQ)/methanol system since it constitutes an important model system for understanding the mechanism and dynamics of intermolecular ESDPT, which leads to tautomerization, a key reaction for chemical mutagenesis of DNA. PQ belongs to the group of bifunctional (H-bond donor/acceptor) heteroazaaromatics that have recently been studied in the condensed phase.^{4–7} This group exhibits dual fluorescence, although, in the case of PQ, with very low quantum yield. The dual fluorescence is attributed to an ESDPT process mediated by a cyclic 1:1 complex with the alcohol solvent. The time scale of the ESDPT process in solution is in the subpicosecond to picosecond range.⁶ In the gas phase, we have recently found different photophysical properties of PQ upon stepwise solvation by methanol. Namely, the laser-induced fluorescence (LIF) of the jet-cooled 1:1 cluster was not observed, while that of the 1:2 and larger complexes was quite strong upon $S_1 \leftarrow S_0$ excitation. This difference in fluorescence was indicative of a fast relaxation channel. Our goal was to investigate in detail the structure and

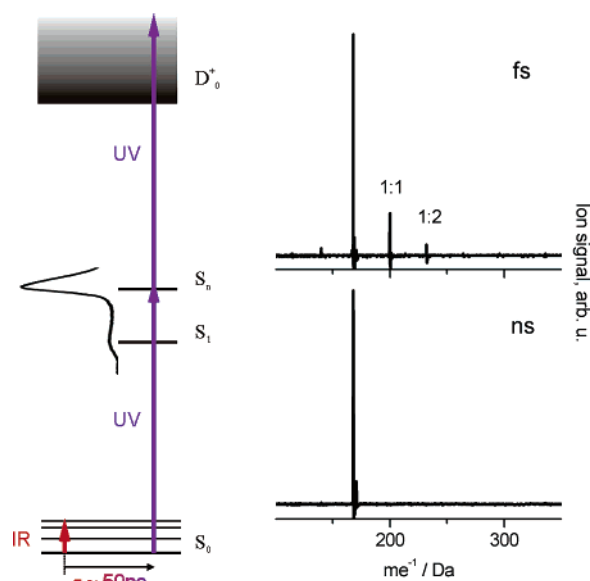


Figure 1. One-color (266 nm) two-photon ionization scheme of PQ solvated by alcohol and mass spectra of jet-cooled PQ/methanol gas mixture obtained with the femtosecond and nanosecond laser pulses under otherwise identical conditions. The UV absorption spectrum of the PQ/alcohol solution is inserted. The timing of the IR/fsMPI experiment is also indicated.

dynamics of such photoreactive complexes and unveil their excited state reaction mechanism. For this purpose, their IR spectra in the NH, OH stretch region should be recorded using an extension of the double resonant IR depletion technique (IR/R2PI).

The essential condition for the “classical” IR/R2PI depletion method is the existence of an electronically excited state of the cluster, halfway to the ionization potential, which can be excited resonantly and lives long enough to be able to ionize the species by nonresonant absorption of a second photon of the same energy. However, if this intermediate state is short-lived ($\ll 1$ ns) due to fast proton or electron transfer or internal conversion, the ion yield observed with nanosecond lasers goes to zero.

An instructive example is given in Figure 1, where mass spectra of the same supersonic expansion of PQ with methanol were recorded for comparison, first with a nanosecond laser and second with a femtosecond laser. The excitation is performed via a higher lying electronic band, which can be attributed to electronically excited states S_4 or/and S_5 of $\pi\pi^*$ character (cf. scheme in Figure 1). Here, the third harmonic of a femtosecond Ti:sapphire laser (266 nm, 300 fs) is used. It is obvious that in the former spectrum the molecular aggregates of PQ with methanol are missing, probably due to their short excited state lifetime. From the displayed mass

[†] University of Frankfurt.

[‡] University of Houston.

[§] Polish Academy of Sciences.

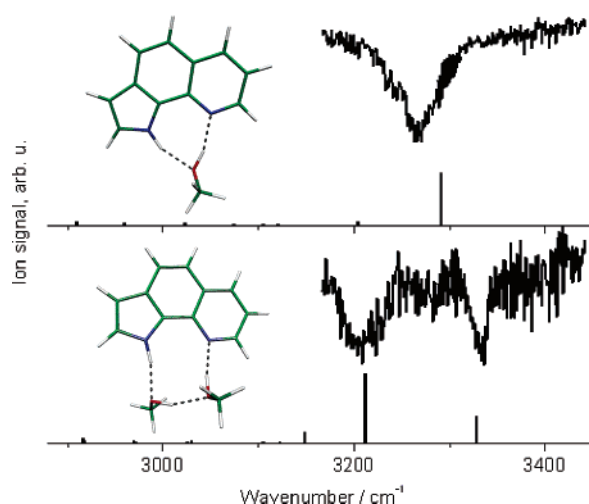


Figure 2. IR/fsMPI spectra measured for PQ:methanol_{n=1,2} mass channels. The calculated IR spectra are plotted with bars. Relevant cluster structures are inserted.

spectra, it is clear that if one is interested in an IR investigation of the PQ:methanol aggregates, this can only be achieved by femtosecond multiphoton ionization (fsMPI).

Our experimental setup consists of a narrow band nanosecond IR-OPO for vibrational excitation, a femtosecond chirped-pulse amplified Ti:Sa laser system for two-photon ionization of the cluster, and a vacuum apparatus equipped with a pulsed nozzle and a home-built time-of-flight mass spectrometer. All components have been described previously in separate publications.⁸

The resulting IR spectra in the region of 3150–3450 cm⁻¹ measured by IR/fsMPI for the PQ:methanol_{n=1,2} ionic aggregates are depicted in Figure 2. Whereas for the 1:1 aggregate only one band at 3268 cm⁻¹ was found, the 1:2 complex exhibited two bands at 3332 and 3209 cm⁻¹. For assignment, these spectra are compared to the results of calculations obtained at the DFT level.⁹ The calculated positions and intensities of the IR bands are plotted in Figure 2. They agree very well with the experimental spectra. The structures of the calculated aggregates are also depicted in Figure 2. In both clusters, the most stable geometries arise when the pyrrole donor and the pyridine acceptor of PQ are connected through H-bonds by a methanol OH bridge.

Thus, the strongest band of the 1:1 aggregate, calculated at 3291 cm⁻¹, is readily identified as the simultaneous anti-phase stretch of the OH group of methanol and the NH of the pyrrole unit of PQ. Due to the strong double H-bond interaction ($E_{\text{binding}} \approx 10$ kcal/mol⁵) in this cyclic complex, the local oscillator modes no longer exist. Similarly, for the 1:2 aggregate, the most intense mode calculated at 3212 cm⁻¹ is the anti-phase stretch of the pyrrole NH and pyridine-bound OH. The vibration predicted at 3328 cm⁻¹ is mainly the methanol dimer OH stretching, mixed, however, with elongations of the OH and NH bonds within the H-bond cycle.

The cyclic NH...OH...N bridge of the 1:1 aggregate was suggested as an intermediate for fast ESDPT in solution, which gives rise to the anomalous fluorescence and quenches the normal one.⁴ After photoexcitation, the protons involved in the H-bonds undergo a concerted, albeit asynchronous, transfer. In principle, such a process is also possible in the 1:2 aggregate, but since there the “proton wire” is longer, a higher chance for dissipative side processes or of disturbances along the way is also conceivable. The different behavior of 1:1 and 1:2 PQ:methanol aggregates can be

deduced from our recent IR nanosecond fluorescence depletion and R2PI¹⁰ studies. As mentioned earlier, both failed to detect the 1:1 complex after excitation to the S₁ state, but the 1:2 and larger clusters appeared. Moreover, the spectra obtained by IR/LIF and IR/fsMPI depletion for the 1:2 species agree nicely, which supports the new method and the presented interpretation.

It should be emphasized that, under the employed experimental conditions (i.e., fixed femtosecond laser wavelength at 266 nm), no spectral selection of a specific cluster size by its UV fingerprints is possible. Therefore, one would expect that the obtained cluster mass spectra are dominated by fragmentation. However, conditions can be found where the parent ions (1:1)⁺, (1:2)⁺ can be measured nearly without contribution from larger clusters. For this purpose, a careful control of the expansion conditions is important, either by changing the vapor pressure of the solvent or by ionizing different segments of the gas pulse containing different cluster sizes.

Additionally, it should be pointed out that very similar results have been obtained for aggregates of PQ with water (spectra not shown here), where also the 1:1 cluster could not be investigated by LIF, but exclusively by the IR/fsMPI method.

In conclusion, we have presented a scheme for measuring the IR spectra of photoreactive molecular clusters, which is based on femtosecond multiphoton ionization probing (IR/fsMPI). We applied it successfully to PQ:methanol_{n=1,2} clusters. One drawback of the method is that, in general, it does not provide size and isomer specificity. However, we could demonstrate that size-specific spectra for small complexes could be obtained if the supersonic expansion and excitation conditions are carefully controlled. In particular, PQ:methanol_{n=1,2} aggregates could be identified and their structure analyzed. A time-resolved study of the ESDPT dynamics is underway. Thus, an important molecular model system for solvent-assisted photoinduced tautomerization reactions can be elucidated in full detail.

Acknowledgment. B.B. thanks the DFG/CNRS for support by a common research program. C.R. is thankful to the Adolf-Messer-Stiftung and alumni organization of the University Frankfurt (VFF) for their support.

Supporting Information Available: Experimental and calculation details as well as full authorship of ref 9a. This material is available free of charge via the Internet at <http://pubs.acs.org>.

References

- (1) Sekiya, H.; Sakota, K. *Bull. Chem. Soc. Jpn.* **2006**, *79*, 373–385.
- (2) Vdovin, A.; Sepiol J.; Urbańska, N.; Pietraszkiewicz, M.; Mordziński, A.; Waluk, J. *J. Am. Chem. Soc.* **2006**, *128*, 2577–2586.
- (3) (a) Page, R. H.; Shen, Y. R.; Lee, Y. T. *J. Chem. Phys.* **1988**, *88*, 4621–4636. (b) Riehn, C.; Lahmann, C.; Wassermann, B.; Brutschy, B. *Chem. Phys. Lett.* **1992**, *197*, 443–450. (c) Tanabe, S.; Ebata, T.; Fujii, M.; Mikami, N. *Chem. Phys. Lett.* **1993**, *215*, 347–352. (d) Pribble, R. N.; Zwier, T. S. *Science* **1994**, *265*, 75–79.
- (4) Kyrchenko, A.; Herbich, J.; Izydorczak, M.; Wu, F.; Thummel, R. P.; Waluk, J. *J. Am. Chem. Soc.* **1999**, *121*, 11179–11188.
- (5) Kyrchenko, A.; Stepanenko, Y.; Waluk, J. *J. Phys. Chem. A* **2000**, *104*, 9542–9555.
- (6) Marks, D.; Zhang, H.; Borowicz, P.; Waluk, J.; Glasbeek, M. *J. Phys. Chem. A* **2000**, *104*, 7167–7175.
- (7) Waluk, J. *Acc. Chem. Res.* **2003**, *36*, 832–838 and references therein.
- (8) (a) Krauss, O.; Brutschy, B. *Chem. Phys. Lett.* **2001**, *350*, 427–433. (b) Weichert, A.; Riehn, C.; Barth, H.-D.; Lembach, G.; Zimmermann, M.; Brutschy, B.; Podenas, D. *Rev. Sci. Instrum.* **2001**, *72*, 2697–2708.
- (9) (a) Frisch, M. J.; et al. *Gaussian 98*; Gaussian, Inc.: Pittsburgh, PA, 1998. (b) El-Azhary, A. A. *Spectrochim. Acta, Part A* **1999**, *55*, 2437–2446.
- (10) Krauss, O. Photoinduzierter Ladungstransfer in Mikrosolvatclustern: Untersuchungen mit LIF-Spektroskopie und IR-UV-Doppelresonanzspektroskopie. Ph.D. Thesis, Goethe University, Frankfurt/M, Germany, 2002.

JA063093E

**9.5 Separation of different hydrogen-bonded clusters by fs
UV-ionization-detected infrared spectroscopy:
1H-pyrrolo[3,2-h]quinoline•(H₂O)(n=1,2) complexes**

Separation of Different Hydrogen-Bonded Clusters by Femtosecond UV-Ionization-Detected Infrared Spectroscopy: 1*H*-Pyrrolo[3,2-*h*]quinoline·(H₂O)_{*n*}=1,2 Complexes

Yevgeniy Nosenko,^{†,‡} Maksim Kunitski,[†] Christoph Riehn,[§] Randolph P. Thummel,^{||} Alexander Kyrychenko,[‡] Jerzy Herbich,[‡] Jacek Waluk,[‡] and Bernhard Brutschy^{*,†}

Institute of Physical and Theoretical Chemistry, University of Frankfurt, Max-von-Laue-Str. 7, 60438 Frankfurt/M, Germany; Institute of Physical Chemistry, Polish Academy of Sciences, Kasprzaka 44, 01-224 Warsaw, Poland; Department of Chemistry, Technical University of Kaiserslautern, Erwin-Schrödinger-Str. 52, 67663 Kaiserslautern, Germany; and Department of Chemistry, University of Houston, Houston, Texas 77204-5003

Received: August 27, 2007; In Final Form: November 14, 2007

Experimental and theoretical studies are presented for complexes of water with 1*H*-pyrrolo[3,2-*h*]quinoline (PQ), a bifunctional compound acting simultaneously as a hydrogen-bond donor and acceptor. A 1:1 complex, which is not fluorescent and only very short-lived in the electronically excited state, was analyzed by isolating the complex under supersonic jet conditions and characterizing its structure by infrared-induced ion depletion spectroscopy utilizing multiphoton ionization by femtosecond UV pulses (IR/fsMPI spectroscopy). On the other hand, a long-lived 1:2 complex was identified as the smallest microhydrate of PQ contributing to the laser-induced fluorescence excitation spectrum. Its structure was assigned by fluorescence-detected IR spectra and analyzed using density functional theory. The structures of the 1:1 and 1:2 clusters are assigned to species in which the water molecule(s) form a hydrogen-bonded solvent bridge between the two functional groups. In accord with calculations, both 1:1 and 1:2 PQ/water complexes reveal weaker hydrogen bonding than the analogous clusters of PQ with methanol.

1. Introduction

A fast phototautomerization process has been demonstrated for 1*H*-pyrrolo[3,2-*h*]quinoline (PQ) in protic solvents.^{1–3} PQ represents a family of bifunctional molecules which possess both a hydrogen-bond donor (e.g., an aromatic NH group) and an acceptor (e.g., a quinoline-type nitrogen atom N_q). In alcohols^{1,2} and water,³ PQ shows dual luminescence, contrary to its behavior in nonpolar and polar aprotic solvents. In order to prove that the appearance of a low-energy emission band is a manifestation of an excited-state proton transfer (ESPT) process, the spectral position of this fluorescence has been compared with the emission of a N_q-methylated molecule synthesized to serve as a chemical model of the tautomeric structure.¹ The driving force for ESPT is provided by large p*K*_a changes upon photoexcitation. For PQ, the quinoline nitrogen becomes much more basic ($\Delta pK_a = +9.6$) and the acidity of the NH group is also strongly enhanced ($\Delta pK_a = -6$). Titration of solutions of PQ in a nonpolar solvent with alcohol (in concentrations low enough to prevent the formation of alcohol oligomers) and the observations of spectral changes both in absorption and emission gave strong evidence that the proton transfer occurs in a 1:1 hydrogen-bonded complex of an excited chromophore with an alcohol molecule. The detailed structural characterization of the reactive precursors is a challenging task for solution studies. It has been assumed that these complexes correspond to a 1:1 “correctly prepared” doubly hydrogen-bonded cyclic structure (Figure 1).^{1–3} This idea has been corroborated by the finding

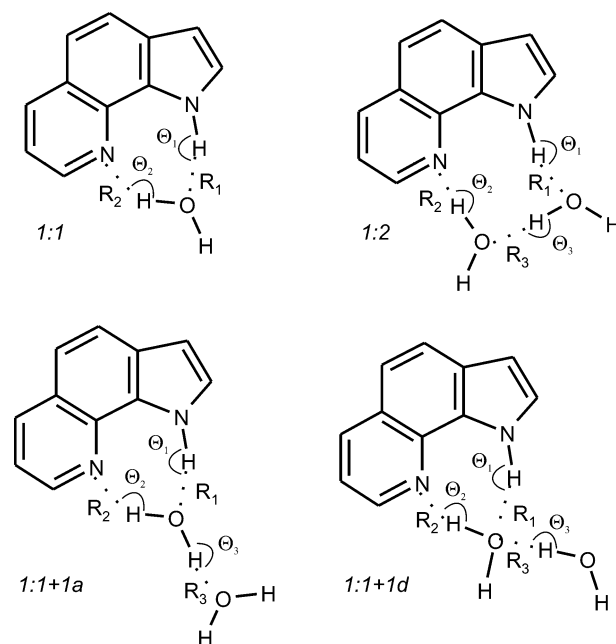


Figure 1. Schematic structures of the considered hydrogen-bonding complexes of PQ with water.

that the low-energy emission is still observed in glasses at temperatures as low as 77 K. Moreover, the photoreaction is extremely fast.⁴ The decay of the primary excited fluorescence is not monoexponential and consists of a fast component (a few picoseconds) and a slow component, which increases from tens to more than a hundred picoseconds with an increase in the viscosity of the surrounding medium. Only the fast component, not much dependent on the properties of the alcohol, is observed

* Corresponding author. E-mail: brutschy@chemie.uni-frankfurt.de.

[†] University of Frankfurt.

[‡] Polish Academy of Sciences.

[§] University of Kaiserslautern.

^{||} University of Houston.

in the rise of the tautomeric fluorescence. Therefore, the general picture for the bulk solution corresponds to a dynamic equilibrium between various solvates of different stoichiometry and/or different structure.¹ Some of these complexes decay radiationlessly within tens or hundred picoseconds, being responsible for the viscosity-dependent fluorescence quenching. This model has also been supported by a recent time-dependent density functional theory (TDDFT) study performed for PQ/water_{*n*} (*n* = 0,1,2) clusters.⁵ It has been demonstrated that the barrier for the ESPT is dramatically reduced from 20.9 kcal/mol in the bare PQ molecule to 3 kcal/mol in the 1:1 PQ/water complex. Moreover, the TDDFT calculations predict that the extension of the hydrogen-bonded chain connecting the hydrogen-bond donor/acceptor groups of PQ in the 1:2 complex (Figure 1) results in an increase of the tautomerization barrier to 5.6 kcal/mol, due to unfavorable hydrogen-bond configurations. Moreover, the fraction of the 1:1 complex of PQ/water compared to PQ/methanol in solution has been estimated by a molecular dynamics (MD) simulation to be a factor of 3.5 smaller,⁶ in agreement with the experimental value of 2.7.³ Most of the previous studies focused on experiments in solution. In order to characterize the structure of these reactive hydrogen-bonded complexes with alcohols and water and to pave the way to unraveling their size-dependent chemical dynamics, we have recently started a study of the clusters isolated under supersonic jet conditions. These issues provided motivation for the present molecular beam investigations of the PQ/water_{*n*} clusters.

We have recently shown that the photophysics of jet-isolated complexes of PQ with methanol is strongly dependent on the cluster size.⁷ Complete lack of fluorescence, observed for the 1:1 complex, was explained by a fast ESPT reaction, that is, a phototautomerization, followed by a nonradiative relaxation of the vibrationally excited tautomer. It has been found that the fluorescence of the 1:2 PQ/methanol cluster is quenched only when the cluster is excited above the reaction barrier of about 1.9 kcal/mol. This value is an order of magnitude lower than the binding energy of the cluster, indicating the onset of a specific deactivation process. Such behavior can be correlated with the viscosity dependence of fluorescence quenching in alcohol solutions, which implies that the radiationless process involves large-amplitude motion of the alcohol molecules bonded to PQ. This motion, in turn, can be vibrationally activated. Accordingly, while for the 1:2 complex a fluorescence-detected infrared (FDIR) spectrum was readily recorded, this spectrum was not observed for the "dark" 1:1 aggregate.

A short excited state (*S*₁) lifetime, as well as an ionization potential higher than twice the value of the energy of the *S*₁ ← *S*₀ transition, prevents both the detection and structural analysis of the reactive precursors by conventional double-resonance IR resonant two-photon ionization depletion spectroscopy (IR/R2PI) using nanosecond lasers.⁸ However, by using femtosecond laser pulses for the photoionization step, we have recently demonstrated that ion depletion spectroscopy can also be successfully applied to multiphoton ionization via resonances in the continuum of excited states, with the drawback that the method is no longer isomer-specific and of limited size selectivity. This new technique was termed infrared/femtosecond multiphoton ionization spectroscopy (IR/fsMPI).⁹ Here the third harmonic of a titanium:sapphire (Ti:Sa) laser (266 nm) was used for a resonant two-photon ionization (R2PI) of PQ and its methanol clusters via a higher singlet excited state (*S*₄ or *S*₅) of ππ* character. By probing the ion signal of the PQ/methanol complexes by IR/fsMPI spectroscopy in the region of the hydrogen-bonded NH and OH stretch vibrations, cyclic doubly

and triply hydrogen-bonded structures were assigned, analogous to the 1:1 and 1:2 complexes depicted in Figure 1.⁹

In the present work we report IR/fsMPI and FDIR spectra of PQ/water_{*n*} complexes. The structural analysis of the vibrational fingerprints is performed by means of DFT calculations.

2. Experimental

2.1. Materials. 1*H*-Pyrrolo[3,2-*h*]quinoline (PQ) was synthesized and purified according to the procedures described earlier.¹⁰ Distilled water and helium of 4.6 grade were used for the preparation of PQ/water clusters under supersonic expansion conditions.

2.2. Methods. The details of laser-induced fluorescence (LIF) excitation and of FDIR¹¹ depletion spectroscopy have been described previously.⁷ The FDIR and IR-UV hole-burning¹² spectra were measured with modification of the earlier experiment with PQ/methanol, utilizing a tunable DMQ dye laser (FL2002/LPX200, LambdaPhysik) as the UV laser source.

The experimental setup for the IR/fsMPI measurements consists of a narrow band, injection-seeded nanosecond IR optical parametric oscillator (OPO) for vibrational excitation, a femtosecond chirped-pulse amplified Ti:Sa laser system for two-photon ionization of the clusters, and a vacuum apparatus, equipped with a heated pulsed nozzle and a home-built linear time-of-flight mass spectrometer. All components have been described previously in separate publications.^{13,14} Below, we briefly describe how these components were combined in the experiment.

The fundamental output (800 nm) of a femtosecond chirped-pulse amplified Ti:Sa laser system was frequency-tripled (efficiency 18%) resulting in laser pulses (30 μJ, 266 nm, 260 fs autocorrelation) that were used to photoionize PQ/water clusters. The femtosecond laser beam was spatially overlapped in the ionization region of the time-of-flight spectrometer with a counter-propagating nanosecond IR-OPO beam. Both laser beams crossed perpendicularly a pulsed molecular beam collimated from a seeded supersonic expansion of PQ and water with helium as the carrier gas at a stagnation pressure of 3 bar. The sample/nozzle temperature was maintained at about 380 K in order to have sufficient vapor pressure of PQ. The partial pressure of water was controlled by means of a gas mixing unit. The wavelength of the IR-OPO pulses (4 mJ, 0.2 cm⁻¹ fwhm, 6 ns) was scanned in the 3100–3450 cm⁻¹ region in order to record the IR/fsMPI depletion spectra. At each spectral point, the amplified and integrated time-of-flight signal corresponding to the selected PQ/water clusters was averaged over 40 laser shots. Finally, the spectra were averaged over up to 5 scans. The synchronization of the pulsed nozzle (General Valve, 10 Hz), IR-OPO (10 Hz), and 1 kHz femtosecond laser system was achieved with a digital delay generator (DG535, Stanford Research Systems) that was triggered by an arbitrary femtosecond laser pulse from the kHz sequence, so that after predetermined time delays, the pulsed nozzle and the IR-OPO laser were started. The nozzle delay was optimized in order to overlap in time a femtosecond laser pulse next to the trigger (1 ms later) with the molecular beam pulse in the ionization region of the mass spectrometer. The IR laser was fired 50 ns prior to the ionizing UV laser. This delay was set and checked with a photodiode. The delay generator was accepting an input trigger only every 100 ms, providing an effective repetition rate of 10 Hz.

3. Results

3.1. DFT Calculations. The geometry optimization of the 1:1 and 1:2 complexes of PQ with water in the ground and the

TABLE 1: Ground-State Binding Energies (in kcal/mol), Selected Distances (in Å), and Angles (in degrees) of Various PQ/Water (Methanol) Complexes

	1:1		1:1+1			1:2	
	methanol	water	methanol	water (1:1+1d)	water (1:1+1a)	methanol	water
$\Delta E(S_0)$	-10.4 ^a	-9.3 ^b	-11.8 ^{a,c}	-9.3 ^c	-11.0 ^c	-13.9 ^{a,c}	-12.6 ^{b,c}
R_1	1.880	1.907	1.938	1.975	1.848	1.870	1.906
R_2	1.831	1.816	1.763	1.740	1.900	1.798	1.785
R_3			1.882	1.905	1.975	1.742	1.753
Θ_1	156.8	156.1	154.5	153.6	158.8	166.0	163.8
Θ_2	165.2	165.7	168.4	168.9	162.0	174.5	173.1
Θ_3			174.4	171.3	178.2	162.4	161.7
\angle ONNO						23.2	17.7

^a Ref 7. ^b Ref 5. ^c The binding energy was evaluated for the interaction between PQ and a water (methanol) dimer, so that it does not include a contribution of water–water (methanol–methanol) hydrogen bonding. The energy of water–water (methanol–methanol) interaction was estimated to be -2.6 (-3.9) kcal/mol at the same level of theory.

first excited singlet states has recently been performed at the B3LYP/cc-pVDZ level of theory.⁵ The cyclic 1:2 complex has been found to be the most stable structure among the hydrogen-bonded clusters that are possible with two water molecules. Since several stable isomers corresponding to local minima could eventually also be stabilized in the supersonic beam, we considered additionally two other isomers of the 1:2 complex. Both configurations correspond to a modified 1:1 complex, in which the second water molecule is hydrogen-bonded to the water molecule of the cyclic 1:1 cluster either as a hydrogen-bonding acceptor (1:1+1a in Figure 1) or as a donor (1:1+1d in Figure 1). The basis set superposition error (BSSE) and zero-point energy (ZPE) corrected ground-state binding energies for all relevant complexes are presented in Table 1 together with the corresponding values for structurally related PQ/methanol clusters.⁷ Generally, the stabilization energies of the PQ/water complexes are lower by 10% than those of the PQ/methanol analogs.

Selected structural parameters (see Figure 1 for definition) of the PQ/water and PQ/methanol clusters are compared in Table 1. The hydrogen-bond length and angle values in the PQ/water clusters compared to PQ/methanol demonstrate systematically weaker hydrogen-bonding of the water bridge at the pyrrole site and a stronger one at the quinoline site. The latter can hardly be explained in terms of the relative hydrogen-bonding donor and acceptor abilities of water and methanol molecules. Apparently, the methanol complexes should be stronger in both senses as the isolated water exhibits both weaker proton affinity¹⁵ and acidity¹⁶ than methanol. In cyclic structures, a solvent-specific cooperativity effect comes into play as revealed by the non-additivity of hydrogen-bonding energies in the $n = 3,4$ clusters of water¹⁷ and methanol.¹⁸ Generally, small clusters of water and methanol form similar structures but the differences between them are determined by the methyl group of methanol. For the 1:2 complexes of PQ, the water bridge provides a more planar hydrogen-bonding network than the one with methanol. The characteristic ONNO dihedral angles in the ground state are 17.7 and 23.2 degrees for the water and methanol complexes, respectively. This effect may be explained by interaction between the methyl groups and the PQ molecule.

The binding energies, structures, and normal modes of the PQ/water complexes were calculated on the B3LYP/cc-pVDZ level of theory using the TURBOMOLE program package, Version 5.7,¹⁹ as published previously.⁵ Ground-state fundamental frequencies were obtained by scaling the harmonic values with a factor of 0.9704 as proposed by Witek and Morokuma.²⁰

3.2. LIF Excitation Spectrum. Changes in the LIF excitation spectrum of PQ after increase of the vapor pressure of water are depicted in Figure 2a. This spectrum was measured with

the apparatus in the Warsaw Laser Centre. New spectral features corresponding to the onset of cluster formation show great similarity to those observed in the spectra with methanol. The band at 28061 cm^{-1} is assigned to the vibrational origin of the smallest cluster of PQ with water which exhibits fluorescence. Relative to the origin of bare PQ at 29524 cm^{-1} ,²¹ it is red-shifted by 1463 cm^{-1} .

We also recorded an IR/UV hole-burning spectrum with the IR-laser tuned to 3411 cm^{-1} . As will be shown in the following, this frequency corresponds to one of the vibrations measured by FDIR detecting a total yield of fluorescence with the UV laser tuned to 28061 cm^{-1} . If all the solvent-induced spectral features in Figure 2a are from the same neutral cluster, their intensity should be equally decreased when recorded with the IR-burn laser switched on. Since this was the case (Figure 2b), we can assign these solvent-induced bands to only one solvated species, which still has to be assigned. For recording the hole-burning spectrum we used the experimental setup in Frankfurt. There it was not possible to measure the LIF spectrum above $\approx 28300 \text{ cm}^{-1}$ due to limited efficiency of the dye used. For this reason we could not extend the hole-burning spectrum beyond this energy limit.

The red-shift of the origin with respect to the location in bare PQ (1463 cm^{-1}) can be compared with the analogous shift observed for the PQ/methanol₂ complex (1651 cm^{-1}) which was unambiguously assigned by means of FDIR spectroscopy.⁷ It should also be pointed out that the LIF spectrum disappears at excess energies above 471 cm^{-1} , which compares well with the spectrum of the PQ/methanol₂ complex which is quenched beyond 663 cm^{-1} .

3.3. FDIR and IR/fsMPI Spectra. The ground-state FDIR depletion spectrum measured by probing the fluorescence signal upon excitation of the band at 28061 cm^{-1} is shown in Figure 3a. While only very weak IR activity, if at all, was detected for the region of free OH vibrations, three intense bands at 3140, 3310, and 3411 cm^{-1} are observed corresponding to the hydrogen-bonded NH and OH stretching vibrations, significantly red-shifted in their values from those observed for the isolated molecules: 3507 cm^{-1} for PQ,⁷ and 3657 and 3756 cm^{-1} for water.²³ Hence, the fluorescent species possesses three hydrogen bonds, indicating that at least two water molecules must be involved in the cluster responsible for the LIF spectrum. Since structurally related PQ/methanol _{$n=1,2$} clusters reveal IR activity in the same region,⁷ we further concentrated on the 3100–3450 cm^{-1} spectral part.

The IR/fsMPI spectra measured in parallel for the PQ⁺/water _{n} ($n = 0, 1, \text{ and } 2$) ion channels are presented in Figure 3 (traces d, c, and b, respectively). These spectra are nearly saturated because they were taken with a tightly focused laser beam in

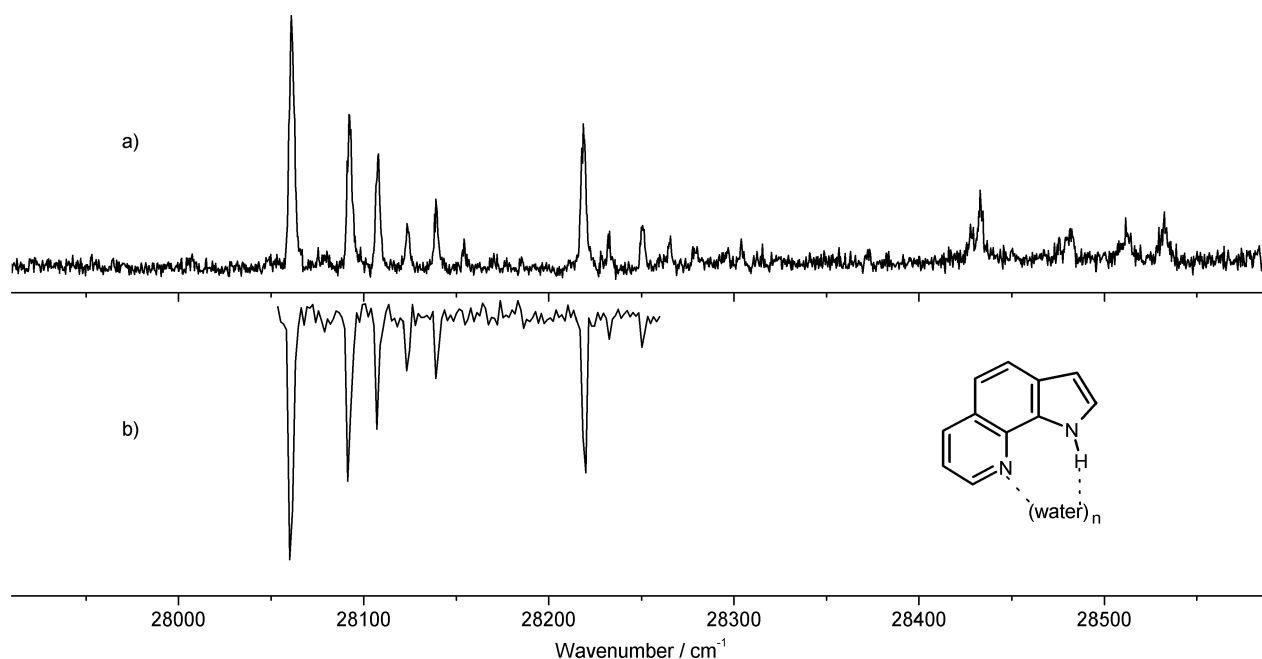


Figure 2. LIF excitation spectrum (a) and IR-UV hole-burning spectrum at 3411 cm^{-1} (b) recorded in the region where the PQ/water_{*n*=1,2} clusters should exhibit spectral activity according to our calculations.⁵

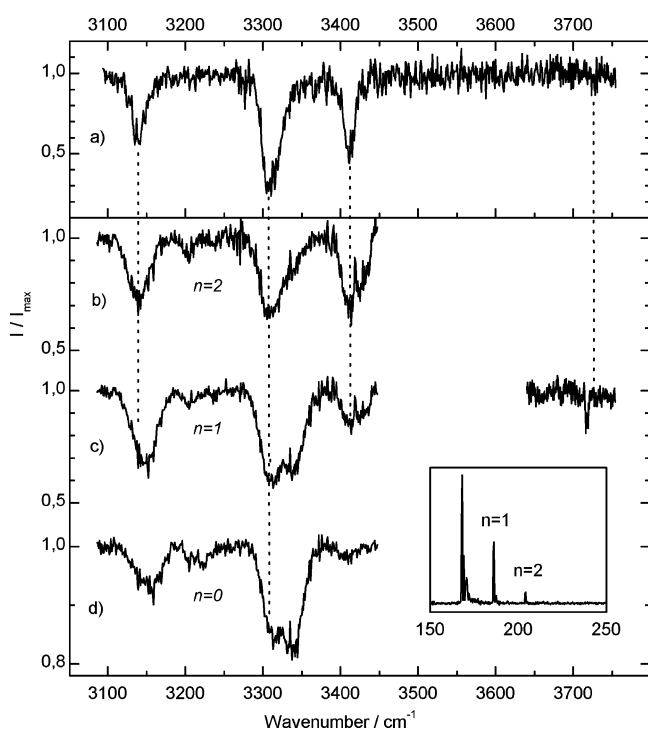


Figure 3. A comparison of the FDIR spectrum (a) measured upon excitation of the transition at 28061 cm^{-1} with the IR/fsMPI spectra recorded in (b) $1^{+}:2$, (c) $1^{+}:1$, and (d) $1^{+}:0$ cluster channels.²² The inserted mass spectrum shows the corresponding cluster ion distribution. The dotted line above 3700 cm^{-1} indicates the very weak free OH stretch, which is also very weak in the calculated spectra (Figure 5).

order to detect weaker double resonance bands. While the depletion of the fluorescence signal reached a value of 75%, significant cluster fragmentation caused the ion depletion not to exceed 40% at signal levels that were one-to-two orders of magnitude weaker than that of fluorescence. The IR/fsMPI spectrum detected for the PQ⁺/water₂ ion signal (Figure 3b) matches the above FDIR spectrum very well. Weaker additional features at 3205 and 3430 cm^{-1} can arise from larger clusters fragmenting into this ion channel or can be due to less stable

isomers of the 1:2 complex. The spectra of the clusters larger than 1:2 were not measured due to insufficient levels of the corresponding ion signals (see the mass spectrum in Figure 3). Close similarity of the spectra depicted in Figure 3, parts a and b, proves that the smallest fluorescent complex of PQ with water contains two solvent molecules. It should be emphasized that the photoionization of the PQ clusters by femtosecond laser pulses at 266 nm is not isomer-selective. It can be therefore concluded that one conformer of the PQ complex with two water molecules is dominant in all spectra under supersonic jet conditions.

The bands at 3310 and 3411 cm^{-1} are common for the spectra of the $1^{+}:1$ and $1^{+}:2$ ions, thus providing evidence for the fragmentation of the heavier complex by loss of one water molecule. In the depletion spectrum of the $1^{+}:1$ channel (Figure 3c) one band appears at 3148 cm^{-1} , at a slightly different wavelength than the band at 3140 cm^{-1} recorded on the $1^{+}:2$ cluster (Figure 3b). This fact indicates two close-lying transitions of the 1:1 and 1:2 clusters which overlap in the lower mass channel. The peak at 3341 cm^{-1} is observed exclusively for the $1^{+}:1$ and the $1^{+}:0$ channels and therefore must stem from the 1:1 complex. Actually, the spectrum recorded at the monomer ion channel (Figure 3d) reveals all the features found for the $1^{+}:1$ ions, however, again with different relative intensities of the particular bands.

It was not possible to find expansion conditions under which only 1:1 complexes were formed. The $1^{+}:1$ channel was contaminated by contributions from fragmenting higher clusters, manifested by the 3310 cm^{-1} band always appearing in the depletion spectrum of the $1^{+}:1$ channel. However, it was straightforward to distinguish between species belonging to different stoichiometry. For that, the spectra recorded in the $1^{+}:1$ channel were compared for different water pressures in Figure 4. The ratio between the peaks at 3341 and 3310 cm^{-1} increased for smaller water concentrations. At the same time, the low-energy band around 3150 cm^{-1} shifted to the blue by about 10 cm^{-1} ; this was accompanied by a decrease in intensity. These findings leave no doubt about the assignment of 3341 and 3310 cm^{-1} bands to 1:1 and 1:2 stoichiometry, respectively. They

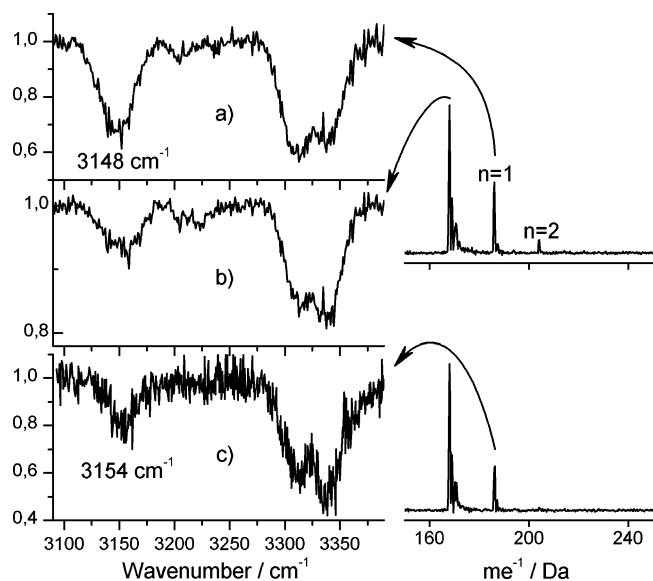


Figure 4. IR/fsMPI spectra measured in the $1^+ : 1$ (a,c) and $1^+ : 0$ (b) PQ/water cluster channels. Parts (a) and (c) represent different cluster distributions. The corresponding mass spectra are shown on the right.

also confirm that both types of complexes absorb at around 3150 cm^{-1} , albeit with different probabilities, and that the corresponding vibrational transition in the 1:1 complex is weaker and blue-shifted with respect to that of the 1:2 species. These conclusions were firmly corroborated by comparing band intensities in the $1^+ : 2$, $1^+ : 1$, and $1^+ : 0$ channels (Figure 3, parts b–d), with the contributions of the bands assigned to 1:1 species being stronger in the $1^+ : 0$ channel than that assigned to the 1:2 complex (it should be stressed that these signals were obtained simultaneously, in the same experiment).

In order to obtain a separate spectrum of the 1:1 complex alone, the depletion spectrum of the $1^+ : 2$ ions (Figure 3b) was subtracted from that recorded in the $1^+ : 1$ channel (Figure 3c). Such methodology is well-established, for example, in the analysis of linear dichroism spectra, where it is known as a “stepwise reduction procedure”.²⁴ In order for this approach to be reliable the peak positions must be separated in the two spectra. This is the case for the bands at 3310 and 3341 cm^{-1} , but not for the bands around 3150 cm^{-1} . The former two can be therefore safely separated by finding a linear combination of the spectra for which the feature at 3310 cm^{-1} disappears completely. In principle, one could use the same weighting factor for the whole spectrum. However, it is quite probable that the fragmentation efficiency is vibrational-mode-dependent (for instance, mode-specific IVR/predissociation dynamics has been demonstrated for phenol dimer in the picosecond IR-UV pump–probe investigations by Ebata et al.²⁵). For this case, a single weighting factor is not justified. We have therefore performed the subtraction using different factors for different bands. The results reveal a remarkable stability in the band frequency ($\pm 2\text{ cm}^{-1}$). An additional criterion for a proper choice of the weighting coefficients is the limitation that the obtained signal should not exceed unity, since only depletion is experimentally observed. Using the above approach, one obtains a spectrum of the 1:1 complex shown in Figure 5a. We consider the band positions in the spectrum to be quite reliable, whereas the relative intensities may be uncertain; we estimate the inaccuracy of the intensity ratio to lie within $\pm 25\%$.

Having obtained by this analysis the vibrations of the complexes with one and two water molecules, one can determine their contributions to the depletion spectrum of the $1^+ : 0$ channel

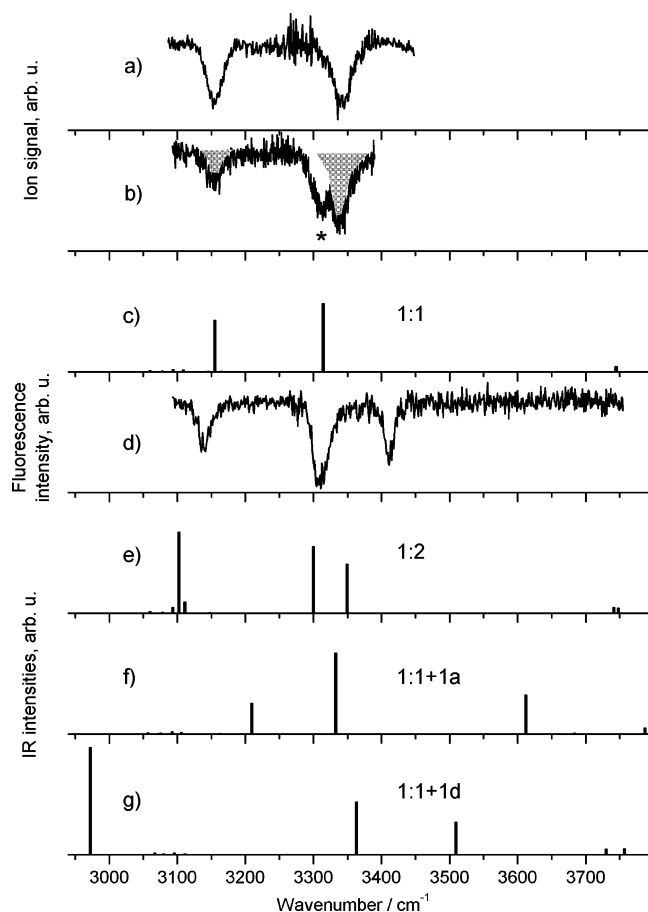


Figure 5. The ground-state vibrational spectra of the 1:1 (a,b) and 1:2 (d) complexes. Spectrum (a) was obtained using the subtraction procedure, and spectrum (b) was recorded directly in the $1^+ : 1$ channel at low water concentration. The asterisk denotes the band of the 1:2 complex caused by fragmentation. The “IR fingerprints” of the relevant clusters, calculated at the B3LYP/cc-pVDZ level of theory, are depicted by the stick spectra (c, e–g).

TABLE 2: Relative Intensities of the Vibrational Bands Detected in the Depletion Spectra in Different Ion Channels by IR/fsMPI Spectroscopy

ion channel	1:1		1:2		
	3155 cm^{-1}	3341 cm^{-1}	3140 cm^{-1}	3310 cm^{-1}	3411 cm^{-1}
$1^+ : 2$			0.30	0.35	0.35
$1^+ : 1$	0.20	0.20	0.20	0.35	0.15
$1^+ : 0$	0.05	0.15	0.05	0.12	0.02

(Figure 3d). The relative intensities of the particular vibrations in the spectra measured in all three ion channels are summarized in Table 2. Their different values in the lower ion channels give evidence that photofragmentation efficiency depends on the mode of the vibrational preexcitation.

3.4. Vibrational Analysis of the IR Spectra. The vibrational spectra assigned above to the PQ/water_{*n*=1,2} complexes and the theoretical IR “fingerprints” are compared in Figure 5. Excellent agreement of the experimental and calculated spectra of the 1:1 cluster (Figure 5, parts a–c) in the region of hydrogen-bonded NH and OH stretch vibrations provides a strong argument for the cyclic double hydrogen-bonded structure (1:1 in Figure 1) of this species. The bands at 3341 and 3155 cm^{-1} are readily identified as simultaneous out-of-phase and in-phase stretches of the hydrogen-bonded NH and OH groups, respectively (Figure 6). The in-phase vibration may be considered as a double proton-transfer promoting mode.

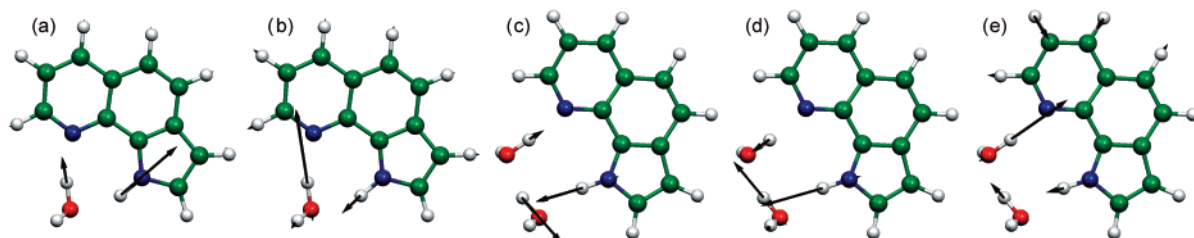


Figure 6. Normal modes showing hydrogen-bonded NH and OH stretching motions, calculated for the 1:1 and 1:2 PQ/water complexes: (a) 3314 cm^{-1} , (b) 3155 cm^{-1} , (c) 3349 cm^{-1} , (d) 3300 cm^{-1} , and (e) 3103 cm^{-1} .

TABLE 3: Experimental and Theoretical Frequencies of Hydrogen-Bonded NH and OH Stretch Vibrations of Selected PQ/Water Complexes

species	$\nu_{\text{calc}}/\text{cm}^{-1}$	$\nu_{\text{exp}}/\text{cm}^{-1}$	mode description
1:1	3314	3341	out-of-phase $\text{NH}\cdots\text{O}$ and $\text{OH}\cdots\text{N}$
	3155	3155	“proton transfer”
1:2	3349	3411	water dimer OH
	3300	3310	out-of-phase $\text{NH}\cdots\text{O}$ and $\text{OH}\cdots\text{N}$
	3103	3140	“proton transfer”
1:1+1a	3612		water dimer OH
	3333		out-of-phase $\text{NH}\cdots\text{O}$ and $\text{OH}\cdots\text{N}$
	3210		“proton transfer”
1:1+1d	3509		water dimer OH
	3363		out-of-phase $\text{NH}\cdots\text{O}$ and $\text{OH}\cdots\text{N}$
	2972		“proton transfer”

Of the three complexes containing two water molecules, the mode pattern calculated for the 1:2 (Figure 5e) exhibits the closest agreement with experiment (Figure 3, parts a and b). Since the spectrum in Figure 3b represents the major spectral features detected in the depletion spectrum of the 1⁺:2 channel and the minor additional features of the latter are assignable to fragmentation, we can rule out a significant amount of the additional complexes of the same stoichiometry, such as the 1:1+1a and 1:1+1d, under our experimental conditions. The calculated binding energies indicate that these clusters should be less stable by several kcal/mol relative to the 1:2 complex (Table 1). Hence, the bands at 3411, 3310, and 3140 cm^{-1} are assigned to the donor OH stretch of the water dimer, the out-of-phase $\text{NH}\cdots\text{O}$ and $\text{OH}\cdots\text{N}$ and the in-phase “proton transfer” vibrational modes, respectively. The above assignment is summarized in Table 3. The relevant normal modes are visualized in Figure 6. Interestingly, the assignment of the 3310 and 3341 cm^{-1} bands to the out-of-phase $\text{NH}\cdots\text{O}$ and $\text{OH}\cdots\text{N}$ modes of the 1:2 and 1:1 complexes, respectively, is corroborated by an enhanced contribution of those bands to the 1⁺:0 fragment channel (Figure 3, Table 2) reflecting the repulsive character of the concerted oscillation of the protons between the chromophore and the water bridge. By comparison of MP2 and DFT calculations, we previously demonstrated that the contribution of particular local stretches to the normal modes may significantly change depending on the level of theory.⁷ However, their sequence frequency is not affected. The same frequency order of the stretch modes has been observed for other systems with a triple hydrogen-bonding cycle, such as 7-hydroxyquinoline/methanol.²⁶

4. Discussion

Even though the IR/fsMPI technique resembles in many aspects the hole-burning procedures, the basic difference has to be pointed out. In general, the IR/fsMPI approach is not specific with respect to stoichiometry (size), structure, or spectra. Therefore, the obtained spectra may at first look rather imperfect, since they can contain contributions from different species. Moreover, the relative contributions, even in the same channel,

may not properly reflect the IR absorption probability, since the signal may be vibrational-mode-specific. However, advantages are overwhelming. One gets a possibility to simultaneously monitor the behavior of different species present in the system, in particular the short-lived ones, which escape detection by other techniques, such as FDIR. In principle, the complicated pattern of peak intensities in various channels could also be used to trace down the pathways of dissociation.

The negative depletion signal in all ion channels suggests that vibrational excitation leads to a decrease of the UV absorption probability or to depopulation of the species, or to a combination of both. The former factor can be caused by a change of Franck–Condon overlap of the optical transition upon IR excitation. This mechanism provides the possibility to measure IR depletion spectra of covalently bound molecules, for which predissociation of subunits is energetically not possible. Noncovalently bound clusters can fragment in this way. The present IR/fsMPI spectra, dominated by fragmentation, indicate that dissociation is the main source of the signal. Depending on the binding energy and photoionization conditions, the process can occur in the ground, excited, and ionic states. As we observed only depletion signals, the fragments had enough initial energy to escape the beam. The required kinetic resource was provided by photoionization with considerable excess energy (2×266 nm).

FDIR and IR/fsMPI measurements demonstrate that the smallest fluorescing microhydrate contributing to the LIF excitation spectrum must be assigned to the PQ/water₂ complex. Failure to detect the 1:1 clusters in the LIF spectrum can be due to its rapid depopulation via ESPT. This is the most reliable explanation based on solution data,^{1,4,27} calculations,^{5–6} and studies of jet-cooled PQ/methanol clusters.^{7,9} Other possible mechanisms of rapid excited-state deactivation, such as intersystem crossing or enhanced internal conversion, have been discussed in numerous previous works.^{27–32} Transient absorption spectroscopy results demonstrated that the intersystem crossing channel becomes inefficient in protic solvents.²⁸ In turn, enhanced internal conversion was found to be efficient in solvates of 1:2 stoichiometry.^{27,28,30}

The 3341 cm^{-1} band, assigned to the 1:1 complex with water, is 73 cm^{-1} higher in energy than the corresponding vibration in the 1:1 complex with methanol (3268 cm^{-1}). Similarly, the 3310 and 3411 cm^{-1} vibrations of the 1:2 complex with water also exhibit blue-shifts of 105 and 79 cm^{-1} in comparison with the 3205 and 3332 cm^{-1} bands, observed with methanol. The energy of the water dimer OH-donor vibration (3411 cm^{-1}) is shifted by -190 cm^{-1} relative to that of the isolated water dimer (3601 cm^{-1}), as reported by Huisken et al.³³ The corresponding frequency reduction of the OH-donor dimer vibration in the case of the methanol 1:2 complex was found to be -242 cm^{-1} . Since for a similar cluster structure the value of the red-shift of a donor stretch correlates with the strength of the hydrogen bond, the hydrogen bond in the 1:1 and 1:2 clusters with methanol is

stronger than with water. The above relations are in good agreement with the calculated binding energies, which are repeatedly larger for the methanol complexes (Table 1).

5. Conclusions

In this work, we have investigated the structure of isolated PQ/water_{*n*} (*n* = 1,2) complexes. By combining the IR/fsMPI and FDIR spectroscopies in the region of hydrogen-bonded NH and OH stretch vibrations with DFT calculations, we detected two different complexes of PQ with water. The structures of the 1:1 and 1:2 clusters were assigned to cyclic doubly and triply hydrogen-bonded species, respectively (Figure 1), similar to the analogous system with methanol. The photofragmentation efficiency of the clusters in the applied IR/fsMPI scheme was found to be affected by vibrational preexcitation, depending on the vibrational mode. Both 1:1 and 1:2 complexes of PQ with water reveal weaker hydrogen bonding than those with methanol.

Acknowledgment. We dedicate this work to the memory of Roger E. Miller, a true pioneer of cluster spectroscopy, who stimulated us by his seminal scientific contributions to this field. Y.N. acknowledges support from the EC Grant G5MA-CT-2002-04026. C.R. acknowledges gratefully the Adolf-Messer-Stiftung, the friends and promoters of the University of Frankfurt/Main, and the DFG. R.P.T. thanks the Robert A. Welch Foundation and the NSF for financial support. B.B. thanks the DFG for funding by the German-French binational research program.

References and Notes

- (1) Kyrychenko, A.; Herbich, J.; Izydorzak, M.; Wu, F.; Thummel, R. P.; Waluk, J. *J. Am. Chem. Soc.* **1999**, *121*, 11179–11188.
- (2) del Valle, J. C.; Domínguez, E.; Kasha, M. *J. Phys. Chem. A* **1999**, *103*, 2467–2475.
- (3) Kijak, M.; Zielińska, A.; Thummel, R. P.; Herbich, J.; Waluk, J. *Chem. Phys. Lett.* **2002**, *366*, 329–335.
- (4) Marks, D.; Zhang, H.; Borowicz, P.; Waluk, J.; Glasbeek, M. *J. Phys. Chem. A* **2000**, *104*, 7167–7175.
- (5) Kyrychenko, A.; Waluk, J. *J. Phys. Chem. A* **2006**, *110*, 11958–11967.
- (6) Kyrychenko, A.; Stepanenko, Y.; Waluk, J. *J. Phys. Chem. A* **2000**, *104*, 9542–9555.
- (7) Nosenko, Y.; Kyrychenko, A.; Thummel, R. P.; Waluk, J.; Brutschy, B.; Herbich, J. *Phys. Chem. Chem. Phys.* **2007**, *9*, 3276–3285.
- (8) (a) Page, R. H.; Shen, Y. R.; Lee, Y. T. *J. Chem. Phys.* **1988**, *88*, 4621–4636. (b) Riehn, C.; Lahmann, C.; Wassermann, B.; Brutschy, B. *Chem. Phys. Lett.* **1992**, *197*, 443–450. (c) Tanabe, S.; Ebata, T.; Fujii, M.; Mikami, N. *Chem. Phys. Lett.* **1993**, *215*, 347–352. (d) Pribble, R. N.; Zwier, T. S. *Science* **1994**, *265*, 75–79.
- (9) Nosenko, Y.; Kunitski, M.; Thummel, R. P.; Kyrychenko, A.; Herbich, J.; Waluk, J.; Riehn, C.; Brutschy, B. *J. Am. Chem. Soc.* **2006**, *128*, 10000–10001.
- (10) Wu, F.; Chamchoumis, C. M.; Thummel, R. P. *Inorg. Chem.* **2000**, *39*, 584–590.
- (11) (a) Walther, Th.; Bitto, H.; Minton, T. K.; Huber, J. R. *Chem. Phys. Lett.* **1994**, *231*, 64–69. (b) Ebata, T.; Mizuochi, N.; Watanabe, T.; Mikami, N. *J. Chem. Phys.* **1996**, *100*, 546–550.
- (12) Brutschy, B. *Chem. Rev.* **2000**, *100*, 3891–3920.
- (13) Weichert, A.; Riehn, C.; Barth, H.-D.; Lembach, G.; Zimmermann, M.; Brutschy, B.; Podenas, D. *Rev. Sci. Instrum.* **2001**, *72*, 2697–2708.
- (14) Krauss, O.; Brutschy, B. *Chem. Phys. Lett.* **2001**, *350*, 427–433.
- (15) Lias, S. G.; Bartmess, J. E.; Liedman, J. F.; Holmes, J. L.; Levin, R. D.; Mallard, W. G. *J. Phys. Chem. Ref. Data* **1988**, *17*, Suppl. 1.
- (16) Taft, R. W.; Koppel, I. A.; Topsom, R. D.; Anvia, F. *J. Am. Chem. Soc.* **1990**, *112*, 2047–2052.
- (17) Lee, H. M.; Suh, S. B.; Lee, J. Y.; Tarakeshwar, P.; Kim, K. S. *J. Chem. Phys.* **2000**, *112*, 9759–9772.
- (18) Hagemeyer, F. C.; Gruenloh, C. J.; Zwier, T. S. *Phys. Chem. A* **1998**, *102*, 82–94.
- (19) Ahlrichs, R.; Bär, M.; Häser, M.; Hom, H.; Kölmel, C. *Chem. Phys. Lett.* **1989**, *162*, 165–169.
- (20) Witek, H. A.; Morokuma, K. *J. Comput. Chem.* **2004**, *25*, 1858–1864.
- (21) Krauss, O. Ph.D. Thesis, Goethe University, Frankfurt/M, Germany, 2002.
- (22) The IR/fsMPI spectra have been recorded in a somewhat smaller range than the FDIR spectrum. This was due to technical problems, such as significantly reduced IR intensity within 3450–3500 cm⁻¹ and thermal pointing instability of the femtosecond laser system, which allowed only a limited scanning range without readjustment. Due to the great similarity of the absorption bands observed in the IR/fsMPI and FDIR spectra (Figure 3, parts a and b), the former was recorded only up to 3450 cm⁻¹.
- (23) Herzberg, G. *Molecular Spectra and Molecular Structure*; Van Nostrand Reinhold: New York, 1945; Vol. 2.
- (24) Thulstrup, E. W.; Michl, J. *J. Am. Chem. Soc.* **1982**, *104*, 5594–5604.
- (25) Ebata, T.; Kayano, M.; Sato, S.; Mikami, N. *J. Phys. Chem. A* **2001**, *105*, 8623–8628.
- (26) Matsumoto, Y.; Ebata, T.; Mikami, N. *J. Phys. Chem. A* **2002**, *106*, 5591–5599.
- (27) Waluk, J. *Acc. Chem. Res.* **2003**, *36*, 832–838.
- (28) Herbich, J.; Hung, C. Y.; Thummel, R. P.; Waluk, J. *J. Am. Chem. Soc.* **1996**, *118*, 3508–3518.
- (29) Dobkowski, J.; Herbich, J.; Galievsky, V.; Thummel, R. P.; Wu, F. Y.; Waluk, J. *Ber. Bunsen-Ges. Phys. Chem.* **1998**, *102*, 469–475.
- (30) Kyrychenko, A.; Herbich, J.; Wu, F.; Thummel, R. P.; Waluk, J. *J. Am. Chem. Soc.* **2000**, *122*, 2818–2827.
- (31) Herbich, J.; Waluk, J.; Thummel, R. P.; Hung, C. Y. *Photochem. Photobiol. A: Chem.* **1994**, *80*, 157–160.
- (32) Herbich, J.; Rettig, W.; Thummel, R. P.; Waluk, J. *Chem. Phys. Lett.* **1992**, *195*, 556–562.
- (33) Huisken, F.; Kaloudis, M.; Kulcke, A. *J. Chem. Phys.* **1996**, *104*, 17–25.

**9.6 Proton transfer with a twist? Femtosecond dynamics of
7-(2'-pyridyl)-indole in condensed phase and in supersonic jets**

Proton transfer with a twist? Femtosecond Dynamics of 7-(2-pyridyl)-indole in Condensed Phase and in Supersonic Jets**

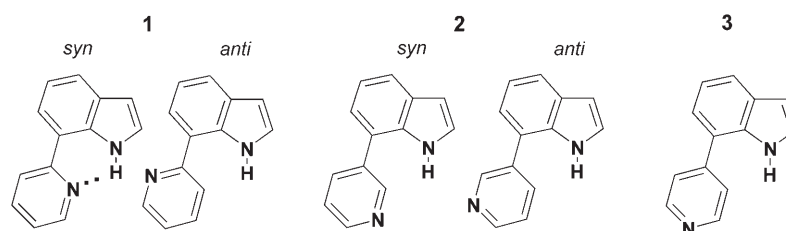
Y. Nosenko, G. Wiosna-Sałyga, M. Kunitski, I. Petkova, A. Singh, W. J. Buma,* R. P. Thummel,* B. Brutschy,* and J. Waluk*

The results of spectral and photophysical studies strongly suggest that photoinduced proton transfer in 7-(2-pyridyl)indole (**1**) is accompanied by mutual twisting of the pyridyl and indole moieties. This conclusion is supported by the unusual finding that the photoreaction is faster in a cold, supersonic-jet-isolated molecule than in solutions at room temperature, and by the ultrafast repopulation of the ground state substrate. The twisting and the presence of S_1 - S_0 conical intersection (CI) are also predicted by calculations. The phenomenon may be quite general for several classes of organic molecules with intramolecular hydrogen bonds.

Recent experimental and theoretical developments demonstrate that proton transfer—a fundamental chemical reaction—is by no means a one-dimensional process.^[1] In particular, for tautomerization occurring along a hydrogen bond, coupling with modes that modulate the hydrogen bond strength may be crucial.^[2] Much less explored is the possibility

of large conformational changes accompanying proton/hydrogen transfer, although the role of torsional motion in the deactivation of phototautomerization products has been discussed in some depth.^[3–9]

Compound **1** is a member of a series of three isomeric 7-pyridylindoles (Scheme 1), which were studied previously in solution.^[10] Compounds **1** and **2** can exist in *syn* and *anti* rotameric forms. In **1** there is no doubt that the dominant



Scheme 1. The structure of three isomeric 7-pyridylindoles.

[*] Prof. Dr. W. J. Buma
Van't Hoff Institute for Molecular Sciences
University of Amsterdam
Nieuwe Achtergracht 166, 1018 WV Amsterdam (The Netherlands)
Fax: (+31) 20 525 5604
E-mail: w.j.buma@uva.nl

A. Singh, Prof. Dr. R. P. Thummel
University of Houston
Houston, TX 77204-5003 (USA)
Fax: (+1) 713-743-2709
E-mail: thummel@uh.edu

Dr. Y. Nosenko, M. Kunitski, Prof. Dr. B. Brutschy
Institut für Physikalische und Theoretische Chemie
Universität Frankfurt
Max-von-Laue-Strasse 7, 60438 Frankfurt/M (Germany)
Fax: (+49) 697-982-9560
E-mail: brutschy@chemie.uni-frankfurt.de

G. Wiosna-Sałyga, Prof. Dr. J. Waluk
Institute of Physical Chemistry
Polish Academy of Sciences
Kasprzaka 44, 01-224 Warsaw (Poland)
Fax: (+48) 22-631-1619
E-mail: waluk@ichf.edu.pl

Dr. I. Petkova
Institute of Organic Chemistry
Bulgarian Academy of Sciences, Sofia (Bulgaria)

[**] The work was sponsored by a KBN grant 1T09A 016 30, EC Grant G5MA-CT-2002-04026, and NWO grant 048.021.2003.011. R.P.T. and A.S. thank the Robert A. Welch Foundation and the NSF. B.B. thanks the Deutsche Forschungsgemeinschaft for funding of the project.

species corresponds to the planar, intramolecularly H-bonded *syn* form. Calculations predict this *syn* rotamer to be about 5 kcal mol⁻¹ more stable than the *anti* rotamer which lacks the intramolecular H-bond and is nonplanar because of steric repulsion between indolyl NH and pyridyl CH. In **2**, both rotamers should have a nonplanar structure and similar energies; calculations predict the *syn* form to be more stable, but only by less than 0.5 kcal mol⁻¹.

For compounds **2** and **3**, in which the indolyl moiety is respectively in the *meta* and *para* positions with respect to the pyridine nitrogen atom, strong fluorescence is observed at 293 K both in nonpolar and polar aprotic solvents.^[10] This is not the case for **1**, which fluoresces extremely weakly. Moreover, fluorescence excitation spectra of **1** do not coincide with the absorption, being shifted to the blue by about 2×10^3 cm⁻¹ (Figure 1). We therefore assign the fluorescence to a small fraction of *anti* rotamers. Such an assignment is corroborated by the fact that the fluorescence quantum yield in *n*-hexane is about ten times weaker than in acetonitrile (0.0005 and 0.006, respectively). Calculations predict a larger dipole moment for the *anti* form and, therefore, its population should increase with solvent polarity. The *anti* population can also be enhanced in alcohols, which can form two independent hydrogen bonds with **1-anti**, one to the indolyl NH and the other to the pyridyl nitrogen atom. Another strong argument for the assignment of the emitting species to the *anti* form is that the energy calculated for transition to the lowest excited singlet state for **1-anti** is 0.4 eV

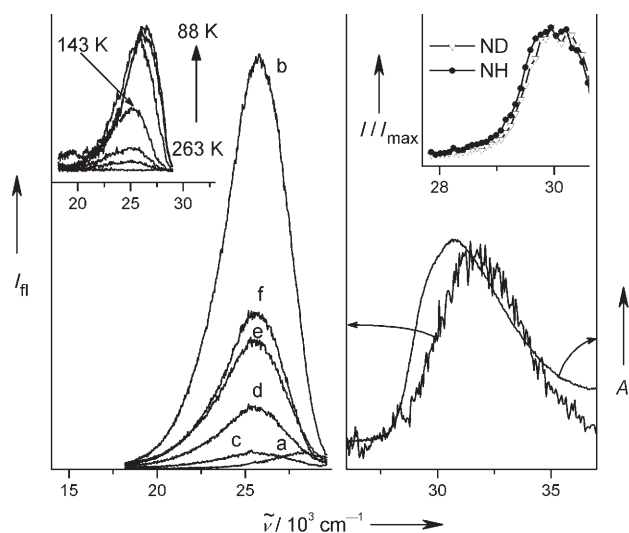


Figure 1. Left: fluorescence of **1** at 293 K: a) *n*-hexane, b) acetonitrile, c) methanol, d) ethanol, e) 1-propanol, f) 1-butanol; inset, temperature dependence measured in the 1:1 methanol:ethanol mixture. Right: room temperature absorption and fluorescence excitation of **1** in 1-propanol (monitored at $25\,000\text{ cm}^{-1}$); inset: one-color REMPI spectra of jet-cooled **1** and its ND isotopologue.

higher than that for **1-syn**.^[9] This prediction is in excellent agreement with the observed difference between the maxima of the fluorescence excitation and absorption spectra.

The lack of detectable fluorescence from **1-syn** implies that nearly all the photoexcited molecules of **1**, that is, those corresponding to the *syn* form, decay very rapidly. This rapid decay was confirmed by transient absorption (TA) spectroscopy (Figure 2). The initially excited species reveals a characteristic TA spectrum, which decays in about $1.0 \pm 0.2\text{ ps}$. After that, no significant signal is observed throughout the whole available spectral range, except for a region around 360 nm, where a component is found decaying in a few ps. Since this region is close, but slightly to the red of the onset of stationary absorption, we assign this decay to cooling of the hot molecule in the ground state. Essentially the same spectra and similar decay time were observed in solvents differing in polarity and proticity: *n*-hexane, acetonitrile, CH_3OH ,

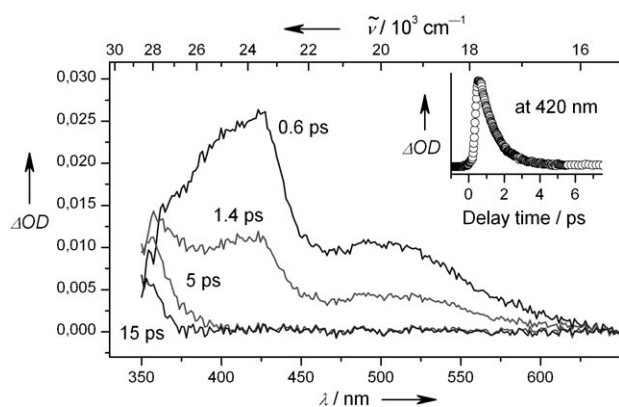


Figure 2. Transient absorption spectra of **1** in acetonitrile at 293 K; inset, decay of TA signal probed at 420 nm.

CH_3OD , 1-propanol, ethylene glycol, and decanol. In decanol and CH_3OD the decay was somewhat slower, 1.7 and 1.9 ps, respectively.

The explanation for the rapid decay of electronically excited **1-syn** is the excited state proton transfer, which occurs along the intramolecular hydrogen bond. Calculations predict that the reaction should be barrierless^[9] and therefore should also occur in a cold, isolated molecule. Attempts to detect photoexcited **1** in a jet using nanosecond laser pulses were not successful, indicating that lowering the temperature does not stop a rapid depopulation of S_1 . Therefore, the jet setup was modified by shortening the excitation/ionization pulses. In these experiments, molecules of **1** were ionized resonantly via S_1 by laser pulses of about 200 fs duration, using either one-color or two-color schemes. The resonance-enhanced multiphoton ionization (REMPI) signal onset was observed at about $29 \times 10^3\text{ cm}^{-1}$, similar to the room-temperature absorption (Figure 1). Figure 3 presents the kinetic profiles of the

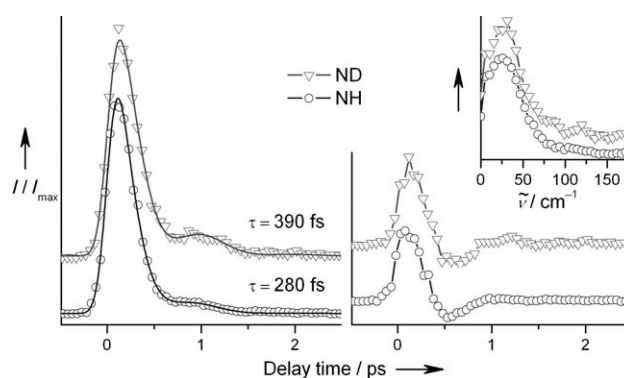


Figure 3. Left: pump-probe REMPI spectra (○) obtained in a supersonic jet for **1** and its N-deuterated analogue (▽); solid lines are the results of the fitting procedure. Right: oscillatory components of the data and their Fourier transforms (inset).

ion signals. Interestingly, the decay is not monotonic: a second small maximum is observed at about 1 ps after excitation and its intensity is higher in the deuterated molecule. Convolution of a Gaussian with a harmonically modulated monoexponential decay: $(1 + a \cdot \cos(\omega t + \phi)) \cdot \exp(-t/\tau)$, provided a satisfactory fit to the experimental data. A very fast decay of the ion signal, 280 fs, was extracted. In the N-deuterated molecule the lifetime of the initially excited species increases to 390 fs. The cosine frequency was about 34 cm^{-1} in both cases.

The *syn* structure of the absorbing species was confirmed by using the IR/fsMPI technique (IR absorption detected by femtosecond multiphoton ionization).^[11,12] The IR/fsMPI spectrum of **1** reveals a band at 3412 cm^{-1} , assigned to the NH stretch of the *syn* form (Figure 4). This value indicates a fairly strong red shift assigned to an intramolecular hydrogen bond; the value for bare indole in the jet is 3525 cm^{-1} .^[13]

For comparison, IR/R2PI spectra (IR absorption detected by resonance two-photon ionization) were also recorded, using ns laser pulses, for 2-(2-pyridyl)indole (**4**) and its bridged derivative, 3,3'-dimethylene-2-(2-pyridyl)indole (**5**). Both molecules should have intramolecular hydrogen bonds weaker than **1**, especially the bridged derivative. These

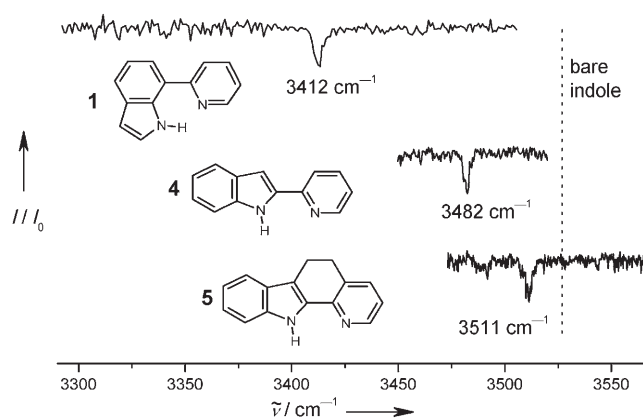


Figure 4. The ionization-detected absorption of three pyridylindoles.

expectations are fully confirmed by the higher NH stretching vibrational transition frequency (Figure 4).

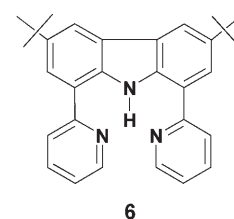
The observation that the photoexcited population of **1** decays in a cold molecule much faster than at room temperature may seem at first rather odd. However, it can be rationalized on the basis of both experiment and calculations. Analysis of the excited state potential energy profile obtained at the CC2/cc-pVDZ level reveals a barrierless hydrogen transfer coupled to the indole-pyridine torsional coordinate.^[9] The initially excited structure is unstable with respect to torsion around the C–C bond joining the two moieties. A shallow excited state minimum has been calculated for the tautomeric species, corresponding to an indole–pyridine angle of 33°. At this geometry, the S_1 – S_0 energy difference is only about 1 eV. Equally important is the finding of a S_1 – S_0 CI at an indole–pyridine dihedral angle close to 90°. Finally, the back reaction, occurring in S_0 , is also predicted to be barrierless.

These computational predictions are in excellent agreement with the photophysical behavior of **1** detected both in solution and a jet. Coupling of hydrogen transfer with twisting implies that tautomerization should be sensitive to changes in torsional potential. In the condensed phase, solvent molecules hinder torsion, thus slowing down the reaction. The barrierless character of tautomerization in a jet-isolated molecule is suggested by the deuterium isotope effect, which is equal, within experimental accuracy, to the square root of two. The same value was obtained from TA decay times measured in CH_3OH and CH_3OD .

The lowest vibrational mode of **1**, calculated at 29 cm^{-1} by DFT at the B3LYP/6-31G(d,p) level, corresponds to the torsional motion of the indole and pyridine moieties, occurring with a period of about 1 ps. The pump-probe REMPI spectra shown in Figure 3 reveal, for both NH and ND isotopologues, a second small maximum delayed by about 1 ps from the primary signal maximum. This feature is an indication of a coherent process. It is tempting to associate it with the torsional vibration, which is mandatory for a partial recurrence/reflection of the initial wave packet at the CI point back into the initially excited state. The next lowest frequency vibration should have a period shorter by a factor of 3, because it was calculated at 89 cm^{-1} .

The presence of a CI and the barrierless character of both forward and reverse tautomerization processes help to rationalize several other experimental findings. Firstly, TA spectra demonstrate a lack of detectable transient species along the decay route all the way down to the initial (possibly vibrationally hot) ground-state form. This result is consistent with the fact that no fluorescence from either **1-syn** or the phototautomer could be detected. Actually, calculations predict a small barrier between the tautomeric species and the CI geometry. The fluorescence of the phototautomer should then be expected in the near infrared, and thus outside our detection range. However, the TA data seem to exclude the possible existence of a measurable fraction of the phototautomeric species.

In summary, experimental and computational evidence strongly suggest that the phototautomerization in 7-(2-pyridyl)indole is coupled with a twisting of the molecule, and that the twisting provides an efficient channel for ultrafast excited state deactivation. Moreover, the tautomerization is barrierless in both the lowest excited electronic singlet and the ground state. This pattern of excited-state tautomerization/deactivation may turn out to be quite general. It was predicted theoretically for 2-(2-hydroxyphenyl)benzotriazole,^[7] methyl salicylate,^[8] and salicylic acid.^[6] Our recent studies of 2,9-(di-2-pyridyl)-4,7-di(*tert*-butyl)carbazole (**6**, Scheme 2), a molecule structurally related to **1**, revealed dual fluorescence, indicating phototautomerization.^[14] Both emissions are very weak at 293 K in solution, but increase significantly upon lowering of temperature. On the contrary, neither fluorescence nor ion signals could be detected using nanosecond lasers for the molecule isolated in the jet. The situation is probably very similar to that of **1** and thus the elusive short-lived species can be detected only with femtosecond pulse excitation/ionization.



Scheme 2. The structure of 2,9-(di-2-pyridyl)-4,7-di(*tert*-butyl)carbazole.

Experimental Section

Synthesis of **1** has been described elsewhere.^[10] Stationary absorption and fluorescence spectra were recorded in spectral grade solvents on a Shimadzu UV 3100 spectrophotometer and on an Edinburgh FS 900 CDT or Jasný spectrofluorimeter, respectively.

The details of the setup employed for the femtosecond transient absorption experiments have been reported previously.^[15] Briefly, a Hurricane (Spectra Physics) laser/amplifier system generated a pulse train (130 fs full width at half-maximum, 800 nm centre wavelength, 1 kHz repetition rate) that was separated into two parts. One part was employed to pump a Spectra Physics OPA 800, which generated pump pulses at 325 nm. The other part was focused on a calcium fluoride crystal to generate a white light continuum from 350 nm to 800 nm that was used for the probe pulse. The polarizations of the two beams were set at the magic angle. The probe beam was coupled into a 400 μm optical fiber after passing the sample and was detected with a CCD spectrometer (Ocean Optics, PC 2000). A chopper (83 Hz, Rofin Ltd) placed in the excitation beam provided I and I_0 depending on the status of the chopper (open or closed). The total instrumental

response was about 200 fs (FWHM). The excitation power was kept as low as approximately 5 μJ per pulse using a pump spot diameter of about 1 mm. Apart from using a relatively low excitation intensity, thermal effects and photodegradation were also taken care of by stirring the solution. Photodegradation was not substantial as shown by comparing absorption spectra taken before and after the transient absorption experiment. All experiments were performed at ambient temperature.

Femtosecond multiphoton ionization (fsMPI), fsMPI-detected infrared (IR/fsMPI) and femtosecond pump-probe photoionization spectra were measured for jet-cooled molecules. The principle and the setup for the IR/fsMPI experiment have been described previously.^[11] The sample/nozzle temperature was typically maintained at 343 K. REMPI signals were generated using the tunable output of an optical parametric converter (TOPAS, Light Conversion) pumped by a femtosecond chirped-pulse amplified Ti:sapphire laser system (1 kHz, 260 fs FWHM autocorrelation at 800 nm). The applied set of dielectric mirrors allowed for a scanning range from 330 to 360 nm with nearly constant energy of 15 μJ per pulse. The tunable UV laser was employed for excitation (pump) and the second harmonic of the Ti:sapphire fundamental for the ionization (probe) of the electronically excited intermediate in the time-resolved pump-probe measurements by the $1 \times \text{UV} + 2 \times 400 \text{ nm}$ process. Both the UV and 400 nm ($80 \mu\text{J pulse}^{-1}$) beams were quasi-collinearly introduced into the detection chamber and overlapped in the ionization region of the mass spectrometer. Each of the beams alone did not produce any ions, so the observed ion signal was purely two-color. Time separation between the pump and probe pulses was controlled by means of an optical delay stage. Partial deuteration was performed by adding a few drops of heavy water to the sample compartment, and subsequent evaporation of the water under vacuum. This procedure resulted in fully resolved mass peaks of the ND and NH species with the ratio between 1:1 and 3:1. Contamination of the ND signal by ^{13}C isotopologues of the NH species did not exceed 20%. Details of measurements of infrared spectra detected by resonance two-photon ionization (IR/R2PI) were described elsewhere.^[16]

Received: March 20, 2008

Published online: July 4, 2008

Keywords: conical intersection · excited state proton transfer · femtochemistry · photochemistry · tautomerism

- [1] *Hydrogen-Transfer Reactions* (Eds.: J. T. Hynes, J. P. Klinman, H. H. Limbach, R. L. Schowen), Wiley-VCH, Weinheim, **2007**.
- [2] M. Kijak, Y. Nosenko, A. Singh, R. P. Thummel, J. Waluk, *J. Am. Chem. Soc.* **2007**, *129*, 2738.
- [3] D. O'Connor, G. W. Scott, D. R. Coulter, A. Gupta, S. P. Webb, S. Yeh, J. H. Clark, *Chem. Phys. Lett.* **1985**, *121*, 417.
- [4] G. Goeller, J. Rieker, A. Maier, J. J. Stezowski, E. Daltrozzo, M. Neureiter, H. Port, M. Wiechmann, H. E. A. Kramer, *J. Phys. Chem.* **1988**, *92*, 1452.
- [5] C. A. S. Potter, R. G. Brown, F. Vollmer, W. Rettig, *J. Chem. Soc. Faraday Trans.* **1994**, *59*.
- [6] A. L. Sobolewski, W. Domcke, *Phys. Chem. Chem. Phys.* **2006**, *8*, 3410.
- [7] A. L. Sobolewski, W. Domcke, C. Hättig, *J. Phys. Chem. A* **2006**, *110*, 6301.
- [8] J. D. Coe, B. G. Levine, T. J. Martinez, *J. Phys. Chem. A* **2007**, *111*, 11302.
- [9] A. L. Sobolewski, W. Domcke, *J. Phys. Chem. A* **2007**, *111*, 11725.
- [10] G. Wiosna, I. Petkova, M. S. Mudadu, R. P. Thummel, J. Waluk, *Chem. Phys. Lett.* **2004**, *400*, 379.
- [11] Y. Nosenko, M. Kunitski, R. P. Thummel, A. Kyrychenko, J. Herbich, J. Waluk, C. Riehn, B. Brutschy, *J. Am. Chem. Soc.* **2006**, *128*, 10000.
- [12] Y. Nosenko, M. Kunitski, C. Riehn, R. P. Thummel, A. Kyrychenko, J. Herbich, J. Waluk, B. Brutschy, *J. Phys. Chem. A* **2008**, *112*, 1150.
- [13] J. R. Carney, T. S. Zwier, *J. Phys. Chem. A* **1999**, *103*, 9943.
- [14] G. Wiosna-Sałyga, J. Dobkowski, M. S. Mudadu, I. Sazanovich, R. P. Thummel, J. Waluk, *Chem. Phys. Lett.* **2006**, *423*, 288.
- [15] G. Balkowski, A. Szemik-Hojniak, I. H. M. van Stokkum, H. Zhang, W. J. Buma, *J. Phys. Chem. A* **2005**, *109*, 3535.
- [16] O. Krauß, B. Brutschy, *Chem. Phys. Lett.* **2001**, *350*, 427.

9.7 The structure of adenine monohydrates studied by femtosecond multiphoton ionization detected IR spectroscopy and quantum chemical calculations

The structure of adenine monohydrates studied by femtosecond multiphoton ionization detected IR spectroscopy and quantum chemical calculations

Yevgeniy Nosenko,^a Maksim Kunitski,^a Christoph Riehn,^b Philipp H. P. Harbach,^a Andreas Dreuw^{*a} and Bernhard Brutschy^{*a}

Received 15th July 2009, Accepted 12th November 2009

First published as an Advance Article on the web 9th December 2009

DOI: 10.1039/b914236c

We present femtosecond multiphoton ionization detected infrared spectra of jet-cooled monohydrates of adenine and 9-methyladenine. By quantum chemical vibrational analysis and comparison with available literature data we identified two isomers of adenine hydrate with one water molecule hydrogen-bonded to either the amino or the N9–H group. These two monohydrates revealed different fragmentation patterns in the ion depletion spectra, indicating isomer specific intermolecular dynamics. This different behaviour is discussed in terms of competing electronically excited state relaxation and dissociation processes.

Introduction

Knowledge of the photophysics of individual nucleic acid bases is a prerequisite for a detailed understanding of DNA photostability under UV irradiation, in particular, since the nucleobases themselves are the UV chromophores of DNA. Within DNA under natural conditions, however, nucleobases interact with each other, with proteins and water influencing their photophysical properties. Thus, the environment requires special attention when the photostability of nucleobases is discussed either within DNA or as a selection criterion of the DNA bases within a hypothetical “prebiotic soup” in the earliest days of arising life on Earth.

As a consequence, many experiments have been performed to elucidate the excited state dynamics of nucleic acids and their constituents in solution.¹ Recently, progress has been achieved also in gas phase.^{2–22} Excited state lifetimes of the isolated nucleobases are of the order of a few picoseconds as revealed in an ion yield study by Kim and co-workers with a time resolution of $\Delta\tau_r \approx 400$ fs.³ Additionally, decay components in the ~ 100 fs region have been observed by Canuel *et al.* ($\Delta\tau_r \approx 80$ fs).⁴ In particular, time constants of 0.1 and 1.1 ps are obtained for adenine (Ade) upon excitation at 267 nm. The slower and faster decay components are assigned to internal conversion (IC) pathways *via* the $n\pi^*$ and $\pi\pi^*$ states, respectively, along the out-of-plane ring deformation mixed with amino group inversion coordinates.^{5–9} The observation of H-atom loss^{10,11} and data derived from time-resolved photoelectron spectroscopy,¹² moreover, suggest a contribution of a $\pi\sigma^*$ state, associated with the N9–H group,¹³ to the faster decay channel at $\lambda \leq 267$ nm.

The corresponding time constant has been determined to be 40 fs ($\Delta\tau_r \approx 160$ fs).¹² Since in DNA the N9–H group is the sugar-binding site, methylation of Ade at this position provides a biologically relevant nucleotide model. While the photoelectron detection is sensitive to the methylation, the ion yield spectra of Ade and 9-methyladenine (9mAde) are essentially the same both in time^{4,14} and frequency^{15,16} domain ($\lambda \geq 267$ nm). A more pronounced effect should appear in the properties of microsolvated Ade as the methyl substitution reduces not only the number of possible tautomers, but also the potential hydration sites (Fig. 1), thus simplifying the analysis of the spectra.

Kang *et al.* have first reported a significant decrease of the excited state lifetime of Ade induced by hydration down to 200 fs, when excited at 262 nm ($\Delta\tau_r \approx 400$ fs). This ultrafast decay of the ion signals has been rationalized in terms of rapid fragmentation of the clusters in their excited states.¹⁷ Ritze *et al.* have found that the adenine–water (Ade–W) complex lives only ~ 100 fs after absorption of a photon with $\lambda = 250–266$ nm ($\Delta\tau_r \approx 130$ fs), assigning this ultrafast decay to excited state relaxation *via* a $\pi\sigma^*$ state.¹⁸ 9mAde hydrates reveal biexponential decays ($\sim 0.1/1$ ps) with a less intense slow component as compared to the monomer.¹⁹

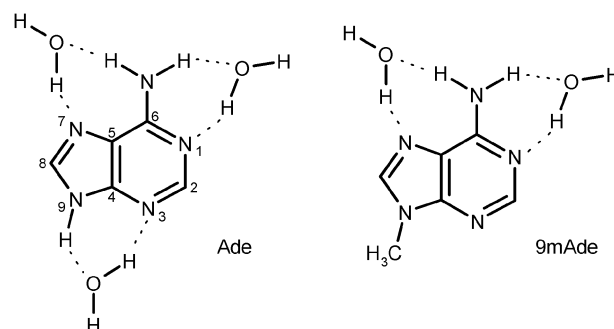


Fig. 1 Schematic primary hydration sites of 9-methyladenine and 9H-adenine. The standard atom numbering is provided for adenine.

^a Institut für Physikalische und Theoretische Chemie, Goethe-Universität, Max-von-Laue-str. 7, 60438 Frankfurt/Main, Germany.

E-mail: andreas.dreuw@theochem.uni-frankfurt.de, brutschy@chemie.uni-frankfurt.de; Fax: +49 69 79829560; Tel: +49 69 79829424

^b Fachbereich Chemie, TU Kaiserslautern, Erwin-Schrödinger-Str. 52, 67663 Kaiserslautern, Germany

Little information exists on the structure of microhydrated nucleobases. Three isomers of the monohydrate of guanine have been distinguished by Crews *et al.* utilizing UV-UV and IR-UV double-resonance techniques,²⁰ but only one isomer has been detected in the case of 9-methylguanine.²¹ Busker *et al.* have reported an IR-UV spectrum of the 1-methylthymine–water complex photoionizing it *via* a long-lived dark ($>1 \mu\text{s}$) electronic state.²² To the best of our knowledge, for the microhydrates of Ade there are no experimental vibrational data available. Theoretically, Hanus *et al.* have studied various isomers of Ade hydrates calculating stabilization energies at the MP2 level of theory.²³ Several comparably stable monohydrates have been found; in the most stable one water is H-bonded to the N9–H group, which is not available in DNA.

Size and isomer selectivity is usually achieved by double-resonance two-photon ionization detected IR (IR/R2PI) spectroscopy making use of spectrally resolved vibronic intermediate states for the R2PI probe.^{24,25} The aforementioned ultrashort excited state lifetime constitutes the main obstacle for the application of this elegant method to vibrational analysis of the Ade microhydrates, since with ns laser pulses the ionization transition is not possible. This problem may be solved by probing the cluster signals by direct one-photon ionization in the vacuum ultraviolet (VUV) spectral region. Recently developed IR-VUV techniques have been reviewed by Matsuda *et al.*²⁶ However, the applicability of this approach for studying the Ade hydrates, characterized by very slowly rising VUV ionization efficiency profiles,²⁷ is still to be proven. An alternative method employs ultrashort UV pulses for the two step photoionization *via* the short-lived electronic intermediate states, as recently demonstrated by our group.²⁸ Here the complex is characterized by femtosecond two-photon ionization detected IR (IR/fsMPI) spectra in the H-bonding sensitive region of the OH/NH stretch vibrations. In addition to the ground state structure, the IR/fsMPI method optionally provides access into the excited state dynamics by a delayed UV-UV pump–probe scheme.²⁹

In the present work, we shed light on the structure of the Ade or 9mAde monohydrates by means of the IR/fsMPI spectroscopy.

Experimental and computational details

Adenine (Fluka, 98%) and 9-methyladenine (Acros Organics, 98%) samples were used without further purification.

The principle and experimental setup for the femtosecond multiphoton ionization detected IR measurements have been described previously.²⁸ In the following we only provide details specific for the present work. The third harmonic of a femtosecond chirped-pulse amplified Ti:Sapphire laser system (20 μJ at 267 nm, 260 fs autocorrelation at 800 nm) was used for two-photon ionization of Ade (9mAde) and its water complexes. In order to increase the signal-to-noise ratio we applied the dual beam technique²⁴ by splitting the UV beam into two by means of a 50% dielectric splitter. Both UV beams were then focused in the source region of the time-of-flight (TOF) mass spectrometer into two spots about 4 mm apart from each other along the axis of the mass spectrometer.

By reducing the extraction electric field of the TOF spectrometer, we separated two resulting ion peaks of 20 ns width each by nearly 50 ns. Of these two femtosecond laser beams only the downstream one was spatially overlapped with a counter-propagating nanosecond IR-OPO beam (2 mJ per pulse, 0.2 cm^{-1} FWHM, 6 ns), while the second UV beam served as a reference. The IR laser was fired 50–100 ns prior to the ionizing UV pulse. The IR/fsMPI spectra were recorded in the 3000–3750 cm^{-1} region as ratio of the IR affected ion signal and the reference one. This ratio was checked in the absence of the IR radiation every $\sim 110 \text{ cm}^{-1}$ during the scans. Between the checkpoints, the baseline was then linearly normalized to unity. Calibration of the IR frequency was accomplished by measuring the red and green wavelengths used at the difference frequency generation stage of the seeded OPO by means of a wavemeter (ATOS LM-007). The final accuracy was hence $\pm 1 \text{ cm}^{-1}$ in the tuning range 2800–3800 cm^{-1} . At each spectral point, the integrated time-of-flight signals corresponding to the selected ion channels were averaged over 40 laser shots. Finally, the spectra were averaged over up to 8 scans.

All laser beams crossed at right angles to the pulsed molecular beam, which was collimated from a seeded supersonic expansion of Ade (9mAde) and water vapours with helium (4.6 grade) as carrier gas expanded at a stagnation pressure of 3 bar. The sample/nozzle temperature was maintained at about 455 and 425 K for Ade and 9mAde, respectively. Special attention was paid to minimize the $2:n^+$ signals to avoid their contribution to the $1:0^+$ and $1:1^+$ channels by fragmentation. The partial pressure of water was controlled by means of a gas mixing unit. The hydrate size distributions studied were as narrow as possible with only traces of the $1:n^+ \geq 2$ ion signals.

In the quantum chemical study, the geometries of 9H-amino form of Ade and three Ade–W conformers (N1, N3 and N7 bound as shown in Fig. 1) were optimized using second order Møller–Plesset perturbation theory (MP2)³⁰ with the standard polarized triple- ζ cc-pVTZ basis set.³¹ Only hydrates of the 9H-amino tautomer of Ade were considered. It is the only tautomer of Ade detected in the present experiment, and even hydrated it can hardly surpass the barrier for tautomerization because the thermal activation energy is too low.³² Counterpoise correction of the basis set superposition error (BSSE)³³ has been employed not only to the energies but also in the course of geometry optimization, since also the geometries can be largely affected by BSSE. In addition, standard Kohn–Sham density functional theory has been used in combination with the three-parameter Becke3–Lee–Yang–Parr (B3LYP)³⁴ exchange-correlation functional and the cc-pVTZ basis set to optimize all geometries including the ones of 9mAde and its water complexes followed by harmonic frequency calculations. Analyses of the frequencies are only affordable at the B3LYP/cc-pVTZ level of theory. As usual, computed frequencies were scaled by a factor of 0.961 which has been chosen such that the computed frequency of the N9–H stretch vibration of Ade coincides with the value determined experimentally.

The computed binding energies of the different isomers of the 1 : 1 water complexes of 9mAde and Ade are given in Table 1 and compared with previous results of Hanus *et al.*²³

Table 1 Relative stabilities of the adenine and 9-methyladenine monohydrates with respect to the free molecules (in kcal mol⁻¹) calculated for the BSSE corrected geometries with the cc-pVTZ basis set

	9mAde		Ade		
	N7	N1	N3	N7	N1
B3LYP	-9.7	-8.5	-9.7	-9.6	-8.5
B3LYP+ZPVE	-7.1	-6.1	-7.5	-7.0	-6.1
MP2	—	—	-10.6	-9.7	-8.9
MP2+ZPVE	—	—	-8.5	-7.4	-6.7
RI-MP2/TZVPP ²³	—	—	-10.6	-9.3	-8.7

The binding energies computed at MP2/cc-pVTZ agree with the previously reported RI-MP2/TZVPP values. It is important to note that the B3LYP/cc-pVTZ method yields the same order of the binding energies of the different isomers. Hanus *et al.*²³ identified an additional fourth isomer of the Ade-W complex, however, geometry optimizations with a very tight convergence criterion only converged to the very closely related N1 isomer. All calculations reported here were performed with the Gaussian03 program package.³⁵

Results

Adenine and 9-methyladenine monomers

IR/R2PI spectra in the region of the NH stretch vibrations of jet-cooled Ade³⁶ and 9mAde¹⁶ have been reported by Plützer *et al.* In the present work, the IR spectra of the monomers were recorded in parallel to those of the hydrates in order to unveil possible fragmentation patterns. The simultaneous analysis of several mass channels was important, because the applied photoionization scheme (260 fs at 267 nm) has limited size selectivity due to considerable cluster fragmentation.³⁷ This is also the reason why only 1 : 1 complexes were considered. For broader cluster size distributions, with 1:n⁺ ≥ 2 signals, the quality of the IR spectra decreased significantly, especially in the case of Ade. Fig. 2 shows the IR/fsMPI spectra of Ade and 9mAde with water as detected in the 1:0⁺ and 1:1⁺ ion channels along with the calculated vibrational stick spectra of the monomers.

In contrast to transitions of the hydrates of both adenines, the IR/fsMPI spectra of the monomers exhibit an ion signal enhancement while in the ns IR/R2PI the vibrations appear as depletion bands.³⁶ Thus for neat Ade, four positive bands were recorded at 3069, 3452, 3508 and 3570 cm⁻¹. The three latter frequencies are within experimental accuracy in agreement with those observed and assigned previously to the symmetric NH₂ (ν_s(NH₂)), N9-H and anti-symmetric NH₂ (ν_a(NH₂)) stretch vibrational modes of the 9H-amino tautomer.³⁶ The additional band at 3069 cm⁻¹ corresponds to the C2-H stretching vibration (3038 cm⁻¹) which is quite strong, if compared to the practically IR inactive C8-H one (3111 cm⁻¹) at the B3LYP/cc-pVTZ level of theory. A similar band, observed at 3061 cm⁻¹ by gas phase IR spectroscopy,³⁸ was initially assigned to the C8-H stretch and subsequently revised to the C2-H stretch.³⁹

The 7H-amino tautomer of Ade, characterized by the vibrational bands at 3437, 3507, 3514 and 3550 cm⁻¹,³⁶ may

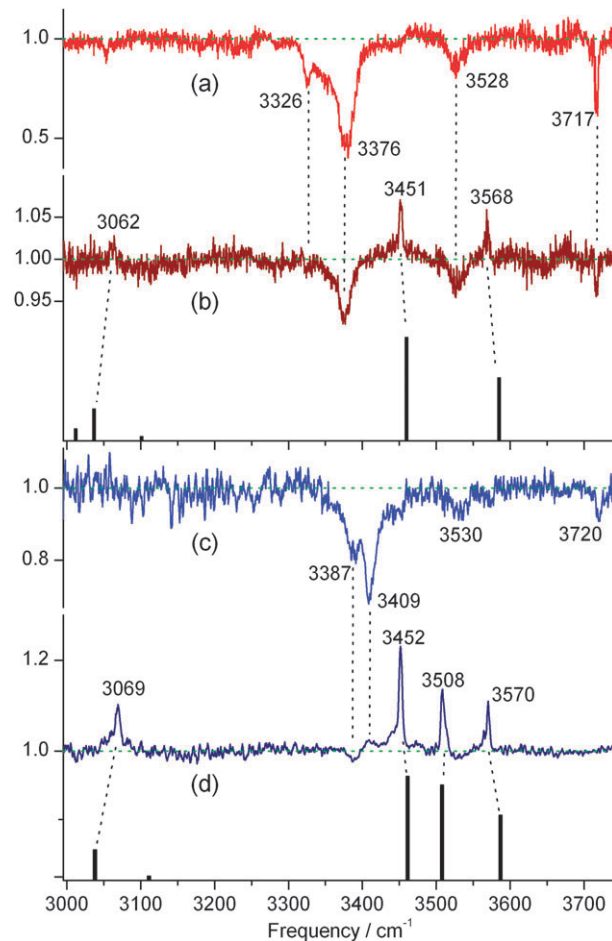


Fig. 2 IR/fsMPI spectra recorded in the 1:1⁺ (a) and 1:0⁺ (b) mass channels of the 9-methyladenine : water; the 1:1⁺ (c) and 1:0⁺ (d) of the adenine : water systems. The IR transitions of the monomers calculated at the B3LYP/cc-pVTZ level of theory are shown as stick spectra.

Table 2 IR/fsMPI bands and corresponding calculated vibrational frequencies of adenine and 9-methyladenine

9mAde		Ade		Assignment
Exp	Theory	Exp	Theory	
3568	3585	3570	3587	NH ₂ (ν _a)
—	n/a	3508	3508	N9-H
3451	3460	3452	3461	NH ₂ (ν _s)
3062	3037	3069	3038	C2-H

show up as shoulders of the bands of the dominant 9H-amino form. If at all, it is a minor contribution. No signatures of other tautomers of Ade were detected. Possible reasons are small relative concentration of the tautomeric species, unfavourable FC for the IR/fsMPI at 267 nm and, finally, lifetime in the electronically excited state significantly shorter than the photoionizing pulse duration.

9mAde revealed three bands at 3568, 3451 and 3062 cm⁻¹ analogously ascribed to the ν_a(NH₂), ν_s(NH₂) and C2-H stretches, respectively. The vibrational frequencies and assignments for both molecules are listed in Table 2.

9-Methyladenine monohydrate

The IR/fsMPI spectra of 9mAde mono- and di-hydrate are displayed in Fig. 3. The latter was measured at higher water vapour pressure in the carrier gas in order to verify a possible contamination of the 1:1⁺ signal by fragmentation of larger clusters. Only a negligible contribution of the 1:2⁺ vibrational fingerprints appear eventually in the 1:1⁺ spectrum at around 3400 cm⁻¹ and in the free OH region where both spectra should overlap.

Since neither the symmetric (ν_1) nor anti-symmetric (ν_3) stretch vibrations of both the amino group and of a water molecule were detected only doubly H-bonded 1 : 1 structures come into consideration. Two such isomers of the 9mAde–W complex are possible: either N1 or N7, with the binding energies of 6.1 and 7.1 kcal mol⁻¹, respectively, at the theoretical level of B3LYP/cc-pVTZ. In both cases the water molecule acts as the H-bonding acceptor with the amino group as a donor. The calculated IR stick spectra are compared with the experimental data in Fig. 3.

Four cluster specific IR bands were observed at 3717, 3528, 3376 and 3326 cm⁻¹. This vibrational fingerprint spectrum resembles that of the 2-aminopyridine–water (2AP–W), with the vibrational frequencies found at 3717, 3548, 3403 and 3315 cm⁻¹, assigned to a hydrate which structurally mimics the N1 isomer.⁴⁰ Hence, the spectrum of the 9mAde hydrate can be assigned to one isomer as follows.

Upon H-bonding, the $\nu_3 = 3756$ cm⁻¹ and $\nu_1 = 3657$ cm⁻¹ stretches of free water⁴¹ transforms into a free or dangling OH ($\nu_f(\text{OH}) = 3717$ cm⁻¹) and an H-bonded OH ($\nu_b(\text{OH}) = 3376$ cm⁻¹) stretches of the hydrate with red-shifts of 39 and 281 cm⁻¹, respectively. These significant and different red-shifts as well as the broadening of the cluster bands

(5 and 30 cm⁻¹ of FWHM, respectively) clearly indicate decoupling of the water OH stretches. In turn, the amino group vibrations, $\nu_a(\text{NH}_2) = 3568$ cm⁻¹ and $\nu_s(\text{NH}_2) = 3451$ cm⁻¹, give rise to the $\nu_f(\text{NH}_2) = 3528$ and $\nu_b(\text{NH}_2) = 3326$ cm⁻¹ bands, red-shifted by 40 and 125 cm⁻¹, respectively. The amino group is a weaker H-bonding donor than water as evidenced by the smaller red-shift of the corresponding H-bonded vibration ν_b . Hence, the NH₂ stretches can preserve a non-local character to some extent. This can also be argued by the width of the $\nu_f(\text{NH}_2)$ band (~20 cm⁻¹ of FWHM) which is comparable to those of the H-bonded modes: 12 cm⁻¹ and 30 cm⁻¹ for the 3326 cm⁻¹ and 3376 cm⁻¹ bands, respectively. Usually, the H-bonding results in broadening of the stretch vibrations by anharmonic coupling with the lower frequency modes. The $\nu_f(\text{NH}_2)$ mode can be affected if the amino group vibrations remain coupled. Additional lifetime broadening cannot be excluded. Although such vibrations may relax within a few ps, the stretches involved in the H-bonds usually dissipate much faster than the free ones.⁴² Thus comparable broadening of the free and H-bonded modes cannot have solely the lifetime origin. The relatively weak intensity of the 3326 cm⁻¹ mode can be rationalized in terms of coupled and thus delocalized H-bonded NH and OH stretches, resulting in anti-phase, $\nu_b(\text{OH} - \text{NH})$, and in-phase, $\nu_b(\text{NH} + \text{OH})$, collective stretch vibrations within the H-bonding cycle. Indeed, the in-phase mode was calculated to be lower in frequency and of significantly weaker intensity than the anti-phase vibration for both the N1 and N7 bound structures (Fig. 3).

The similarity of the calculated vibrational fingerprints and stabilities of the N7 and N1 bound hydrates imply an ambiguity in the assignment given the fact that fsMPI detection using only 267 nm is not isomer selective. Moreover, this wavelength excites the species well above the lowest conical intersection, limiting thus the experimental sensitivity to the excited state dynamics. Hence, we cannot rule out the presence of both conformers in comparable quantities under the experimental conditions applied. With this assumption an alternative assignment can be proposed. The reason for the width of the 3528 cm⁻¹ band (~20 cm⁻¹) is thus a superposition of the $\nu_f(\text{NH}_2)$ vibrations of two isomers. Corresponding theoretical frequencies differ by 19 cm⁻¹, in contrast to the $\nu_f(\text{OH})$ modes whose energies are identical within a wavenumber. Remarkably, the experimental $\nu_f(\text{OH}) = 3717$ cm⁻¹ band is quite narrow (FWHM = 5 cm⁻¹). The $\nu_b(\text{OH} - \text{NH})$ and $\nu_b(\text{NH} + \text{OH})$ stretches of two isomers should then overlap within the 3326/3376 cm⁻¹ doublet. One of the $\nu_b(\text{NH} + \text{OH})$ bands may not be observed due to its weakness or broadness. In summary, if both the N7 and N1 isomers of the 9mAde–W complex were detected they were indistinguishable in the present experiment. These two species are termed in the following “amino-bound” hydrates.

Adenine monohydrate

Compared to 9mAde, one additional hydration site is available for Ade with water bound between the N9–H group as an H-bonding donor and the N3 nitrogen atom as an acceptor. Moreover such a hydrate has the largest theoretical

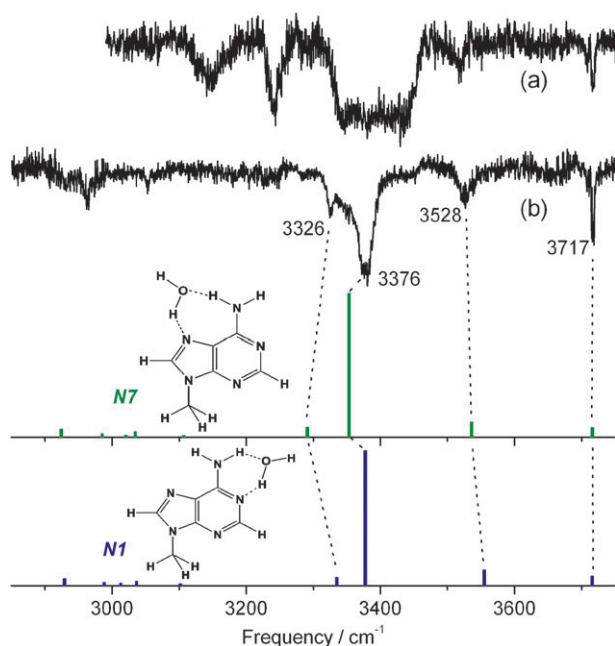


Fig. 3 IR/fsMPI spectra of the 9-methyladenine–water₂ (a) and 9-methyladenine–water (b) complexes compared to calculated stick spectra of the two strongest bound structures of 9-methyladenine monohydrate.

stabilization energy (see Table 1). BSSE and ZPVE corrected B3LYP/cc-pVTZ binding energies for the N3, N7 and N1 bound hydrates were calculated as high as 7.5, 7.0 and 6.1 kcal mol⁻¹, respectively. The order of stability of the hydrates was the same at the MP2 level of theory, in agreement with the calculations of Hanus *et al.*²³ These similar binding energies may result in the formation of different isomers of the monohydrate in the molecular beam. The contribution of more than one isomer to the IR-UV spectrum of Ade-W is indirectly supported by the relatively weak individual depletion signals, which were less than 30%, compared to a 50% depletion readily achieved for the 9mAde-W complex under similar laser conditions (Fig. 2). Such a decrease regularly appears when the signal is made up from several contributions.

Fig. 4 shows the IR spectrum, detected in the 1:1⁺ channel of the Ade-W system, in comparison with the stick spectra, calculated for the doubly H-bonded geometries of the Ade hydrate. The frequencies and spectral shifts are listed in Table 3. Generally, the vibrational fingerprint of the Ade-W complex is similar to that of the 9mAde hydrate. The $\nu_r(\text{NH}_2)$ vibration (3530 cm⁻¹) indicates the presence of the amino-bound species. On the other hand, weak but reproducible features at 3453 and 3574 cm⁻¹ are characteristic stretches of a free amino group of adenine (Table 2) and therefore suggest the contribution of the N3 isomer. Interestingly, blue-shifts of a few wavenumbers were nicely reproduced for the NH₂ stretch vibrations of this hydrate by our calculations. We, thus, conclude that both amino and N3 bound conformers contribute to the observed spectrum of the Ade monohydrate. The strongest transition for each of the calculated complexes is the anti-phase stretching of the H-bonded NH and OH groups: $\nu_b(\text{OH} - \text{NH})$. Its frequency for the N3 isomer was blue-shifted relative to both of the amino-bound hydrates. Consequently we assign the 3387 and 3409 cm⁻¹ bands to the amino and N3 bound complexes, respectively. Compared to the 9mAde-W system, the $\nu_b(\text{OH} - \text{NH})$ mode of the amino-bound Ade-W complex reveals a shift of 11 cm⁻¹. Of the N1 and N7 isomers, only the latter was calculated to be comparably sensitive to methylation of Ade in the N9-H position

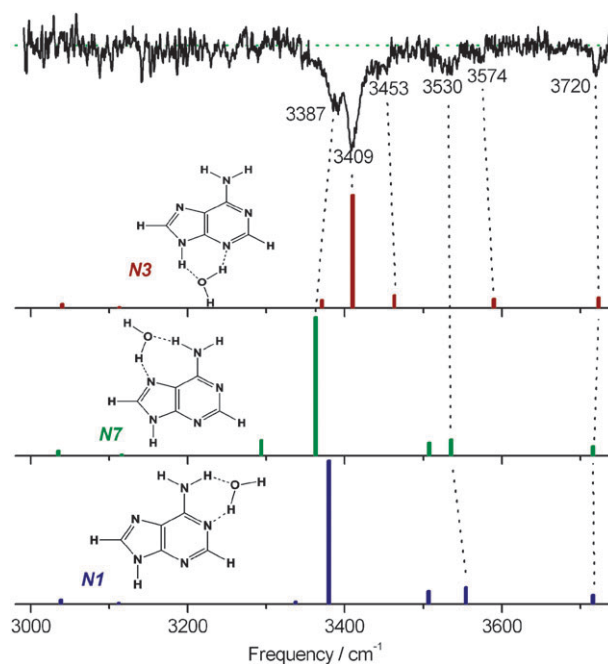


Fig. 4 IR/fsMPI spectrum of adenine-water complex compared to calculated stick spectra of the three most stable structures of 9H-adenine monohydrate.

(see Table 3). The corresponding red-shifts were 2 and 10 cm⁻¹, respectively. This can be understood in terms of a higher population of the N7 as compared to the N1 isomer, in agreement with their relative stabilities. Nevertheless, these species remain unresolved.

The in-phase $\nu_b(\text{NH} + \text{OH})$ vibration of the amino-bound isomer, an analogue of the 3326 cm⁻¹ band of the 9mAde-W complex, was probably too weak to be detected. A similar mode of the N3 isomer is perhaps masked by the 3387 cm⁻¹ band. The H-bonding topology of the N3 bound hydrate closely resembles that of the 7-azaindole-water complex, for which the H-bonding stretches at 3369 ($\nu_b(\text{NH} + \text{OH})$) and 3412 cm⁻¹ ($\nu_b(\text{OH} - \text{NH})$) have been observed with the intensity ratio of $\sim 1/4$.⁴³ Remarkably, the latter frequency is

Table 3 Selected theoretical^a and experimental vibrational frequencies (in cm⁻¹) of adenine hydrates. The H-bonding induced spectral shifts are given in parentheses

	9mAde-W		IR/fsMPI	Ade-W			IR/fsMPI
	N7	N1		N3	N7	N1	
$\nu_r(\text{OH})$	3716	3716	3717	3723	3716	3716	3720
	(-38)	(-38)	(-39)	(-31)	(-38)	(-38)	(-36)
$\nu_a(\text{NH}_2)$			—	3590			3574
				(+3)			(+4)
$\nu_r(\text{NH}_2)$	3536	3555	3528		3536	3554	3530
	(-49)	(-30)	(-40)		(-51)	(-33)	(-40)
$\nu(\text{N9-H})$			—		3508	3507	—
$\nu_s(\text{NH}_2)$			—	3463			3453
				(+2)			(+1)
$\nu_b(\text{OH} - \text{NH})$	3353	3378	3376	3410	3363	3380	3387/3409
	(-303)	(-278)	(-281)	(-246)	(-293)	(-276)	(-270)/(-248)
$\nu_b(\text{NH} + \text{OH})$	3291	3335	3326	3371	3294	3337	—
	(-169)	(-125)	(-125)	(-137)	(-167)	(-124)	

^a Calculated at the B3LYP/cc-pVTZ level of theory for BSSE corrected energy minimum structures.

only 3 cm^{-1} away from that of the N3 isomer, validating such a comparison excellently. Then the $\nu_b(\text{NH} + \text{OH})$ transition would be on the low-energy shoulder of the 3387 cm^{-1} band.

The dangling OH stretch of the most stable Ade-W isomer was calculated to be blue-shifted by 7 cm^{-1} with respect to those of the amino-bound structures. Experimentally, the free OH transition of the Ade hydrate is blue-shifted by 3 cm^{-1} and broader (8 vs. 5 cm^{-1} of FWHM) compared to the corresponding band of the 9mAde-W complex. This could indicate overlapping bands of the Ade hydrate conformers.

Summarizing the frequency analysis, we identified two isomers of the Ade monohydrate. One can notice that the 3409 cm^{-1} band (N3 isomer) is twice as intense as the 3387 cm^{-1} band (amino-bound isomer). As the latter was calculated to be more intense by 20% and assuming similar ionization cross sections, as we are well above the IP threshold, we conclude higher population of the former complex, in line with the fact that the N3 bound isomer is theoretically the most stable one (Table 1).

Interestingly, the bands assigned to the amino-bound hydrate show depletion in the $1:0^+$ channel (Fig. 2b), while that of the N3 isomer (3409 cm^{-1} , Fig. 2d) surprisingly exhibit an enhancement.

Discussion

IR induced ion signal enhancement, which was observed in the present work for the monomers of adenines, does not often occur. Usually, IR absorption results in the ion signal depletion due to predissociation of the cluster, depopulation of the vibrational ground state or a vibrationally induced decrease of the Franck-Condon (FC) factors. An increase of the ion signal is monitored when the IR photon compensates a lack of energy for the ionization step in R2PI, provided by appropriately chosen UV photons.^{44,45} This was not the case here, since nearly 9.3 eV ($2 \times 267\text{ nm}$) were deposited into a molecule with a vertical two-photon ionization threshold of 8.6 eV .³⁶ Generally, for fsMPI *via* a vibronic continuum the IR induced change of the FC overlap becomes crucial for non-dissociating monomers. So, the UV signal enhancement can be caused by an IR induced increase of the FC overlap for excitation and/or ionization steps, like for the 7-azaindole dimer,⁴⁴ or by involvement of a new excited and/or cationic state with higher transition dipole moments. Indeed, the excited state relaxation of Ade involves significant structural rearrangement. This implies a better FC overlap for vibrationally excited molecules. Also vibrationally hot molecules may preferentially access the $\pi\pi^*$ (1L_a) electronic state which presumably plays an important role in the IC of Ade.^{6-9,19} In this case the corresponding electronic state is located at around 267 nm (4.65 eV). This is 170 meV above the origin of the $\pi\pi^*$ (1L_b) state, which is in good agreement with theory predicting the 1L_a - 1L_b gap of 50 - 150 meV .⁶⁻⁹ On the other hand, activation of the $\pi\sigma^*$ state cannot be ruled out, particularly in the case of Ade. This is however improbable, since there would be no IR induced fsMPI enhancement for the 9mAde, whose $\pi\sigma^*$ states lie significantly higher than the excitation energy (267 nm).^{11,12} So both, increasing FC factor and activation of the $\pi\pi^*$ (1L_a) state, are in line with the

observation that the R2PI signal of Ade grows with energy excess in the electronically excited state.⁴⁶ This is also supported by the fact that Ade reveals a more pronounced ion signal enhancement than its methylated homologue (Fig. 2). Because of the methyl group, 9mAde possesses a higher density of states and relaxes closer to the zero vibrational level than Ade after IR absorption.

As the photoionization efficiency signal of neat Ade^{27,30} grows with energy, similar arguments can be applied regarding the transition from the electronically excited to the cationic state.

More challenging is the treatment of the fragmentation patterns of the monohydrates observed in the $1:0^+$ channels (Fig. 2b and d). The dramatic difference for the N3 and amino-bound species is nicely illustrated by the $3387/3409\text{ cm}^{-1}$ doublet of the Ade hydrate (Fig. 5). The band at 3409 cm^{-1} (N3 isomer) is seen as a positive peak in the monomer ion channel, whilst the 3387 cm^{-1} band (amino-bound isomer) appears as a depletion band of the $1:0^+$ signal. The latter could be explained by lowering the FC overlap for the photoionization of the vibrationally hot amino-bound hydrates. But, the opposite behaviour of the FC factor of the monomer, together with the fact that the hydrates were photoionized *via* a vibronic continuum, suggests that this mechanism is not dominant. Here, the dynamics of the hydrates in the ground, electronically excited and cationic states have additionally to be taken into account, since loss of a water molecule by the complexes is energetically possible at all three stages of the photoionization process.

The energy of the vibrational excitation, 8 - 11 kcal mol^{-1} , is higher than the binding energies of the hydrates under study, calculated to be 6 - 8 kcal mol^{-1} . So, any of the reported vibrational excitations can lead to dissociation of the cluster already in the ground state. The predissociation rate can be strongly mode dependent and thus isomer dependent. Unfortunately, the vibrational relaxation dynamics of the Ade hydrates is not known. In this context, a comparative time-resolved IR study of the 2-aminopyridine and 7-azaindole monohydrates would be of great interest. There are two reasons to suppose similar predissociation rates for the 3387 and 3409 cm^{-1} modes. The first one is the similar binding

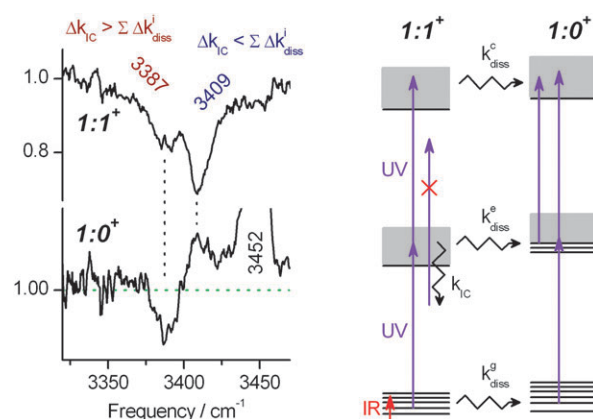


Fig. 5 Fragmentation of the adenine hydrates in the region of the $\nu_b(\text{OH} - \text{NH})$ vibration (left) and corresponding energy diagram (right). Δk denotes change of a process rate after IR absorption.

energies (Table 1). Secondly, these bands represent essentially the same vibration, $\nu_b(\text{OH} - \text{NH})$, oscillating in similar H-bonding $\text{NH} \cdots \text{OH} \cdots \text{N}$ bridges. Therefore the S_0 dissociation of the hydrate is assumed to cause comparable enhancement of the monomer ion signal for both vibrations.

The binding energy of a cation can be several kcal mol^{-1} higher than that of a neutral molecule due to an additional charge–dipole interaction. The appearance energy of the Ade monohydrate ion is 8.2 eV.²⁷ Two-photon ionization by 267 nm radiation results in an energy excess of about 1.1 eV ($\sim 25 \text{ kcal mol}^{-1}$). This is enough to destroy the cluster if most of this energy remains in the cluster ion. It is known that cationic Ade microhydrates dissociate when photoionized by 266 nm ns laser pulses.⁴⁷ If this is the case for fsMPI, a vibrationally hot hydrate is expected to fragment more extensively, providing thus an IR induced enhancement of the monomer ion signal. A depletion of this signal due to a chemical reaction of the Ade cation catalysed by hydration seems improbable. On the contrary, hydration provides intermolecular degrees of freedom to dissipate excess energy protecting the chromophore against photochemical reactions.

As mentioned in the Introduction, Ade hydrates are extremely short-lived in their excited states. Fast excited state relaxation of an isolated complex must lead to dissociation, which is its primary dissipation channel.⁴⁸ Depending on the nature of the electronically excited states involved the hydrate may dissociate either directly (faster than the UV pulse duration) or after vibronic relaxation.

So on one hand, the vibrationally induced dissociation in the ground and electronically excited states of the 1 : 1 complex produces additional monomer molecules ready for the photoionization, leading to an increase of the monomer ion signal. This also happens when the cation fragments. On the other hand, direct excited state cluster fragmentation competes with the IC pathways, which make the second step of ionization of the hydrate less probable or even impossible. Thus both the $1:1^+$ and $1:0^+$ signals are depleted. The corresponding processes are schematically depicted in Fig. 5. It should be pointed out that the fragmentation of the hydrates did occur upon UV photoionization even without application of IR radiation. Otherwise, there would be no depletion signal of the IR cluster bands in the monomer ion channels. The question is: how does the vibrational preexcitation affect the fragmentation in the different electronic states?

The fast IC mechanism prevails for the amino-bound hydrates, all giving depletion signals in both ion channels (e.g. 3376 and 3387 cm^{-1} bands in Fig. 2). Generally, to affect the fsMPI signal the relevant process must occur at a timescale faster than the duration of the laser pulse (260 fs). Excited by 267 nm radiation the 9mAde monohydrate decays biexponentially with the time constants of 110 fs and 1 ps.¹⁹ Consequently the 110 fs process, associated with the $\pi\pi^*$ state relaxation, should be responsible for the observed IR/fsMPI effect in the amino-bound hydrates. The out-of-plane ring deformations accompanying the IC should be weakly coupled with the in-plane dissociative intermolecular motion prohibiting fast fragmentation. This explains qualitatively why dissociation in the electronically excited state should be much slower than the IC for the amino-bound hydrates.

Interestingly, the IR induced predissociation in the S_0 as well as in the cationic states also plays a minor role in the IR/fsMPI effect compared to ultrafast IC. Instead, absorption of the IR radiation with subsequent IVR heats up among others the out-of-plane vibrational modes, which promote IC. Such vibrationally hot molecules relax more efficiently after absorption of an UV photon, providing the observed IR/fsMPI depletion in both the $1:1^+$ and $1:0^+$ channels (Fig. 2a and b).

The opposite situation is observed for the N9–H bound Ade hydrate, i.e. an IR induced enhancement of the fragmentation signal (Fig. 5, 3409 cm^{-1}). This dissimilarity could be explained by different FC overlaps of the vibrationally hot isomeric hydrates. Here, more experimental data are required either to prove or to discard this mechanism. Taking into account the available literature we propose an explanation based on different excited state dynamics. A rapid excited state dissociation which is faster than the competing IC has been postulated for Ade hydrates to explain the dramatic decrease of the ion signals with longer laser pulses.¹⁷ This interpretation is very well supported by the recent time-resolved data. The $\pi\sigma^*$ state, associated with the N9–H group, is dissociative by nature. It can be operative in the case of the N9–H bound (N3) isomer, directly coupling the energy of the electronic excitation into the intermolecular motion of the hydrate moieties. In the isolated Ade, this state is assigned to a 40 fs decay of the photoelectron signal,¹² therefore it is in any case competitive with other slower relaxation channels. Due to the large dipole moment of the $\pi\sigma^*$ state,¹³ it is stabilized in the hydrate with respect to the $n\pi^*$ and $\pi\pi^*$ states,¹⁸ making it the dominant path for a relaxation. Then vibrational preexcitation facilitates the excited state fragmentation by higher excess energy. In fact, only a 80 fs decay was observed for the Ade–W complex¹⁸ with no sign of a 1 ps decay component, characteristic of the amino-bound hydrates.¹⁹ Lack of this picosecond decay does not contradict the observation of both amino and N9–H bound hydrates by the IR/fsMPI. The amino-bound species are not dominant here. Then, keeping in mind that the picosecond component is quite weak itself,¹⁹ we realize that the relative amount of detected amino-bound isomer must be lower in the experiment of Ritze *et al.*¹⁸ than in the present work since our laser pulses (260 fs) were twice as long as those in the forementioned work. Hence, the time-resolved signal corresponding to the 1 ps decay has probably been on the noise level.

Based on the present IR/fsMPI results, the biexponential 0.1/1 ps decay has to be assigned to the amino-bound hydrates, whereas the N9–H bound complex should decay faster than 100 fs.

Conclusions

We have detected Ade in its global minimum tautomeric form, 9H-amino, by photoionization using short laser pulses (260 fs at 267 nm). The IR spectra of Ade and 9mAde hydrates were measured for the first time utilizing femtosecond two-photon ionization detection. A doubly hydrogen-bonded structure was observed for the 9mAde monohydrate. Quantum chemical calculations suggest the existence of two vibrationally indistinguishable amino-bound isomers.

Moreover, we have identified two Ade hydrates: amino and N9–H bound forms, by comparison of the experimental spectra with the results of quantum chemical calculations. These isomeric Ade hydrates exhibit dramatically different fragmentation patterns in the ion depletion spectra, which must be due to isomer specific intermolecular dynamics. A significant abundance of the N9–H bound species, which cannot be formed in the case of 9mAde, can qualitatively explain the differences in the photodynamics of Ade and 9mAde hydrates. In particular, for the N9–H bound hydrate, excited state dissociation is suggested to be more efficient than internal conversion (IC), whereas for the amino-bound species, IC is dominant.

Acknowledgements

We thank the German Science foundation (grant DFG BR848/7-1) and Sponsors of the Goethe-University Frankfurt/Main for financial support. AD holds a Heisenberg-Professorship funded by the German Science foundation.

References

- C. Crespo-Hernández, B. Cohen, P. Hare and B. Kohler, *Chem. Rev.*, 2004, **104**, 1977.
- M. de Vries and P. Hobza, *Annu. Rev. Phys. Chem.*, 2007, **58**, 585.
- H. Kang, K. T. Lee, B. Jung, Y. J. Ko and S. K. Kim, *J. Am. Chem. Soc.*, 2002, **124**, 12958.
- C. Canuel, M. Mons, F. Piuzzi, B. Tardivel, I. Dimicoli and M. Elhanine, *J. Chem. Phys.*, 2005, **122**, 74316.
- A. Broo, *J. Phys. Chem. A*, 1998, **102**, 526.
- S. Perun, A. L. Sobolewski and W. Domcke, *J. Am. Chem. Soc.*, 2005, **127**, 6257.
- C. Marian, *J. Chem. Phys.*, 2005, **122**, 104314.
- H. Chen and S. Li, *J. Phys. Chem. A*, 2005, **109**, 8443.
- L. Blancafort, *J. Am. Chem. Soc.*, 2006, **128**, 210.
- I. Hünig, C. Plützer, K. Seefeld, D. Löwenich, M. Nispel and K. Kleinermanns, *ChemPhysChem*, 2004, **5**, 1427.
- M. Zierhut, W. Roth and I. Fischer, *Phys. Chem. Chem. Phys.*, 2004, **6**, 5178.
- S. Ullrich, T. Schultz, M. Zgierski and A. Stolow, *J. Am. Chem. Soc.*, 2004, **126**, 2262; S. Ullrich, T. Schultz, M. Zgierski and A. Stolow, *Phys. Chem. Chem. Phys.*, 2004, **6**, 2796; H. Satzger, D. Townsend, M. Zgierski, S. Patchkovskii, S. Ullrich and A. Stolow, *Proc. Natl. Acad. Sci. U. S. A.*, 2006, **103**, 10196; C. Bisgaard, H. Satzger, S. Ullrich and A. Stolow, *ChemPhysChem*, 2009, **10**, 101.
- A. L. Sobolewski and W. Domcke, *Eur. Phys. J. D*, 2002, **20**, 369; S. Perun, A. L. Sobolewski and W. Domcke, *Chem. Phys.*, 2005, **313**, 107.
- H. Kang, B. Jung and S. K. Kim, *J. Chem. Phys.*, 2003, **118**, 6717.
- D. Lührs, J. Viallon and I. Fischer, *Phys. Chem. Chem. Phys.*, 2001, **3**, 1827.
- C. Plützer, I. Hünig, K. Kleinermanns, E. Nir and M. de Vries, *ChemPhysChem*, 2003, **4**, 838.
- H. Kang, K. T. Lee and S. K. Kim, *Chem. Phys. Lett.*, 2002, **359**, 213.
- H.-H. Ritze, H. Lippert, E. Samoylova, V. R. Smith, I. V. Hertel, W. Radloff and T. Schultz, *J. Chem. Phys.*, 2005, **122**, 224320.
- C. Canuel, M. Elhanine, M. Mons, F. Piuzzi, B. Tardivel and I. Dimicoli, *Phys. Chem. Chem. Phys.*, 2006, **8**, 3978.
- B. Crews, A. Abo-Riziq, L. Grace, M. Callahan, M. Kabeláč, P. Hobza and M. de Vries, *Phys. Chem. Chem. Phys.*, 2005, **7**, 3015.
- W. Chin, M. Mons, F. Piuzzi, B. Tardivel, I. Dimicoli, L. Gorb and J. Leszczynski, *J. Phys. Chem. A*, 2004, **108**, 8237.
- M. Busker, M. Nispel, T. Häber, K. Kleinermanns, M. Etinski and T. Fleig, *ChemPhysChem*, 2008, **9**, 1570.
- M. Hanus, M. Kabeláč, J. Rejnek, F. Ryjáček and P. Hobza, *J. Phys. Chem. B*, 2004, **108**, 2087.
- R. H. Page, Y. R. Shen and Y. T. Lee, *J. Chem. Phys.*, 1988, **88**, 4621.
- C. Riehn, C. Lahmann, B. Wassermann and B. Brutschy, *Chem. Phys. Lett.*, 1992, **197**, 443; S. Tanabe, T. Ebata, M. Fujii and N. Mikami, *Chem. Phys. Lett.*, 1993, **215**, 347; R. N. Pribble and T. S. Zwier, *Science*, 1994, **265**, 75.
- Y. Matsuda, N. Mikami and A. Fujii, *Phys. Chem. Chem. Phys.*, 2009, **11**, 1279.
- L. Belau, K. Wilson, S. Leone and M. Ahmed, *J. Phys. Chem. A*, 2007, **111**, 7562.
- Y. Nosenko, M. Kunitski, R. P. Thummel, A. Kyrchenko, J. Herbich, J. Waluk, C. Riehn and B. Brutschy, *J. Am. Chem. Soc.*, 2006, **128**, 10000.
- Y. Nosenko, G. Wiosna-Salyga, M. Kunitski, I. Petkova, A. Singh, W. J. Buma, R. P. Thummel, B. Brutschy and J. Waluk, *Angew. Chem., Int. Ed.*, 2008, **47**, 6037.
- C. Möller and M. S. Plesset, *Phys. Rev.*, 1934, **46**, 618.
- T. H. Dunning Jr., *J. Chem. Phys.*, 1989, **90**, 1007.
- H.-S. Kim, D.-S. Ahn, S.-Y. Chung, S. K. Kim and S. Lee, *J. Phys. Chem. A*, 2007, **111**, 8007.
- S. F. Boys and F. Bernardi, *Mol. Phys.*, 1970, **19**, 553.
- A. D. Becke, *J. Chem. Phys.*, 1993, **98**, 5648.
- M. J. Frisch, G. W. Trucks, H. B. Schlegel, G. E. Scuseria, M. A. Rob, J. R. Cheeseman, J. A. Montgomery Jr., T. Vreven, K. N. Kudin, J. C. Burant, J. M. Millam, S. S. Iyengar, J. Tomasi, V. Barone, B. Mennucci, M. Cossi, G. Scalmani, N. Rega, G. A. Petersson, H. Nakatsuji, M. Hada, M. Ehara, K. Toyota, R. Fukuda, J. Hasegawa, M. Ishida, T. Nakajima, Y. Honda, O. Kitao, H. Nakai, M. Klene, X. Li, J. E. Knox, H. P. Hratchian, J. B. Cross, V. Bakken, C. Adamo, J. Jaramillo, R. Gomperts, R. E. Stratmann, O. Yazyev, A. J. Austin, R. Cammi, C. Pomelli, J. W. Ochterski, P. Y. Ayala, K. Morokuma, G. A. Voth, P. Salvador, J. J. Dannenberg, V. G. Zakrzewski, S. Dapprich, A. D. Daniels, M. C. Strain, O. Farkas, D. K. Malick, A. D. Rabuck, K. Raghavachari, J. B. Foresman, J. V. Ortiz, Q. Cui, A. G. Baboul, S. Clifford, J. Cioslowski, B. B. Stefanov, G. Liu, A. Liashenko, P. Piskorz, I. Komaromi, R. L. Martin, D. J. Fox, T. Keith, M. A. Al-Laham, C. Y. Peng, A. Nanayakkara, M. Challacombe, P. M. W. Gill, B. Johnson, W. Chen, M. W. Wong, C. Gonzalez and J. A. Pople, *GAUSSIAN 03*, Gaussian, Inc., Wallingford, CT, 2003.
- C. Plützer and K. Kleinermanns, *Phys. Chem. Chem. Phys.*, 2002, **4**, 4877.
- Y. Nosenko, M. Kunitski, Ch. Riehn, R. P. Thummel, A. Kyrchenko, J. Herbich, J. Waluk and B. Brutschy, *J. Phys. Chem. A*, 2008, **112**, 1150.
- P. Colarusso, K. Zhang, B. Guo and P. Bernath, *Chem. Phys. Lett.*, 1997, **269**, 39.
- W. Zierkiewicz, L. Komorowski, D. Michalska, J. Černý and P. Hobza, *J. Phys. Chem. B*, 2008, **112**, 16734.
- R. Wu, P. Nachtigall and B. Brutschy, *Phys. Chem. Chem. Phys.*, 2004, **6**, 515.
- T. Shimanouchi, *Tables of Molecular Vibrational Frequencies Consolidated Volume I*, National Bureau of Standards, Washington, 1972.
- Y. Yamada, N. Mikami and T. Ebata, *Proc. Natl. Acad. Sci. U. S. A.*, 2008, **105**, 12690.
- H. Yokoyama, H. Watanabe, T. Omi, S. Ishiuchi and M. Fujii, *J. Phys. Chem. A*, 2001, **105**, 9366.
- M. Sakai, S. Ishiuchi and M. Fujii, *Eur. Phys. J. D*, 2002, **20**, 399.
- E. Fujimaki, A. Fujii, T. Ebata and N. Mikami, *J. Chem. Phys.*, 2000, **112**, 137.
- N. J. Kim, G. Jeong, Y. S. Kim, J. Sung and S. K. Kim, *J. Chem. Phys.*, 2000, **113**, 10051.
- N. J. Kim, Y. S. Kim, G. Jeong, T. K. Ahn and S. K. Kim, *Int. J. Mass Spectrom.*, 2002, **219**, 11.
- M. Zakharov, O. Krauss, Y. Nosenko, B. Brutschy and A. Drew, *J. Am. Chem. Soc.*, 2009, **131**, 461.

Acknowledgments

The results of the current thesis were obtained in the time period from November 2004 to November 2009 at the Institute of Physical and Theoretical Chemistry of Goethe-University Frankfurt am Main in the research group of **Prof. Dr. Bernhard Brutschy**.

Here I would like to thank people without whose this work has not been made possible.

I am highly indebted to my supervisor **Prof. Dr. Bernhard Brutschy** for giving me the opportunity to work in his research group, for his ideas, advices, guidance and incessant support. He has taught me to work effectively, for which I am deeply appreciative.

I gratefully thank to **PD Dr. Christoph Riehn** for introducing me to the femtosecond world, for his fruitful ideas and help. I have learned a lot from his vast experience in the femtosecond lab.

I would like to thank my dear friend **Dr. Victor Matylitsky** for all that he has done for me, concerning not only the scientific side of life.

I am also thankful to **Dr. Yevgeniy Nosenko** for a very fruitful collaboration and extending my knowledge in the field of molecular beam spectroscopy.

I am grateful to **Dr. Maxim Gelin** for being always ready to help, for lots of discussions and advices concerning the theoretical aspects of femtosecond degenerate four-wave mixing spectroscopy.

I am obliged to **Prof. Dr. A. Dreuw, Dr. S. Knippenberg, Philipp Harbach** and **Dr. P. Tarakeshwar** for support with quantum chemistry calculations.

I would like to thank **Mr. Martin Engels** for the many electronic devices he made for the experimental setup and the workshop-team under the direction of **Mr Helmut Jäger** and **Mr Herbert Ott** for their help in developing experimental setup.



I would like to thank **Mrs Renate Gregori** for her persistent help with red-tape, which allows me to concentrate more on the scientific stuff.

Many thanks to the former and present members of the research group of Prof. B. Brutschy for their help, advices and good working atmosphere. In particular, **Dr. Hans-Dieter Barth, Dr. Nina Morgner, Michael Barashkov, Dr. Fuat Altunsu, Jan Hoffmann, Lucie Sokolova, Mihaela Cazacu, Peter Richter**.

Finally, I would like to acknowledge my wife **Zoya** for her love, encouragement and support throughout these years.

Curriculum Vitae

Personal

Name	Maksim Kunitski
Address	Burgstr. 2, 60316 Frankfurt am Main, Germany
	+49(0)69-798-29-434
	kunitski@chemie.uni-frankfurt.de
Date of Birth:	8 th June 1980
Place of Birth:	Gresk, Weißrussland

Education

nov. 04 - dec. 09	PhD student at institute of physical and theoretical chemistry of Goethe University Frankfurt Dissertation: "Structure and dynamics of molecules and molecular aggregates in gas phase studied by femtosecond spectroscopy" Adviser: Prof Dr. Brutschy
sep. 02- okt. 04	Junior scientist at Scientific-Research Institute for Applied Physics Problems (Minsk, Weißrussland)
sep. 97- aug. 02	Department of radio physics and electronics of Belarusian State University
sep. 95- aug. 97	Lycée of Belarusian State University

Publications

"Missing levels lead to additional lines: the influence of nuclear spin statistics on femtosecond degenerate four wave mixing spectroscopy of polyatomic systems"

C. Riehn, M.I. Kunitski, V.V. Matylitsky, M.F. Gelin, and B. Brutschy
Physical Chemistry Chemical Physics, 2005, **7**(23): p. 3955-3962.

"Pseudorotation in pyrrolidine: rotational coherence spectroscopy and ab initio calculations of a large amplitude intramolecular motion"

M. Kunitski, C. Riehn, V.V. Matylitsky, P. Tarakeshwar, and B. Brutschy
Physical Chemistry Chemical Physics, 2010, **12**: p. 72-81.

"Ring-puckering motion in cyclopentene studied by time-resolved rotational coherence spectroscopy and ab initio calculations"

M. Kunitski, S. Knippenberg, M. Gelin, C. Riehn, A. Dreuw, and B. Brutschy
Physical Chemistry Chemical Physics, 2010, **12**: p. 8190-8200.

"Detection and structural characterization of clusters with ultrashort-lived electronically excited states: IR absorption detected by femtosecond multiphoton ionization"

Y. Nosenko, M. Kunitski, R.P. Thummel, A. Kyrychenko, J. Herbich, J. Waluk, C. Riehn, and B. Brutschy

Journal of the American Chemical Society, 2006, **128**(31): p. 10000-10001.

"Separation of different hydrogen-bonded clusters by fs UV-ionization-detected infrared spectroscopy: 1H-pyrrolo[3,2-h]quipoiline•(H₂O)_(n=1,2) complexes"

Y. Nosenko, M. Kunitski, C. Riehn, R.P. Thummel, A. Kyrychenko, J. Herbich, J. Waluk, and B. Brutschy

Journal of Physical Chemistry A, 2008, **112**(6): p. 1150-1156.

"Proton transfer with a twist? Femtosecond dynamics of 7-(2'-pyridyl)-indole in condensed phase and in supersonic jets"

Y. Nosenko, G. Wiosna-Salyga, M. Kunitski, I. Petkova, A. Singh, W.J. Buma, R.P. Thummel, B. Brutschy, and J. Waluk

Angewandte Chemie-International Edition, 2008, **47**(32): p. 6037-6040.

"The structure of adenine monohydrates studied by femtosecond multiphoton ionization detected IR spectroscopy and quantum chemical calculations"

Y. Nosenko, M. Kunitski, C. Riehn, P.H.P. Harbach, A. Dreuw, and B. Brutschy

Physical Chemistry Chemical Physics, 2010, **12**: p. 863–870.

Talks

Physikertagung der Deutschen Physikalischen Gesellschaft

Frankfurt am Main, 13-17 March 2006

105. Bunsentagung

Erlangen, 25-27 Mai 2006

PTC seminar

Frankfurt am Main, 14 January 2008

107. Bunsentagung

Saarbrücken, 1-3 May 2008

Posters

104. Bunsentagung

Frankfurt am Main, 05-07 May 2005

Femtochemistry and Femtobiology 8

Oxford, 22-27 July 2007

Femtochemistry and Femtobiology 9*Beijing, 08-13 August 2009***International Bunsen Discussion Meeting***Leipzig, 27-30 September 2009*